

**On the Effects of Geometry in Discrete Element
Numerical Earthquake Simulations**

by

Seth A. McGinnis

S.B., Massachusetts Institute of Technology, 1995

A thesis submitted to the
Faculty of the Graduate School of the
University of Colorado in partial fulfillment
of the requirements for the degree of
Doctor of Philosophy
Geophysics Graduate Program
Department of Geological Sciences

2001

This thesis entitled:
On the Effects of Geometry in Discrete Element Numerical Earthquake Simulations
written by Seth A. McGinnis
has been approved for the Department of Geological Sciences

John B. Rundle

Elizabeth Bradley

Date _____

The final copy of this thesis has been examined by the signatories, and we find that both the content and the form meet acceptable presentation standards of scholarly work in the above mentioned discipline.

McGinnis, Seth A. (Ph.D., Geophysics)

On the Effects of Geometry in Discrete Element Numerical Earthquake Simulations

Thesis directed by Professor John B. Rundle

Computer simulation is a widely-used component of earthquake research, but while many computer models of earthquakes exist, there are none that simulate both sub-fault activity and three-dimensional geometry. I develop a computer model of earthquakes that simulates activity on fault systems with three-dimensional geometry by calculating stress transfer between fault elements as a three-dimensional tensor quantity. This model is a discrete, quasi-static, cellular-automaton type model that generates failure cascade sequences of all sizes. The fault is represented as a collection of rectangular sub-faults or “fault patches” that are not constrained to a two-dimensional plane. Stress transfer is calculated as a tensor field originating from point sources in a linear elastic whole-space, though the effects of normal stress on the friction holding the surfaces of a fault element in place are neglected.

I then develop a procedure for studying the effects of geometry on the evolution of synthetic event histories in a computer model by systematically varying the configuration of a z-shaped or “zig-zag” fault and studying the results using scaling, clustering, correlation, and phase dynamic probability change (PDPC) analysis. I also study the effects of roughness and coupling parameters.

I find that, in the absence of normal stress effects, geometry does not act as a barrier to the development and propagation of events, but that differences in the rate of stress accumulation due to tectonic loading forces do; that geometric roughness does not change the dynamics of the system in a qualitative way; and that the PDPC analysis methodology cannot be effectively applied to simulation data of the quality that can be currently generated.

To Them What Kept Me Sane:

Jerry, Chris, Rose, Karen, Thomas, Jeff, Alice, Neal, Rhonda, Nick, Jen, Jay, Laura, Joe,

and Kate...

...as well as Bryan, Jean-Pauli, Eddie, Cyrus, Gustav, Lillian, Fang, Smurch, Harmonic

Fifth, and Norm the Indefinite Elephant.

Acknowledgements

This work could never have been completed without the assistance, support and contributions of a great many people. I would particularly like to thank:

My advisor, John Rundle, for his insight, guidance, willingness to let me follow nontraditional paths, and, especially, his patience.

My colleagues Jorge de sa Martins, Susanna Gross, and especially Kristy Tiampo, for their invaluable advice, counsel, and willingness to listen, time and again, whether it was work-related or not.

The members of my thesis committee, Liz Bradley, Lang Farmer, Michael Grant, and Doug Robertson, for their commentary and criticism, and for supporting cross-disciplinary research in degree both large and small.

My fellow graduate students Marian Anghel, Eric Blough, Diane Fritz, Peter Furey, Hersh Gilbert, Shannon Hazler, Rich Pelaia, Kristy Tiampo, and Seth Veitzer, for their help, advice, assistance, and for sharing the experience.

The University of Colorado Chancellor's Fellowship program, NASA's Earth Science Systems fellowship program (grant number ESS/97-0110), and the United States Department of Energy (grant number DE-FG03-95-ER14499), whose contributions funded this research.

And finally, my friends and family, without whose support I would have given up long ago.

Contents

Chapter

1	Introduction	1
1.1	Background	1
1.2	Motivation	4
2	Earthquake Models	7
2.1	Cellular Automaton Earthquake Models	8
2.1.1	The Slider-Block Model	8
2.1.2	Uniform Interaction Models	10
2.1.3	Truncated Interaction Models	11
2.1.4	Range-Dependent Interaction Models	11
2.2	The Fault-Patch Model	12
2.3	Algorithmic Considerations	14
2.4	Stress Transfer: Finite vs Point Sources	16
2.5	Friction Laws and Stress Leakage	21
3	Analysis Tools	27
3.1	Gutenberg-Richter Scaling	28
3.2	Eigenmode Analysis	29
3.3	PDPC Analysis	32
3.4	Stress Clustering Analysis	35

3.5 Recurrence Plot Analysis	37
4 Parametric Effects	40
4.1 Stress Decay	40
4.1.1 Statistics of Stress Decay	48
4.1.2 Temporal Clustering	53
4.2 Interaction Strength	60
5 The Z-Shaped Fault	67
5.1 Geometry	68
5.2 Statistics of Seismic Activity	69
5.2.1 History and Transient Behavior	69
5.2.2 Scaling	72
5.3 Cluster Analysis	80
5.4 Correlation Analysis	91
5.4.1 Phase Correlation	91
5.4.2 Activity Correlation	95
5.5 PDPC Analysis	112
5.6 Recurrence Plot Analysis	117
6 Conclusion	121
6.1 Summary	121
6.2 Future Work	123
Bibliography	125

Appendix

A Co-authored Papers	137
-----------------------------	-----

Figures

Figure

2.1	Normal-Force Contribution Histogram	25
3.1	PDPC Index for Southern California, 1991-1978	34
3.2	Recurrence Plot for Lorenz Attractor Data	38
4.1	Flat Fault Loading Stress	41
4.2	Event Size Distributions and α	43
4.3	Space-Time Diagram, $\alpha = 0.00, 0.05$	45
4.4	Space-Time Diagram, $\alpha = 0.12, 0.18$	46
4.5	Space-Time Diagram, $\alpha = 0.22, 0.27$	47
4.6	Gutenberg-Richter Scaling as a function of α	49
4.7	Magnitude-Frequency Scaling for $\alpha = 0.00$	49
4.8	Magnitude-Frequency Scaling for $\alpha = 0.05$	50
4.9	Event Size Histogram, $\alpha = 0.05$	50
4.10	Magnitude-Frequency Scaling for $\alpha = 0.10$	51
4.11	Event Size Histogram, $\alpha = 0.10$	51
4.12	Magnitude-Frequency Scaling for $\alpha = 0.18$	52
4.13	Event Size Histogram, $\alpha = 0.10$	52
4.14	Recurrence Interval Histogram, $\alpha = 0.00$	54
4.15	Recurrence Interval Histogram, $\alpha = 0.03$	55

4.16 Recurrence Interval Histogram, $\alpha = 0.08$	55
4.17 Recurrence Interval Histogram, $\alpha = 0.12$	56
4.18 Recurrence Interval Histogram, $\alpha = 0.15$	56
4.19 Recurrence Interval Histogram, $\alpha = 0.18$	57
4.20 Event Size Distributions and the SNR	61
4.21 Magnitude-Frequency Scaling, SNR = 60	63
4.22 Magnitude-Frequency Scaling, SNR = 70	64
4.23 Magnitude-Frequency Scaling, SNR = 90	65
4.24 Magnitude-Frequency Scaling, SNR = 120	66
5.1 The Z-Shaped Fault	68
5.2 Seismic Histories for Various θ	70
5.3 Evolution from Different Seeds	71
5.4 Transient Large Events	73
5.5 Large Event Spacing	74
5.6 Synthetic Event History	75
5.7 Post-Transient Event Areas	76
5.8 Steady-State Event History, $\theta = 0$	77
5.9 Steady-State Event History, $\theta = 45$	78
5.10 Steady-State Event History, $\theta = 90$	79
5.11 Moment-Area scaling, $\theta = 45$	81
5.12 Moment-Frequency Scaling	82
5.13 B-Value for Several Values of θ	83
5.14 Cluster Stress Evolution, $z = -2.5$, $\theta = 0$	85
5.15 Vertically-Averaged Cluster Stress Evolution, $\theta = 0$	86
5.16 Vertically-Averaged Cluster Stress Evolution, $\theta = 30$	87
5.17 Vertically-Averaged Cluster Stress Evolution, $\theta = 90$	88

5.18 Stress Cluster Area Distribution Evolution, $\theta = 30$	89
5.19 Stress Cluster Area Distribution, All Geometries	90
5.20 Phase Correlation Matrix, $\theta = 0$	92
5.21 Phase Correlation Matrix, $\theta = 30$	93
5.22 Phase Correlation Matrix, $\theta = 90$	94
5.23 Stress Snapshot, $\theta = 90$	94
5.24 Expanded Correlation Matrix, $\theta = 0$	96
5.25 Expanded Correlation Matrix, $\theta = 60$	97
5.26 Correlation Matrix, $\theta = 0$	99
5.27 Correlation Matrix, $\theta = 30$	100
5.28 Correlation Matrix, $\theta = 60$	101
5.29 Correlation Matrix, $\theta = 90$	102
5.30 Correlation Matrix, Three-Part Neural Net	104
5.31 First Thirty EOFs, $\theta = 60$	105
5.32 First Thirty EOFs, Synthetic $1/x$ Correlation Matrix	106
5.33 Correlation Matrix, $\theta = 45$ With Fast Central Segment	109
5.34 Correlation Matrix, $\theta = 45$ With Slow Central Segment	110
5.35 Correlation Matrix, $\theta = 45$ With Differential Loading	111
5.36 PDPC Index Evolution for Synthetic Data, $\theta = 0$	113
5.37 PDPC Index Evolution for Rebinned Synthetic Data, $\theta = 0$	115
5.38 Recurrent Plot, Interval = 500	118
5.39 Recurrence Plot Diagonal Segment Lengths	119

Chapter 1

Introduction

Large earthquakes present a significant hazard to life and property to all those who live in seismically active regions. Understanding the physics of earthquakes is an important component of any effective strategy for mitigating that hazard. Large earthquakes are impossible to reproduce experimentally in the laboratory; ignorance regarding the governing equations prevents the creation of dynamically similar scale models, and full-sized models would be tens or even hundreds of kilometers in length[93]. For this reason, much modern research on the physics of earthquakes has focused on computer simulations of earthquakes. This research has culminated in the development of a two-dimensional cellular-automaton type earthquake model; this model is simple, robust, and exhibits many of the features of real seismicity. The goal of my research is to extend this model from two dimensions into three.

1.1 Background

The use of computational simulation of earthquake activity as a stratagem for understanding seismicity begins with a paper written by Burridge and Knopoff in 1967 [28]. In this paper, they proposed that a vertical strike-slip fault in the Earth's crust can be modeled as a one-dimensional string of sliding blocks connected to one another by springs. When the tectonic forces acting on one part of the fault, represented by a single block, build up sufficient strength to overcome the cohesive strength of the fault, it slips to relieve the stress: the block begins to slide. As the block slides, the springs connecting it to its neighbors change length, altering the

forces acting on them as well. If the change in force is sufficient, the neighboring blocks can begin to slide as well. The blocks slide until the frictional force (a function of velocity) opposing the slip is great enough to halt their motion. The slip of the blocks models the slip of the two surfaces of the fault past one another during an earthquake. After an earthquake has ended, the surfaces re-adhere to one another and the cycle begins again. In this model, the build-up of tectonic forces is represented by the externally-driven motion of a “loader plate” that is connected to the blocks. In the canonical Burridge-Knopoff (B-K) model, each block is connected to a loader spring, while in the so-called “train” model only the end block is. Burridge and Knopoff also presented numerical simulation results in their paper showing that the stick-slip behavior of this model is similar to that of a real earthquake fault. Since then, many variations on the B-K model have been proposed.

The first major revision of the B-K model’s dynamics, much ignored in the literature, was by Rundle and Jackson [128], who formulated the dynamics in a quasistatic form. Under this simplification, each block is allowed to slip to a rest state independently while the other blocks remain stuck. This assumption gives the model a formulation that is significantly simpler to calculate than solving the equations of motion of many coupled blocks slipping simultaneously. Although this is often referred to as a “cellular automaton (CA)” version of the B-K model, it is technically a coupled map lattice (CML) rather than a CA, as it is discrete in time and space but continuous in state space. [20] Rundle and Jackson’s model also replaces the random cohesive strengths of the B-K model with a uniform failure strength plus a random overshoot.

Many of these modifications were repeated and, in some cases, refined by other researchers. Carlson and Langer [31] made the B-K model deterministic by replacing the spatially-varying cohesive strength with a uniform strength. The only source of randomness in their model is in the initial conditions, showing that the complex behavior of the system is inherent to its internal dynamics, rather than generated by the variations in the properties of the fault surface. Nakanishi [101] also simplified the B-K model by changing the dynamics to a quasistatic form.

Before other researchers began simplifying the dynamics of the B-K model, Otsuka [111]

generalized it to two dimensions. The sliders now form a square lattice covering the plane. This modification was largely neglected until Brown, et al, created a coupled map lattice version of this model [25, 122] by generalizing the one-dimensional model of Rundle and Jackson to two dimensions. The Rundle-Jackson-Brown or RJB model can equivalently be thought of as combining the quasistatic “jump rule” and uniform failure strength of Nakanishi and Carlson-Langer, respectively, with the two-dimensional formulation of Otsuka.

A parallel line of development begins with Bak, Tang, and Wiesenfeld [181] who created the “sandpile” cellular automaton, which exhibits self-organized criticality. After the suggestion that earthquakes may also be an example of self-organized criticality [13], Feder and Feder [54] generalized the sandpile model to a non-conservative, continuous local force model, making it a CML rather than a CA. Although there have been many arguments against the view that earthquakes exhibit self-organized criticality [123, 147, 132, 55], the Feder and Feder model was useful in the development of other models. Olami, Feder, and Christiansen [110] synthesized the Feder and Feder model and the Nakanishi model to create a 2-D “OFC” model derivable from the original B-K model. The OFC model and the RJB model are dynamically identical, but the former is formulated in terms of stress variables and the latter in terms of slip variables. Stress variables are in many ways more convenient for computer simulation, while slip variables are useful for statistical mechanical calculations.

Recent variations on the RJB/OFC model include an RJB model with extended-range interactions, [87] and the addition of viscous relaxation to the OFC model,[112, 70, 69, 71]. Kwantai, et al, [92] relaxed the constraint that all blocks must slip only in the x-direction by replacing the leaf springs that connect blocks laterally with coil springs.

Many more results have been obtained for variations on the one-dimensional B-K model as well, including simulations on models with plastic creep [66, 67] and nonlinear springs [8]. Experiments with different random and fractal distributions of quenched disorder in the cohesive strength [89, 170, 172] have shown that these distributions have only a minor effect on the dynamics of the system. Other researchers have discovered traveling wave [52] and self-sustaining

shock wave [100] solutions for the system, as well as chaos and synchronized chaos in two-block [77, 104] and three-block [43] systems, respectively. Increasing the number of blocks shows a transition from chaos to Gutenberg-Richter scaling via a route of increasing intermittency [40].

While many of these variations are interesting, they serve mostly to establish the simplicity of the minimal model. The RJB/OFC model remains the foundation model for two-dimensional systems, for reasons of both computational practicality and completeness of study. The next evolutionary step in this field of research is the development of an equivalent three-dimensional model.

1.2 Motivation

Even the most sophisticated discrete-element earthquake models are fundamentally two-dimensional in nature; there are no mechanisms present that would allow us to model the interactions between different parts of a fault that arise due to three-dimensional geometries. Certainly in the real world, geometry can have a significant effect on the activity of a fault system. [76, 86, 106, 116, 143, 150, 151, 149] Therefore, I decided to create a computer model that would retain the structure of the RBJ and OFC models, but also be able to simulate activity on faults with any sort of three-dimensional geometry. Retention of a structural connection between the slider-block model and the new model provides a standard for comparison; any statistical features of the former should carry over to the latter in an appropriate configuration. In addition, the generalization of slider-block model to a three-dimensional analogue is conceptually straightforward. Despite the intellectual simplicity of this change, however, it is still significant, and it is beyond the scope of a single research project to model all the effects of a realistic three-dimensional fault configuration. In particular, I found it necessary to omit the effects of normal forces on the frictional cohesion of the fault and those of a free surface on stress transfer from the model.

Another goal of this research is to establish a protocol for studying three-dimensional earthquake fault simulations. The configuration space of 3-D models is vast in comparison to

that of 2-D models, and a systematic approach is needed to overcome the problem of near-infinite choice that it presents. A careful examination of a basic system also creates a baseline of data against which future research can be compared as new dynamical features (such as the effects of normal force on friction) are added to these models.

I decided to study a family of simple but realistic configurations that can be parametrically varied to change the severity of the geometry. I began with an examination of the effects of several system parameters on a flat fault. Because this geometry is equivalent to that of the well-studied RJB / OFC model, I used it to verify that the dynamics were also equivalent. In other words, I began with a check that the established two-dimensional models can be reproduced as a special case of the three-dimensional model. I then chose to model a fault with a realistic size and shape: a long, thin fault with two bends. Many natural faults, like the San Andreas, are hundreds of kilometers long, but only a few tens of kilometers deep [7, 65]; I used three fault segments with an aspect ratio of 10 : 1. I chose to use a z-shaped fault (a fault that bends left, then right) because the existence of two opposite angles allows for the possibility of frustration, in that two segments of the fault can have an opposite influence on the third. This is an interaction that is very difficult to model in a two-dimensional slider-block model. I studied the effects of this geometry by parametrically increasing the bend angle from zero degrees (a straight fault) up to a ninety-degree right angle and simulating event histories on each configuration.

Finally, a third goal of the research is to examine the utility of various mathematical tools in the understanding of the behavior the simulated system. Previous research on slider-block systems has often limited analysis of the data to a few space-time plots of activity and some analysis of the statistical distribution of event sizes and recurrence intervals. Many sophisticated mathematical constructs have proven useful in the study of observed seismicity [78, 131, 158, 136, 156, 159, 157, 161], and a crucial step in the understanding of the physics of earthquakes is to understand how the patterns and features of real seismicity relate to those of synthetic seismicity, which in turn can lead to a greater understanding of the differences between real and

simulated earthquake activity.

The thrust of this research, then, is to define a slider-block computer earthquake model analogue in such a way as to include three-dimensional geometry, particularly three-dimensional shear stress transfer; to explore the configurations of a fault with simple but non-trivial geometry in a systematic fashion, thereby establishing a procedure or protocol for studying the effects of three-dimensionality on the model; and to analyze the resulting synthetic activity catalogs with a variety of mathematical tools in an effort to understand the patterns of activity produced.

Chapter 2

Earthquake Models

Modeling is an important component of the scientific effort to understand the physics of earthquakes. Southern California is inconveniently sized to fit into a laboratory for experimentation, and many of the physical processes involved in earthquakes are not understood well enough for researchers to reliably extrapolate the small-scale laboratory experiments that they can perform to the scale at which earthquakes occur. In addition, earthquake processes are noisy, so to apply many of the mathematical and statistical methods that have been developed, we must study entire ensembles of event histories and not restrict ourselves to the singular history found in nature. To overcome these difficulties, we make computer models.

There are three general classes of synthetic earthquake models. The first is the microscopic model [98, 117]. These models take an ultra-reductionist approach: they model the very smallest scale (individual grains of rock or fault gouge in the fault zone) as accurately as possible, under the assumption that if the micromechanics are correct, the macromechanics will follow on their own. This seems a promising approach, but only a few researchers have undertaken it, and the computational requirements are sufficiently high that modeling a fault system on the synoptic scale with this class of model seems a doomed enterprise with our current technology.

The mid-scale approach to earthquake modeling is the elastodynamic model. Elastodynamic models are concerned with the accurate portrayal of the kinematics of rupture, and attempt to realistically model the temporal evolution of each event using finite-element or finite-difference codes [16, 17, 50, 107]. These models are very useful for the study of rupture propagation

tion and are especially valuable as back-ends for programs that model the resulting seismic waves and their effects. However, the accuracy and stability of finite element models depends critically on having a sufficient mesh density and resolution. Modeling large three-dimensional fault systems is therefore computationally prohibitive, especially (given the inherently small time-steps these models use) if we desire to study the long-term behavior of a complicated system.

The approach most amenable to large-scale modeling is the quasi-static model. These models neglect the deterministic details of any given event in order to focus more upon the development of space-time patterns and correlations in a sequence of many events, and on the effects of each event on the evolution of the system as a whole. There are two sub-types of this model: slip-rate based models [174, 126], and so-called cellular automaton (CA) type models. The CA family is of primary interest here and is discussed in more detail below. Quasi-static models can effectively approach problems on the large temporal and spatial scales, and are therefore ideal for generating long-term synthetic event histories. We believe that these large datasets are essential for understanding earthquake physics; because all parts of a large fault system interact with one another, the system must be approached in a holistic fashion to be understood. The existence of precursory signals in the fault network before large events [158] (signals detected using the PDPC index measurement, discussed further in Chapter 3) supports this idea of an entire seismic region as a strongly correlated system.

2.1 Cellular Automaton Earthquake Models

2.1.1 The Slider-Block Model

The cellular automaton class of earthquake model derives from the spring-block or slider-block construction of Burridge and Knopoff [28], and its members are therefore often also referred to as “slider-block” models. Conceptually, the elements of the slider-block model are like massless blocks resting on the top of a table. The blocks are free to slide, but are held in place by frictional forces. Each block is connected to its neighbors by springs. The interfaces between block and

table represent pieces of the fault surface, and the springs represent the elastic medium in which the fault is embedded. Rock typically has very linear, albeit very stiff, elastic behavior on short time scales, so Hookean springs are a good approximant of the medium. It is generally accepted that the two sides of the fault are prevented from sliding past one another by friction. Finally, the model is driven by attaching each block by another spring to a “loader plate”, which can be conceptualized as another table hanging down above the first one and moving very slowly in parallel to the surface. This construction represents the driving forces that are generated by tectonic plate motion. [133]

As the loader plate creeps slowly along, the springs connecting it to the blocks stretch, exerting more and more force on the blocks. When the elastic force acting on the block is sufficient to overcome the frictional force holding it in place, the block will “fail” and slide to a new position of lower energy. When it does so, not only will the length of the loader spring change, the lengths of the connector springs will also change. This changes the net force acting on the neighboring blocks, and may induce them to fail as well. This avalanche of failures is what allows a large event to grow from the failure of a single block.

We can write down the equations of motion for this system as follows: The force acting on the i th block is:

$$\sigma_i = -K_L\phi_i - \sum_j K_{ij}(\phi_j - \phi_i), \quad (2.1)$$

where $\phi = -(Vt - s)$ is the negative of the slip deficit, which corresponds to the difference between the block’s displacement and the loader plate’s displacement; K_L is the spring constant of the loader spring; and K_{ij} is the spring constant of the spring connecting the i th and j th blocks.

The evolution of the system through time is governed by a rule that describes the behavior of a block when it fails. If the residual stress of the i th block is denoted by σ_i^R , the slip distance

$$\Delta s_i = (\sigma_i - \sigma_i^R)/(K_L + \sum_j K_{ij}) \quad (2.2)$$

will drop the force on the block down to the residual level when it exceeds the static failure

threshold σ^F and begins to slip. Thus, we can construct a “jump rule” to apply to the system that will evolve its state forward in time:

$$s_i(t+1) = s_i(t) + \Theta(\sigma_i - \sigma_i^F) \left((\sigma_i - \sigma_i^R)/(K_L + \sum_j K_{ij}) \right) \quad (2.3)$$

where $\Theta(x)$ is a Heaviside step-function.

If certain simplifying assumptions can be made, it is possible to abstract away the physical system of springs and blocks and cast the model in the form of a cellular automaton. It is helpful if quantities such as σ^F are spatially constant, but the most important requirement is that the interaction matrix K have a form that allows it to be rewritten as a set of interaction coefficients in a neighborhood of the block. This in turn requires that the blocks be arranged in a lattice, but as many simulations proceed under this assumption already, it is not a burdensome requirement.

2.1.2 Uniform Interaction Models

Within the scope of the equations above there are still many variations on the basic form of the model, based for the most part on the form of the connectivity matrix K_{ij} . One of the simplest forms of the model to consider is the uniform interaction case: in this construction, all blocks are identical and each is connected to every other block in the model [88, 130, 55]. This is a useful scenario to consider because as the number N of blocks approaches infinity, the model approaches the mean-field limit of behavior. It is worth noting that this system is geometry-free; the blocks are indistinguishable and all of the interactions are the same. Since there are no features differentiating one part of the model from another, there is effectively no such thing as space in this model. Since each element “sees” all other elements of the model equally, the net interaction force on each element is proportional to the mean slip-deficit of all the blocks in the model. Thus, as the size of the model increases and slip-deficit fluctuations away from the mean decrease, the system will approach a limit where each element is isolated in a thermal bath. Since large events occur only when the slip-deficits of many elements are correlated and near the failure threshold, we can see that the finite size of the model is key to the

existence of large-scale fluctuations that generate interesting behavior. However, this finite-size requirement applies only to the uniform, infinite-range interaction CA model.

2.1.3 Truncated Interaction Models

If we wish to step back from the mean-field thermodynamic limit, we can introduce some basic spatial dependence into the model by giving it a truncated interaction range [55, 87]. In this model, all cells that are within some radius R of one another interact uniformly, and beyond that distance they do not interact. While this implementation of spatial effects is simplistic and perhaps a little unnatural, it is sufficient to eliminate the effects of the global mean slip-deficit and allow large correlated regions of fluctuation away from the mean to exist. It is a formulation which allows the algorithms for calculating interaction to be very simple, and therefore allows models with a very large number of elements to be run in a short time.

2.1.4 Range-Dependent Interaction Models

The most sophisticated model (geometrically) for which the equations above still apply incorporates range-dependent interactions [136, 126, 124, 132]. The unstated assumption of equations 2.1-2.3 is that the blocks rest on the same plane and slide in the same direction. That being the case, all vector force quantities can be treated as scalars. The most complex geometry that we can accommodate within this assumption is therefore the two-dimensional plane. In the range-dependent CA model, the strength of the force acting on one element due to the slip-deficit of another is proportional to the distance R between them. In general, a $1/R^3$ rule is used – that is, the strength of the connector springs dies off as $1/R^3$. This is because in a three-dimensional elastic medium, the stress due to a point dislocation (a force double-couple) drops off as the cube of the distance. The $1/R^3$ rule therefore is the most realistic treatment of geometry that is still restricted to two dimensions.

2.2 The Fault-Patch Model

This research introduces the Fault-Patch model. The Fault-Patch model can be thought of as the result of generalizing a spring-block model from a two-dimensional lattice to a collection of elements with arbitrary position and orientation in three dimensions. It can also be thought of as a simple model representing the quasi-static interaction between realistic three-dimensional faults. In either case, my paramount design objective in creating the model was to constrain the geometry of the fault system as little as possible in a slider-block type model.

The spring-block model consists of two basic elements: springs and blocks. If we consider the functions of these elements in the model, the conversion from two to three dimensions will be clear.

Consider first the blocks. The interface between the blocks and the surface that they contact represents the surface of the fault; each block is a piece of the fault that can slip independently of the other pieces. Though we often think of them as physical blocks resting on a table, they are massless according to the definition of the model. It is clear, then, that the actual blocks themselves are irrelevant; it is only the pair of surfaces (block and table) that matter. To leave behind the two-dimensional constraint of blocks on table, we simply discard the blocks and keep the pairs of surfaces where the blocks contact the surface they rest on. Embed the pair of surfaces in an elastic medium, and they become a simple plane discontinuity within the medium.

Alternatively, the simplest way to represent an earthquake fault in three dimensions is as a set of planar discontinuities in the earth. A real fault, of course, is not a geometric plane – it is not even a simple surface, but is a zone of broken rock with some finite thickness. However, on the scale of hundreds to thousands of meters, representing it as a surface is not a bad approximation. The surface is gridded into individual disconnected patches of fault, as in the slider block, but as the patches are now free to take on any orientation and position. Only the size of the patch limits the degree of roughness or other geometric complexity that can be

represented by the model.

In slider-block models, the blocks interact with one another through force transfer via springs. In three dimensions, the situation is considerably more complex. The patches no longer all have the same orientation, so they must interact through tensorial stresses instead of scalar forces. I replace the springs with the elastic medium in which the fault patches are embedded; when a patch slips, it causes a Volterra-type dislocation of the medium along the fault surface. The dislocation generates a field of strain (and therefore stress) throughout the medium. By using Green's functions, we can find analytic forms for the stress at any given observation point due to such a dislocation [152, 27].

Thus, instead of considering the lateral force applied to a block, we can calculate the shearing stress acting in the plane of the fault patch at its center to determine whether the patch will fail. Unlike the slider-block model, in the Fault-Patch model it is possible for the shear stress to be non-uniform across the surface of the patch; however, the assumption that the stress field is smooth at the patch length scale is a realistic one, and makes the problem tractable.

The only element of the model remaining to be considered is the driving force. In the slider-block model, a loader plate representing tectonic plate motion is used to drive the system. In nature, earthquakes are driven indirectly, by plate motions. As the portions of the lithosphere on two sides of a fault move past one another, the locked fault does not move. Strain (and equivalently, stress) builds up until the stress overcomes the frictional forces holding the fault in place. So it is really an accumulation of stress over time that drives the earthquake cycle. For the Fault-Patch model, I declined to model the relative plate motions and instead decided to use the loading stress rate to drive the model. This is simply a rate of stress accumulation for each patch, prescribed by the modeler, which is applied during the interseismic interval.

Though the model according to its definition does not have any constraints on the loading, it is worthwhile to briefly discuss the three most basic loading models. The first is simple uniform loading: every patch accumulates the same stress (in the patch's local frame of reference) at the

same rate. This method has the advantage of simplicity, but it may be physically unrealistic if the geometry of the model is not very simple. A similar but more general approach is to prescribe some stress rate in a global reference frame which is rotated into the local reference frame for each patch. This is an appropriate method of loading when some estimate of the regional stress field changes can be made. Finally, there is the slip-inversion or “backslip” method of loading. If an average slip rate can be defined for each patch, then displacing each patch backwards by one year and calculating the resulting stresses on every patch will give the annual stress rate that will (on average) result in the prescribed slip-rates [125, 174]. Each method of loading has its advantages and disadvantages and is appropriate for different modeling scenarios. The advantage of using a prescribed stress rate as the driving mechanism is that the modeler is free to choose the most appropriate method for the task at hand.

2.3 Algorithmic Considerations

In order to be useful, a computer simulation must run to completion in a short amount of wall-clock time using the computational resources available. This fact places some constraints on the implementation of the model that should be examined in order to understand its workings.

The processes at work in an earthquake system separate naturally into two groups according to whether they operate on a fast or slow time scale. Therefore, time in the Fault-Patch model is divided into two regimes: coseismic time and interseismic time. Interseismic time is the time between events. By definition, nothing happens in an interseismic interval except for the accumulation of stress leading up to the next event. Because the distribution of inter-event times is highly variable, we want to avoid using a fixed timestep to evaluate the stress accumulation. The ultimate expression of the adaptive timestep is to simply jump forward exactly to the beginning of the next event. This is possible, provided that the equations of stress evolution can be manipulated to give an expression for the time-to-failure of a patch.

A patch will fail when the shear stress exceeds the frictional stress threshold: $\sigma^S(t) \geq \sigma^F$.

Loading stress accumulates linearly over time, so the time dependence of any component of stress

is simply $\sigma(t) = \sigma(0) + \sigma^L t$. Combining these two facts and expanding the shear stress into its directional components, we obtain the following equation for the failure condition in the reference frame where \hat{z} is normal to the plane of the patch:

$$(\sigma_{xz}(0) + \sigma_{xz}^L t)^2 + (\sigma_{yz}(0) + \sigma_{yz}^L t)^2 \geq (\sigma^F + \mu N)^2 \quad (2.4)$$

This equation includes the effects of Coulomb friction μN on the static frictional threshold.

We can then solve for t to find an equation for the time-to-failure of a patch, given the stress σ^0 at time $t = 0$ and the loading-rate stress tensor σ^L :

$$t_f \geq -\frac{\sigma_{xz}^0 \sigma_{xz}^L + \sigma_{yz}^0 \sigma_{yz}^L \pm \sqrt{((\sigma^F + \mu N) \sigma_{xz}^L)^2 + ((\sigma^F + \mu N) \sigma_{yz}^L)^2 - (\sigma_{yz}^0 \sigma_{xz}^L - \sigma_{xz}^0 \sigma_{yz}^L)^2}}{(\sigma_{xz}^L)^2 + (\sigma_{yz}^L)^2} \quad (2.5)$$

This equation assumes that the zz component of the loading stress is zero, but a similar equation holds if it is not.

Given this analytic form for the stress as a function of (interseismic) time, we can evolve the system directly from one event to the beginning of the next. We simply evaluate the time-to-failure function for each patch, and step forward by the smallest value so found, which puts the model at the beginning of the next failure cascade. At this point, we halt interseismic time and begin coseismic time, so no loading occurs while the event is being resolved.

The failure cascade proceeds in a series of two-part sweeps over the collection of patches. In the first part of the sweep, we check which patches are about to fail. We also calculate for each failing patch how much slip is needed to relieve the stress acting on it. In the second part of the sweep, each of the failing patches is allowed to slip by the calculated distance. This cycle of checking and slipping continues until every patch in the model is below the failure threshold, at which point the event is over and we return to interseismic time.

When calculating the slip distance to relieve existing stress, each patch is considered independently. It is possible that this approach will introduce errors in the form of excess slip (since some stress may be relieved by the slip of other patches), or worse, allow oscillatory numeric instabilities to develop. However, by ignoring the patch-patch interactions in this

calculation, we avoid having to invert an $N \times N$ element matrix at every timestep, N being the number of patches, and the resulting decrease in computation is a considerable benefit.

Another source of possible instability comes from simultaneity of operations on the patches. Because the patches are all considered independently before any slip occurs, they are all evaluated at the same time. I chose this approach in order to avoid introducing any bias into the failure cascade due to the order of patch evaluation. However, it does allow instabilities similar to the “checkerboard” instability in an Ising model to occur [74]. These instabilities arise in situations where two sets of patches can slip in opposite directions at the same time, each set inducing upon the other a stress equal to or greater than the stress that was just relieved. This problem could be avoided with a randomized evaluation ordering, but this solution would require considerable extra time in development and has not been implemented.

Finally, it should be noted that “coseismic time” is not actually time. The Fault-Patch model does not enforce any sort of causality on the slip ordering, as would be required by a finite p- or s-wave velocity, nor is there any velocity to the slip. Each patch, when it slips, slips instantly down to its residual stress value and instantly transfers stress throughout the medium. However, this algorithm is a sufficient approximation for our purposes because we are interested in the correlations between events, rather than the deterministic details of a single event; therefore, we require only a long-term catalog of events. Attempting to approximate deterministic dynamics to any degree would add significantly to the complexity, development time, and execution time of the model, while the results would still be subject to considerable uncertainty and indeterminacy.

2.4 Stress Transfer: Finite vs Point Sources

The vast majority of the calculations that the model must perform are related to stress transfer between patches. In comparison to the calculations that cellular automata and CA-like models perform, the stress-transfer calculations are very complicated and time-consuming. Ideally, the model should take advantage of the fixed geometry of the system by calculating

interaction coefficients once and storing them for use in a lookup table. Unfortunately, this solution is just out of reach of today's computational resources. Studies of seismicity in California show regional correlations in activity that can extend over tens or hundreds of kilometers, which means that for a realistic model, the interaction range should be regarded as essentially infinite. If every element in the model can interact with every other element, there are N^2 interaction coefficients to consider. Each interaction coefficient must store twelve numbers (six unique components of the stress tensor, times two for the two directions of slip), each of which is eight bytes long. If N is in the low thousands, the total storage requirements are several hundred megabytes, which is not quite within the reach of a modern desktop workstation.

Since the stress-transfer coefficients cannot be precalculated and stored, they must be recalculated each time a patch slips. There are two ways this can be done: quickly, or correctly. If the elastic medium is assumed to be linear and homogeneous in nature, the Green's functions for stress due to a finite discontinuity can be analytically derived. Okada [108] gives the general equations for all six components of strain (and therefore stress) due to slip in any direction of a finite rectangular discontinuity in a half-space. The only constraint on the source is that it must have one edge parallel to the free surface of the halfspace; there are no constraints on the observation point. These equations are complicated; a typical computation for a single component of the strain tensor involves approximately four hundred function calls of more than a hundred floating point operations apiece. They are, however, completely correct, at least for the geometrically ideal cases of elastic theory. They are also much too slow to be of practical use.

We can overcome this barrier by using an approximation. Instead of calculating the exact strain generated by a finite source, we calculate the strain due to a point source located at the center of the patch. The strain field generated by a point-source double-couple is known and relatively simple. Comparison of the strain fields generated by the two sources at distances greater than one patch width (the minimum spacing between two patch centers) shows that the fields are identical in the direction of slip and have an average difference of less than 4%

elsewhere, making the point-source a good approximation. The stress due to the point source at the center of the patch is singular; treatment of this problem is discussed further below.

The following equations [62] describe the stress at an observation point (x, y, z) due to a point-source located at the origin with slip in the x -direction and the normal to the plane in the z -direction:

$$\sigma_{xx} = \frac{3\mu M_0}{4\pi\rho r^5} 2xz\left[\left(\frac{1}{\beta^2} - \frac{1}{\alpha^2}\right)\left(2 - 5\frac{x^2}{r^2}\right) - \frac{2}{\alpha^2}\right] \quad (2.6)$$

$$\sigma_{yy} = \frac{3\mu M_0}{4\pi\rho r^5} 2xz\left[\left(\frac{1}{\beta^2} - \frac{1}{\alpha^2}\right)\left(1 - 5\frac{y^2}{r^2}\right) - \frac{1}{\alpha^2}\right] \quad (2.7)$$

$$\sigma_{zz} = \frac{3\mu M_0}{4\pi\rho r^5} 2xz\left[\left(\frac{1}{\beta^2} - \frac{1}{\alpha^2}\right)\left(2 - 5\frac{z^2}{r^2}\right) - \frac{2}{\alpha^2}\right] \quad (2.8)$$

$$\sigma_{xy} = \frac{3\mu M_0}{4\pi\rho r^5} yz\left[\left(\frac{1}{\beta^2} - \frac{1}{\alpha^2}\right)\left(1 - 10\frac{x^2}{r^2}\right) - \frac{1}{\alpha^2}\right] \quad (2.9)$$

$$\sigma_{yz} = \frac{3\mu M_0}{4\pi\rho r^5} xy\left[\left(\frac{1}{\beta^2} - \frac{1}{\alpha^2}\right)\left(1 - 10\frac{z^2}{r^2}\right) - \frac{1}{\alpha^2}\right] \quad (2.10)$$

$$\sigma_{zx} = \frac{3\mu M_0}{4\pi\rho r^5} \left[\left(\frac{1}{\beta^2} - \frac{1}{\alpha^2}\right)(x^2 + z^2 - 10\frac{x^2 z^2}{r^2}) + \frac{3y^2 - r^2}{3\alpha^2}\right] \quad (2.11)$$

M_0 is the moment of the source, and is equal to $(\mu \times area \times slip)$; μ , ρ , α , and β are constitutive properties of the elastic medium: the shear modulus, density, P-wave velocity, and S-wave velocity, respectively.

The distance r can be factored out of these equations, leaving only the directional dependence. The stress field varies smoothly enough that further computational savings can be achieved by evaluating the stress at points on a unit sphere once during initialization and storing the results in a lookup table [63]. With 100 divisions of the sphere in the polar direction and twice as many in the azimuthal, bilinear interpolation on this table gives stress values with an average error of less than 5% relative to directly calculated values. The resulting increase in computational speed is better than a factor of two, while the associated error is an order of magnitude smaller than the stress fluctuations due to noise in the form of residual stress, making this an acceptable simplifying assumption.

There are, however, two other important factors to consider besides the speed improvement when using this method of stress transfer calculation. The first is the matter of the free surface. Because the surface of the halfspace must be free of tractions [58], the stress from an

image source must be added to the stress due to the original point source. This involves some extra algebra much in the spirit of other math already underway and is trivial to implement. However, while the image source cancels all other components of stress at the surface, it doubles the normal component. We must then also add the response of the medium to the normal load, and in order to do so rapidly, we would require a closed-form formulation for the stress induced at any point in an elastic halfspace due to the integrated projection of a point-source double-couple radiation field onto the surface, for any arbitrary distance and orientation of the source. Perhaps unsurprisingly, no such formulation presently is known. The only solution to this dilemma, then, is to dispense with the free surface and run the model in a wholespace instead of a halfspace. Several considerations make this assumption valid. First, strike-slip faulting, which is our primary interest in the configurations studied, occurs primarily in a plane-strain context that is confined to two dimensions. Also important is the fact that free surface is a second-order correction to the deformation and strains generated by faulting in the earth, and has the most effect in the bulk medium away from the surface of the fault, outside the regime modeled by the Fault-Patch model. Most importantly, this research aims to study features of fault dynamics that are universal and independent of depth; there is no meaningful depth without a free surface, but this research has no need for depth, either. Therefore, I have omitted the effects of a free surface.

The second point to note is that we use point sources instead of finite sources to model the stress field generated by fault slip. On the surface, this might appear to be a gross oversimplification. However, the finite source is equally at odds with reality in a different fashion. A natural earthquake fault is neither flat nor rectangular. It is not even a two-dimensional surface; it is actually a zone of broken rock with a thickness to it. Both representations of the fault are severely simplified approximations of a physical system that cannot be directly observed, but only inferred. In this research I must therefore attempt to study features that are relatively independent of the representation of the surface: if the details of the surface structure of the fault are important, there is no hope for correct results, because those details

are unobservable. In a sense, all representations of the fault surface are wrong in unknown and (with current technology) unknowable ways. The point source, however, is wrong much faster. Furthermore, as the point sources shrink in size and increase in density, the stress field they generate approaches that of the finite source, making them an acceptable substitute. However, if the spacing between patch centers is less than the characteristic patch length, the point-source approximation breaks down and should be replaced with a finite-source representation. This situation is only possible if the fault system has three-dimensional geometry.

Finally, it should be noted that the stress acting on a patch is only evaluated at a single point: the center of the patch. While the representation of the fault is generally created by a gridding procedure, where the rough surface of the fault is broken into small, contiguous flat rectangles, it is more correct to think of the Fault-Patch model as representing the fault not as pieces of a surface, but as a collection of fault particles, each of which is a single point in three-dimensional space with an associated orientation and amorphous area. The total area of the patch is used in all stress-transfer calculations; it is only in calculation of the self interaction that the configuration of the area is relevant. However, the fault-patch must be treated as a finite object when calculating the amount of slip needed to relieve the stress acting at the center of the patch, for the simple reason that the stress field generated by a point source is infinite at its exact center.

If we are using the aforementioned Okada equations for stress transfer, they remain valid on the surface of the discontinuity. We can simply evaluate them at the patch center and store the results, as stresses relieved by slip in the strike and slip directions are linearly independent and linear in the amount of slip. On the other hand, if we are using the point-source approximation for stress transfer, we cannot use the Okada equations to determine the self interaction terms because they are formulated for a semi-infinite medium and point-source stress transfer occurs in an infinite medium. In an infinite medium, however, all components of the self terms will be zero except for the zx and zy components. These components must be derived from the transferred stress. We use the value for stress induced in the slip direction at unit distance and multiply it

by a negative quantity termed the “Self-Neighbor Ratio”, or SNR. The SNR must be negative to relieve stress on the patch rather than induce it. Because it acts as an overall coupling constant determining the strength of the interaction between patches, the SNR is one of the parameters that governs whether the system will exhibit realistic scaling behavior. Unfortunately, there is no clear way to derive a good value for the SNR from the physical properties of the system. Therefore, it must be found empirically, by testing a range of SNR values and using the one that produces the most realistic behavior. The existence of tunable parameters that affect critical behavior is common to many slider-block models [41, 45].

2.5 Friction Laws and Stress Leakage

Although the majority of the work done in implementing the model is calculating stress-transfers, the treatment of the fault surface is also very important. A wide variety of friction laws have been proposed for earthquake faults. Many of these mechanisms have a slip velocity term in them, and so are unsuitable for the Fault-Patch model, because the jump-rule formulation means that slip occurs at infinite velocity.

The simplest possible friction law is one that merely assigns to each patch some frictional threshold below which it will not slip and above which it will. Slightly more complicated is basic Coulomb friction, where friction is proportional to the normal force ($-\sigma_{zz}$ in patch-centered coordinates): $F = \mu N$. Coulomb friction is also the only friction law that has been shown scale-invariant in slider-block models under all conditions [44].

There are several issues to consider with regard to the question of Coulomb friction. The first is that of tensile stress: because the Fault-Patch model places no constraints on the relative orientations of patches, it is possible that slip on one patch will generate tensile stress on another patch. If enough tensile stress builds up, the normal force can drop to or below zero, in which case the frictional threshold is also zero. If such a situation comes to pass in nature, the fault pulls apart in an opening mode. Unfortunately, in the Fault-Patch model such behavior would violate the basic assumption that the patch is a flat plane, and much effort would be required

to accommodate this possibility. A better way to prevent the problem is to give each patch some minimum strength, so that the frictional threshold is always the maximum of μN and the minimum strength.

Another question that must be addressed is how to treat the overburden. Rock is very dense, so the pressure generated by the weight of the rock overhead (the overburden) is simply huge, especially considering that the seismogenic zone we wish to model is in general ten to twenty kilometers in depth. If we were to simply incorporate the ambient lithostatic pressure as part of the normal stress on the fault, the strength of the fault at depth would be so much greater than at the surface that all rupture would be very shallow. Examination of the rupture characteristics of real events shows that there is little variation in rupture propagation with depth within the seismogenic zone, which implies that the fault strength is roughly constant with depth, an observation which is borne out by studies of moment-release. Many researchers [39, 63, 143, 153] believe that pore fluids within the fault can act to screen the fault from the pressure component of the normal stresses. The normal force acting on the surface of the fault due to overburden is balanced by an equal pressure force from the fluids within the fault. Thus, it is the **deviatoric** normal stress (stress minus pressure) acting on the fault that is important, not the total normal stress. Because the overburden produces only pressure, it should be ignored.

A post-slip residual stress level is an important component of any friction law. Physically, as two rock faces slip past one another in a fault, the force pushing them drops as stress is released. At some point the force will drop enough that friction will come back into play and cause the slip to stop. We model this process by preventing a fault-patch from slipping all the way to zero stress; instead, we allow it to slip to a value between zero and a chosen residual stress level σ^R . The randomness of the residual stress reflects physical inhomogeneity on the surface of the fault. It also compensates for the overshoot caused by dynamic and inertial effects that are ignored in a quasi-static formulation [1]. This roughness is an important source of noise in the model; without its presence, the model would be able to reach highly degenerate states where all patches have exactly the same stress level and fail at the same time, falling into

a numerically stable but unrealistic limit cycle.

Finally, there is the question of healing. There is no consensus in the scientific community on where exactly the strength of a fault comes from, but it is clear that faults are weaker after a rupture than they are before. Certainly, it makes sense that a region of the fault that has already failed in the current rupture will be more susceptible to further slippage during the same event than an unbroken region of the fault would be. To model this behavior, we delay healing until the event has halted: after a patch has failed, its strength drops to σ^R until the end of the event. The timescale on which healing processes occur is irrelevant as long as it is shorter than the timescale of the loading tectonic processes [171].

One further process affects the evolution of the stress field in an important way: stress leakage. This is what we call the various processes occurring at sub-scale length that smooth the stress field. Much of the characteristic distribution of event sizes grows out of the competition between stress roughening and stress smoothing processes. The noisy roughening processes, such as random residuals, decorrelate the stress field and lead to smaller events, while the stress smoothing processes generate correlated regions of stress which can produce large events. Without some smoothing process besides that inherent in the failure cascade process, the Fault-Patch model will not generate large events; the stress field remains too random. We can solve this problem by adding a decay factor α , which allows the stress to decay in proportion to its intensity:

$$\dot{\sigma} = L - \alpha\sigma \quad (2.12)$$

Here, L represents the loading rate, which has units of stress per time, and α is the decay rate, which has units of inverse time. Each independent component of stress then obeys the following equation, with loading linear and decay exponential:

$$\sigma(t) = \sigma_0 e^{-\alpha t} + \frac{L}{\alpha} (1 - e^{-\alpha t}) \quad (2.13)$$

This is a simple and convenient way to introduce smoothing into the model, and it is also physically correct. Tullis [48] and Karner and Marone [85] have discovered, based on laboratory

experiments of frictional behavior, that the stress on the interface between two sliding rock samples decays in an exponential fashion before it reaches the failure threshold and begins to slide. This stress decay is caused by microscale slippage proportional to the stress, just as in the equation above.

Stress decay is simple to implement in the model in all ways but one. Because the stress leakage is caused by small slips, it relieves shear stress on the fault patch, but not normal stress. (It is easy to see by symmetry arguments that a shear slip cannot generate a normal stress on the fault surface.) If equation 2.13 is substituted for each component of shear stress in equation 2.5, the result can be solved for t only if the failure threshold is constant in time. In other words, if a Coulomb friction law is used, the zz component of the loading stress must be zero or the equation for time-to-failure cannot be solved.

If we must choose two out of three of the features adaptive timestep, stress decay, and Coulomb friction, it is friction that is the least important. The adaptive timestep is essential if the model is to run in a reasonable amount of time, and stress decay is essential for the model to create the large events we are interested in studying.

Normal stress effects, in contrast, have a short-range effect on the local details of an event, and must be transient in nature if the model is to function. In the absence of a process that will relieve the buildup of normal stress, any fault segment that is shut down by normal force clamping will never re-activate. Because patches cannot slip to cancel normal stress, the process would have to be a time-dependent one operating independently of the event evolution; physical processes that are likely relevant in the real earth include viscoelastic relaxation and pressure-screening fluid flow. Not only are these processes very complicated to model, they are also by their very time-dependent nature incompatible with the adaptive timestep jump-rule formulation. Consequently, the effects of normal stress must be neglected.

Fortunately, analysis of the stresses transferred between two patches with arbitrary orientation and position relative to one another shows that the errors introduced by this assumption are small. First, if two fault patches are coplanar, the normal component of stress transferred

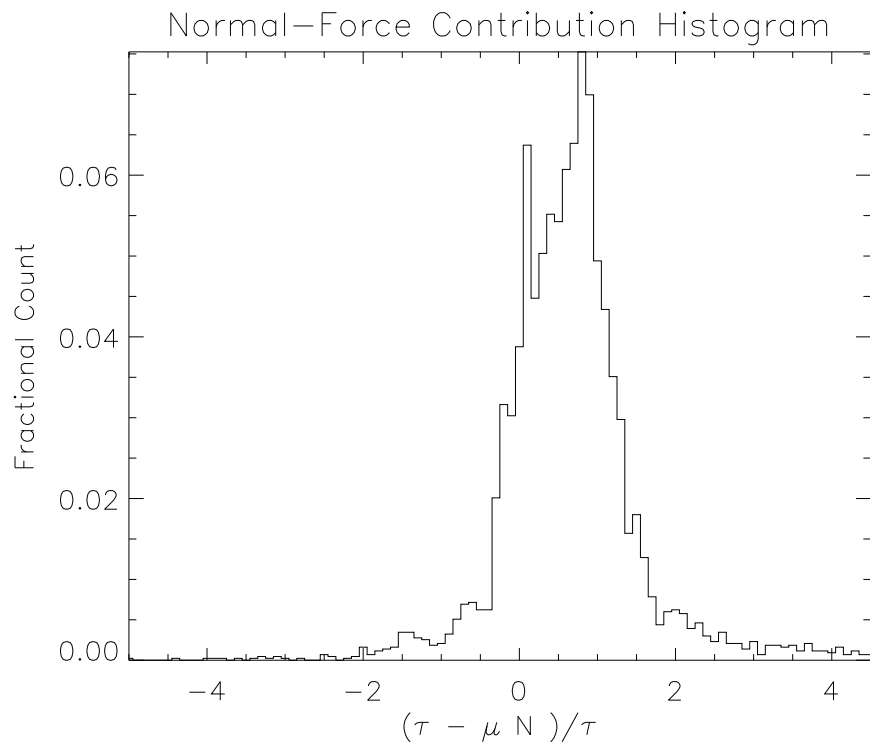


Figure 2.1: Histogram of values of CFF/τ , a measure of the contribution due to normal force to the change in time to failure of a patch, for geometric configurations relevant to this research. 76% of the geometries have a value between zero and two, with the peak centered close to unity (no normal-force contribution).

between them is zero. This eliminates most of the stress interactions: the fault configurations simulated in this research consist of vertical strike-slip planes with the occasional bend of 90 degrees or less between segments. Of the remaining stress interactions, the fault configurations allow us to restrict the relative azimuthal angle of the patch to which stress is transferred as seen from the reference frame of the slipping patch to between zero and 90 degrees, and the relative declination angle to have magnitude always less than the bend angle between segments and sign matching that of the bend angle. Calculating the transmitted shear stress τ and deviatoric normal force N allows us to calculate the Coulomb Failure Function $CFF = \tau - \mu N$ and estimate the error associated with neglecting normal force effects.

For the subset of configuration space in question, the fraction of geometries with a ratio of $CFF : \tau$ outside the range $[-5, 5]$ is negligible. Within that range, 76% of the geometries have a value of CFF/τ of between zero and two, centered close to unity, as shown in figure 2.1. In these cases, the change in time to failure of a fault-patch caused by neglecting normal friction is sufficiently small that it can be ignored. As for those geometries with a CFF/τ ratio outside that range, examination of all the configurations I performed simulations on shows that every such relative geometry has an R^3 coefficient of at least 860, giving a nearly 1000-fold diminution in the effect of the change in stress due to the neglect of normal friction. Therefore, we are justified in neglecting the effects of normal stress on friction and using a simple static frictional threshold in the simulations discussed in this work.

Chapter 3

Analysis Tools

Understanding the tools that we use to study data of interest is an important prerequisite to understanding the study itself. This chapter describes the primary analytic tools that I used in this research, both in examining catalog data from the real world and the data generated by synthetic computer models.

These tools, even the simple plots of data, are statistical in nature. There are several reasons for this; the first is that it is the only way we can really meaningfully compare synthetic results with actual data. Earthquakes are not a simple deterministic process – if they were, we would understand them completely. Noise and chaos and other difficult-to-predict signals are folded into the evolution of any particular sequence of earthquakes, both in models and (we believe) in the real world. Therefore, any attempt to reproduce an exact set of behaviors (that is, a particular event catalog) with a model is doomed to failure from the very outset. We must view the observed data as one embodiment or instance of a whole ensemble of possibilities. When we say that a model captures features of real earthquake catalogs, we mean that the statistical features of the model match the statistical features of the observed data.

Statistical approaches are also important because of the sheer quantity of data that can be observed relating to a single event. Real-world observations are limited in scope, but the number of features of a synthetic event that can be calculated and observed is literally infinite. By confining ourselves to statistical features of the data, we reduce the observation space to something more tractable than the combinatorial explosion of all possible features.

Finally, by studying the statistical features of earthquake model data, we can start to understand how the model's qualitative behavior depends upon the details of the lower-level processes. Earthquake data is both noisy and complex; it has both structure and randomness. The goal of studies like this one is to figure out which detailed sub-scale processes may be replaced by parameters and/or noise. If the entities which interact to create earthquakes are hierarchical in their organization and nature, then the behavior of any sub-element passes through a surface that integrates and blurs the details into noise. [11, 10] By studying the sensitivity of the top-level process to the bottom-level details, we can infer features of the dynamic structure that connects them into a system.

3.1 Gutenberg-Richter Scaling

The first statistical measure of the data is magnitude-frequency scaling. It has been long observed that earthquakes have so-called Gutenberg-Richter scaling – that is, the distribution of events according to size follows a simple power law[166]. In other words, if the number of events of a given size or larger is plotted versus that size, the result will be a straight line on a log-log plot. In observational data, the b-value (the slope of the line) varies from region to region, but is universally close to unity.

This is a simple statistical quantity to calculate, provided that the correct procedure is followed [93]. First, a suitable definition of “size” must be decided upon. For observed data, the total moment M_0 of an event is generally used. Moment is equal to force times distance, and force can further be decomposed into stress times area. Moment is thus calculated as the total stress drop integrated over the surface of rupture, multiplied by the distance the rupture surfaces are displaced relative to one another. In real earthquakes, this quantity is inferred from the resulting ground motions, but in a computer model it is possible to measure these quantities (stress-drop, area, and displacement distance) directly.

In calculating the moment-frequency scaling, I convert the linear moment to logarithmic

moment-magnitude according to the relation

$$M_w = \frac{\log M_0}{1.5} - 10.73 \quad (3.1)$$

before counting the events. This ensures that the bins have a constant size relative to one another when considered on a logarithmic scale. It is also important to calculate **cumulative** statistics – that is, the value of interest at $M = 3.2$ is the total number of events of magnitude 3.2 and greater, not the number of events of magnitudes between, say, 3.2 and 3.4. This method of counting can introduce some subtle biases (in the form of spurious slope changes) due to the smoothing effect of cumulative-frequency data and the existence of a maximum event size, [95] but as I have used this statistic merely to check that the simulations exhibit behavior consistent with real earthquake fault systems, these effects are unimportant.

It is important that we remain aware of the fact that Gutenberg-Richter scaling is a property of large-scale systems. If a catalog contains only data from a single fault, it may well not conform to the scaling; some debate exists as to whether the power-law scaling results from characteristic repeated earthquakes distributed across faults with a fractal spatial structure, from critical-point scaling of the stress fields on the fault surfaces, from some combination of the two, or from other causes. Nevertheless, the Gutenberg-Richter scaling relation remains reliably constant across earthquake catalogs from around the world. [166] At the very least, it should be checked as a minimal requirement for synthetic models: any model which does not reproduce Gutenberg-Richter scaling is at severe odds with the observed record.

3.2 Eigenmode Analysis

Many researchers in the earth sciences have found eigenmode analysis to be a useful tool that can reveal correlations and patterns in the spatio-temporal distribution of events [59, 73, 113, 114, 115, 118, 138, 161]. The eigenmodes of a dynamical system define a set of independent activity states for the system; if a set of orthonormal solutions to the equations of motion for a system can be found, then observed behavior can be decomposed into superpositions

of these modes. Related methods can be applied to systems where the underlying dynamics are unknown and only the activity can be observed.

Eigenmode analysis is known by many names, including Empirical Orthogonal Function (EOF) analysis, Principal Component Analysis (PCA), and Karhunen-Loeve decomposition. [99, 118, 161] Many extensions to the method including frequency-dependent and complex decomposition exist as well. Regardless of the differences in nomenclature and detail, all the methods are used to analyze data in fundamentally the same way: by reconstructing the observed data as a superposition of activity in a set of statistically stationary and independent spatial modes.

To construct the empirical orthogonal functions of a dataset, we first construct the equal-time covariance matrix C . Given a data matrix D of values indexed by n times t and m locations

x :

$$D = \begin{bmatrix} y(x_1, t_1) & y(x_1, t_2) & \cdots & y(x_1, t_n) \\ y(x_2, t_1) & y(x_2, t_2) & & y(x_2, t_n) \\ \vdots & & & \ddots \\ y(x_m, t_1) & y(x_m, t_2) & & y(x_m, t_n) \end{bmatrix}, \quad (3.2)$$

the covariance matrix is the outer product of D with itself: $C = DD^T$. That is, each element C_{ij} is the dot product of the time series for locations x_i and x_j . This manipulation of the observations is easiest to understand if the data starts out in the form of a time series of observations for each of several observation points, but it can also be constructed from a set of spatio-temporal observations (such as a catalog of times and locations of earthquakes) by simple discretization of times and locations.

Once the covariance matrix C is known, standard linear algebraic techniques will find the eigenvalues and eigenvectors. In this research, since C is symmetric, I used the Householder transformation to reduce the matrix to tridiagonal form, and the QL algorithm to find the eigenvalues and eigenvectors [175].

Each eigenvector e_j can be regarded as a spatial covariance pattern – that is, the eigen-

vectors are the “modes” of co-variance of the measured value amongst the different locations. I will refer to these eigenvectors as the eigenmodes of the system. These modes form a set of basis functions (the Empirical Orthogonal Functions, or EOFs) in which we can expand the data. The eigenvalue λ_j corresponding to each e_j is a measure of that mode’s contribution to total variance of the dataset and therefore the fraction of the signal which is explained by that mode. Because the eigenvectors form an orthonormal basis, the observed data D can be decomposed into a sum of EOFs, each with a time-varying expansion coefficients $a_j(t)$. These “principal component” time series are the dot product of the observed data and the eigenmode:

$$a_j(t) = \sum_{x=1}^m y(x, t)e_j(x). \quad (3.3)$$

In my studies of seismicity data, I have found it useful to use a correlation matrix to represent equal-time seismicity interactions instead of a covariance matrix. In this case, the observational data can be represented as an integer, the number of events occurring at a given time and location; or it can be represented in boolean form, with a 1 indicating the presence of activity and a 0 the absence of activity. If the expectation $\langle x \rangle$ is defined as [175]

$$\langle x \rangle = \frac{1}{N} \sum_{t=1}^N x(t), \quad (3.4)$$

the covariance $cov(x, y)$ as

$$cov(x, y) = \langle xy \rangle - \langle x \rangle \langle y \rangle, \quad (3.5)$$

and the standard deviation $\sigma(x)$ as

$$\sigma(x) = \sqrt{\langle x^2 \rangle - \langle x \rangle^2}, \quad (3.6)$$

then the correlation $cor(x, y)$ is simply

$$cor(x, y) = \frac{cov(x, y)}{\sigma(x)\sigma(y)}. \quad (3.7)$$

There are several differences between covariance and correlation, but the most important is that covariance is always positive, while correlations lie in the interval $[-1, 1]$. This is significant because one of the interactions between faults that we expect based on physics is an inhibitory

interaction. Since we wish to observe seismic activity in a region not only enhancing the rate of seismic activity in another region, but also suppressing it, we must be able to calculate anti-correlations (which are negative) as well as positive covariances.

3.3 PDPC Analysis

The Phase Dynamic Probability Change (PDPC) index is a new analytic tool that finds regions of enhanced future seismic potential based on deviations from background level in the seismic rate [131, 158, 159, 157, 161]. It has been used to study the seismic record in Southern California and is effective at forecasting large events based on past activity. So far (except for one set of plots made before the 1999 Hector Mine event[160]), the only tests of this tool have been retrospective studies, but as this is the only timely manner of testing long-scale forecasts of future events, this is a viable method of testing. No reliable statistical test of the accuracy of PDPC forecasts has been developed. Regardless of the utility of the forecasts this analysis produces, however, it does detect a precursory signal to large earthquakes in observed seismicity, and is therefore a useful tool to compare the accuracy of computer models with real data.

The procedure for calculating the PDPC index is as follows:

We begin with a catalog of events: a listing of the times and locations of all the earthquakes in the physical region of interest. In practice, we perform a magnitude cut and exclude all events with magnitude $M < 3$; this serves as a proxy for the removal of the first activity eigenpattern, which is the detectability mode. Over the last seventy-five years, the density and sensitivity of the observational array in Southern California has increased substantially, and the number of small events which can be reliably sensed and located has improved commensurately. The content of the catalog at higher magnitudes, however, has remained unchanged. By removing the small events, we remove the resulting temporal signal. In data from a computer model, all events are perfectly detectable and therefore no magnitude cut is necessary, though an argument could be made that the first and most general eigenmode should be removed from the data regardless. However, the prohibitive computational cost of this procedure has led me

to omit this step from this research.

We then discretize the event locations into bins of equal size. By integrating the total activity from time t_0 to t we create a seismic activity rate vector \vec{S} :

$$\vec{S}(t_0, t) = \frac{1}{t - t_0} \int_{t_0}^t \vec{N}(t) dt, \quad (3.8)$$

where $N_i(t)$ is the number of events in location bin i at time t . We also normalize the rate vectors to have mean zero. If we then subtract two rate vectors with the same t_0 we get the seismic activity rate anomaly between the years t_1 and t_2 relative to the base year t_0 :

$$\vec{R}(t_0, t_1, t_2) = (\vec{S}(t_0, t_2) - \langle S(t_0, t_2) \rangle) - (\vec{S}(t_0, t_1) - \langle S(t_0, t_1) \rangle). \quad (3.9)$$

If we then integrate over all possible base years, we have effectively performed a Feynman path integral through time of the seismic anomalies. We allow the base years to range from minus infinity to t_1 , though in practice t_0 is the beginning of the dataset. Because it is the phase and not the amplitude of the anomaly that we are interested in, we integrate the complex exponential of the seismic activity rate anomaly:

$$\vec{Q}(t_i, t_f) = \lim_{t_0 \rightarrow -\infty} \frac{1}{t_0 - t_i} \int_{t_0}^{t_i} e^{i\vec{R}(t', t_i, t_f)} dt'. \quad (3.10)$$

The result is a probability change amplitude, similar to quantum-mechanical probability amplitudes. To convert it to an actual probability change, we square the quantity Q and subtract the mean. (Because probability is conserved, any change in probability should sum to zero when integrated across all space.) The resulting quantity is the PDPC index P :

$$\vec{P}(t_i, t_f) = |\vec{Q}(t_i, t_f)|^2 - \langle Q(t_i, t_f) \rangle. \quad (3.11)$$

I calculated the PDPC index for seismicity in Southern California, using spatial bins one tenth of a degree (approximately eleven kilometers) on a side. For the interval $(t_1, t_2) = (1978, 1991)$ the result is shown in figure 3.1. The larger the value of the PDPC index, the

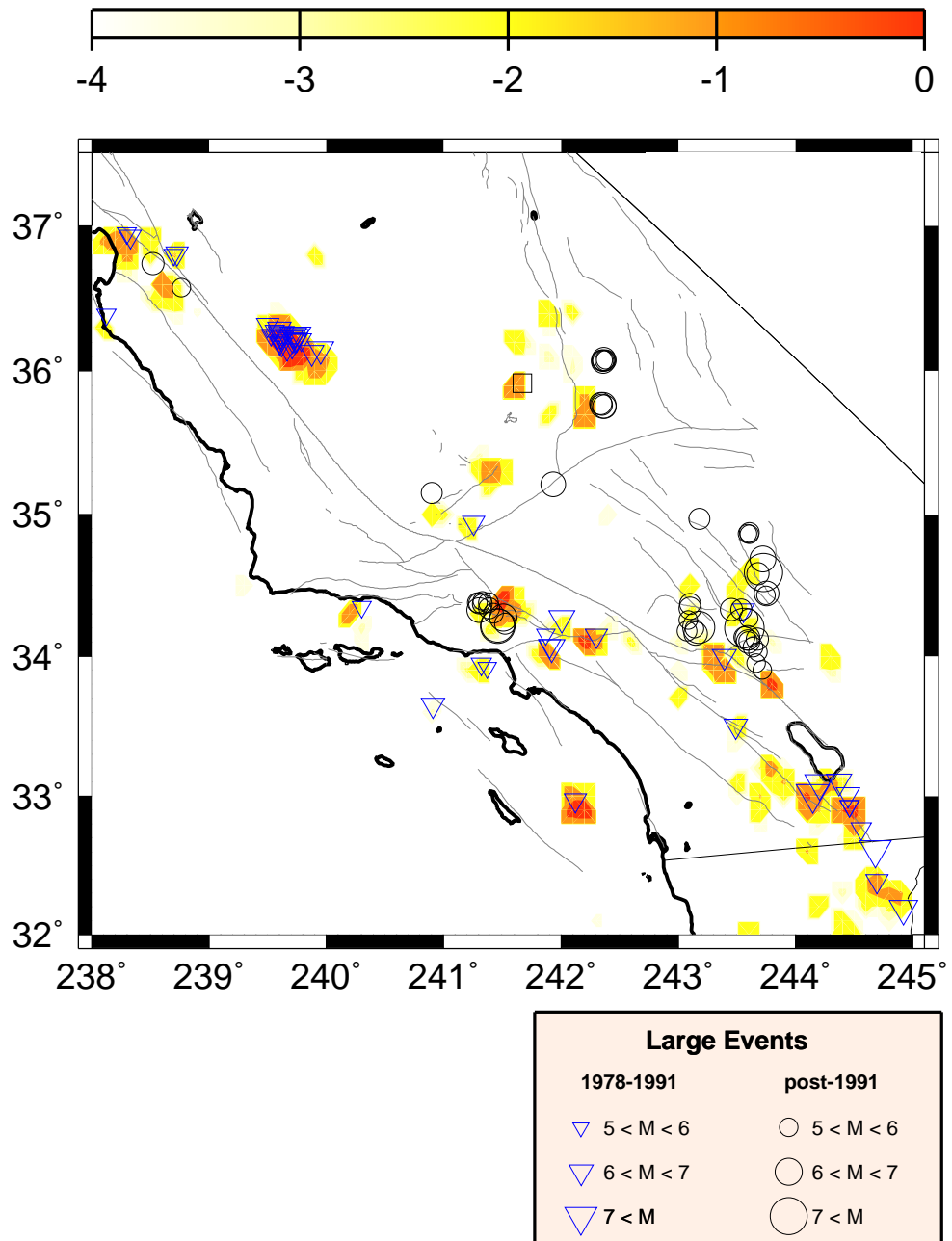


Figure 3.1: The PDPC index calculated for historical Southern California seismicity, with $t_1 = 1978$ and $t_2 = 1991$, here contoured in color. High values of PDPC (hotter colors) in the region of the Northridge and Landers events, both of which occur after the end of the dataset, in 1994 and 1992 respectively, show that the method successfully finds precursory signals associated with large earthquakes in real seismic data.

greater the expected probability of a future large event in that location. Large events that occurred between 1978 and 1991 are plotted as triangles, while large earthquakes that happened after 1991 are plotted as circles. Note that although no data whatsoever from after December 31, 1991 was included in this calculation, the PDPC index is strong in the regions of the 1992 Landers (latitude 34.2, longitude 243.8) and 1994 Northridge (latitude 34.2, longitude 241.5) earthquakes and their associated aftershock sequences. This technique, then, shows promise as a possible method for forecasting the locations of large earthquakes.

While the function of the mathematics of the PDPC index is clear (it finds anomalous fluctuations away from the mean in background seismicity rates), the physical mechanism relating these precursory signals to the large events that frequently follow them is not yet fully understood. It is clear that both phenomena are associated with large regions of correlated stress, but much research on this method remains to be done. Nevertheless, it is effective in retrospective studies of the earthquake catalogs for Southern California, and is therefore a useful tool for comparing simulation with observation.

3.4 Stress Clustering Analysis

Statistical mechanics approaches to the problem of earthquake rupture initiation and arrest regard the earthquake as a nucleation event in a stress field which is near a critical point. Once the event has begun, it propagates outwards until it has reached a large enough fluctuation in the stress level to halt the further propagation of the rupture [124]. Viewed in this manner, it is clear that large earthquakes will be associated with areas of correlated stress along the fault – that is, that the boundaries of a coming event will be described by the boundaries of a region where the stress field is nearly uniform. To examine this phenomenon, we wish to analyze short-range correlations in the stress field.

From the construction of the Fault-Patch model, we know that large events will occur where regions of correlated stress exist, because the transferred stress falls off in intensity as $1/R^3$. While it is theoretically possible for a failing patch to trigger another patch a long distance

away, it is statistically very unlikely, and therefore a failure front will only continue to propagate while its neighbors (or sometimes next-nearest neighbors) are also close to the failure threshold. Therefore, the larger the physical size of a region where every element is close to the failure threshold, the larger the number of elements that will be involved in the event.

To calculate the size of a region of correlated stress, I use a simple clustering algorithm. This algorithm is a variation of the Hoshen-Kopelman algorithm [148] used to identify clusters in percolation theory, and is related to a set of algorithms commonly used in computer science applications to identify objects in a visual image. Its use is based on the assumption that the elements of the model can be treated as pixels in a two-dimensional array. First, each model element (pixel) is given a unique label. The algorithm then iterates over all elements, examining them and their neighbors. If the “value” of the pixel is within a chosen interval of its neighbor’s value, they are considered part of a cluster. The neighbor is relabeled to have the same label as the pixel under consideration, as are all other pixels with labels matching the neighbor. When the iteration is finished, all pixels with the same labels are a part of a single cluster. The members of the cluster can therefore be identified, and statistical quantities such as the cluster area, average stress, and so on can be calculated.

The algorithm is very simple and straightforward; it is a rather brute-force approach to the problem, but for models with elements numbering in the thousands, it is practical to perform the algorithm on a standard desktop computer. It is also possible (though in this study generally unnecessary) to generalize the algorithm to geometric situations which are not easily mapped to a two-dimensional surface with gridded sample points. In the case of a more complicated spatial distribution of elements, instead of considering the lattice neighbors of the element under consideration, we need merely consider all elements within some three-dimensional neighborhood. A secondary consideration in using this algorithm has to do with the numeric value associated with each element; in an gray-scale image, each pixel has a single scalar value. For the planar faults studied in this thesis, I used the normalized shear stress acting on the fault-patch: σ_s/σ_f . This value gives a measure of the position of the patch in the stick-slip

cycle, and is sufficient for cases where the same tensor stress acting on two adjacent elements would bring them both closer to failure. If the same stress were excitatory on one element and inhibitory on a neighbor, it would be necessary to perform a more complex comparison of stress-states to decide whether two neighbors were part of the same cluster.

3.5 Recurrence Plot Analysis

Recurrence plot analysis is a method that has been used to study a variety of noisy dynamical systems, including neural signals, breathing patterns, and mathematical chaos [36, 49, 53, 90, 164, 29, 37, 186]. The construction of a recurrence plot (RP) from a time series begins with the determination of the system's trajectory through phase-space. For univariate time series such as those described above, this is done by embedding the data using time delays in a sufficient number of dimensions to reconstruct the attractor. If the multivariate state of a deterministic dynamical system follows an orbit in phase space with a D-dimensional attractor, then the trajectory

$$x(t) = u(t), u(t + \tau), \dots, u(t + N\tau) \quad (3.12)$$

where N is greater than twice the box-counting dimension D , reconstructed from the univariate time series $u(t)$ will follow a diffeomorphic copy of the original attractor [154, 18].

Using this embedded time series, we then calculate for each pair of points x_i and x_j the distance between the points. In an $M \times M$ matrix, where M is the number of points on the trajectory, we place a dot at (i, j) if the distance between the two points is less than some cutoff distance ϵ . Alternately, we can also map the distances onto a color scale and color the entire matrix accordingly. The resulting RP is a graphic representation of the pairwise distances between states sampled regularly through the dataset.

Figure 3.2 shows a recurrence plot for data generated by the famous Lorenz equations [154]. Each point represents a pair of times when the states of system were close to one another. Diagonal stripes indicate trajectories that shadow one another. The structure of the RP on the whole can be taken to describe the repeatability of the system's behavior.

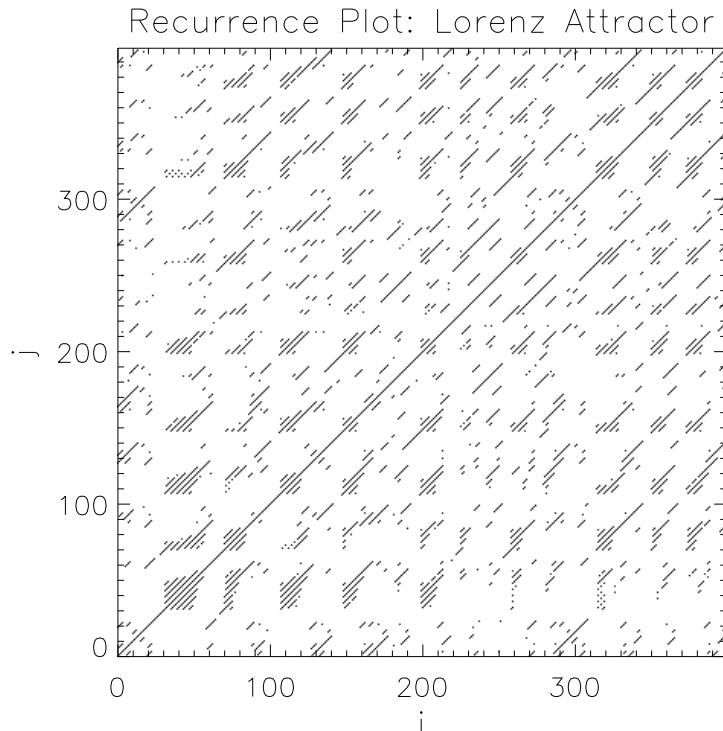


Figure 3.2: A recurrence plot constructed from data generated by the Lorenz equations. I used a fixed-timestep integrator and sampled the output every thousand steps. The data were then embedded in five dimensions with a delay (τ) of 1; dots are plotted where the distance between states is less than 10% of the maximum.

While published instances of recurrence plot analysis use an embedded univariate time series to represent the state of the system, it is not necessary to use this representation. All that is required to construct a recurrence plot is a measure of the distance between states of the system at different times. In the case of Fault-Patch simulations, the state of the model can be captured with a snapshot of the stresses. I chose to calculate the distance between two stress snapshots as follows:

$$d(t_1, t_2) = \sum_i |\sigma_i(t_1) - \sigma_i(t_2)| \quad (3.13)$$

That is, the distance between two states is the sum over all sites of the absolute value of the difference in shear stress. If the shear stresses are normalized to have a maximum value of 1, then the maximum distance between states is equal to the number of patches.

Recurrence plot analysis is useful because it can reveal temporal structure that is difficult to see with other methods. In this research, it is most useful as a way to measure the temporal persistence of stress patterns.

Chapter 4

Parametric Effects

The Fault-Patch model contains many numeric parameters that affect its overall dynamic behavior; values for most of these parameters can be derived from the physical properties of real earth materials, but there are two exceptions. The rate of stress decay (α) and the interaction strength (SNR, or self-neighbor ratio) cannot be calculated from first principles, but must be chosen based on whether or not the values cause the model to behave in a statistically correct fashion. To choose optimal values for these parameters, I studied them in the absence of geometry, so as to isolate their effects. This chapter describes the results of that study. It also provides a baseline of behavior to compare the geometric results against.

To explore the effects of these two parameters, I constructed a flat vertical strike slip fault of square patches one-half kilometer on a side. The fault had one thousand elements in a 10:1 aspect ratio with the strike along the long axis. This fault is the same geometry as one segment of the “zig-zag” fault studied in great detail elsewhere. I generated the loading stresses by prescribing an annual uniform slip rate of one millimeter (ten centimeters per century) in the strike direction. The result is shown in figure 4.1. For each value of the parameter of interest, I then generated at least 30,000 events, starting each run with the same random number seed.

4.1 Stress Decay

Earthquake ruptures grow to large size because of the presence of spatial correlations in the stress field on the surface of the fault. [124] When an earthquake starts, the stress at

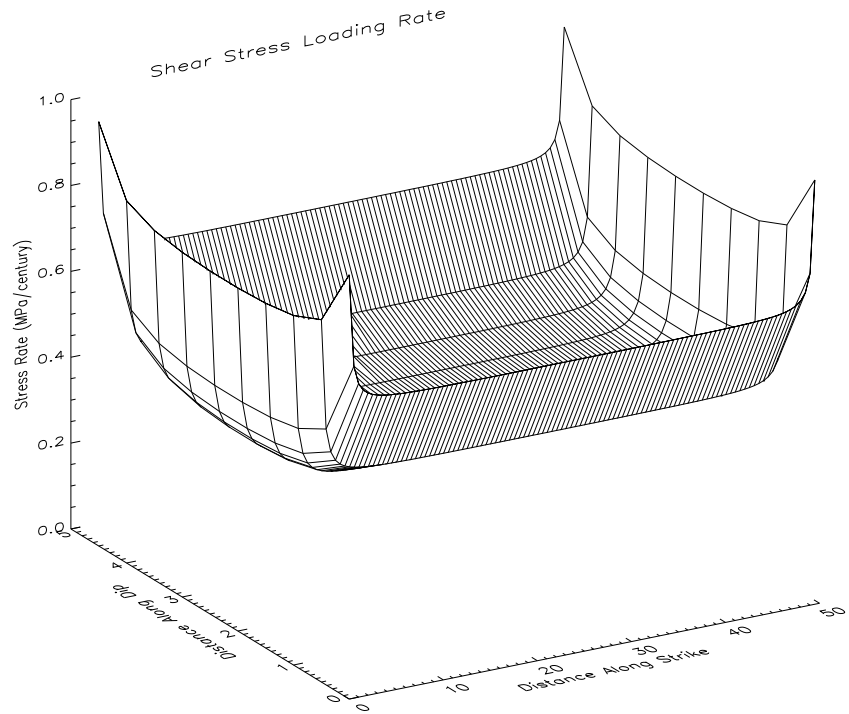


Figure 4.1: The loading stress field generated by uniform slip rate on a flat fault. Plotted on the z-axis is the magnitude of the total shear stress; most of the stress is σ_{xz} , but there is some small variation in σ_{yz} , both measured in the strike-dip-normal reference frame. The fault is thin enough that the edges affect most of the system. The assumption of a uniform average slip rate for the entire fault may be slightly unrealistic, but knowledge of slip rate patterns on real faults is insufficient to justify a more complicated loading scheme.

some point on the fault surface has exceeded the strength of the fault, causing the two halves of the fault to start sliding past one another. While the sliding relieves stress on the moving part of the fault, it induces it on the parts of the fault that are still locked. The rupture will propagate outwards from the hypocenter as long as the stress step generated by a sliding part of the fault is enough to bring nearby sections of the fault to failure. Thus, the rupture halts when it encounters a fluctuation in the stress field (that is, a portion of the fault that is sufficiently unstressed) large enough that the induced stress step does not induce failure on that part of the fault. Conversely, in order for an earthquake to be large, the stress field the rupture propagates through must be equally near the failure threshold over a large area. In other words, the stress field must have large-scale spatial correlations.

The failure process itself acts to generate stress-field correlations in a nonlinear threshold-type system like the Fault-Patch model. When a patch fails, the stress acting on it is reduced to zero. If this failure triggers a second patch to fail, its stress is also reduced to zero, correlating the stress field in those two locations. Therefore, at the end of an event, all patches that were involved in the event will have correlated stress states. In the absence of any noise, this process will create a degenerate state where all patches are perfectly synchronized. In order to counter this effect, I incorporated noise into the system in the form of a random residual stress: when a patch slips, some fraction of the shear stress is left uncompensated. For the simulations in this research, the residual was a uniformly distributed random variate between 0 and 0.5.

The correlations generated by the failure process remain small even after many events; the largest event in a simulation with 40,000 post-transient events had an area only fifteen percent of the lattice size. Therefore, to generate statistics more consistent with observed data another smoothing process is required. This smoothing was implemented as a nonlinear stress decay where shear stress decays exponentially with a time constant α . I varied α from zero up to 0.3 to study its effects.

Figure 4.2 shows the dramatic effect that α has on the dynamics of the model. When alpha is zero or very small, the smoothing effect is insufficient to generate large correlated

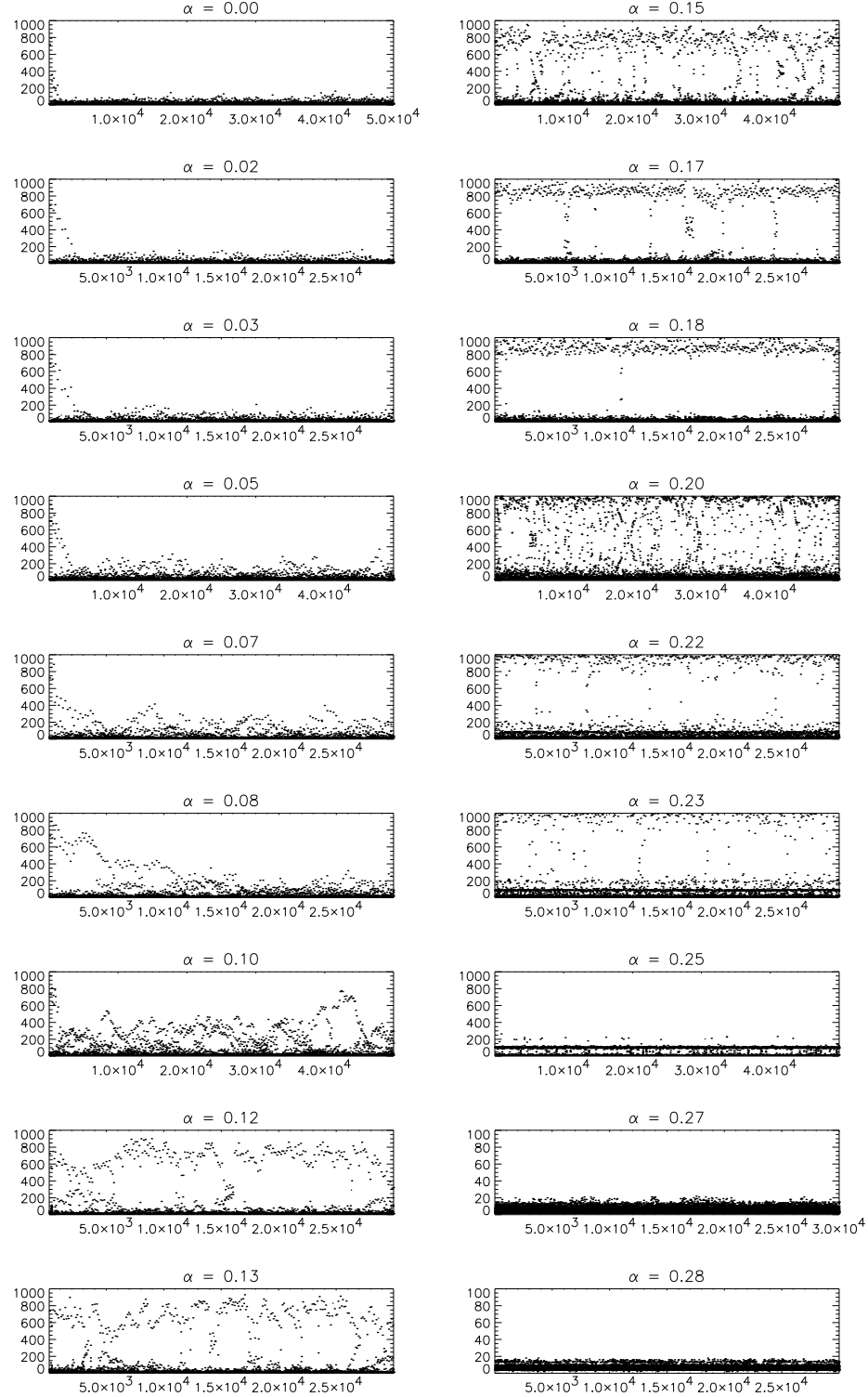


Figure 4.2: Temporal evolution of event sizes for varying values of α . Event areas are plotted on the y-axis against event number on the x-axis. For small values of α , the stress-decay rate, there is an initial transient lasting for 5,000 to 10,000 events. Large values of α produce an increasing fraction of characteristic events. At the highest values, characteristic events are replaced by creeping behavior. Note exaggerated vertical scale on final two plots.

regions. (Large events exist in the initial transient because the random state used to initialize the model does not have the same statistical distribution of stresses as the steady state of the model.) Large events begin to appear for values of α between 0.05 and 0.10; “characteristic” events [140, 180, 178] spanning the system appear as α rises to 0.15 and become common at higher values. These very large events in turn disappear when the leakage rate exceeds the loading rate near the center of the fault as α nears 0.25. Above a value of 0.3, the loading rate is insufficient to induce any patches to slip; stress decays as rapidly as it accumulates, corresponding to creeping or stably-sliding behavior. This sequence of behaviors follows the progression hypothesized for real-earth faults as they age and become smoother.

Figures 4.3 through 4.5 show the space-time distribution of events changing as α is varied. The first figure shows a synthetic history of 1000 events for small values of α . The plot on the left is the case with no stress decay, and it shows no events of noteworthy size. In contrast, several large events can be seen in the plot on the right, with $\alpha = 0.05$, and the stress-field correlations associated with them can be inferred from the quiescent regions preceding and following the large events.

Figure 4.4 shows the transition from Gutenberg-Richter scaling with events of all sizes to characteristic behavior dominated by events spanning the largest spatial scale available. On the left, where $\alpha = 0.12$, we can see the first system-scale events have appeared, and on the right they have become common. Both plots also show possible foreshock sequences: a series of small events in roughly the same location leading up to the edge of a large event. As in the real world, the definition of what is or is not a foreshock is not inarguable.

Finally, in figure 4.5 we can see the results of pushing α to very high values. The left plot shows that a large value of α will damp out all fluctuations in the stress field; the only spatial variation worth noting is due to the difference in driving rate between the central patches and those at the edge of the fault. In the final plot, these are the only patches still slipping; on the central patches, the loading stress rate is no longer sufficient to build fault patches up to failure. Stress leaks away as rapidly as it builds up, leading to a creeping scenario.

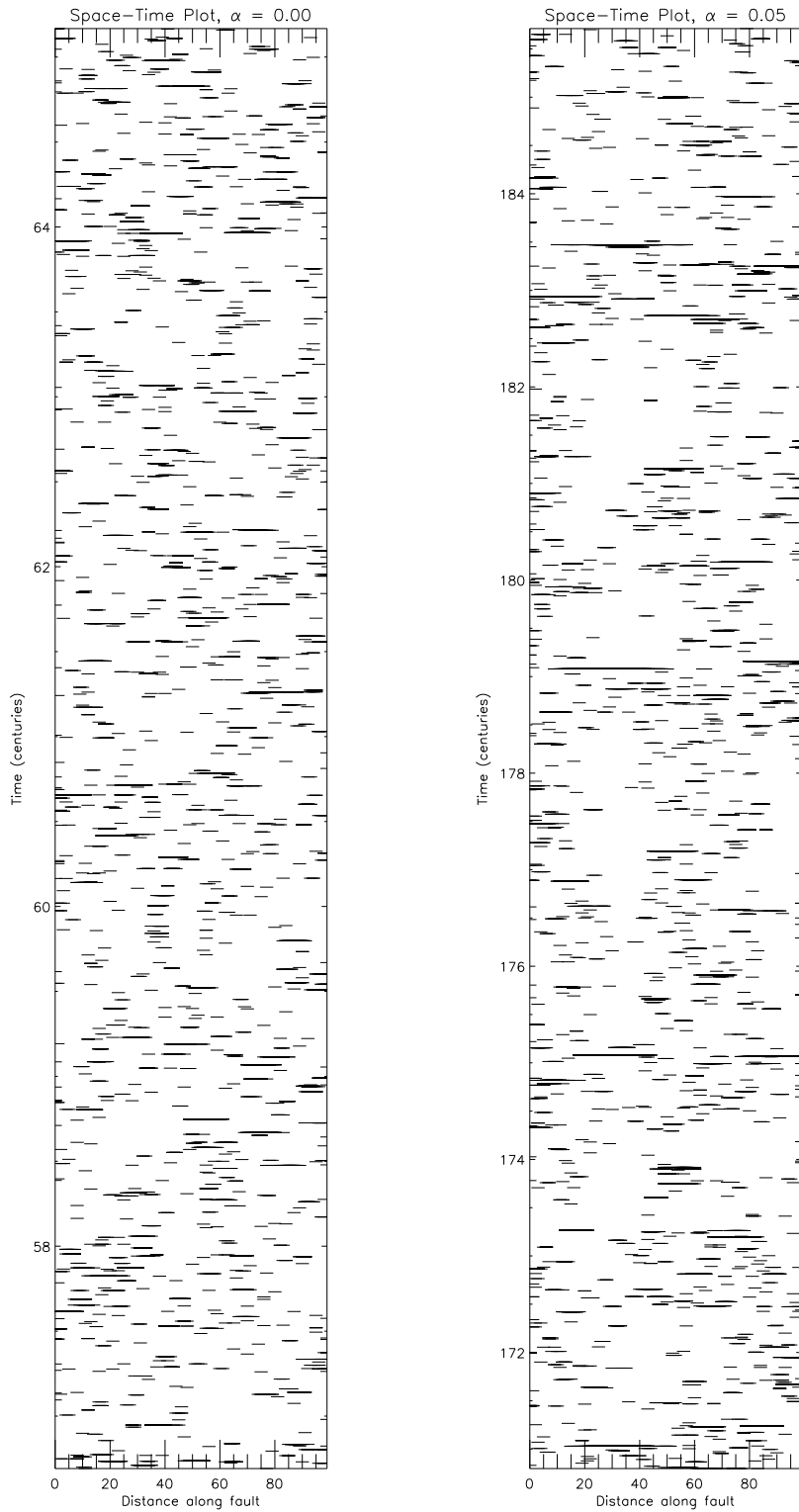


Figure 4.3: Typical rupture histories for small values of α . At left, there are no large events for $\alpha = 0$. At right, stress decay of 0.05 generates correlations that allow large events.

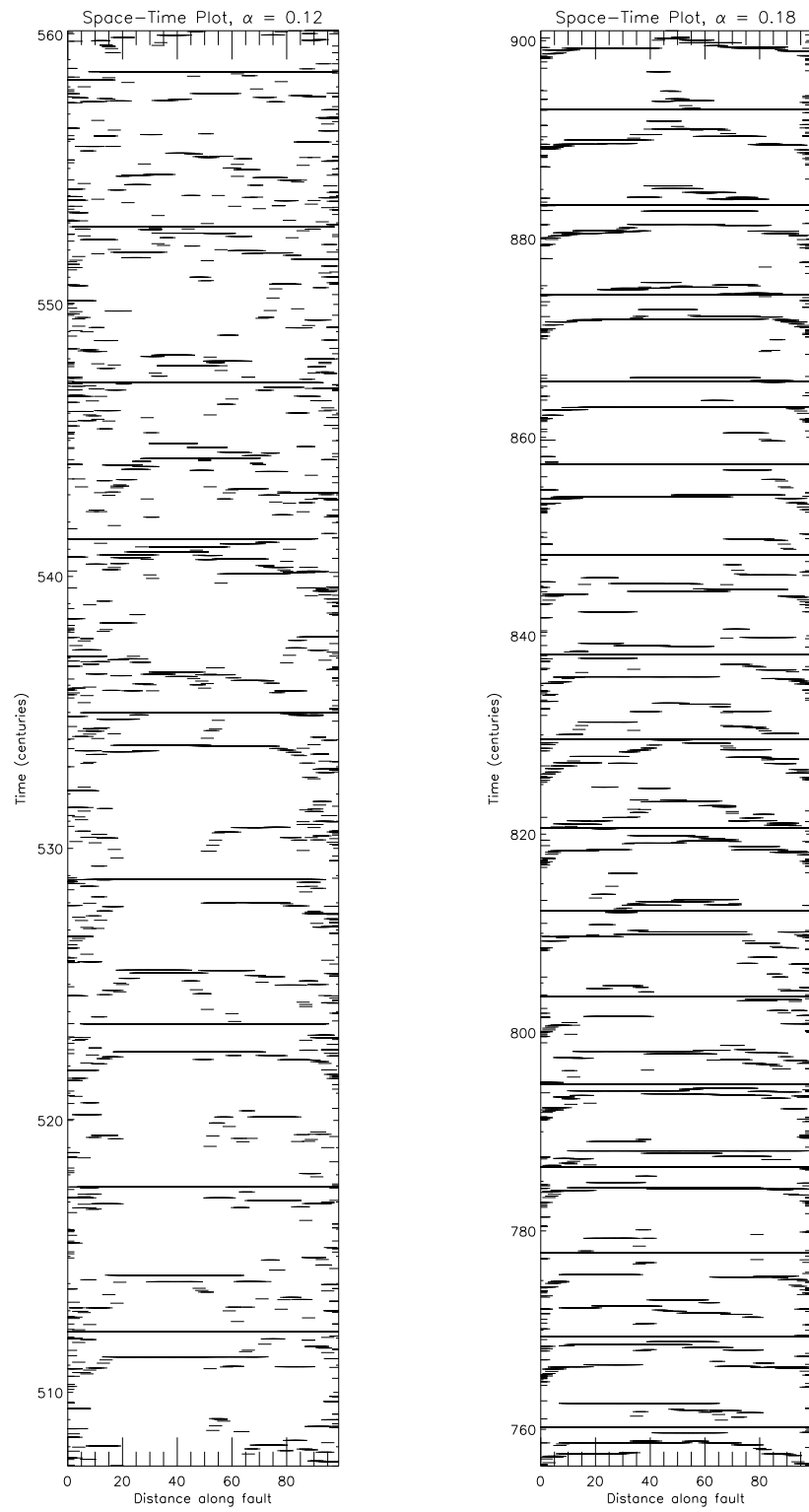


Figure 4.4: Typical rupture histories for intermediate values of α . Lattice-spanning or characteristic events have begun to appear at left with $\alpha = 0.12$. At right, they have begun to dominate the history. Note possible “foreshock” sequences leading up to the edges of some large events in both plots.

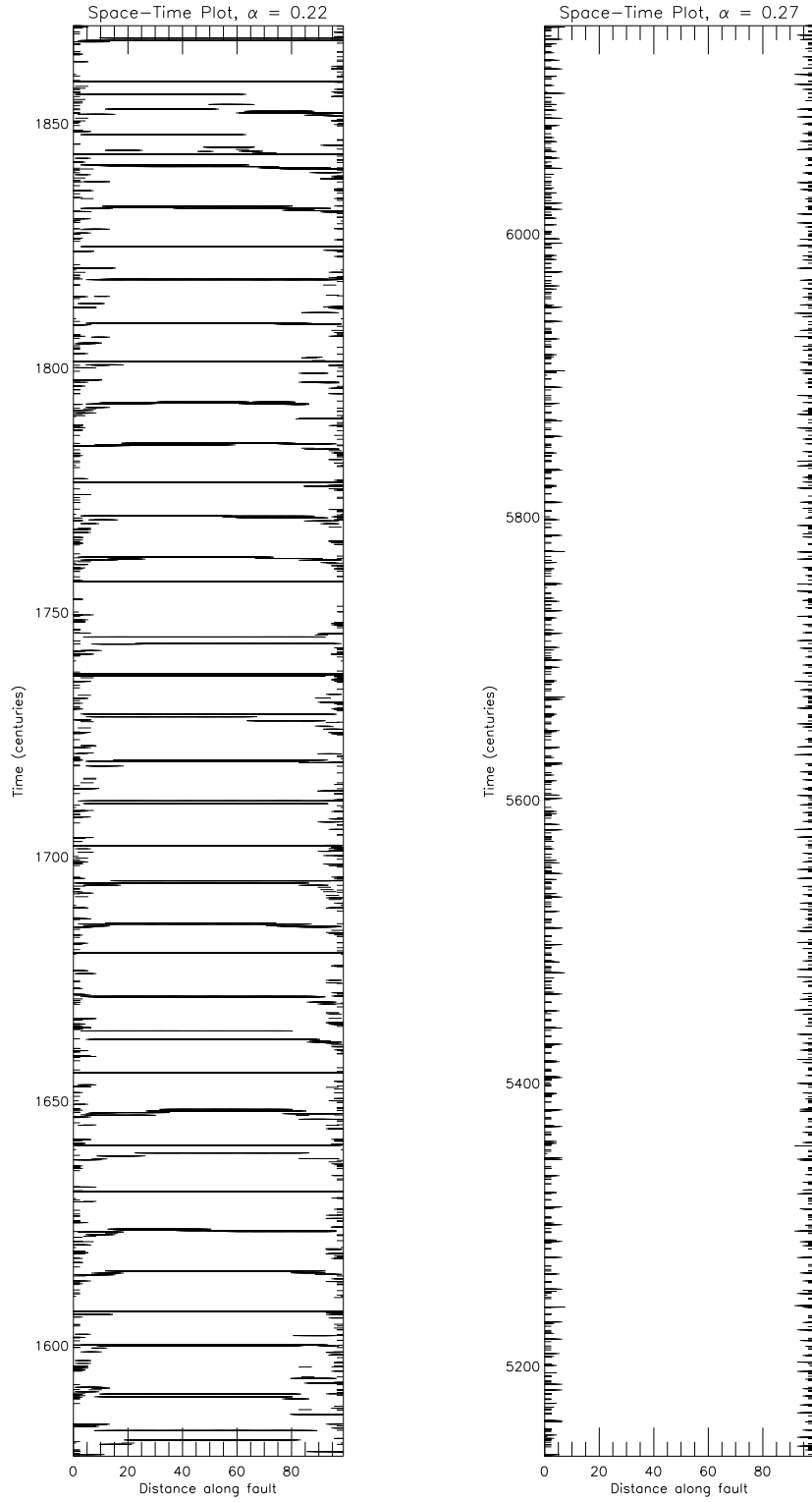


Figure 4.5: Typical rupture histories for large values of α . The ladder-like sequence at left shows that nearly all events are either small and limited to the edges, or very large and span the lattice. At right, the stress decay is large enough that only peripheral patches with higher loading slip; central patches creep stably.

4.1.1 Statistics of Stress Decay

The strength of the stress decay effect determines the size of the largest event. When the largest event spans the entire lattice of the fault, the statistics change from the Gutenberg-Richter type scaling seen on most Southern California faults to the characteristic event distributions typical of Northern California. Because I wished to simulate a network similar to that in southern California, I chose to use a value of 0.05 for α in my simulations. This value is also comparable to the scale of stress decay observed in the laboratory in rock friction experiments.

[85]

The effects of the stress decay parameter α are also apparent in the cumulative magnitude-frequency statistics of the simulation. The observed Gutenberg-Richter scaling of real seismicity is an important feature to match in a simulation. Figure 4.6 is a surface plot of the cumulative frequency of occurrence of events as a function of magnitude and α . The datasets from these simulations did not contain a record of the moment of each event, so I calculated an approximate magnitude from the area of each rupture, which scales linearly with the moment released.

Figures 4.7 through 4.13 show the changes that occur in the event size distributions as α increases. With no stress decay, (Figure 4.7), the plot of cumulative frequency versus magnitude does not show a distinct scaling region. There is a scaling region, but because the range of event sizes is small, it is masked by the rolloff near the maximum event size. Figure 4.8 shows more clearly the classic log-linear scaling regime of natural seismicity between rupture areas of 10 and 100, with a b-value of 0.78. A noncumulative event size histogram (Figure 4.9) of the same data shows that the scaling persists through the entire data set. This is a good value of α to use for simulating events with a Gutenberg-Richter size distribution. It is also consistent with recent research on the behavior of rock near the failure point that suggests that pre-failure slippage relieves stress on the order of a few percent. [85]

Figures 4.10 and 4.11 show the statistics beginning to depart from power-law behavior at $\alpha = 0.10$. The abundance of large events visible in the size histogram creates a bend in the

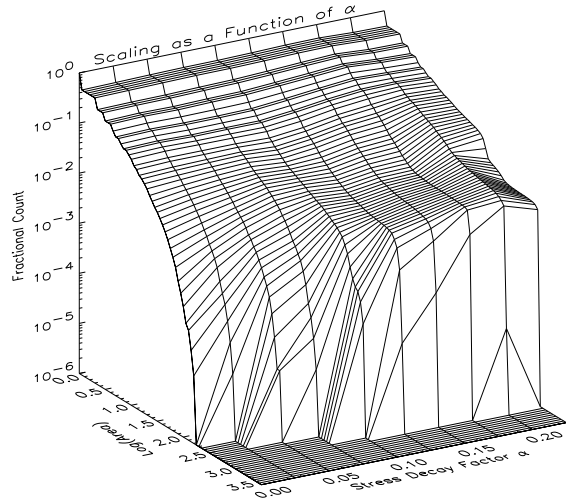


Figure 4.6: Magnitude-frequency relation as a function of α . The stress decay increases along the x-axis and event size along y. Characteristic events appear as α exceeds 0.10, creating a plateau in the large event counts.

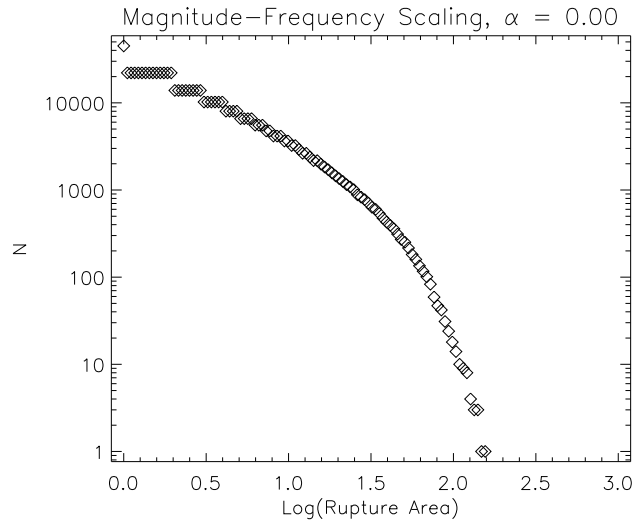


Figure 4.7: Magnitude-frequency scaling in the absence of stress decay. The narrow range of event sizes prevents a clear scaling region from being visible.

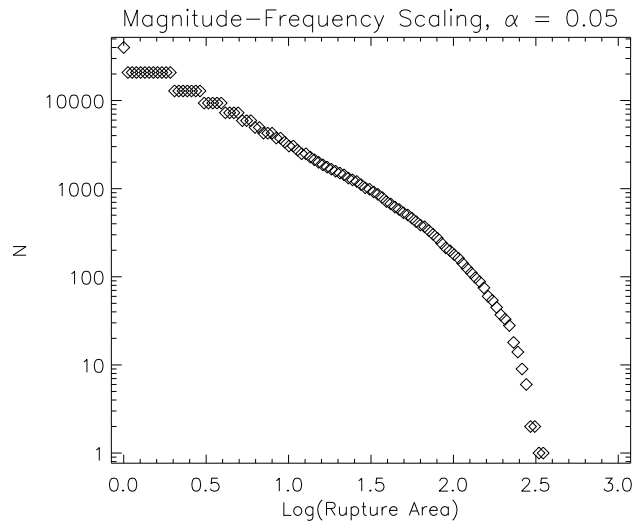


Figure 4.8: With $\alpha = 0.05$, the magnitude-frequency plot shows a region of strong power-law behavior over a broad range of event sizes. This is a good value of α for simulations with a Gutenberg-Richter distribution of events.

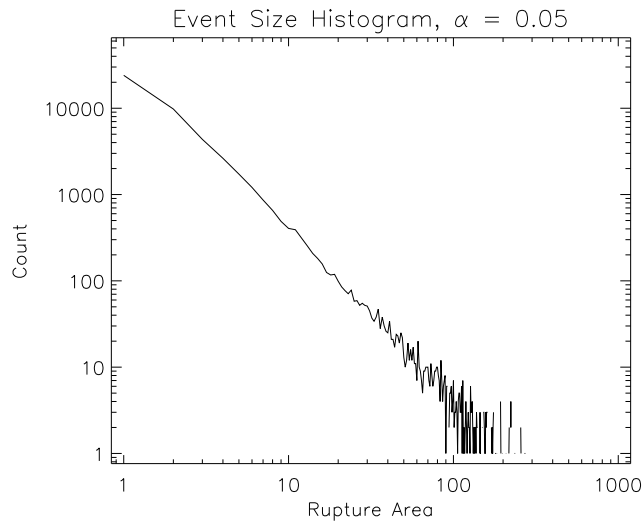


Figure 4.9: A histogram of event areas shows that they follow a power-law distribution over the entire range of rupture areas.

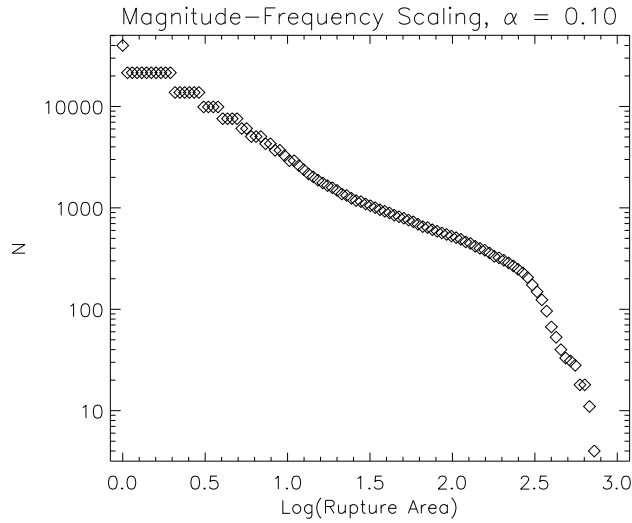


Figure 4.10: As α is increased to 0.10, the magnitude-frequency curve seems to exhibit two scaling regions with a break. In actuality, an increased number of large events distorts the cumulative statistics, making it difficult to determine the b-value of the curve.

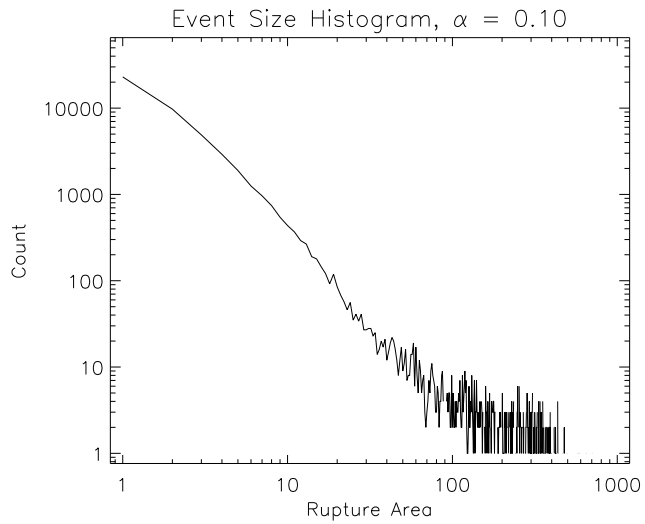


Figure 4.11: The noncumulative histogram of event sizes for $\alpha = 0.10$ shows power-law behavior with an increased number of large events. This behavior is intermediate between a Gutenberg-Richter scaling distribution and a characteristic distribution.

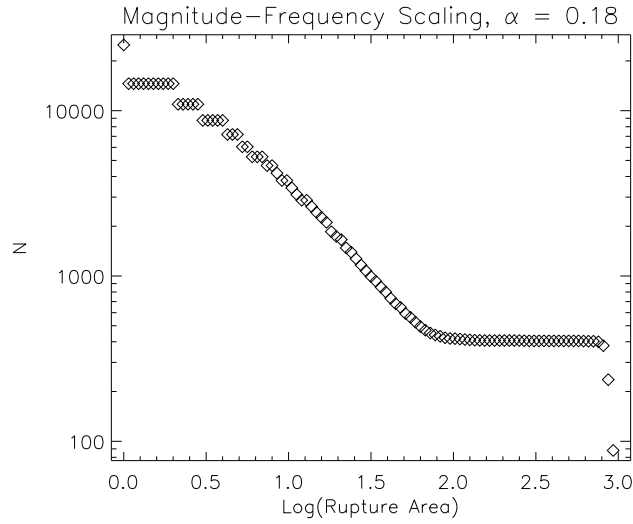


Figure 4.12: At $\alpha = 0.18$, the Gutenberg-Richter scaling of small events is again visible with a tail caused by frequent very large, system-scale events. This is the “characteristic earthquake” distribution.

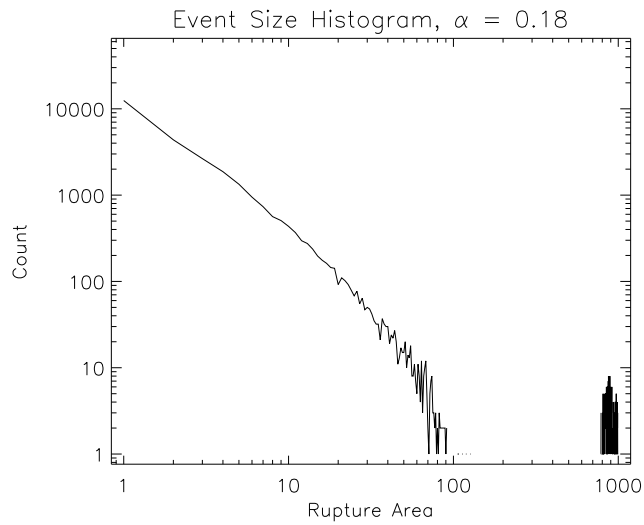


Figure 4.13: A histogram of event sizes at $\alpha = 0.18$ shows clearly the cluster of “characteristic earthquakes” that rupture nearly the entire fault surface.

cumulative frequency counts. As α is increased to 0.18, the magnitude-frequency count (Figure 4.12) gains a long tail; this is the scaling associated with a characteristic event distribution. The size histogram (Figure 4.13) shows clearly the high-end peak of very large, lattice-spanning events.

4.1.2 Temporal Clustering

Another feature of natural seismicity that we would like to look for in this data is the presence of fore- and aftershocks. Foreshocks and aftershocks are most easily characterized by their temporal clustering. A natural fault has a typical recurrence interval; the tectonic forces acting on the fault are very constant on the short timescale, and a mature fault has a well-established cohesion strength. So the characteristic recurrence interval τ is simply the strength of the fault divided by the loading rate:

$$\tau = \frac{\sigma_F - \sigma_R}{L} \quad (4.1)$$

If τ is uniform (or nearly so) throughout the system, we expect that the time between events at any particular location will have a distribution centered on τ . Random fluctuations due to stress, residual noise, and interaction with other fault patches will give the distribution some spread, but the average inter-event time will be close to τ .

Foreshocks and aftershocks, by definition, cluster temporally and spatially around a large event. Temporal clustering implies shorter than normal inter-event times; thus, the time between a mainshock and an aftershock will be significantly less than τ . If aftershocks are present in the system, then, we will find evidence for them by examining the spectrum of inter-event times. Along with the main peak at τ , if fore- or aftershocks are present they will create a second peak, at a shorter interval, in the distribution of recurrence times.

To study this distribution, I constructed an individual event history for each fault patch. I then calculated the histogram of inter-event times for each fault. Though there were 30,000 post-transient events to work with for each value of α , there were also 1000 patches on which

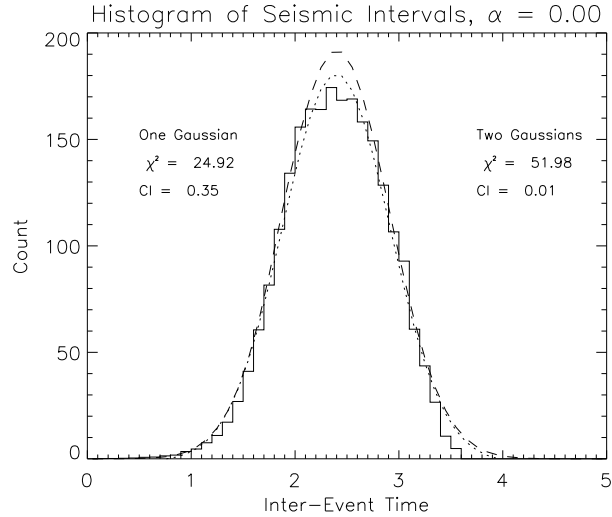


Figure 4.14: With no stress decay, the event recurrence intervals cluster around a single value of τ . The dotted line is the single Gaussian fit curve, dashed line is the double Gaussian.

those events occurred. Even though there were many very large events, the power-law scaling of event sizes means that the vast majority of the events are small, and the total number of failures for each patch is therefore relatively small, measuring only in the tens of events. This is an insufficient sample for reliable statistics on the distribution of time between successive events. However, since all patches are identical, they can be regarded as interchangeable. This means that, at least with regard to the interval between events, the system as a whole should be ergodic (though true ergodicity has been proven only in the mean field [134]) and long-time statistics may be interchanged with ensemble statistics. So I summed the histograms from all the patches to create a single ensemble histogram of recurrence times. The results are shown in Figures 4.14 through 4.19.

Not knowing any details about the shape of the distributions, I assumed that they were Gaussian, since the Central Limit Theorem dictates that the sum of many independent, identically-distributed random numbers (such as random variations away from the expected recurrence interval τ) will converge to a Gaussian distribution. To test the hypothesis that the distribution of inter-seismic intervals was the sum of two such Gaussians (one centered on τ and

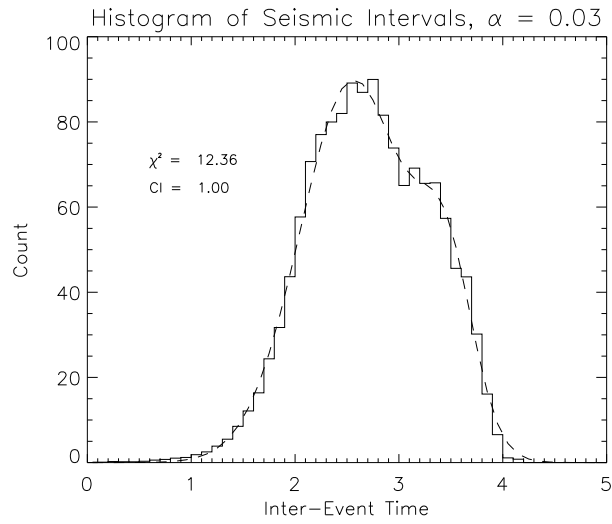


Figure 4.15: At $\alpha = 0.03$, the peak of large events has begun to move out from the larger peak of background seismicity. The distribution is well-characterized as the sum of two Gaussians, suggesting that aftershocks may be present.

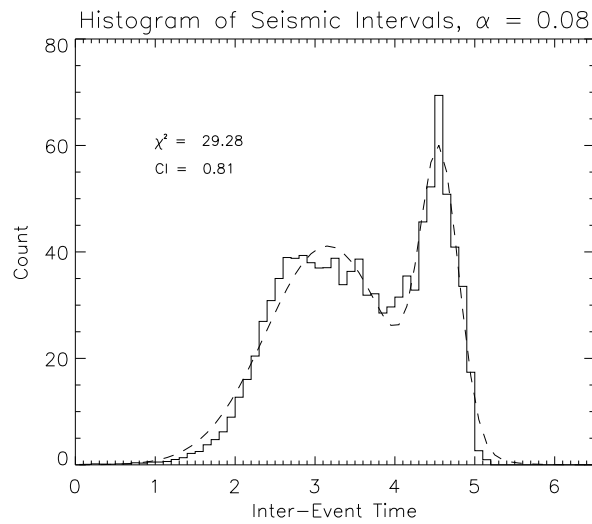


Figure 4.16: The separation of the recurrence interval distribution into two peaks is now unmistakable. As large events become more prevalent, their numbers increase the height of the large-event peak at the expense of the smaller events. The distribution can still be fit well with a double Gaussian, but some discrepancies are becoming visible.

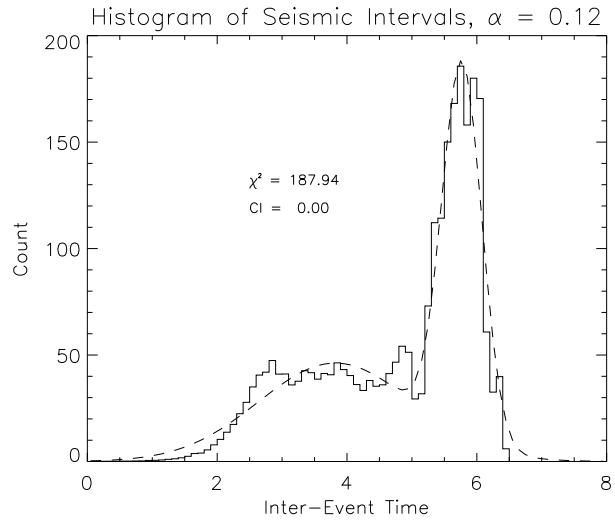


Figure 4.17: At $\alpha = 0.12$, the possibility that there are more than two peaks becomes evident. The structure present in the lower peak suggests that the distribution of interevent times may depend on more than simply the division of events into two groups, mainshocks and foreshocks/aftershocks.

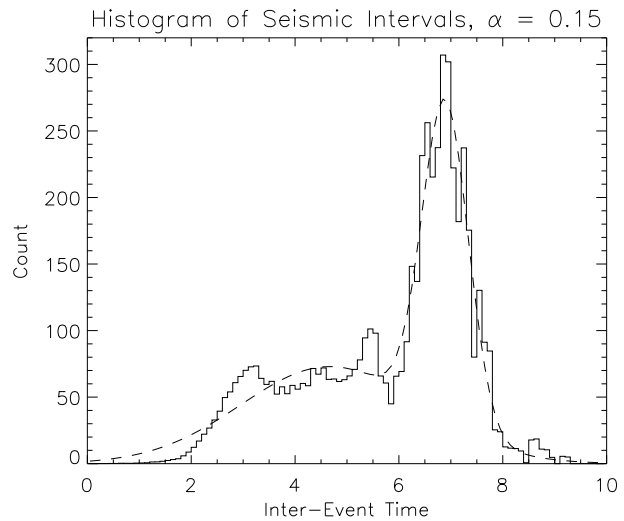


Figure 4.18: The double Gaussian is no longer a good fit for the recurrence time distribution. Corresponding space-time plots show some possible foreshock sequences, but no aftershocks. While the lower peak could represent foreshocks, the distribution should be smoother if that were so.

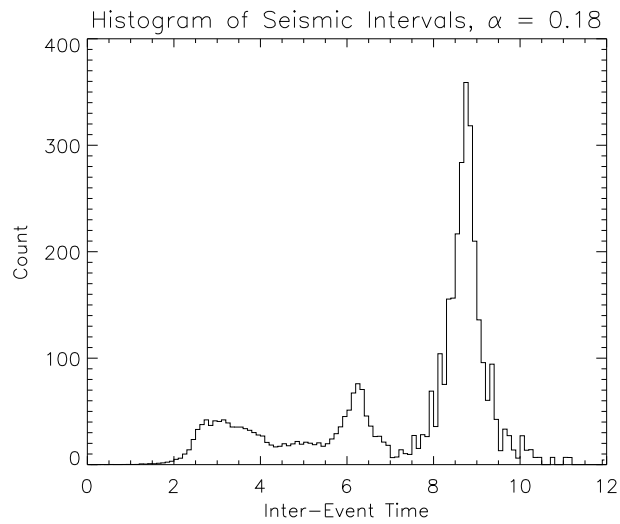


Figure 4.19: At $\alpha = 0.18$ the presence of a second peak near recurrence time 6.2 is unmistakable. The original peak centered on $\tau \approx 3$ is still present, though small. This cluster of small events is more likely to be caused by the higher loading rate at the edges of the fault than by foreshocks preceding large events. These patches remain active even after the central patches change from failure to creeping behavior.

one representing the fore- and after-shocks), I used a non-linear least-squares fit procedure using the Levenberg-Marquardt algorithm [175] to fit both a single Gaussian and a double Gaussian to the histogram.

For $\alpha = 0$, the histogram has only a single hump. It is much better fit with a single Gaussian (reduced χ^2 value of around twenty-five) than with two Gaussians (reduced χ^2 around fifty). As α is increased to 0.03, a second hump begins to separate from the main Gaussian, moving off to the right. This distribution is fit very well by the sum of two normal curves, with a reduced χ^2 of only 12.4. This second peak is actually the distribution centered on τ ; as the rate of stress leakage is increased, the recurrence interval between large events becomes larger as well.

Increasing α to 0.08, the presence of two peaks becomes quite obvious, and the double-Gaussian fit remains very good. However, as we increase α further still, it starts to become evident that the distribution is more complicated in structure than just the sum of two Gaussian curves. Figure 4.17 shows the case for $\alpha = 0.12$. The χ^2 value has become quite large, and the confidence interval of the fit has shrunk to zero. Even to the eye, it is clear that the double Gaussian is not a good fit. However, it is also clear that this is because there is more structure in the lower peak of inter-event times than the higher, a situation which persists and is enhanced as α is increased further to 0.15 and 0.18.

The large recurrence intervals correspond to large events, whose prevalence grows with α , as shown in previous Figures. As it separates from the shorter peak, it is tempting to identify the latter as the signature of fore- and after-shocks to the long-interval mainshocks. However, the space-time plots of activity show no evidence of either foreshocks or aftershocks as large events begin to appear. It should also be noted that when the two peaks in the recurrence time histogram separate, the lower peak remains where it started, centered a little below 3.0. The main peak is the one that moves, increasing the time between large events. This is because the lower peak represents not fore- and aftershocks, but background seismicity that is unaffected by stress leakage. The source of this background activity is the patches along the edge of the

fault, which remain active even when the central patches have ceased to slip. The patches at the edges of the fault are loaded more rapidly, and consequently will have a shorter recurrence interval than the rest of the fault.

Although the recurrence interval histograms are explained by spatial variations in loading rather than temporal event clustering, there remains some minor and less compelling evidence for aftershocks. At $\alpha = 0.12$, the space-time plot of activity does show sequences of events that could be interpreted as foreshocks and aftershocks. At several point in the simulation, a small region will fail repeatedly before meeting up with the beginning of a large event at its edge. These sequences could be foreshocks, and the recurrence histogram for that value of α shows signs of a possible third peak separating from the base of the main peak. This third peak is very distinct at $\alpha = 0.18$, and possible foreshocks are visible in the space-time diagram for that value as well.

The existence of aftershocks is harder to argue. Mechanisms exist for the generation of foreshocks; the primary cause would be incomplete stress relief for a small region generating a larger region of correlated stress by stress transfer and subsequent stress decay. A mechanism for aftershocks is harder to find, as the large mainshock transfers much more stress than a small foreshock; any correlated region that is brought closer to failure by stress transfer from mainshock activity is likely to be triggered, rather than merely advanced in its seismic cycle, especially if it is close to the primary rupture. In addition, natural aftershocks generally occur on or very near the ruptured surface, an occurrence which is not possible in the Fault-Patch model by its construction; once a fault patch has ruptured, the stress acting on it has been relieved and so it takes a long time for that patch to build stress back up to the failure level again.

If aftershocks indeed are dependent on some physical mechanism for stress-transfer and release on intermediate timescales, it is perhaps no surprise that they are absent from the simulations. However, in turn, that suggests that the presence of foreshocks would indicate that they do not depend on some special physical property or mechanism, but are an inherent

feature of lattice threshold systems with stress leakage. A thorough and systematic study of a fault system with a variety of loading and stress decay rates would be necessary to determine whether foreshocks can exist in models of this type, and is beyond the scope of this research.

4.2 Interaction Strength

The interaction strength between patches is another important parameter determining the range of possible event sizes. The self-neighbor ratio is the ratio between the amount of stress that a unit slip will radiate to a point at a distance of one kilometer and the amount of stress that it will relieve at the center of the patch. Because the amount of stress to be relieved upon failure is generally uniform throughout the system, the SNR acts in large degree as a measure of the strength of the coupling between the elements of the model. If the SNR is large, the coupling will be weak; a given slip will produce a much larger stress at the center of the patch, so a patch will slip much less when it fails. Conversely, if the SNR is small, then every time a patch fails, it will transmit a large amount of stress to all its neighbors, possibly triggering them to fail as well and increasing the size of the event.

I simulated 30,000 events at a variety of SNR values from unity up to 120; without exception, all simulations with SNR less than 50 became numerically unstable right away. The remainder exhibited normal behavior while enhancing or suppressing the growth of individual ruptures. Figure 4.20 shows the event histories for four different values of the self-neighbor ratio. At a value of 50, the model has fallen into a limit cycle. Large events that involve every element in the lattice happen regularly, and only the edge patches are involved in any events outside the large one.

If the SNR is increased to 60, the model resumes its noisy behavior, but the large effective connectivity results in an overabundance of very large events. At a value of 70 (the default value used in this research), the model has resumed its normal event distribution. At 80 and higher, the model retains the form of its event-size distribution, but the effective connectivity is low and results in an overall decrease in event sizes.

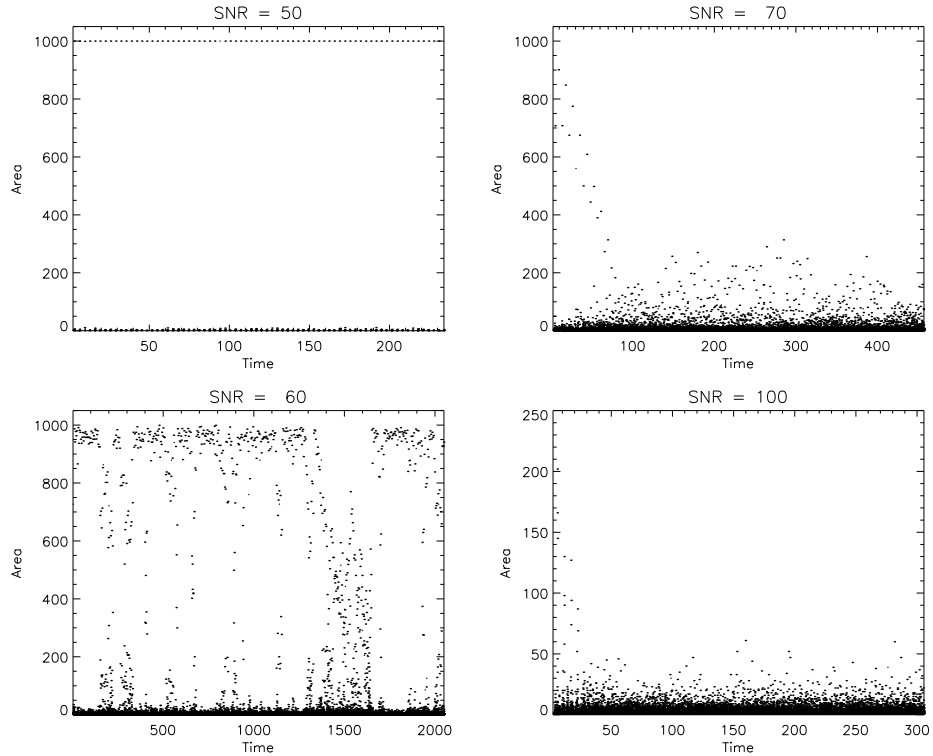


Figure 4.20: Temporal evolution of event sizes shows the effect of SNR on the model's behavior. Note that at $\text{SNR} = 50$, the system has fallen into a limit cycle where the entire fault ruptures every few years. Once the SNR exceeds 70, large events die away smoothly until all that remains is noise.

Figures 4.21 through 4.24 show this effect in the magnitude-frequency scaling. When the SNR is large, the depletion of large events is shown by an upward curvature to the cumulative frequency and by a downward roll-off at lower magnitudes. The magnitude-frequency scaling for these datasets was calculated from the total moment released in each event. Again, the value we use in these simulations ($SNR = 70$) is the one that produces data that best matches the empirical Gutenberg-Richter scaling. There is some evidence from simulations with irregular geometry that the best value may be a function of the average (or perhaps minimum) inter-patch spacing, but the principle of how to find the best value remains the same, as does the qualitative effect of the SNR value.

Having found values of α and the self-neighbor ratio that will produce Gutenberg-Richter scaling over a large range of event sizes, we can simulate event histories that are statistically consistent with observed seismicity in southern California. Although other values of these parameters may produce realistic behavior as well, whether for this or other seismically active regions, the primary focus of this research is the effect of geometry, not rheology; using one pair of realistic parameter values reduces the number of scenarios to be simulated dramatically, and is sufficient for our purposes.

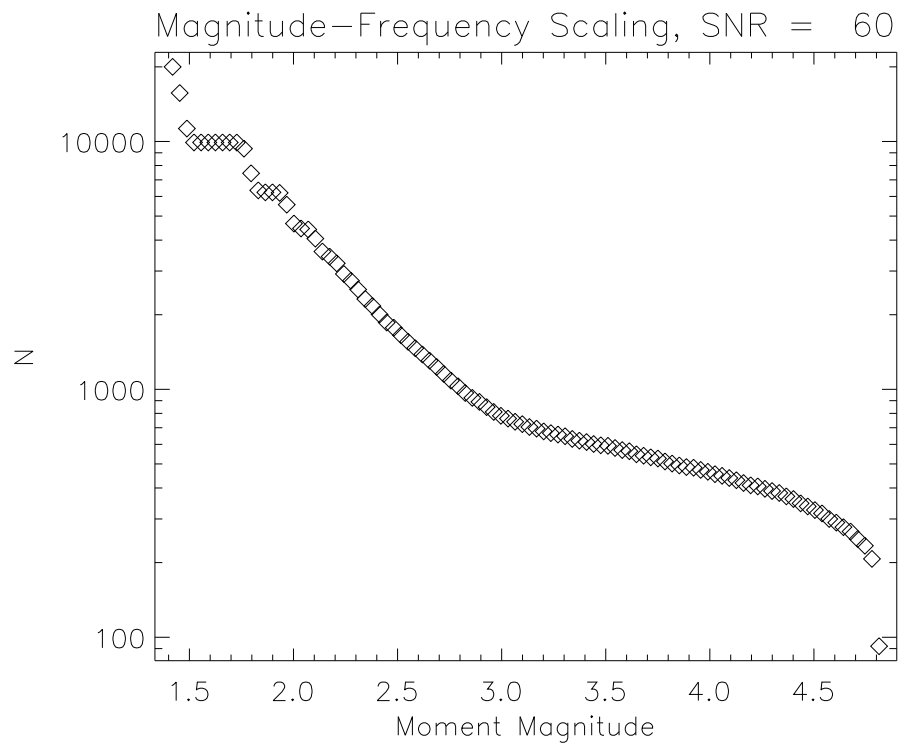


Figure 4.21: Magnitude-frequency scaling for a self-neighbor ratio of 60. The interaction strength has drastically increased the number of very large events, and is too high to produce Gutenberg-Richter scaling behavior. At lower values of the SNR, the model enters a limit cycle or becomes numerically unstable.

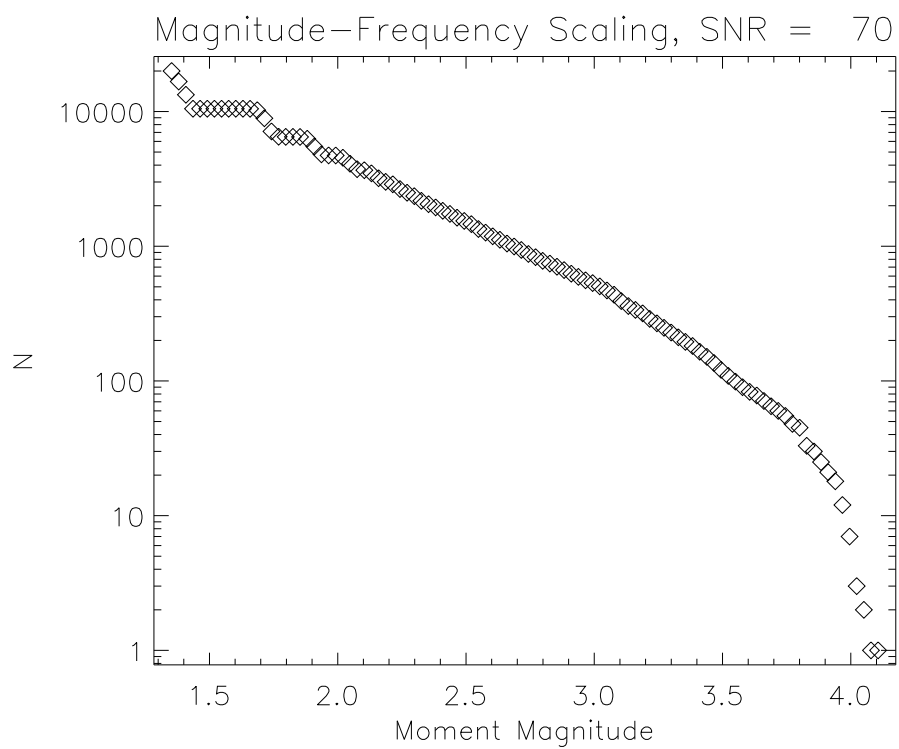


Figure 4.22: With the SNR set at 70, the magnitude-frequency relation shows a distinct scaling region spanning nearly a decade and a half in magnitude.

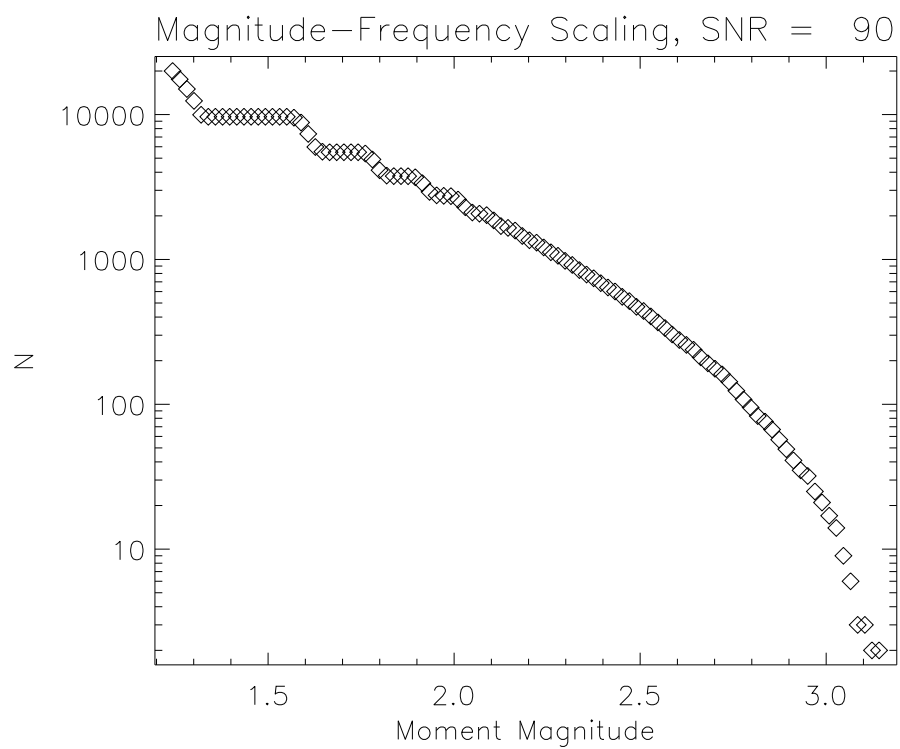


Figure 4.23: The model is now under-connected; the SNR has been raised to 90 and a commensurate loss of large events can be seen.

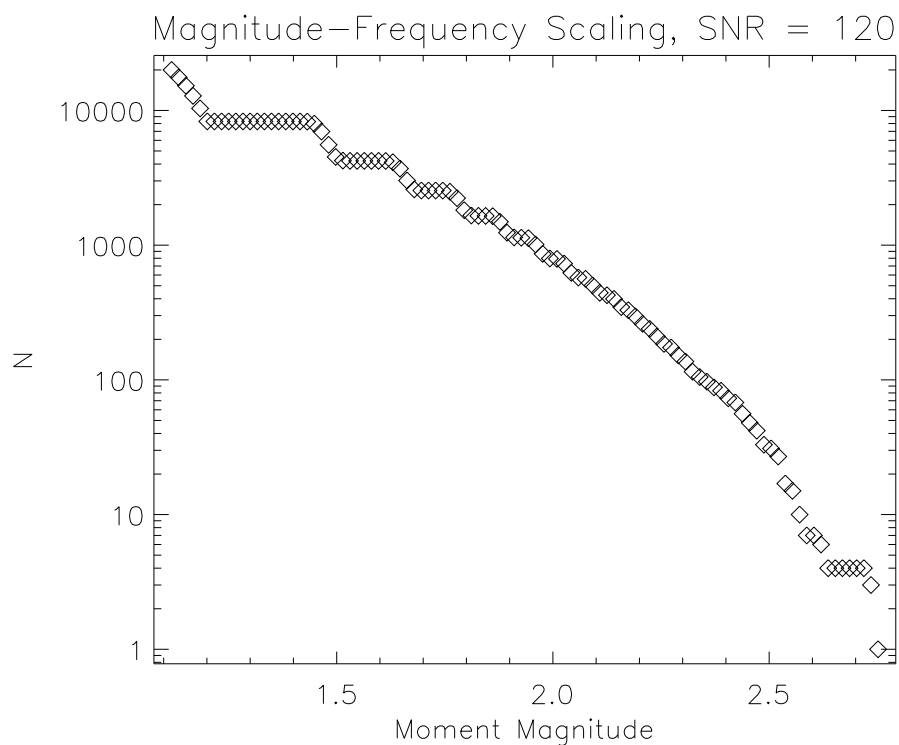


Figure 4.24: Though the curve of the magnitude-frequency relation is now less prominent, the number of large events remains very low. Note the extent of the x-axis is much less than that of analogous plots for other values of the SNR.

Chapter 5

The Z-Shaped Fault

When the number of spatial dimensions that a model earthquake fault resides in is increased from two to three, the differences are not merely quantitative; they are qualitative as well. When constrained to two dimensions, all realistic earthquake faults can be approximated by a rectangle. A single number, the aspect ratio of the approximating rectangle, will capture the vast majority of the geometric complexity of all planar faults. When the faults have three-dimensional geometry, on the other hand, the parameter space of possible configurations becomes enormous.

In order to study the effects of three-dimensional geometry without becoming overwhelmed by the possibilities, I chose to study a single configuration in detail. I wanted to study a fault system that was simple, but that possessed features that were qualitatively different from those that can be simulated using a planar fault. The system I chose to study was a single fault with two bends, each in opposite directions. Unlike a planar fault, this configuration of faults has the potential to develop both excitatory and inhibitory interactions through the action of tensor stresses. It is also particularly relevant to the study of real earthquakes, as it reflects the geometry of the San Andreas fault in California, which strikes northwest on the whole but with a segment trending more to the west just south of the fault's intersection with the Garlock fault.

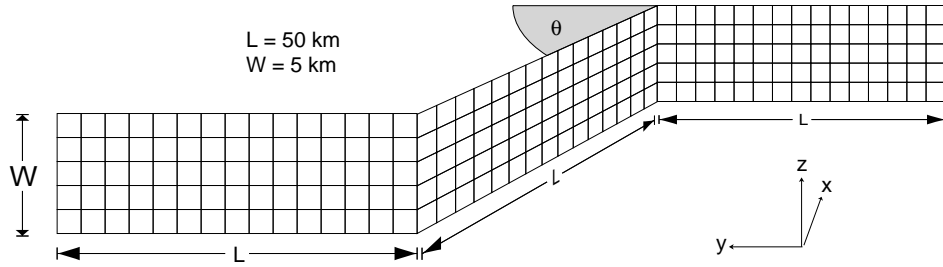


Figure 5.1: The z-shaped or “zig-zag” fault. Each segment consists of a grid of 1000 half-kilometer square patches in a 10:1 aspect ratio. (Figure is not to scale) The angle θ varies from 0 to 90 degrees.

5.1 Geometry

The zig-zag or z-shaped fault consists of three vertical strike-slip fault segments. Each segment is fifty kilometers long (that is, along strike) and five kilometers deep, and is divided into one thousand half-kilometer square patches, giving the segments a 10:1 aspect ratio. The three segments are placed end-to-end with the first and last segments parallel, and the middle segment angled by some amount. For simplicity, the end segments are always oriented striking northward in the map view. The angle θ of the strike of the middle segment (measured counter-clockwise from north) then characterizes the configuration of a z-shaped fault; $\theta = 0$ corresponds to a straight fault with a 30:1 aspect ratio, and an angle of -135 degrees would make an ‘N’-shape.

I studied the effects of this geometry on the seismicity by regarding the angle θ as a parameter and varying it from 0 to 90 degrees in five-degree increments, keeping all other aspects of the simulation constant. I drove the model with a uniform slip rate of 1 mm/year. I chose to use a uniform slip rate so that each segment of the fault would have roughly the same rate of seismic activity, allowing me to study the effect of geometry on the interaction between segments. I also drove the faults in a right-lateral sense to avoid opening up a gap on the middle segment. This scenario becomes unphysical as the angle θ approaches the physically unrealistic 90 degrees, but it approaches that limit gracefully.

For each θ -value, I simulated 30,000 events. Observation showed that this was a long

enough time for the model to evolve past any initial transient and into a steady state. I calculated the statistics and correlations of the activity from the post-transient subset of these events; to examine the activity correlation from the basis of a statistically strong sample, I also simulated a further 50,000 events after the 30,000 event mark for geometries with $\theta = 0, 30, 45, 60$, and 90 degrees. Phase correlations, stress clusters, and other calculations with regard to the statistics of the stress distributions on the surface of the fault were similarly calculated from events occurring after the 30,000 event mark so that I could be certain that the transient behavior had died out.

5.2 Statistics of Seismic Activity

5.2.1 History and Transient Behavior

Figure 5.2 shows the evolution of seismic activity on four different zig-zag faults, including an initial transient phase. These histories are typical of all the geometries simulated, with the transient dying away in roughly the first 10,000 events. The only exceptions were $\theta = 15, 45$, and 70 degrees, where the transient lasted some twenty or twenty-five thousand events. The fact that the transient lasted longer in these cases is not indicative of any geometric effects; figure 5.3 shows the event histories for two different simulations on a zig-zag fault with $\theta = 45$ degrees. These two simulations were identical except for the seed value used to initialize the random number generator.

The transient behavior consists of occasional very large events that involve a large fraction of the patches in the fault. These events recur at regular intervals, gradually shrinking in size until they are indistinguishable from the large events that arise from the interplay between the stress-field roughening effects of the random residual and the smoothing effects of the stress leakage. A plot of event size versus time (figure 5.4), rather than event number, shows that the very large events in the transient are evenly spaced in time. I calculated the average time between large events for each value of the bend angle; the results are shown in figure 5.5. The average time between large events in the transient for all values of the bend angle was 4.3

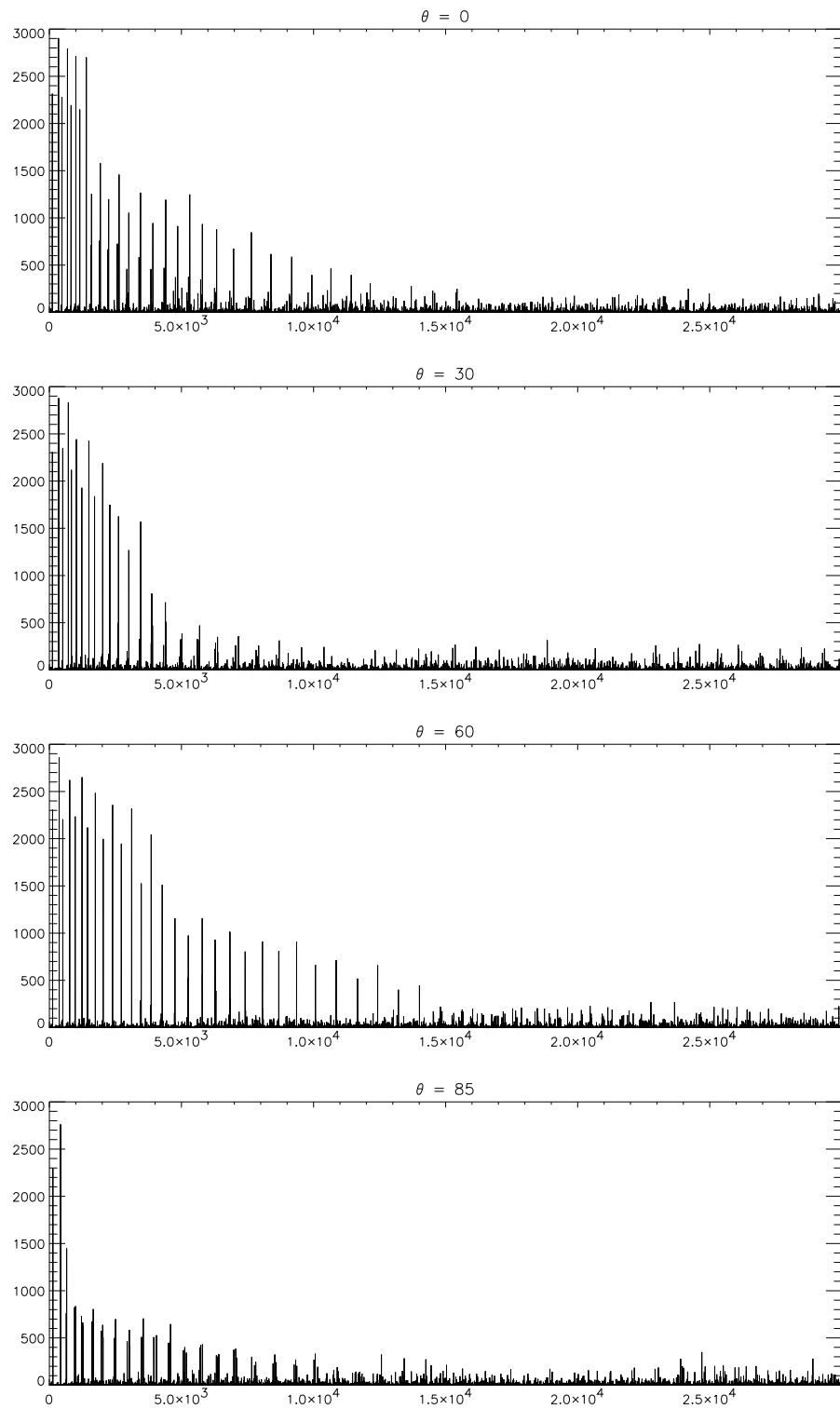


Figure 5.2: Four typical event histories for different values of the bend angle θ . Event area (number of patches) is plotted on the y-axis, event number on the x-axis. The histories for other, intermediate values of θ were similar. In all cases, the initial transient behavior dies out well before event 30,000.

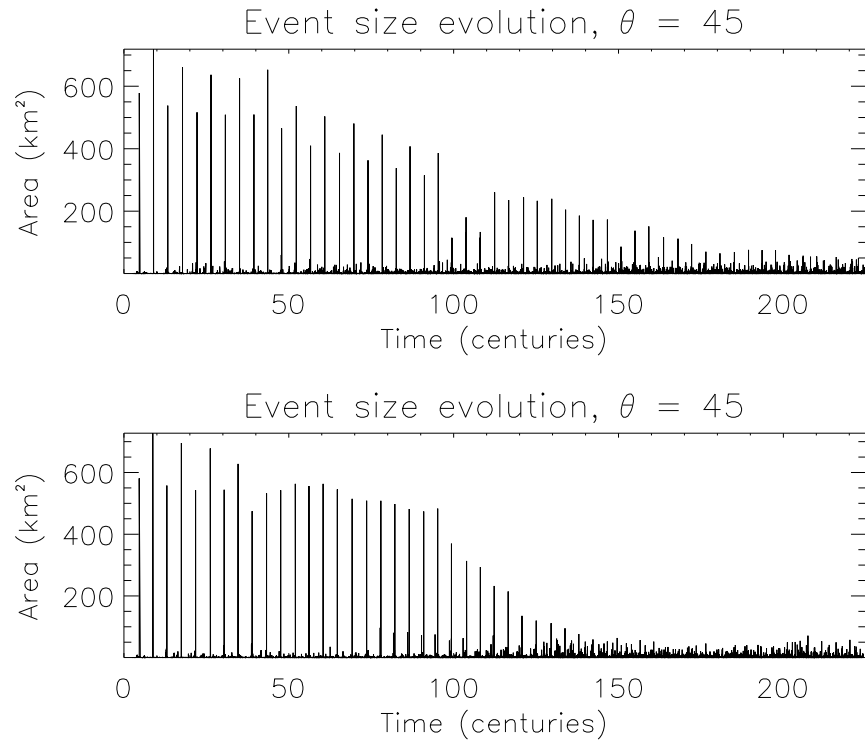


Figure 5.3: The lifetime of the initial transient phase does not depend on geometry. These two graphs show the event histories for two simulations of a fault with 45-degree zig-zag geometry. The simulations were identical but for the seed value of the random number generator, which determines the initial stress distribution and the residual stress values.

centuries.

This value of the interval between large events can be predicted by noting that the patches have a uniform strength of 3 MPa, and that the loading stress rate at the upper and lower edges of the fault is around 0.68 MPa per century. Given that loading rate, the 4.3 century interval is sufficient to bring the patches back to failure and begin the cycle anew.

If the simulation is allowed to continue until the initial transient has died away and the stress field has reached a steady-state distribution, the largest event size becomes much smaller. Figure 5.7 shows the event rupture areas (number of 0.5 by 0.5 kilometer patches, out of 3,000 total) for the 50,000 supplementary events simulated after the transient had ended on the 45-degree zig-zag fault. Figures 5.8 - 5.10 show typical event sequence histories within that supplementary interval; as with the event histories that contain the transient, there are no obvious effects of geometry, even at the $\theta = 0$ and $\theta = 90$ degree extremes.

5.2.2 Scaling

The moment release of a synthetic event is calculated as the total of all the individual patch slips multiplied by the corresponding patch areas and the Lamé parameter μ . Because an individual patch can (and often does) slip more than once during the course of an event, the question arises how the moment scales with the size of the events. According to elasticity theory, the moment generated by slip on a circular or penny-shaped crack will scale as $A^{1.5}$, A being the area of the crack. [141, 145] Figure 5.11 shows the total moment as a function of rupture area for events on a $\theta = 45$ degree zig-zag fault. This plot is tighter and more linear than a plot of moment as a function of number of patch failures, indicating that the moment scales with the area of the rupture and not the number of failures. A linear least-squares fit of the data gives a slope of 1.0861 ± 0.0002 , which is consistent with area-moment scaling relationships found by empirical studies. [176] This scaling between moment and area has important implications for more simplistic earthquake models, namely that the size of the event (the moment) can be well-approximated by the rupture area but not by the total number of failures. A simple model

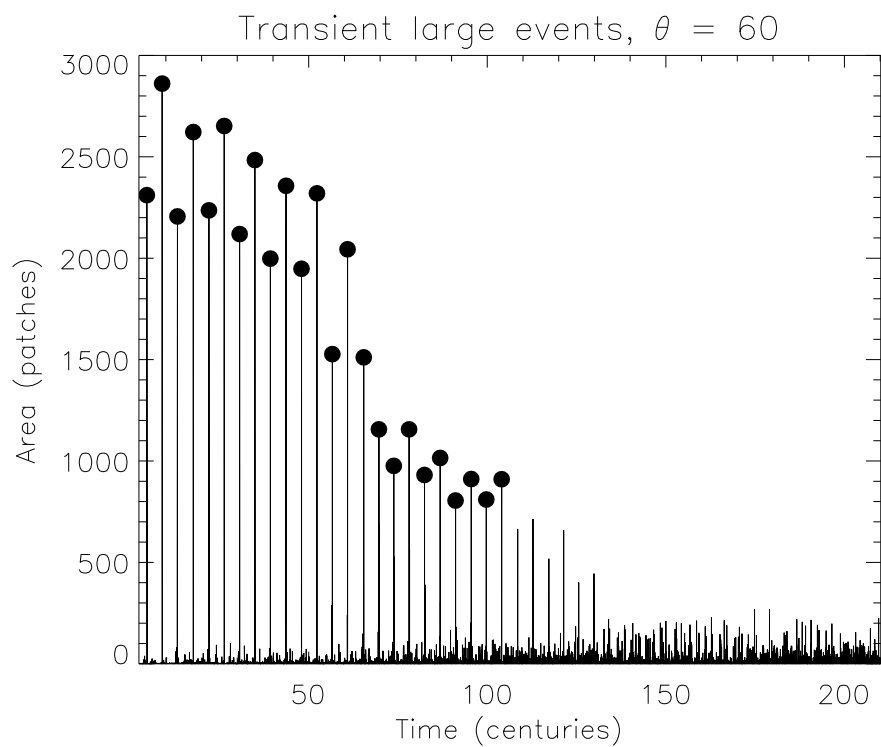


Figure 5.4: The initial transient behavior is characterized by large events that span large fractions of the fault lattice. These events are spaced evenly in time; the circles indicate events that were used to calculate an average lattice-spanning interval.

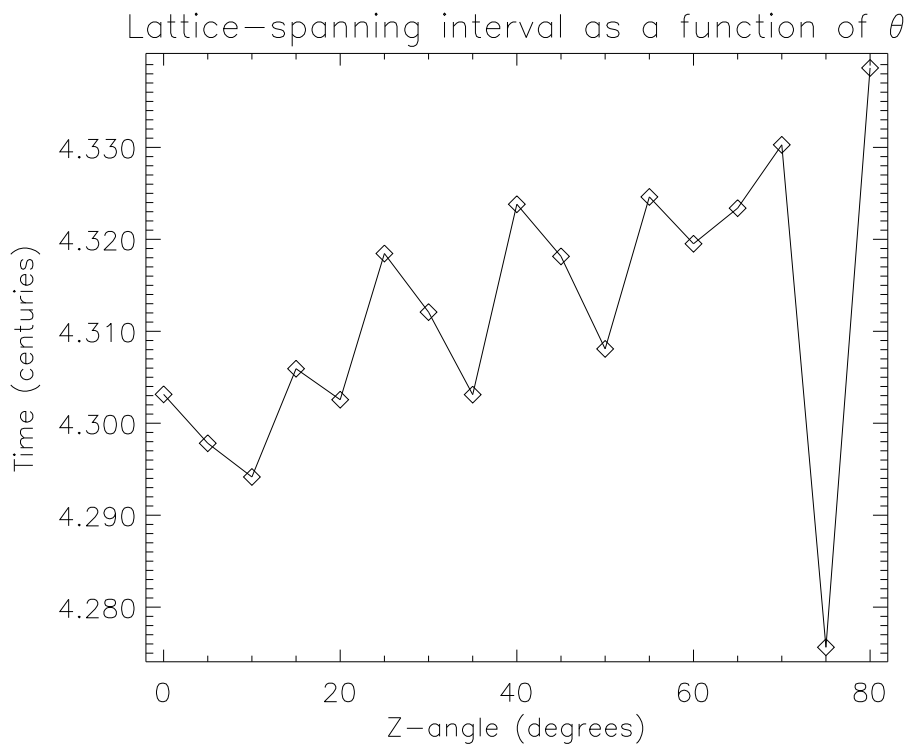


Figure 5.5: The time between large events in the transient is consistent among the various geometries. The average time between large, “lattice-spanning” events is plotted as a function of the bend angle θ .

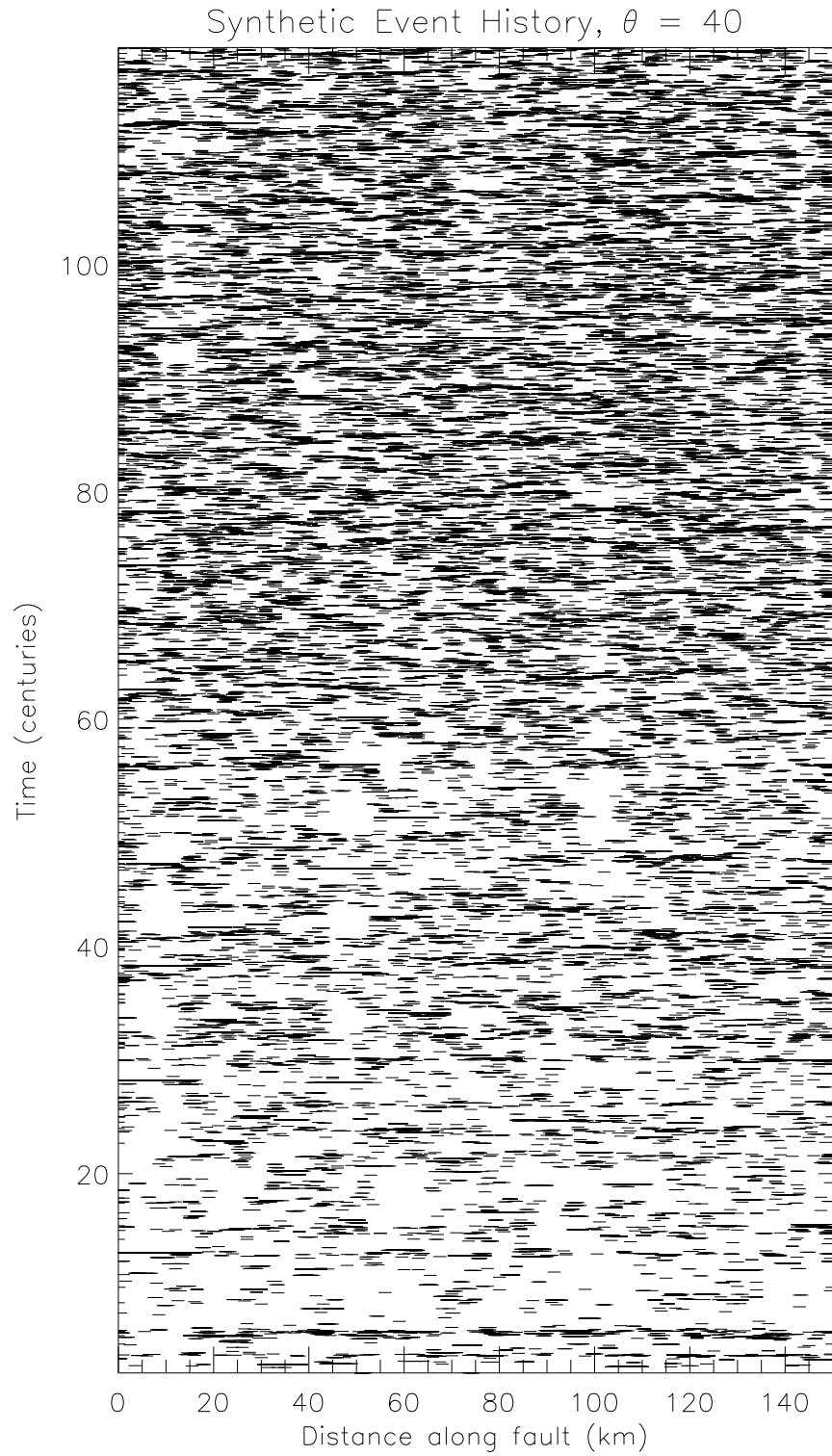


Figure 5.6: A synthetic seismic history for $\theta = 40$ degrees. Each event is represented by a line showing where the fault broke; time increases up the page. This plot is typical of all geometries, and shows no obvious effects of geometry.

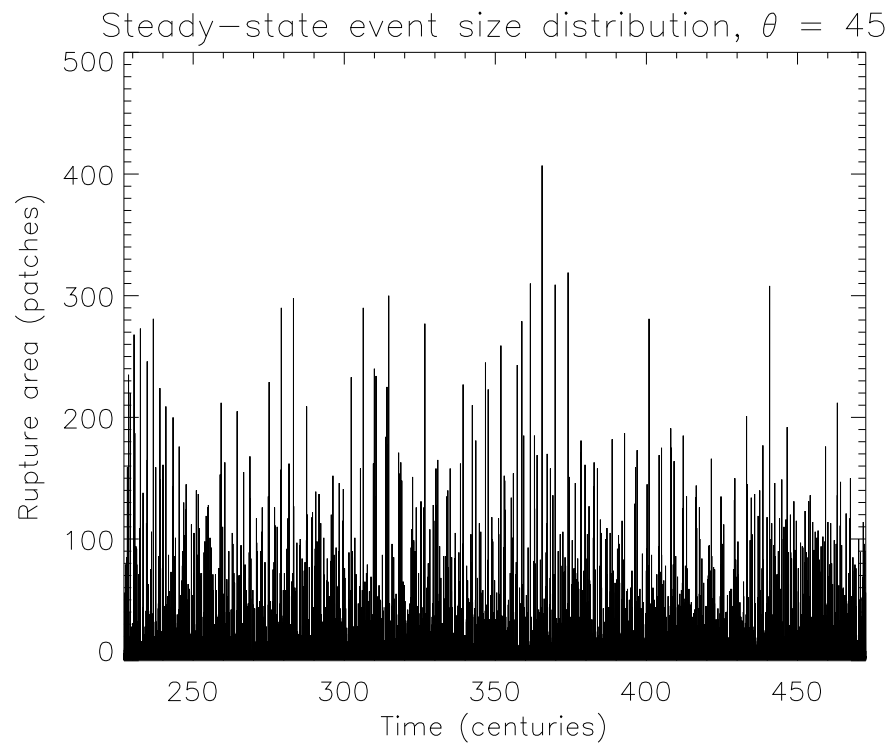


Figure 5.7: The progression of events after the transient initial long-range correlation has broken up and the steady-state behavior has been achieved. This figure is typical of all geometries. Note that the largest event now is only around 400 patches in area, less than half the extent of a single segment of the fault.

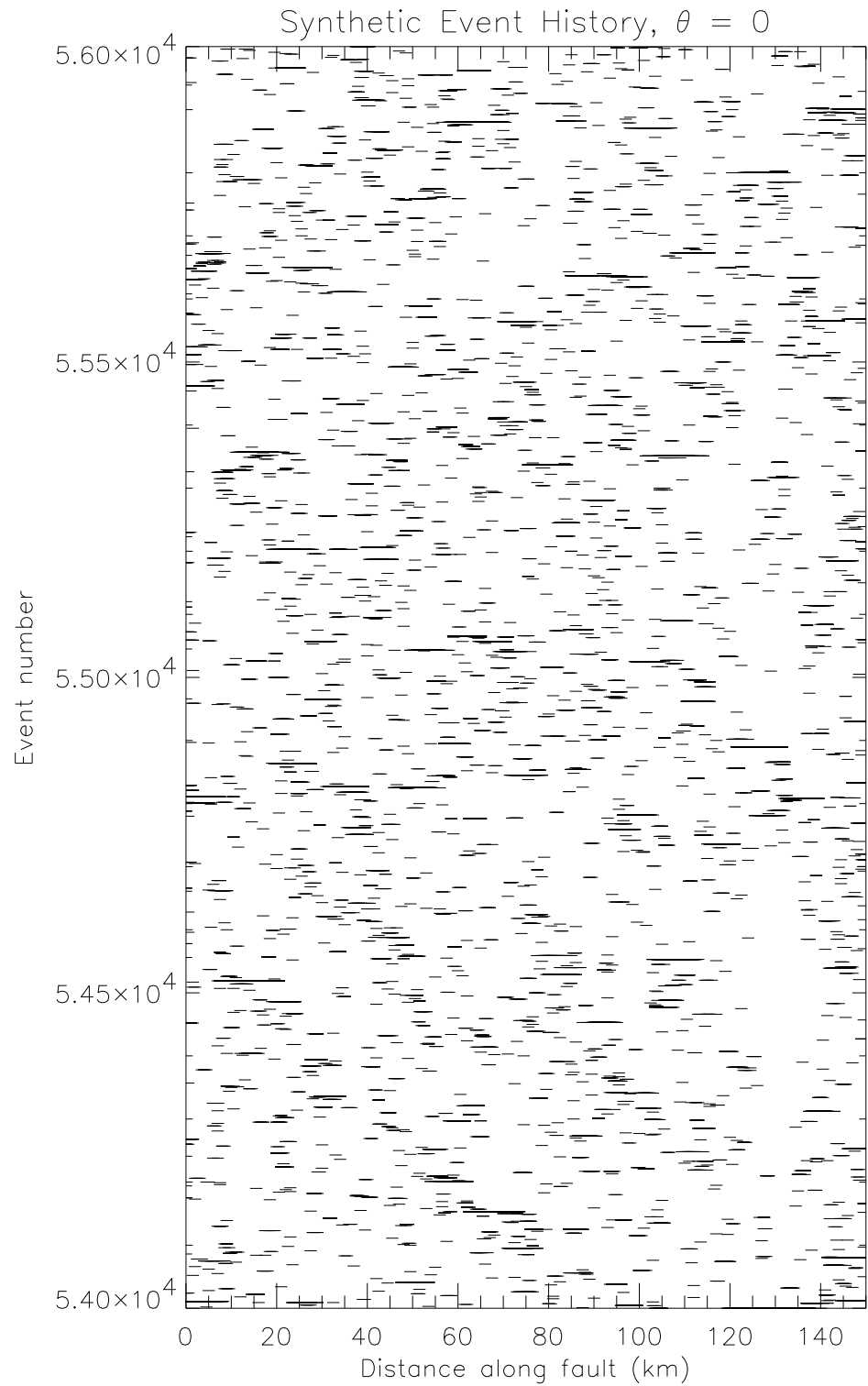


Figure 5.8: A typical sequence of 2000 events from data in the steady-state regime. Event number (time) increases moving up; each rupture is depicted as a horizontal line indicating the portion of the fault that failed during that event. Note that variation in depth has been ignored; a rupture involving patches at the bottom of the fault is plotted the same as one involving patches at the top. $\theta = 0$ in this figure.

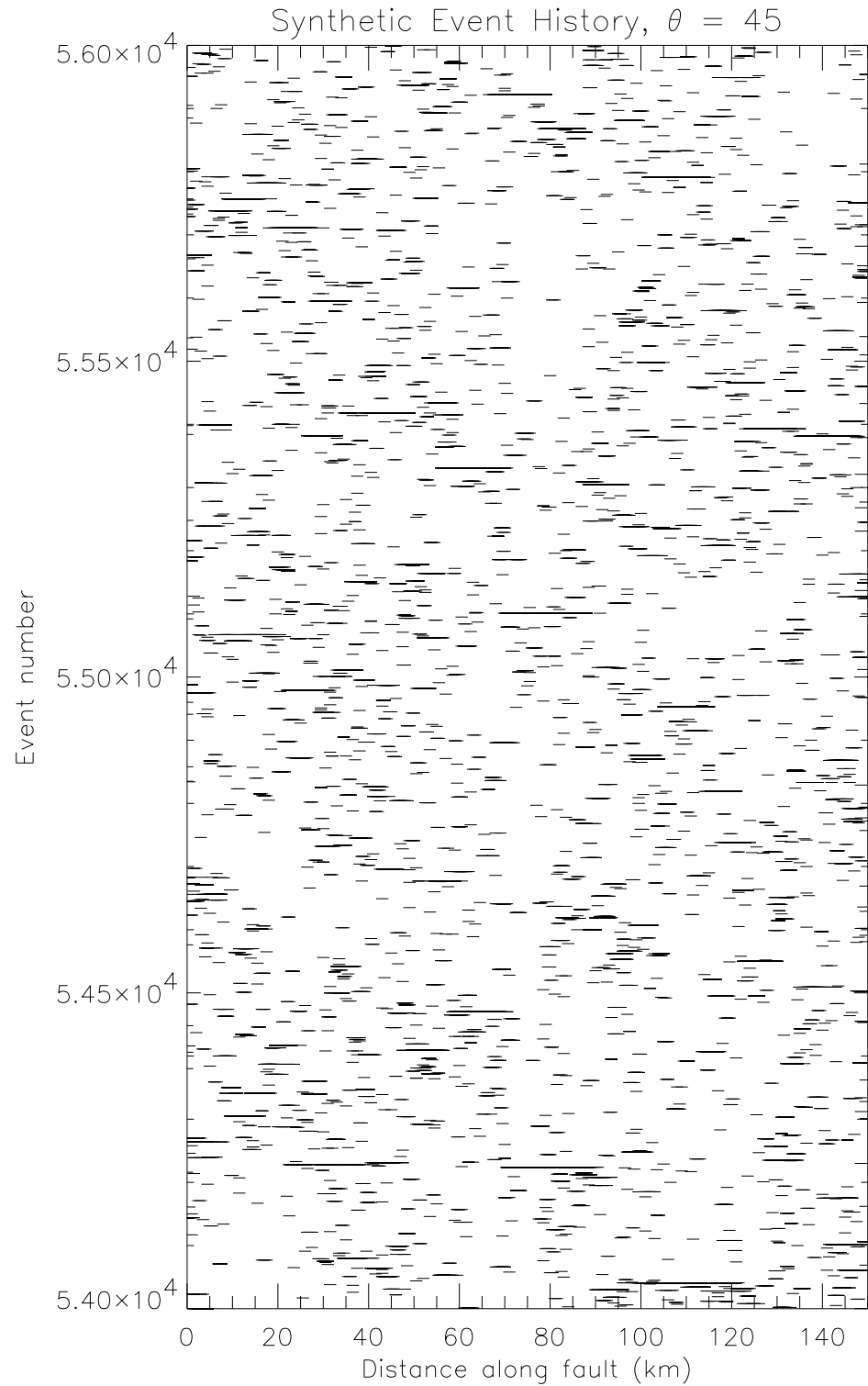


Figure 5.9: As figure 5.8, but for the 45-degree case. There is no difference between the two geometries readily discernible to the eye. This figure is typical of the entire post-transient history.

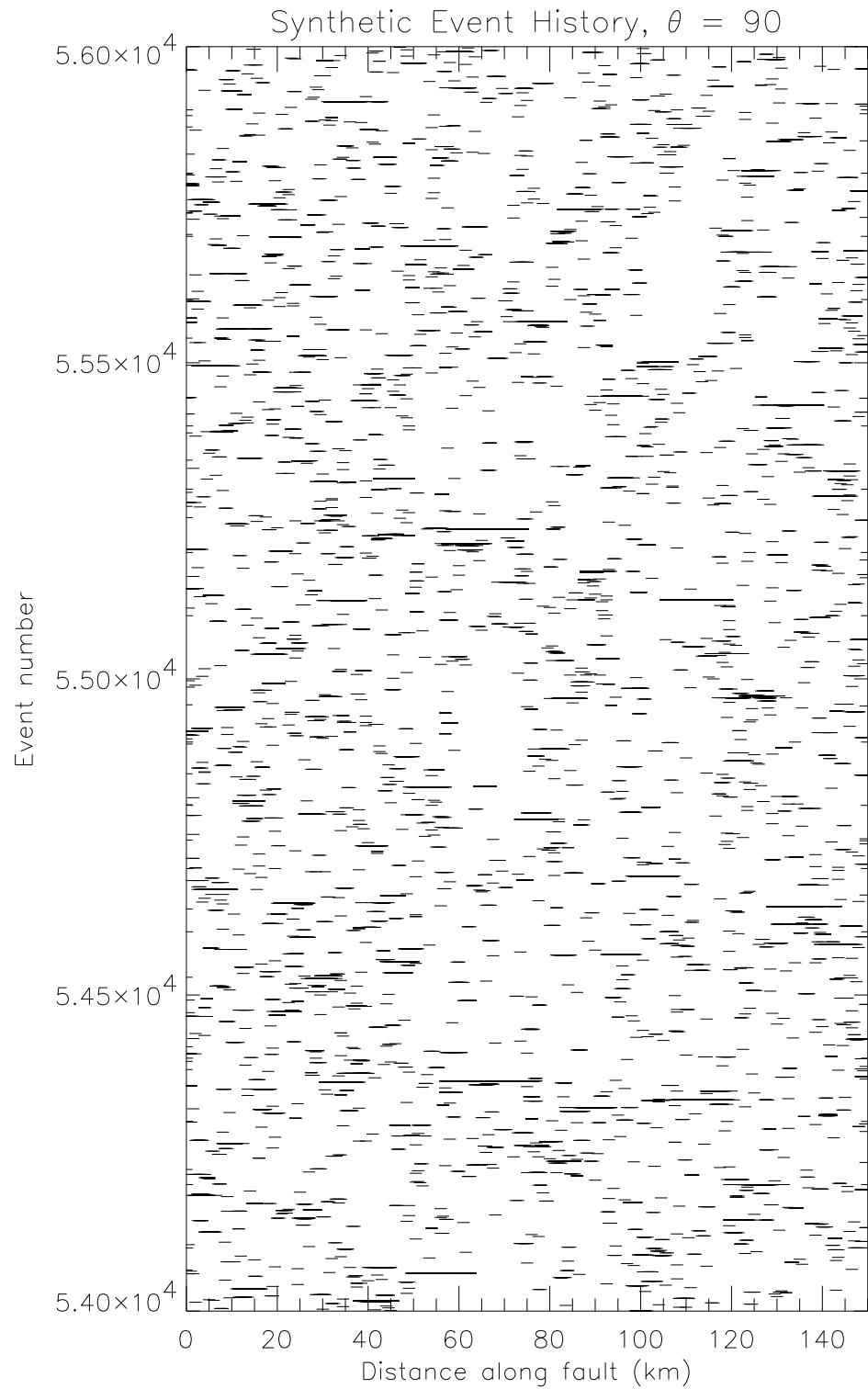


Figure 5.10: As the previous two figures, but for a zig-zag fault with 90-degree bends. Even at this extreme of geometry, the bends have no apparent effect, and some ruptures can even be seen to propagate around the corners located fifty and one hundred kilometers along the fault. One particularly obvious example occurs at the fifty-kilometer bend around event 54,250.

that records only minimal event data should therefore take care to track area and not number of failures.

Another type of scaling found in these simulations is Gutenberg-Richter moment-frequency scaling. This scaling is one of the most basic statistical features of real seismicity, so it should be present in any model that purports to represent the dynamics of fault networks. Figure 5.12 shows a cumulative histogram of events larger than a given magnitude for a zig-zag fault with a bend angle of 60 degrees. There is a clear scaling region between magnitudes 2.0 and 3.0 and a roll-off at higher magnitudes, exactly as is seen in real seismicity. The magnitude range is not as large as in a real fault system, but that is to be expected, since the simulation models only a single, relatively small fault. This moment-frequency scaling distribution is present in the data from all geometries; figure 5.13 shows a plot of b -values found by fitting a line to the scaling region of the histogram for each of the geometries that I modeled. The average b -value is very near unity, well within the range of b -values found in nature.[166]

5.3 Cluster Analysis

In the Fault-Patch model, an event begins when the stress acting on a patch exceeds its cohesive strength. It will continue as long as the stress transferred to other patches in the model is sufficient to trigger another failure in the cascade. The magnitude of transferred stress dies off as R^3 ; therefore, when the patches are in a planar or near-planar configuration, we expect by the physics of the model that any event will be confined to the region of neighboring patches that are also near failure. The only way for a distant patch to be triggered is if it is very near the failure threshold, which is unlikely if the patches are sufficiently separated that they are uncorrelated in phase.

Consequently, one statistical feature of interest is how the stresses in the model are correlated with one another. I simulated 1000 events after the model had reached stability for each of several bend angles, recording the stress state of every patch in the model at twenty-event intervals. Each dataset consists of fifty “snapshots” of the stress state of the model. Using the

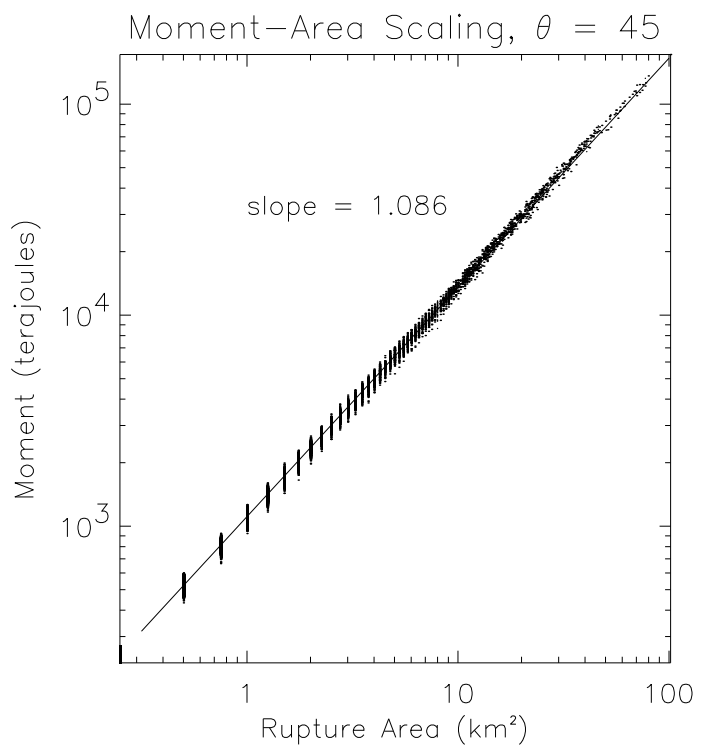


Figure 5.11: The seismic moment of a synthetic event is related to the area of the event by a scaling factor of approximately 1.1. This type of scaling holds for all geometries.

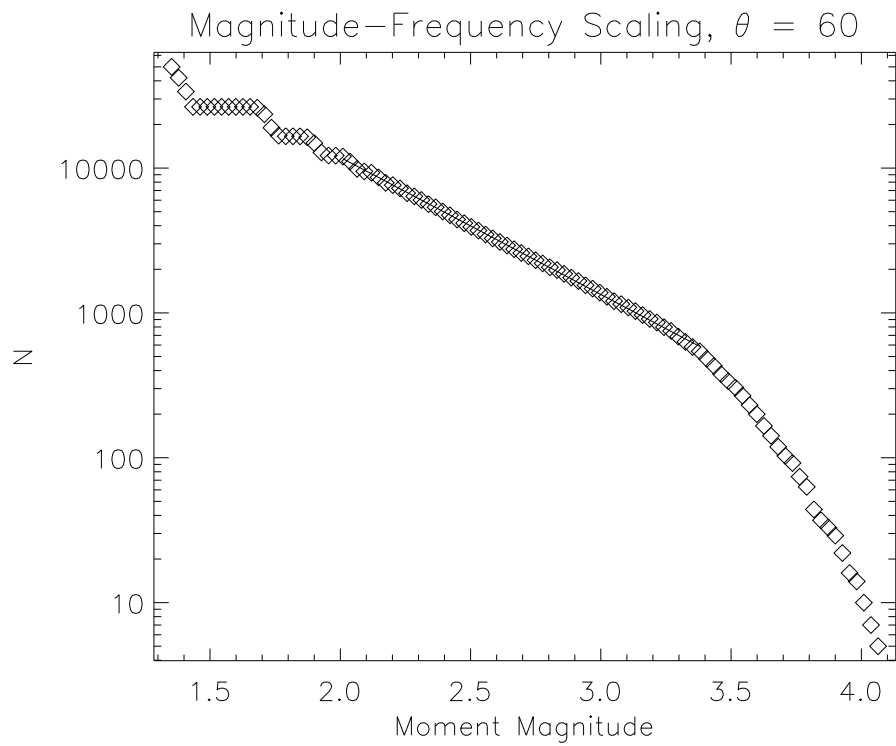


Figure 5.12: Gutenberg-Richter-type moment-frequency scaling: event size (moment) is distributed according to a power-law in frequency of occurrence. The scaling region between $M \approx 2$ and $M \approx 3.3$ has a slope very near -1, consistent with similar scaling relations in observed seismicity.

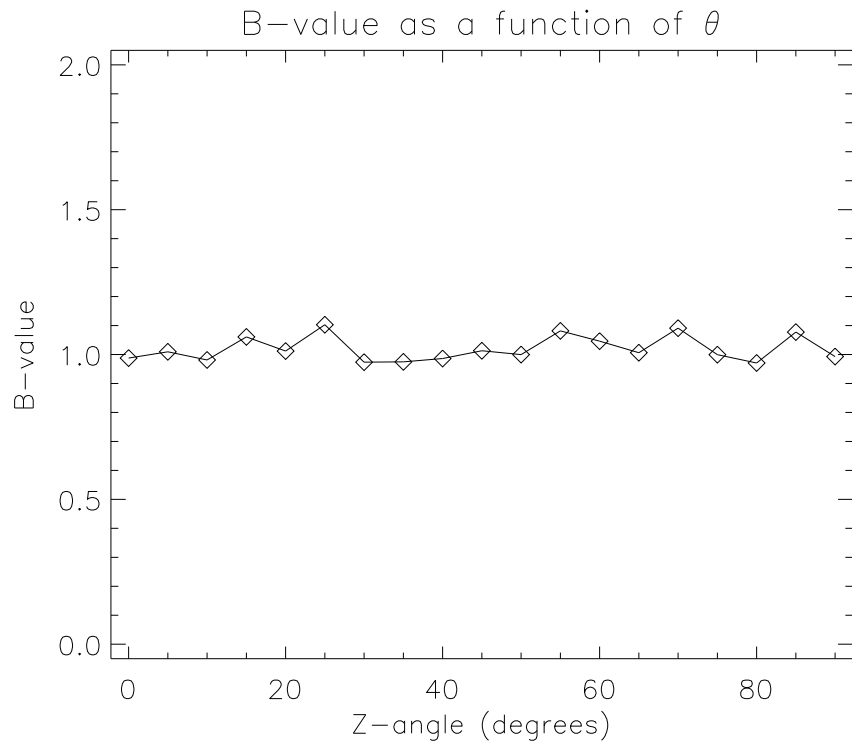


Figure 5.13: The b -values of the moment-frequency distributions are unaffected by geometry. These b -values were obtained by a linear least-squares fit to the scaling region of the cumulative distribution histogram for each geometric configuration from $\theta = 0$ to 90 degrees. The average b -value is 1.019, with a standard deviation of 0.002.

algorithm described in Chapter 3, I then identified clusters of correlated stress and calculated the location and average stress of each.

Figure 5.14 shows the average cluster stress as a function of time along the centerline of the fault, at a depth of 2.5 kilometers, for a z-shaped fault with a bend angle of 0. Amount of stress is denoted by color, with brighter colors denoting higher values of stress and dimmer colors lower values. Figures 5.15 through 5.17 show vertically-averaged cluster stress, for z-shaped faults with bend angles of 0, 30, and 90 degrees. Overplotted on each figure are dots showing the time and (horizontal) location of all patch failures in the dataset. These figures are typical of all the geometries that I simulated, and show how the size of an event is largely predetermined by the size of the pre-existing stress clusters.

If the size of an event is determined by the size of the correlated stress cluster in which it begins, the distribution of cluster sizes should have the same Gutenberg-Richter scaling characteristics as the distribution of event sizes. This correspondence is shown in figure 5.18, which is typical of all geometries. This figure shows power-law scaling in the distribution of cluster sizes for small clusters; large clusters appear not to scale, but this due primarily to incomplete statistics; the histograms of cluster size are calculated for a single state of stress. The persistence of large clusters can be seen as “tracks” along the lower margin of the figure, with occasional breaks occurring when smaller clusters coalesce into larger or large clusters break apart.

Since the effects of fault geometry on the distribution of cluster areas seem to be minimal, we can regard stress snapshots from different geometries as being taken from a larger ensemble. Using one stress state from each member of the ensemble allows us to calculate a more statistically complete histogram of cluster sizes. Figure 5.19 shows the result of this calculation. The range of sizes that exhibits Gutenberg-Richter size-frequency scaling is now larger, indicating that the high-end variability is indeed due to incomplete statistics.

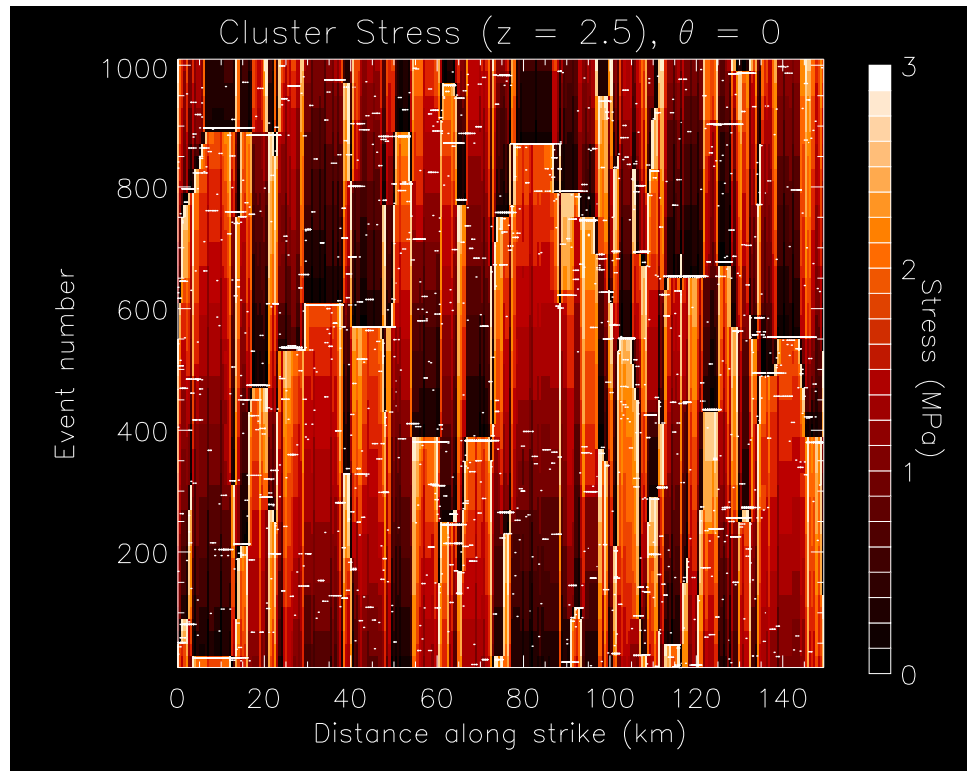


Figure 5.14: Average cluster stress as a function of time along the centerline of the fault. Color indicates average stress level of a correlated stress cluster; brighter color means higher stress. Overplotted dots at event locations show that an event's area is largely determined by the region of correlated stress.

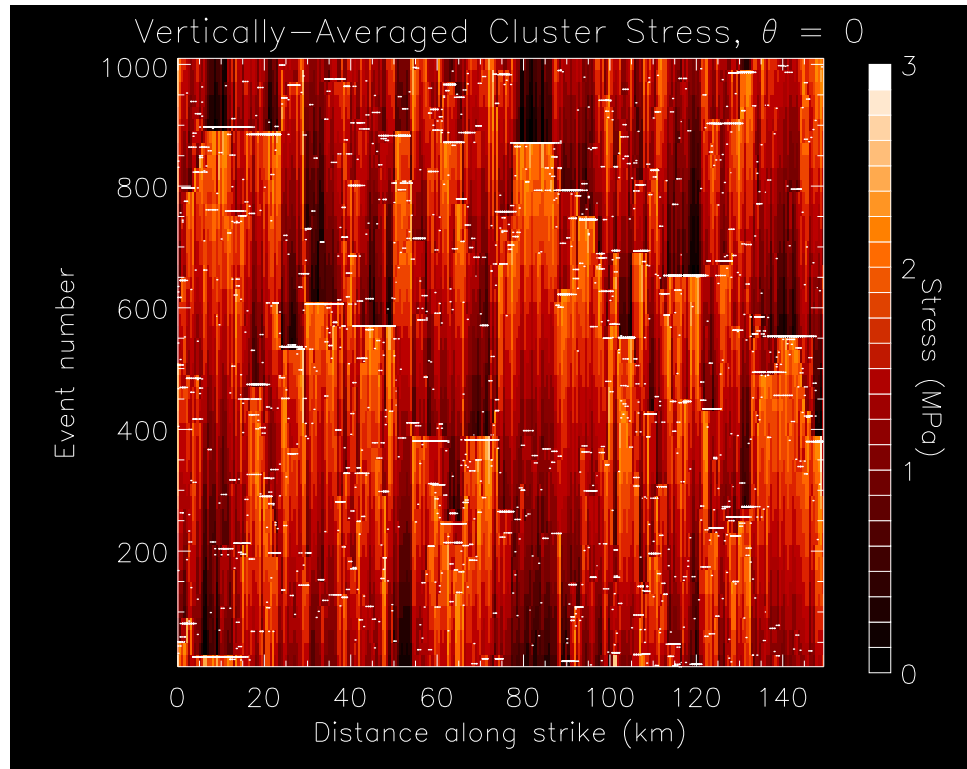


Figure 5.15: Cluster stress (averaged along dip) as a function of time for a z-shaped fault with bend angle 0. Color indicates stress level of the region of correlated stress; brighter color means higher stress. As in figure 5.14, the dots at event locations show that the area of an event is determined by the region of correlated stress.

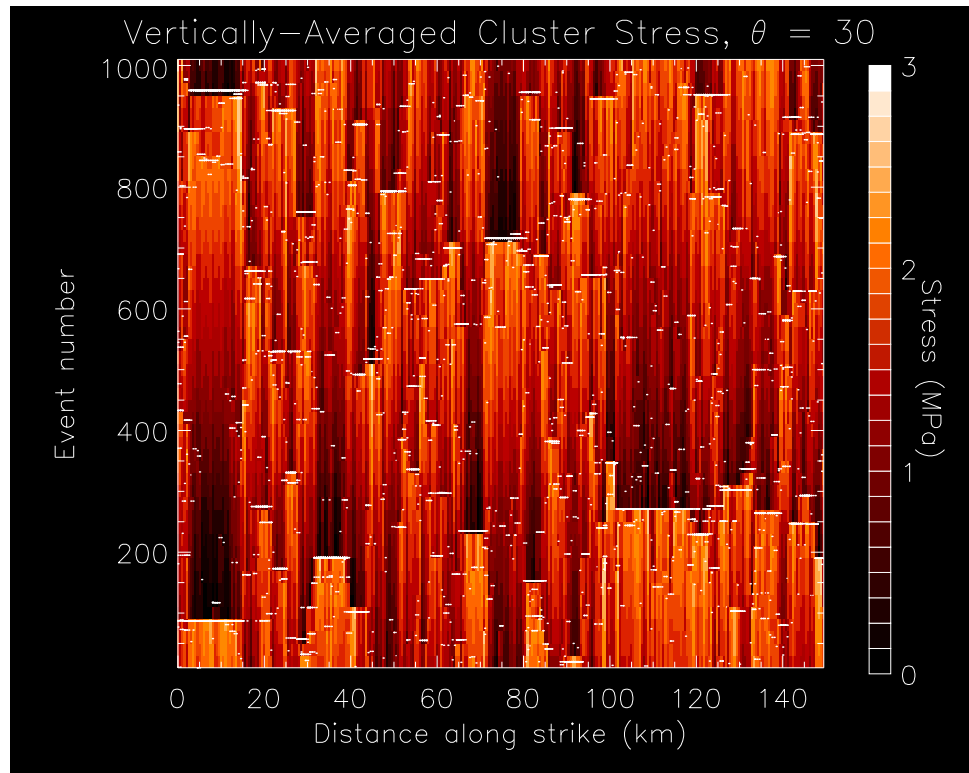


Figure 5.16: As figure 5.15, but for a z-shaped fault with $\theta = 30$. There are no obvious effects of geometry; while no stress clusters extend across the segment boundaries at 50 and 100 km along strike, there are also no clear-cut demarcations between segments.

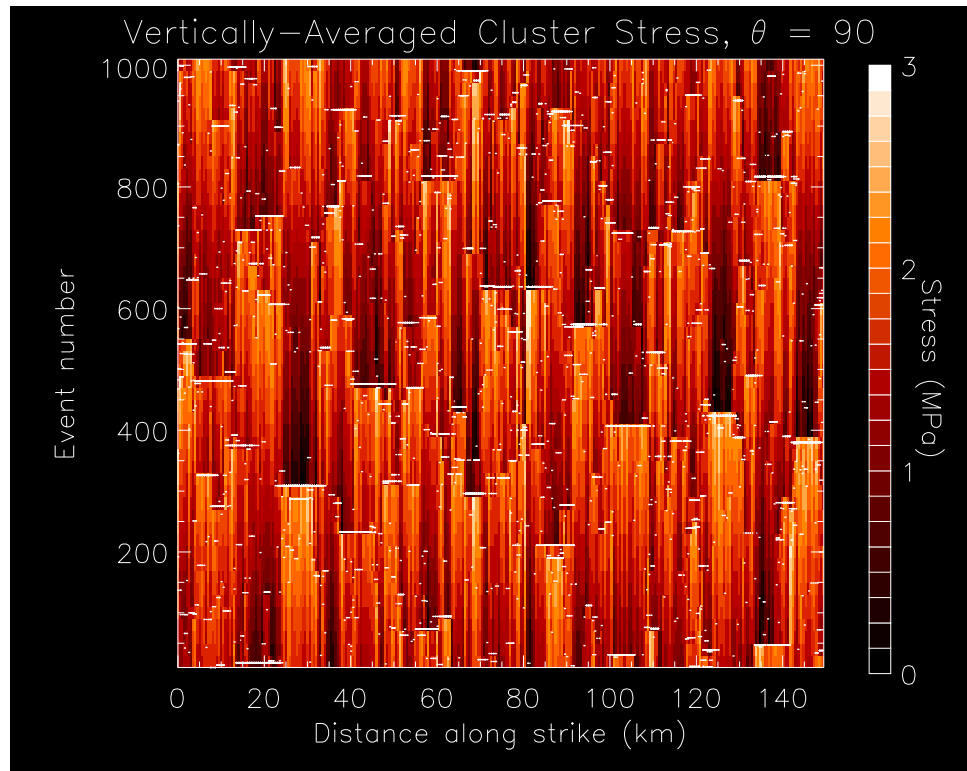


Figure 5.17: As figures 5.15 and 5.16, but for a z-shaped fault with $\theta = 90$. In this figure, the effects of geometry are clearly small; a large correlated stress cluster crosses the boundary between two fault segments at 100 km along strike, despite the right angle turn the fault makes there.

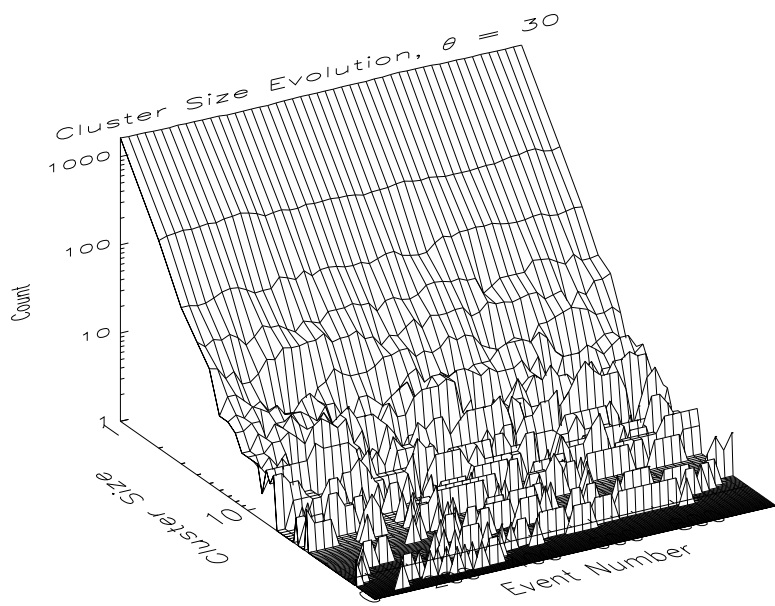


Figure 5.18: Histogram of correlated-stress cluster areas as a function of time for a z-shaped fault with a 30-degree bend angle. Height of the surface indicates number of clusters; cluster area is plotted on the x-axis and time along the y-axis. The distribution of cluster sizes shows power-law type scaling for clusters with small areas. The persistence of large stress clusters can be inferred from the linear structures at large values of x.

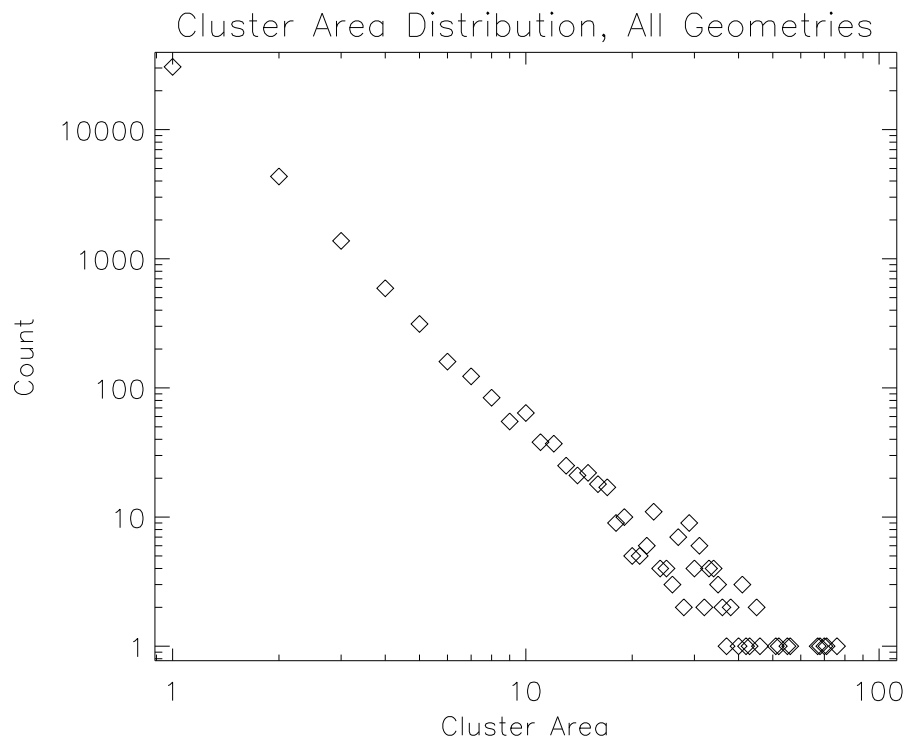


Figure 5.19: Histogram of correlated-stress cluster areas calculated with data from faults with all bend angles regarded as a single ensemble. Gutenberg-Richter type scaling of event size with frequency is clear. Variation from this scaling as area becomes large can be attributed to incomplete statistics.

5.4 Correlation Analysis

Applying an equal-time correlation operator to a seismic history will generate a correlation matrix that describes how different locations tend to be active at the same or different times. The correlation matrix can then be decomposed into eigenvectors that correspond to normal modes of activity of the system. This technique has been applied to observed seismicity in Southern California [161] to reveal inhibitory interactions between different faults, as well as to many other geophysical systems. I applied a similar analysis to my simulated data in an attempt to learn about the interactions between different segments of a single fault system.

5.4.1 Phase Correlation

The elements of the Fault-Patch model (and other models from the slider-block family) can be regarded as oscillators. Absent any interactions with other patches, the stress on a fault patch will increase over time until it reaches the failure threshold, then drop down to a residual value and begin again, generating a sawtooth function in time. In the case where friction is constant, the scalar shear stress is bounded on $[0, S]$, where S is the inherent strength (or cohesion, uniformly set at 3.0 MPa in these simulations) of the fault patch. It is reasonable, then, to map that value onto the interval $[0, 2\pi]$ and regard it as the phase of an oscillator. The correlation between two oscillators is $\cos(\phi_1 - \phi_2)$: if $\phi_1 = \phi_2$, they are exactly in phase and the correlation is 1, while if they are 180 degrees out of phase, the correlation will be -1.

I analyzed the same datasets that I performed stress cluster analysis on: sets of fifty “snapshots” of the stress state, each separated from the next by twenty events, one set for each bend angle from 0 to 90 degrees by 5-degree increments. For each dataset, I mapped the scalar shear stress onto a phase angle as described above, then averaged the phase angles over the vertical axis of the fault, creating fifty 300-element average-phase vectors. I then calculated phase-correlation matrices by taking the cosine of the difference of each pair of average phases. Thus, the phase correlation of the i th element and the j th element is the element of the matrix

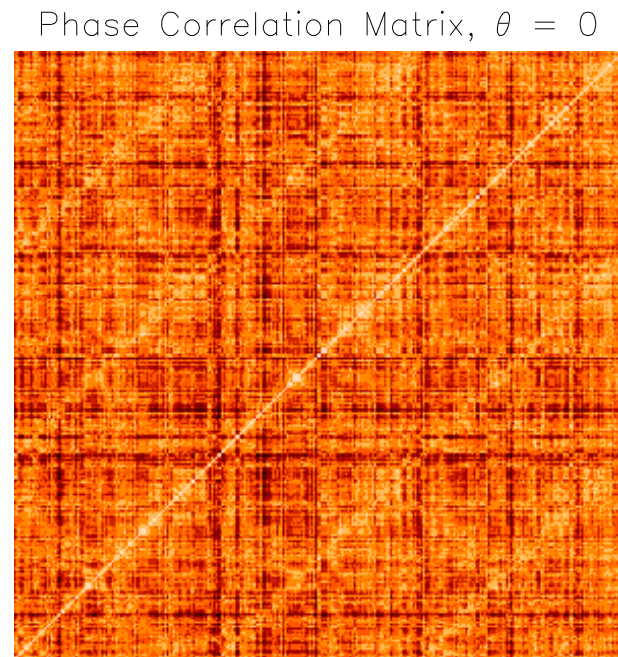


Figure 5.20: 300×300 element phase-correlation matrix for stress snapshots from a z-shaped fault with bend angle 0. Correlations range from -1 to 1; brighter colors represent higher correlation. Phase correlation is calculated as $\cos(\phi_i - \phi_j)$, where ϕ_i is the shear stress of the i th fault patch, mapped from $[0, \sigma_{fail}]$ to $[0, 2\pi]$.

Phase Correlation Matrix, $\theta = 30$

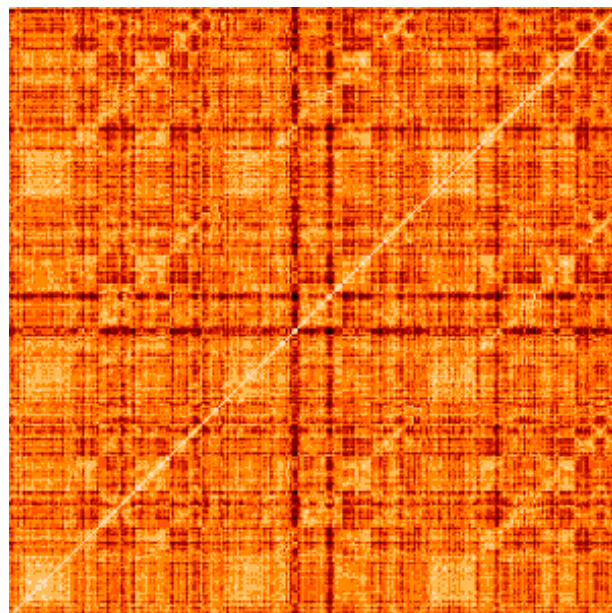


Figure 5.21: Phase correlation matrix for z-shaped fault with bend angle 30 degrees. Correlations range from -1 to 1, with brighter colors representing higher correlation. The structure of the matrix is related to the distribution of stress clusters in the model.

Phase Correlation Matrix, $\theta = 90$

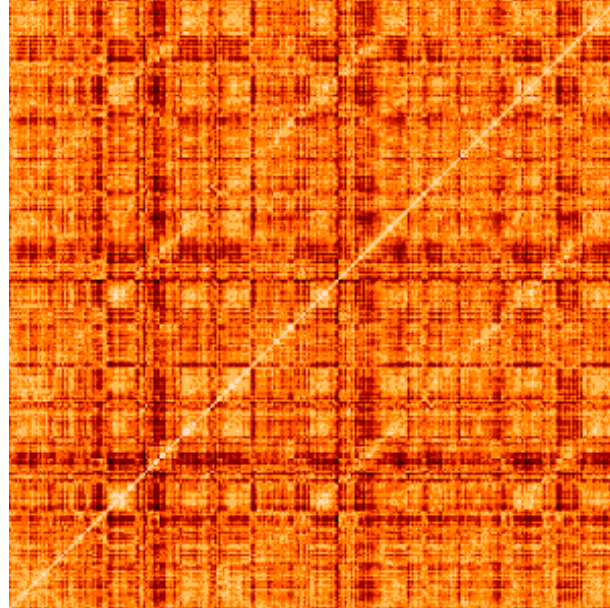


Figure 5.22: Phase correlation matrix for a z-shaped fault with bend angle 90. Correlations range from -1 to 1; brighter colors represent higher correlation. Comparison with the linear distribution of stress clusters in figure 5.23 shows that the structure of the phase correlation matrix is determined by the distribution and relative stress phases of the existing stress clusters. Most large clusters persist throughout the 1000-event period for which this correlation matrix was calculated.

Stress Snapshot, $\theta = 90$



Figure 5.23: Stress snapshot of a z-shaped fault with bend angle 90 degrees. Figure is to scale; the fault is 150 kilometers long and 5 kilometers wide. Each pixel represents a single fault patch. Stresses range from 0 MPa to 3 MPa (the uniform failure threshold); brighter colors represent a higher state of shear stress. This snapshot is taken at event number 700 according to the numbering used in figure 5.17.

$C_{ij} = \cos(\phi_i - \phi_j)$. I calculated the equal-time phase correlation for each of the fifty phase vectors, then averaged the fifty resulting phase correlation matrices to get an average phase correlation matrix.

The phase correlation matrices do not appear to show any effects of geometry on the stress state of the system; geometric effects should divide the matrix into thirds. Comparison of the correlation matrix in figure 5.22 with the stress snap shot in figure 5.23 and with the stress cluster evolution diagram in figure 5.17 reveals the reason why: the structure of the phase correlation matrix reveals the relative phases of the stress clusters in the model at a particular time. The stress cluster evolution figures show that the 1000-event period covered by the sequence of stress snapshots spans only a single seismic cycle for large stress clusters. A single iteration of the cycle of stress buildup and release is insufficient time for a large stress cluster to decorrelate and break apart into smaller clusters. Consequently, the stress state at the end of the dataset is not far removed from the stress state at the beginning of the dataset, and so the structure of the phase correlation matrix largely reflects that particular stress state. To observe the effects of geometry through this analysis would require averaging the phase correlations of a large ensemble of stress states far removed from one another. The limitations of data storage and computation time prohibit the simulation of such an ensemble at this time. Thus, I must conclude only that over short times, the phase correlation matrix will reflect the stress state of the system and little else.

5.4.2 Activity Correlation

I used an activity correlation matrix to study the effects of geometry on the evolution and distribution of events on the z-shaped fault. Following the procedure outlined in section 3.2, I constructed boolean equal-time correlation matrices from the activity data for several different fault configurations. The term “boolean” refers to the fact that I counted only a single failure for each location when calculating covariance; this choice highlight the shapes of the events. Non-boolean calculation do not produce significantly different results.

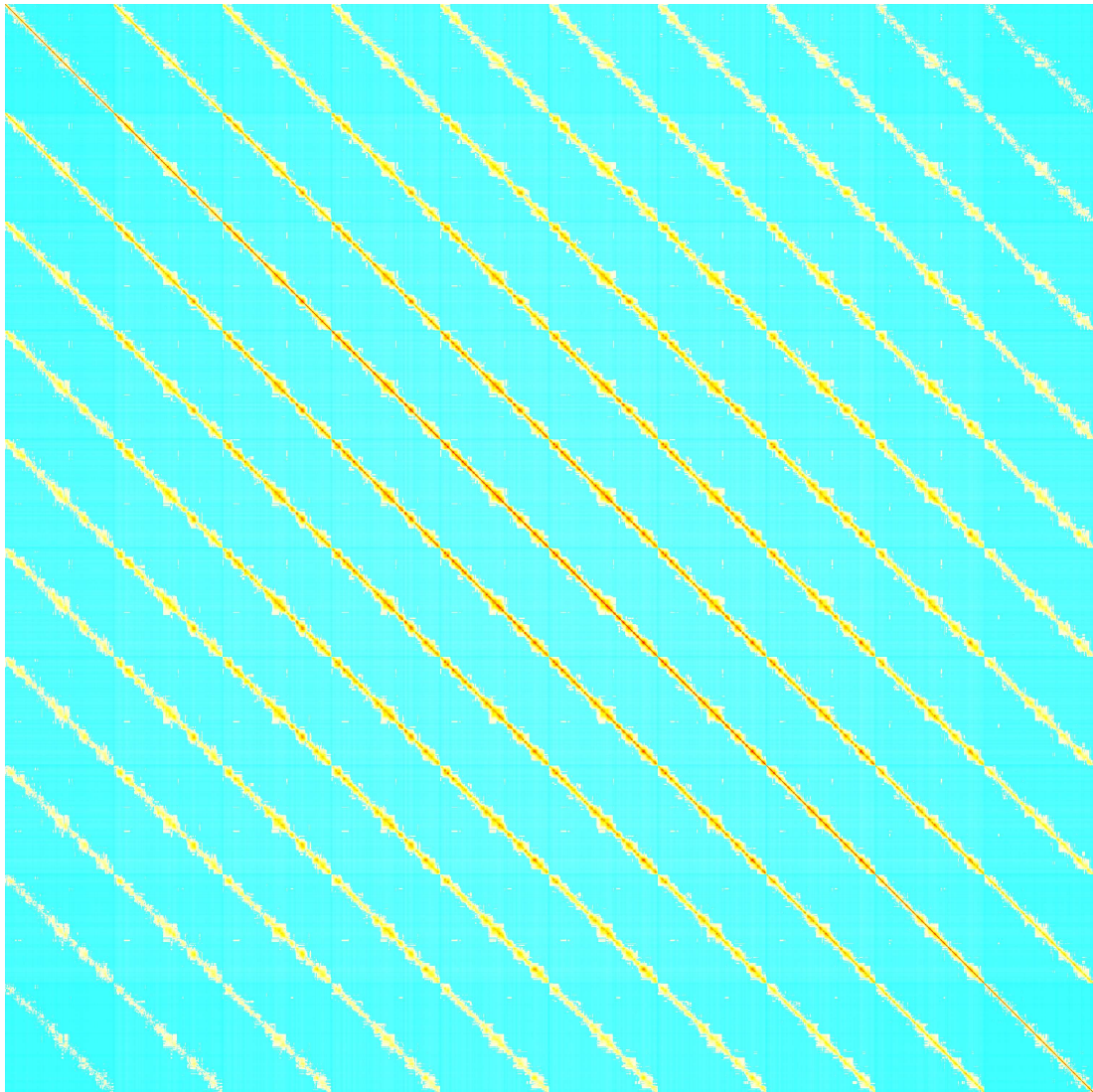


Figure 5.24: The 3000×3000 element boolean equal-time activity correlation matrix for a flat fault (bend angle 0). Positive values are shown as hot colors, increasing from yellow to red, negative values are cool colors, darker being more negative, and zero values are white. Positive correlations range from 0 to 1, and negative correlations from 0 to -0.01. Locations are indexed horizontally first, then vertically; the diagonal stripes reflect the influence of a patch on its vertical neighbors.

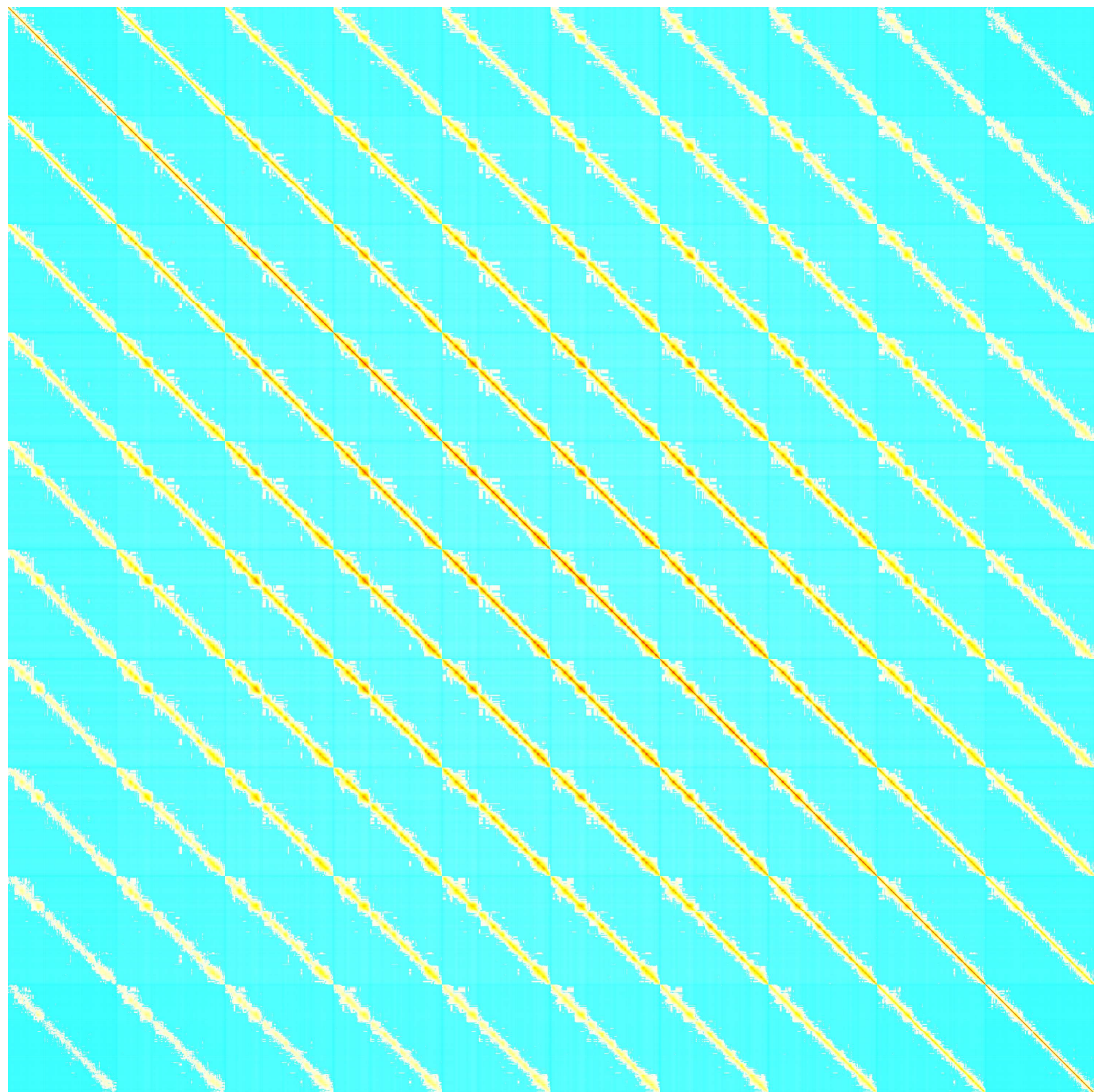


Figure 5.25: As figure 5.24, but for a z-shaped fault with bend angle 60.

The z-shaped fault has 3000 fault-patches; a complete correlation matrix has nine million elements and is computationally arduous to calculate and visualize. It would be beneficial if the size of the matrix could be somehow decreased. To this end, I considered the structure of the fault. The z-shaped fault is nearly linear, with a 30:1 aspect ratio. Moreover, all of the geometric variation occurs along the strike axis; we would expect on a physical basis that the activity on the fault will show little variation in the vertical dimension. That being the case, we could collapse the vertical dimension and consider only the horizontal position of a fault patch when calculating the activity correlation and decrease the size of the matrix by a factor of 100.

Figures 5.24 and 5.25 show the 3000^2 element activity correlation matrices for z-shaped faults with bend angles of 0 and 60 degrees. The fault patches are indexed first horizontally, then vertically; the ten* diagonal stripes in each matrix correspond to the correlations between elements that are vertically offset from one another by 0-9 lattice spacings. The banded nature of these matrices shows that the vertical variation in activity does not significantly affect the disposition of the events. There is also, despite the large difference in bend angle, little difference in the structure of the correlation matrices for the two cases. This suggests that omitting the vertical dimension from the correlation calculation will not significantly change the results.

Figures 5.26 through 5.29 show the collapsed boolean activity correlation matrices for z-shaped faults with bend angles of 0, 30, 60, and 90 degrees, respectively. Though some small effect of the segment boundaries can be seen, particularly in the 90-degree case, the effect of geometry on activity patterns is small. The most visually apparent effect is on the negative cross-correlations with edge elements, and the anti-correlations are displayed on an exaggerated scale. In general, the correlation matrix takes the form of a peak along the identity diagonal that drops off smoothly and for the most part uniformly with distance. The peak width is affected to only a small degree by the segment boundaries, and only at very short distance.

It is important to note that these results are obtained in the absence of any normal force effects on friction; certainly if normal stresses were not neglected, the variation with geometry

* There are only ten diagonal stripes because the matrix is symmetric.

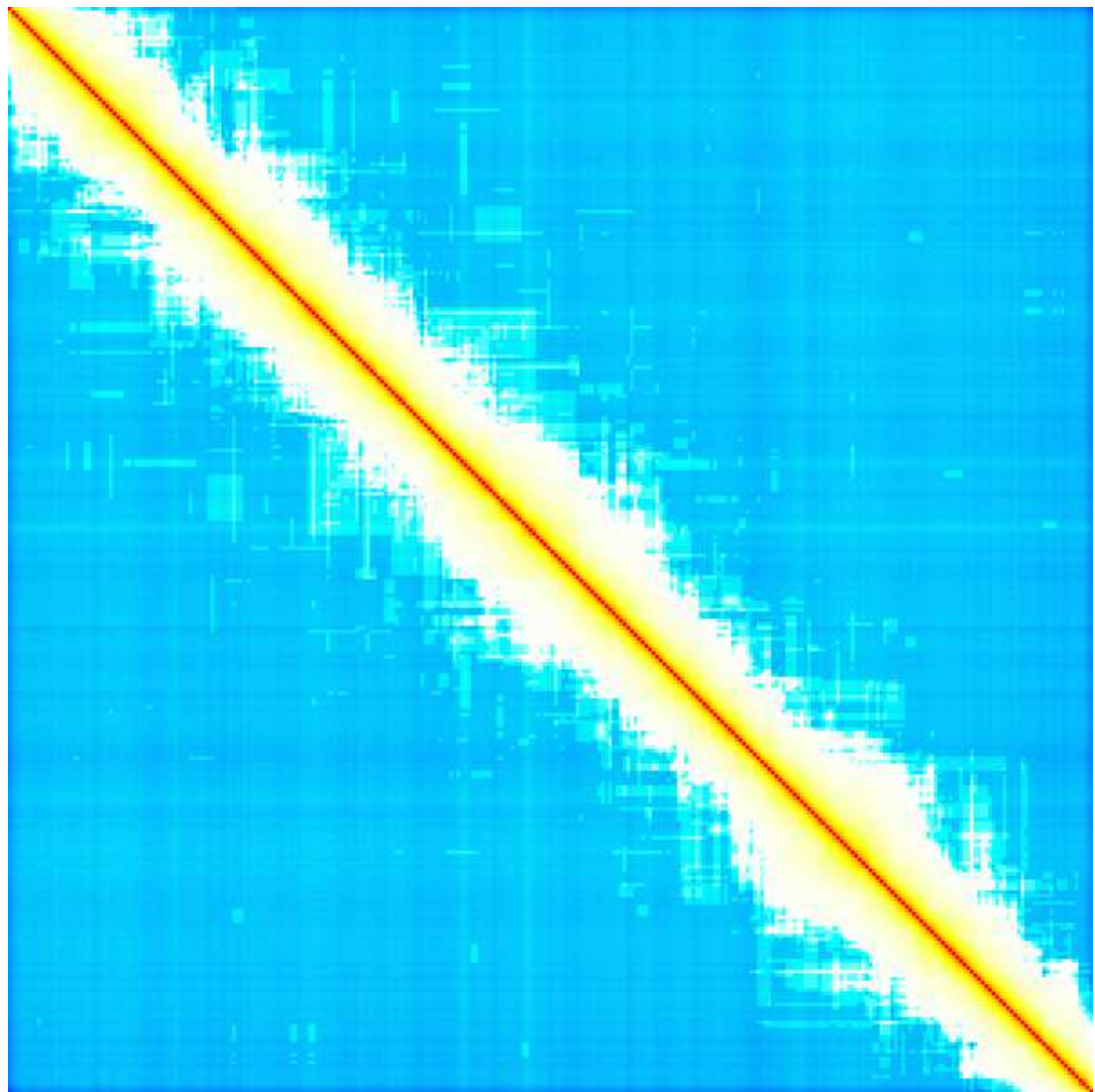


Figure 5.26: Equal-time boolean activity correlation matrix for a flat fault with vertical dimension collapsed. Positive correlations range from 0 (white) to 1 (red); negative values range from 0 to -0.02 (dark blue).

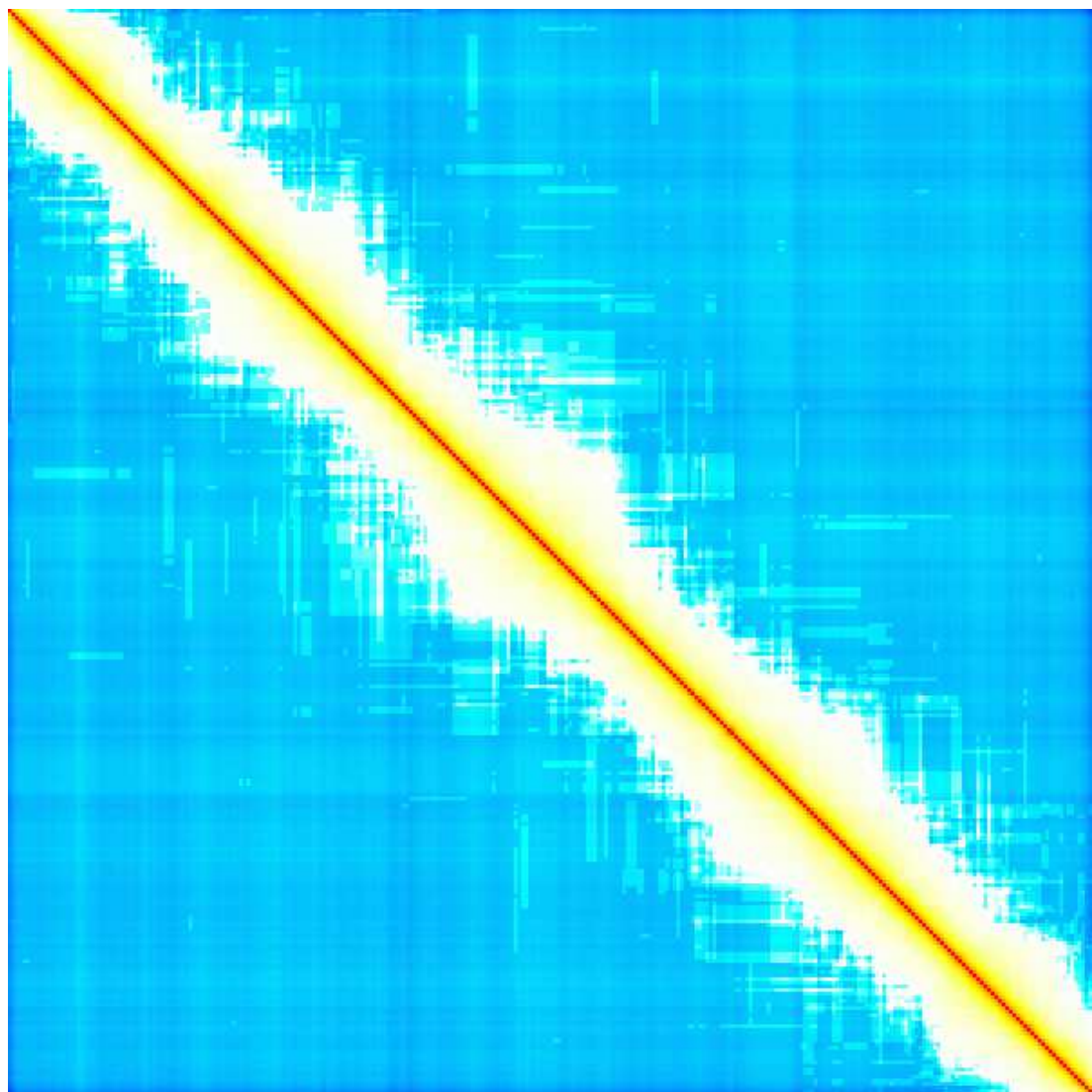


Figure 5.27: As figure 5.26, but for a z-shaped fault with a bend angle of 30 degrees.

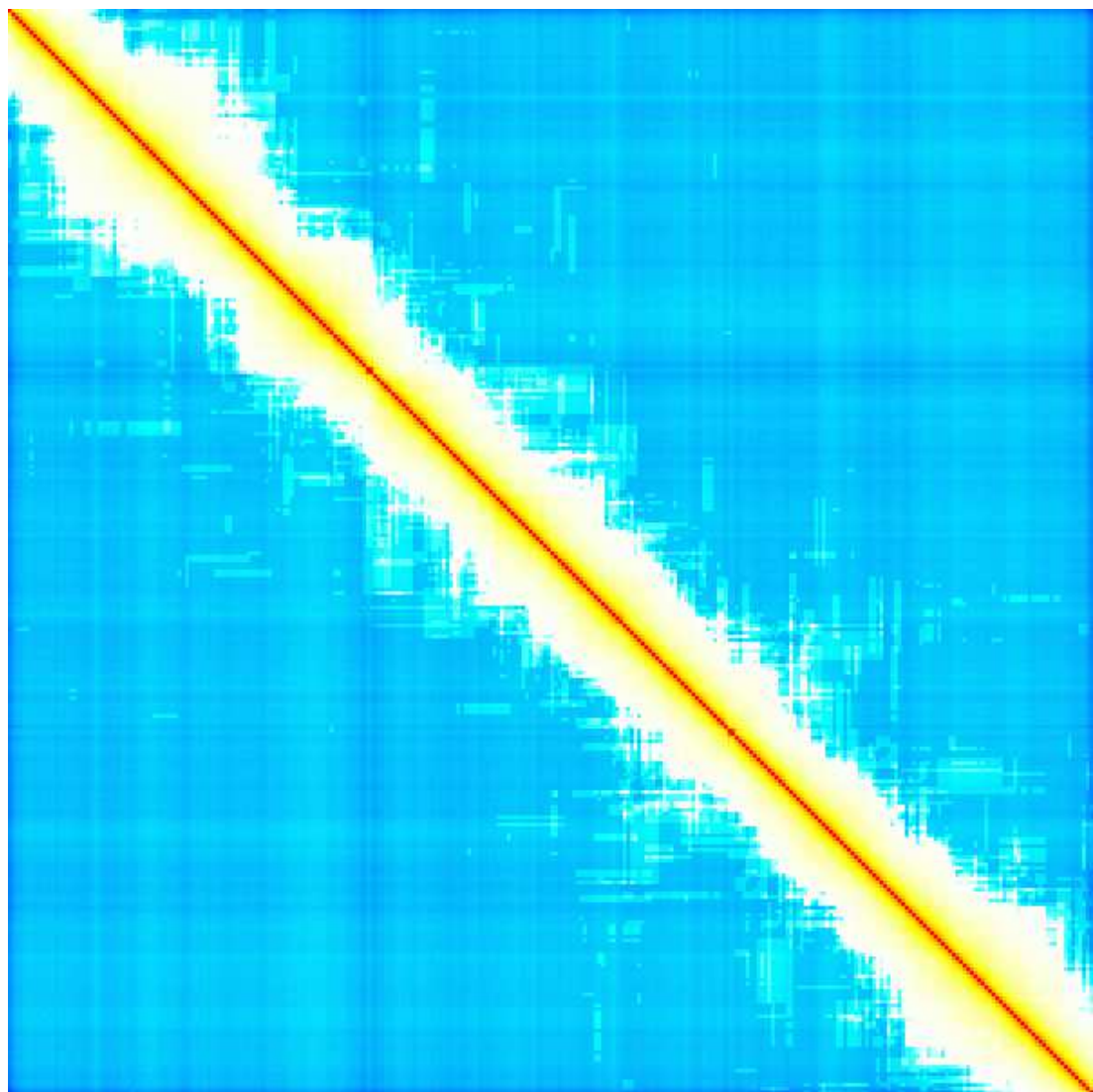


Figure 5.28: As figure 5.26, but for a z-shaped fault with a bend angle of 60 degrees. Some evidence of the bends dividing the fault into thirds can be seen in the correlations, but it is very small.

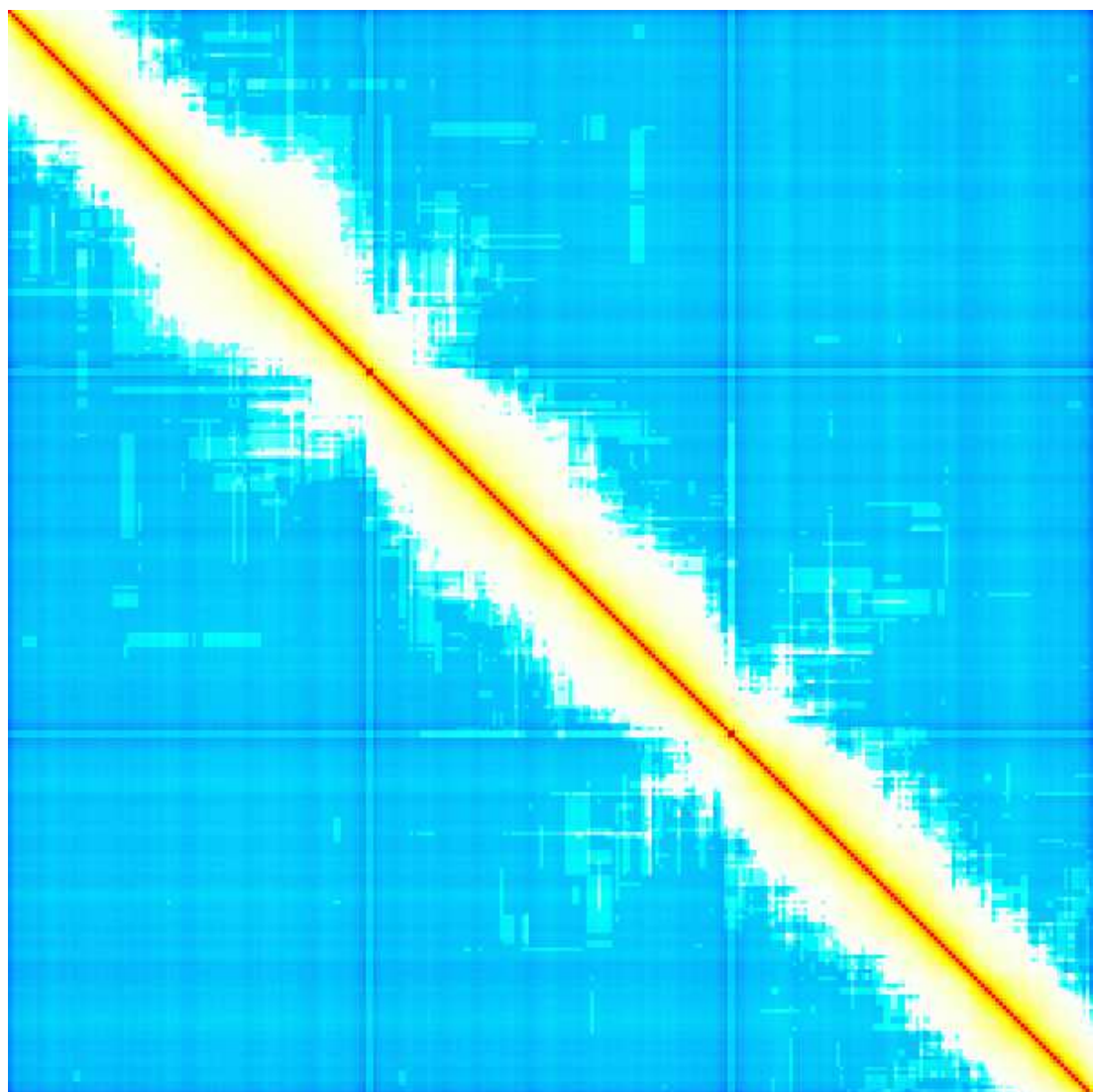


Figure 5.29: As figure 5.26, but for a z-shaped fault with a 90-degree bend angle. The segmentation of the fault into thirds is now quite plain in the negative values, but even at this extreme angle the effect on the correlations near the boundaries remains small.

would be much more prominent, as some of the stress transfers would either clamp or unclamp other portions of the fault, greatly inhibiting or exciting failure. Nevertheless, these results show that the effects of geometry on shear stress are very small for all but the most extreme geometric configurations.

To compare these results with a known quantity, I simulated fifty thousand events using a different model: a three-part leaky neural-net. An integrate-and-fire neural net is mathematically equivalent to a slider-block cellular automaton; the addition of a charge leakage function makes it equivalent to a slider-block with stable pre-slip as the elements approach failure. The neural net configuration I used consisted of three 10x100 square lattices which were completely disconnected from one another. Thus, the data produced by this model corresponds to that which would be generated by a three-part fault system where no fault segment influenced any other fault segment.

Figure 5.30 shows the activity correlation matrix generated by this simulation; the features of interest are the two “bottlenecks” that divide the diagonal into three pieces. These correspond to the indexing divisions between cells in the three disconnected parts of the model, and show how a discontinuity in communication between adjacent elements would appear in the correlation matrix.

A very small bottleneck can be seen in the $\theta = 90$ correlation matrix, and arguably in the $\theta = 60$ degree case as well, but both features are much less pronounced than in the above-mentioned theoretical case. Overall, the correlation peak maintains a consistent width for all the z-shaped faults, and the bend angles appear to form very little barrier to communication between segments. The eigenmodes of the correlation matrices bear this observation out.

Figure 5.31 shows the first thirty EOFs of the activity on a z-shaped fault with bend angle 60 degrees. These eigenvectors are typical of the activity correlation matrices generated by all the geometries I simulated, sharing the same slightly irregular sinusoidal form and the same lack of segmentation. I verified this visual similarity by calculating the average dot product of corresponding eigenvectors from different matrices. The average inner product of EOFs from

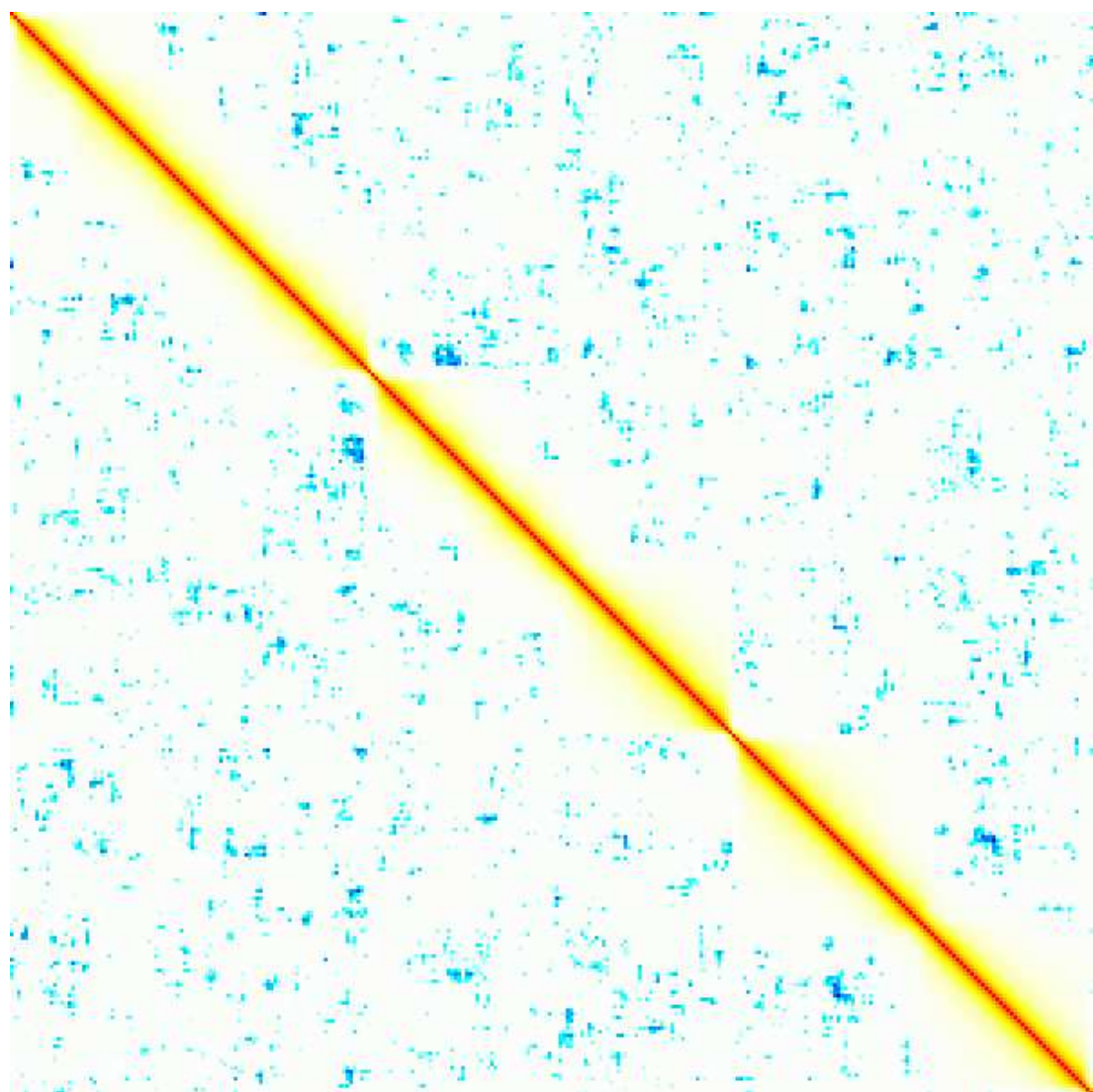


Figure 5.30: Equal-time boolean activity correlation matrix for a neural net with three non-interacting segments. This correlation matrix shows characteristic “bottlenecks” in the correlation peak near the segment boundaries. Anticorrelations are caused by random statistical fluctuations.

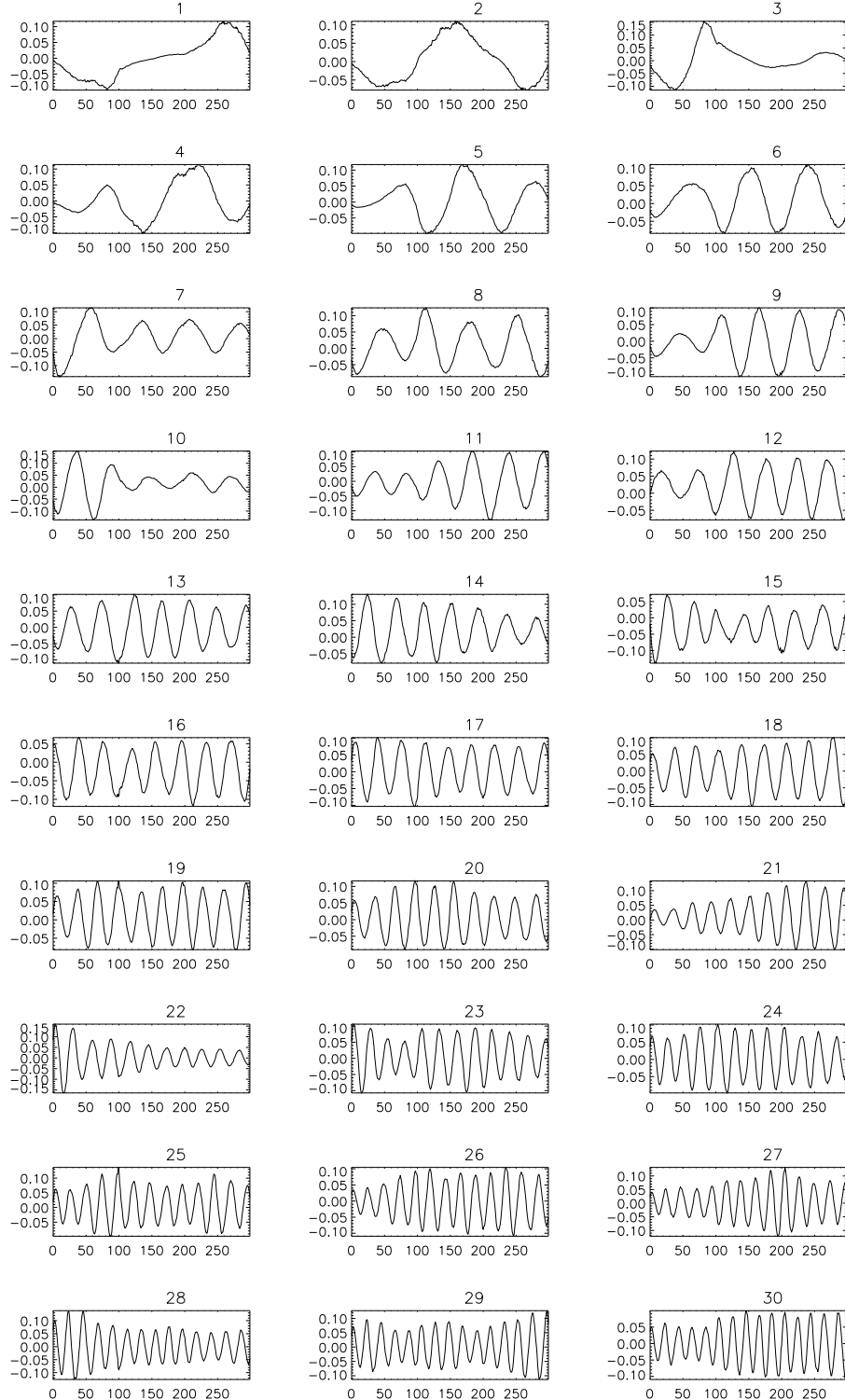


Figure 5.31: The first thirty EOFs, sorted by the fraction of the signal each explains, of the activity on a z-shaped fault with bend angle 60. The fourier-like form of this orthogonal basis is typical of the EOFs for all z-shaped geometries.

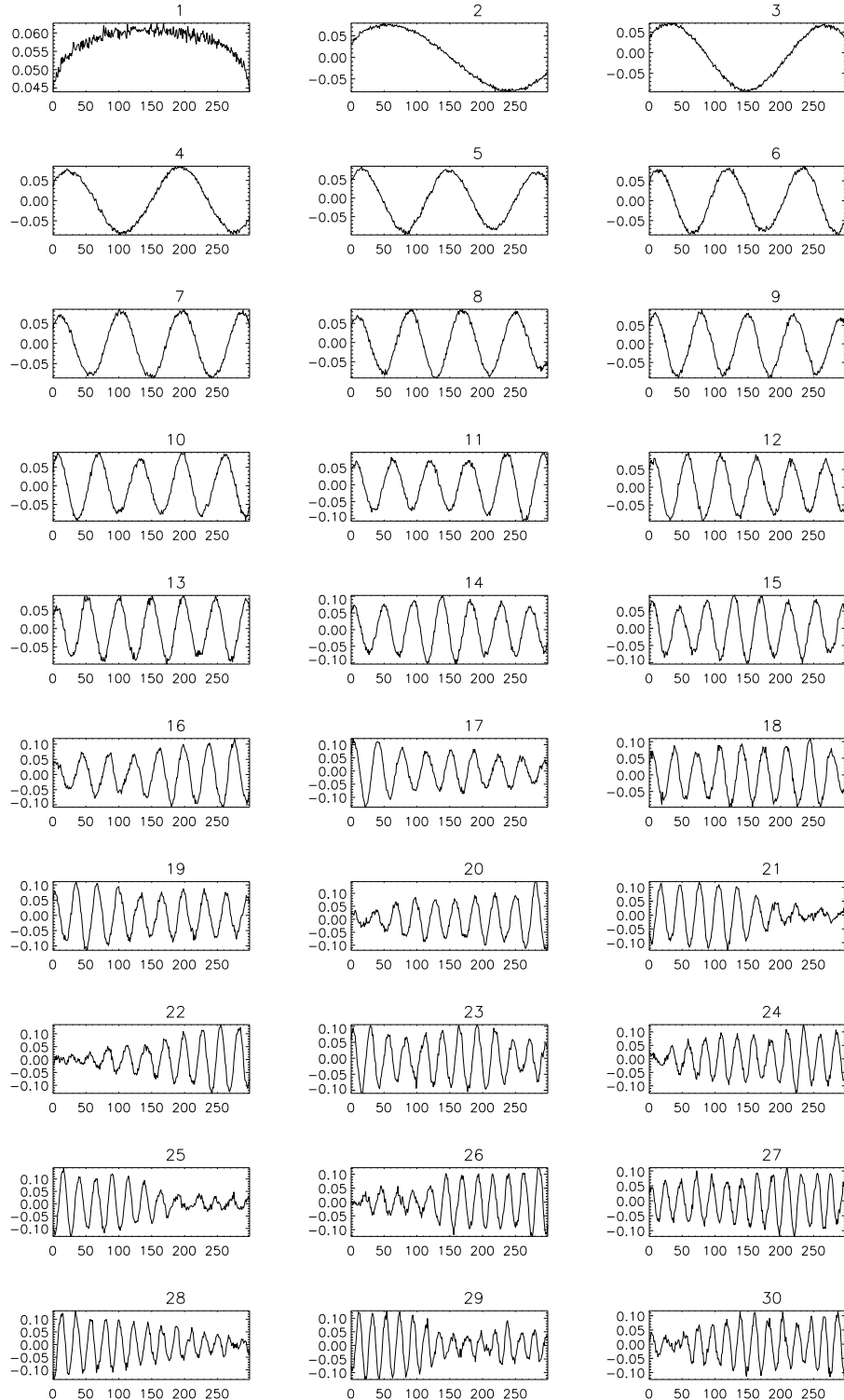


Figure 5.32: The first thirty EOFs of a synthetic correlation matrix with a $1/x$ correlation drop-off away from the identity. The $1/x$ structure creates sinusoidal eigenvectors; the irregular envelopes are generated by the addition of noise.

two sets of random data is around 0.003, as is the average EOF dot product between a random correlation matrix and an activity correlation matrix. The average inner product between the activity EOFs for two different fault geometries, on the other hand, is 0.155, a factor of fifty larger. This shows that the basis functions derived from the activity correlation matrices are similar to one another, regardless of the originating geometry.

A brief study of the form of the correlation matrix reveals the origin of these eigenmodes. Along the diagonal, the correlation matrix by definition has a value of unity. If the rows of the correlation matrix are plotted centered on the diagonal index, average curve is seen to follow a curve that approximates $1/(x + 1)$; in other words, the correlation between two fault patches is roughly equal to the distance between them in lattice units.

I constructed a synthetic correlation matrix according to the equation

$$C_{ij} = \frac{1}{(1 + |i - j|)} + \eta, \quad (5.1)$$

where η is a uniform random variate between 0 and 0.05. The eigenmodes of this matrix are shown in figure 5.32; a matrix with a $1/(x + 1)$ fall-off away from the diagonal has sinusoidal eigenmodes when decomposed using the QL algorithm, and irregular envelopes of the sinusoids are caused by random noise, which in the simulation data is caused by finite statistics.

The fact that this correlation matrix, the correlation matrices of activity on z-shaped faults, and the correlation matrix calculated from the much simpler neural-net model data all have the same form argues that realistic stress transfer calculations are not necessary to generate behavior that is consistent with realistic fault dynamics; a mean-field approximation with distance dependence is sufficient.

That being the case, the question arises as to what aspect of geometry acts as a constraint or influence on real fault system dynamics, where events are often strongly shaped by the fault system can occur. The answer is in how geometry interacts with loading.

The Fault-Patch model can be driven using any of several different loading schemes; the simulations exploring the range bend angles all use a uniform-loading scheme, where each fault

patch is given the same average slip rate and loading stress rates are back-fitted to match. This scheme allows the model to run without numeric instability even as the bend angle approaches the physically unrealistic 90 degrees. However, the Fault-Patch model can also be driven using a uniform far-field slip rate or a global strain rate. In either case, a change in the orientation of a fault segment would cause that segment to be stressed at a different rate.

For example, if the segments of a z-shaped fault are constrained to have the same net northward slip rate, the middle segment will slip faster in the strike direction than the two end segments by a factor equal to the secant of the bend angle. As the bend angle approaches 90 degrees, the middle segment's slip rate must approach infinity to produce a constant northward slip rate. Figure 5.33 shows the correlation matrix for a z-shaped fault with a 45-degree bend angle and a central segment with a higher slip rate than the end segments. The effects of differential loading clearly have an impact, though it is unclear from this example whether the loading boundaries act as segmentation boundaries as well.

In order to separate the direct geometric effects from the effects of changes in loading rate, I constructed a system where the geometric boundaries did not match the loading rate boundaries. I simulated events on a z-shaped fault with changes in the loading rate occurring not at the 100 and 200 kilometer positions of the bend angles, but at the 50, 150, and 250 kilometer positions, in the middle of each fault segment. The portions of the fault from 0 to 50 kilometers and from 150 to 250 kilometers were assigned slip rates of 1 mm/year, and the portions of the fault from 50 to 150 kilometers and from 250 to 300 kilometers were assigned slip rates of 5 mm/year. The correlation matrix calculated from the resulting data is shown in figure 5.35.

In this figure, the difference between the direct geometric effects and the indirect geometric effects of loading differentials can be clearly seen. The bend angle of 45 degrees produces no apparent changes in the activity correlation, while the loading differential produces bottlenecks at all loading boundaries. The implication is that the direct effect of geometry on the dynamics of a fault system are not as important as the indirect effects of geometry in the form of different

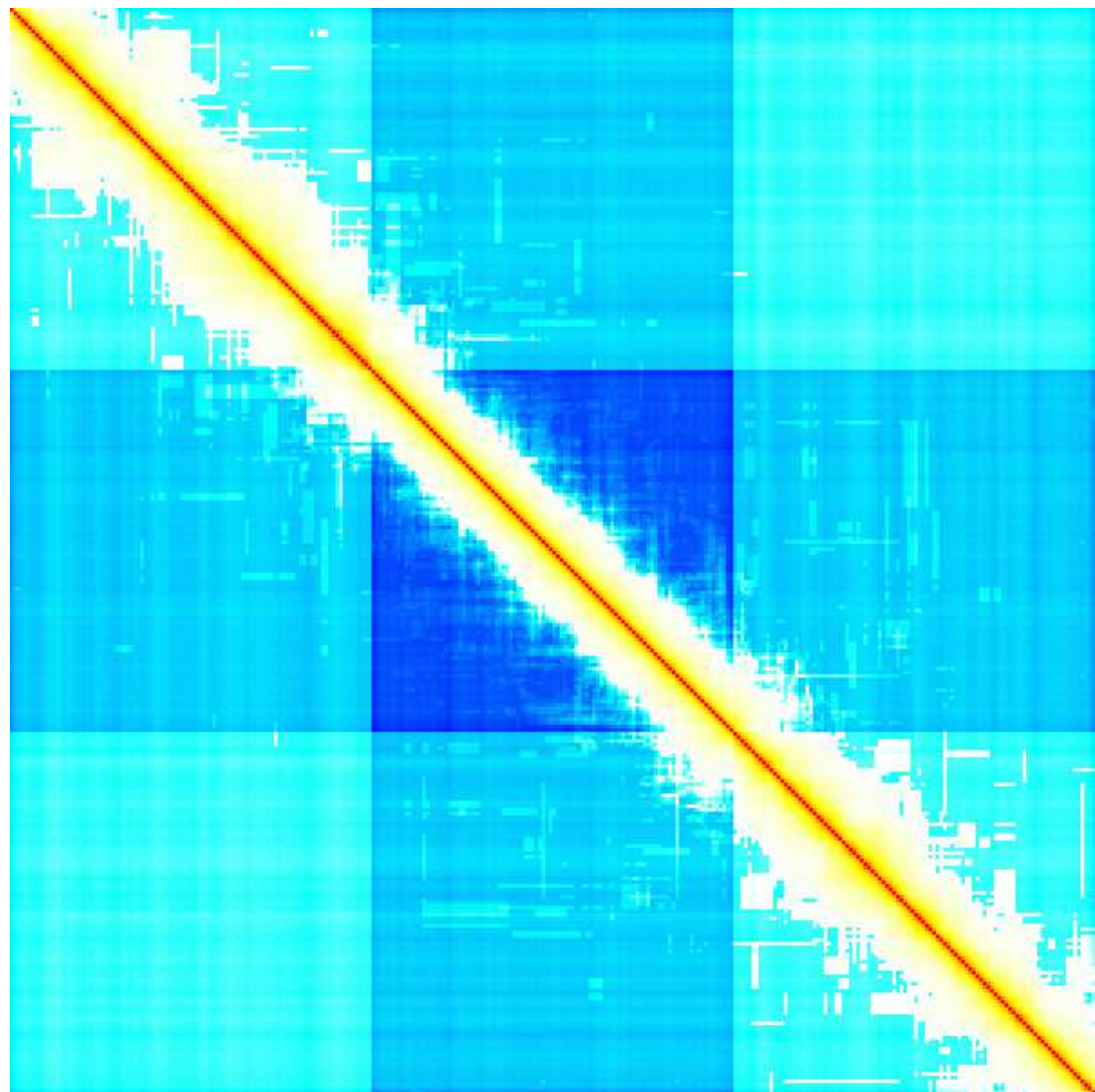


Figure 5.33: Equal-time collapsed boolean activity correlation matrix for a z-shaped fault with bend angle 45 degrees and a central segment that slips proportionately faster than the end segments.

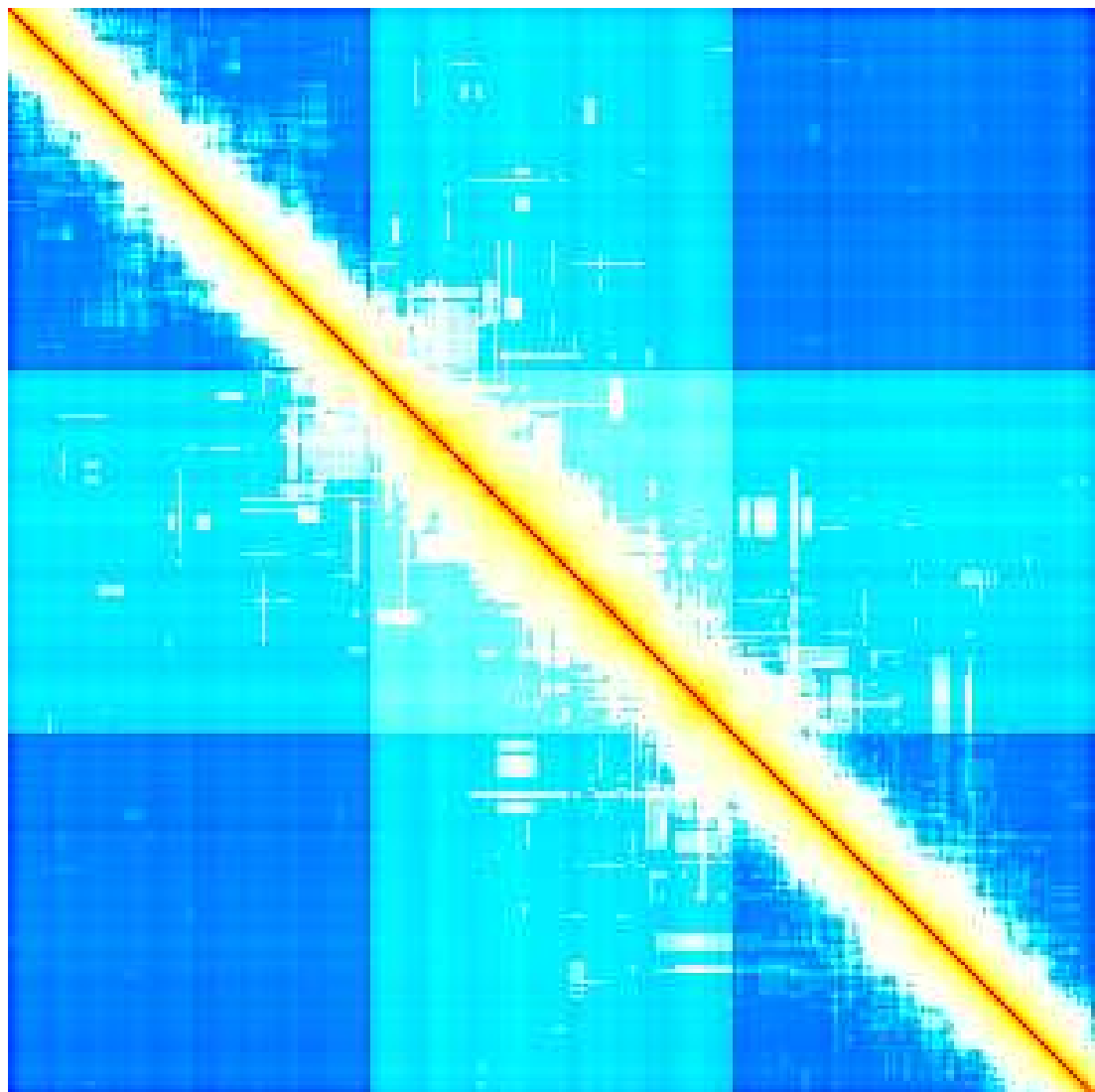


Figure 5.34: As figure 5.33, but with the central segment proportionally slower than the end segments. This geometry approximates that of the San Andreas fault and its orientation with respect to the local tectonic environment.

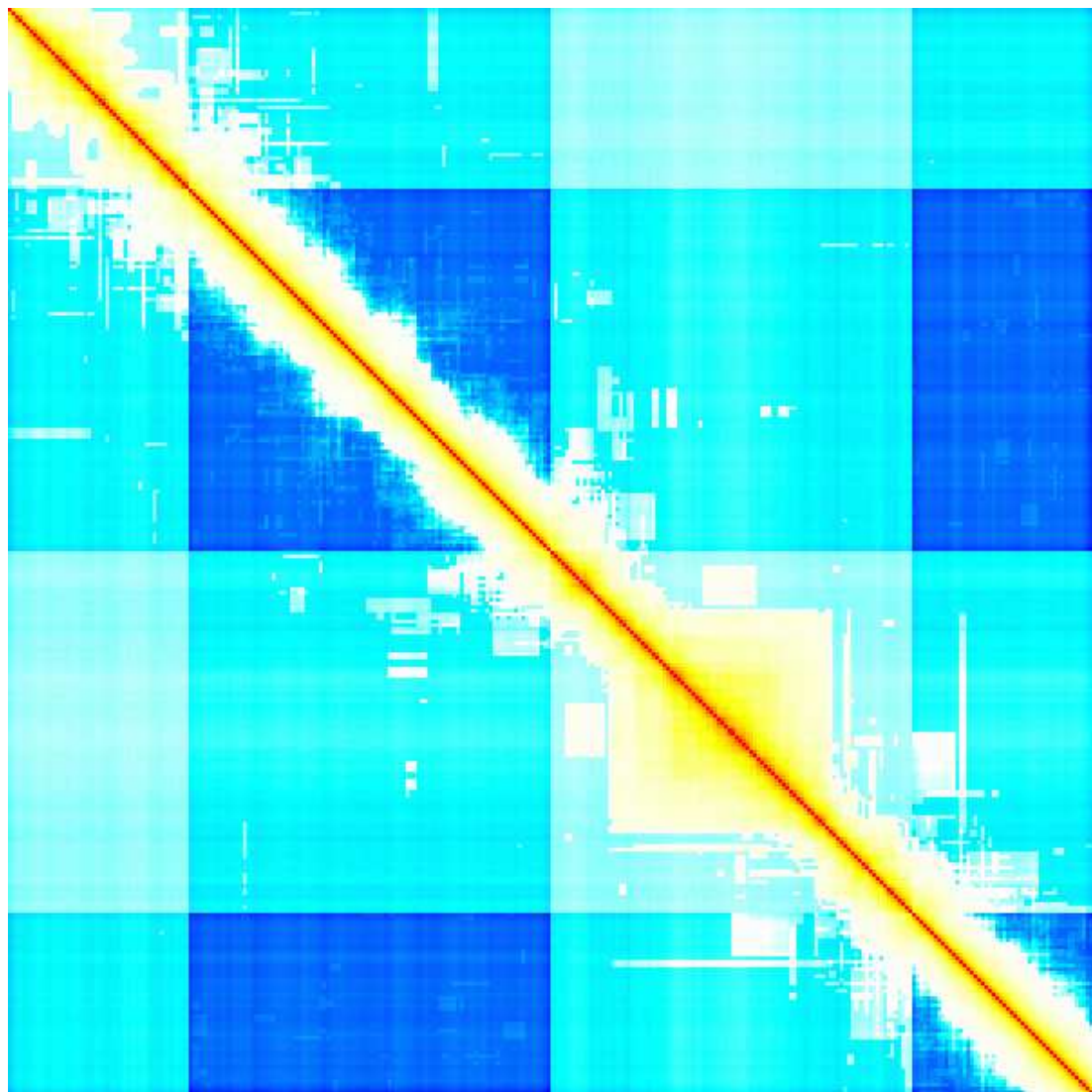


Figure 5.35: Equal-time collapsed boolean activity correlation matrix for a z-shaped fault with bend angle 45 degrees and differential loading. The effects of different loading rates are clearly much more important than the effects of geometry; loading from $x = 0$ to $x = 50$ and from $x = 150$ to $x = 250$ km is 20% that of the other regions, creating bottlenecks in the correlation peak at the point of transition.

loading rates on faults with different orientations relative to the driving tectonic stress regime.

5.5 PDPC Analysis

Other research [161, 131, 158] has shown that the PDPC methodology can be successfully used to find signals precursory to large events in real seismic data. I decided to apply the method to synthetic data in order to explore the relationship between the precursory signals detected by the PDPC index and the regions of correlated stress that determine the eventual size of an event in the Fault-Patch model. What I found was that PDPC analysis is largely ineffective on model data due to a lack of sufficient background activity in the model.

I used the same event catalogs for PDPC analysis as I did for analysis of stress clusters. Each catalog consists of 1000 post-transient events simulated on a z-shaped fault, with bend angles ranging from 0 to 90 degrees in five-degree increments. The activity showed little vertical variation, so I chose to decrease the number of locations from 3000 to 300 by collapsing the z-dimension of the fault and using only the linear position along the faultline as a location in the calculations. This is consistent with the way in which the PDPC index is calculated for real data, where only latitude and longitude, not depth, are used to determine the location bin an earthquake falls into. Because location is now a one-dimensional variable, it becomes possible to plot the evolution of the PDPC index through time.

Rather than calculating the PDPC index for a single (t_1, t_2) interval as we have typically done for Southern California, because I wished to study its evolution through time I chose to calculate the PDPC index using a sliding window of fixed length. Thus, with a 20-event window, I calculated the PDPC index for the interval (3000,3020), then for the interval (3020,3040), and so on. A typical result of this calculation, for a window length of 20 events and a bend angle of 0 degrees, is shown in figure 5.36. This result is typical, and does not change qualitatively with either geometry or window size.

It is clear that in this instance, the PDPC index is completely ineffective in detecting any sort of precursory signal before large events such as the ones at 60 kilometers location near

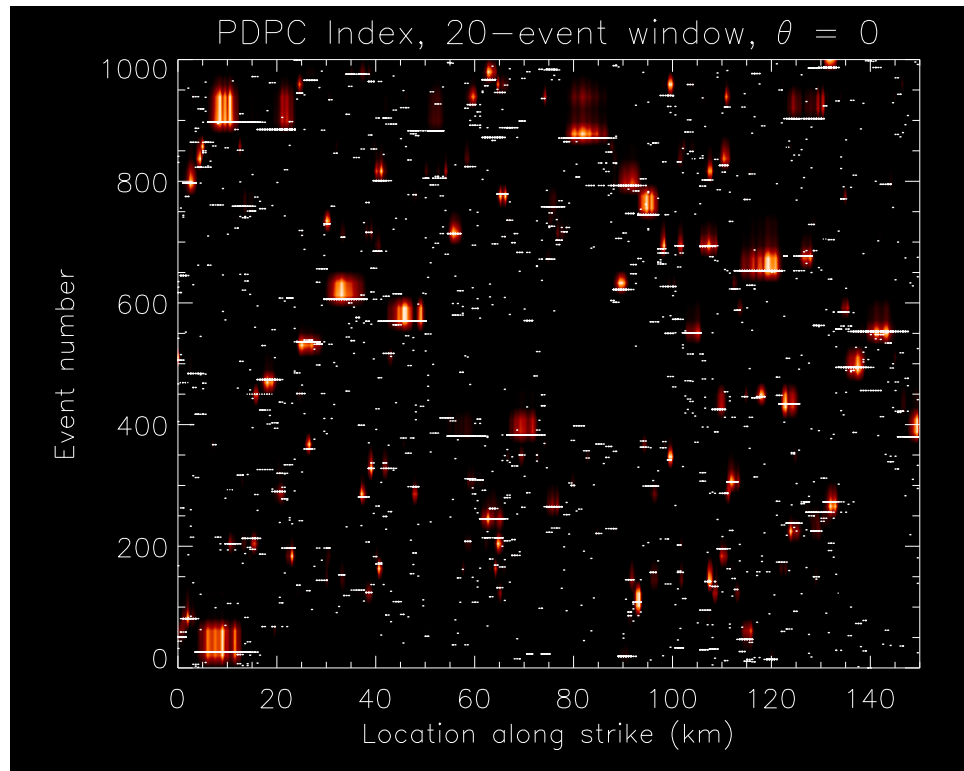


Figure 5.36: Color contours of high PDPC index are shown here on a space-time diagram; brighter colors indicate a higher PDPC index. Synthetic events are indicated by overplotted dots, the location of the event (distance along the faultline) plotted along the x-axis and time plotted along the y-axis. The PDPC index was calculated with a moving 20-event window for the (t_1, t_2) interval. Although the vertical (along-dip) dimension of the fault was collapsed, this form of the PDPC calculation shows no indication of detecting precursory signals; none of the zones of large PDPC index occurs before the interval that includes the associated large event.

event 400. Some reflection on the nature of the PDPC calculation reveals the reason why: the PDPC index is a measure of activity fluctuation away from a background level. If each patch is regarded as a single location, then by the construction of the model there is no background activity; every patch is stable until it fails, and it is meaningless to attempt to find fluctuations in the background seismicity rate. Consequently, in applying the PDPC algorithm to synthetic data, it is absolutely essential that some rebinning of the data take place. Therefore, I repeated the analysis after rebinning the data into 10 by 10 blocks, giving 30 adjacent location bins total. The results of this analysis are shown in figure 5.37.

The results of this analysis are more promising; regions of increased PDPC index are not limited to the intervals including a large event, as they were when the data was not binned in large blocks, but the results are still far from conclusive. Some large events (like the one at position 90 kilometers, time 212) are preceded by obvious zones of increased PDPC index, but others (such as the one near position 140 kilometers, time 210.7) are not, and not all regions of increased PDPC index are associated with subsequent large events. As yet, no good statistical test for the predictive accuracy of the PDPC index has been developed even for real data sets, so it is cannot be said conclusively that the PDPC index shows no correlation with the synthetic data, but the results clearly differ vastly from the degree of success shown in analysis of real data.

The reason for this difference most likely lies in the granularity of the data. In the real world, earthquake ruptures vary vastly in scale; the majority of the data in the Southern California catalogs are earthquakes with magnitude between $M_0 = 3$ and $M_0 = 4$. The fluctuations in the occurrence rate of these events as detected by the PDPC index gives a forecast signal for very large events such as the Landers and Northridge earthquakes, with magnitudes near $M_0 = 7$, a magnitude difference of more than 3.

In the simulated data, on the other hand, the smallest possible event is a single patch failure; the large events I am attempting to predict have an area of only around 400 patches. Assuming similar slip distances, the equivalent magnitude difference is only at most 1.5. A

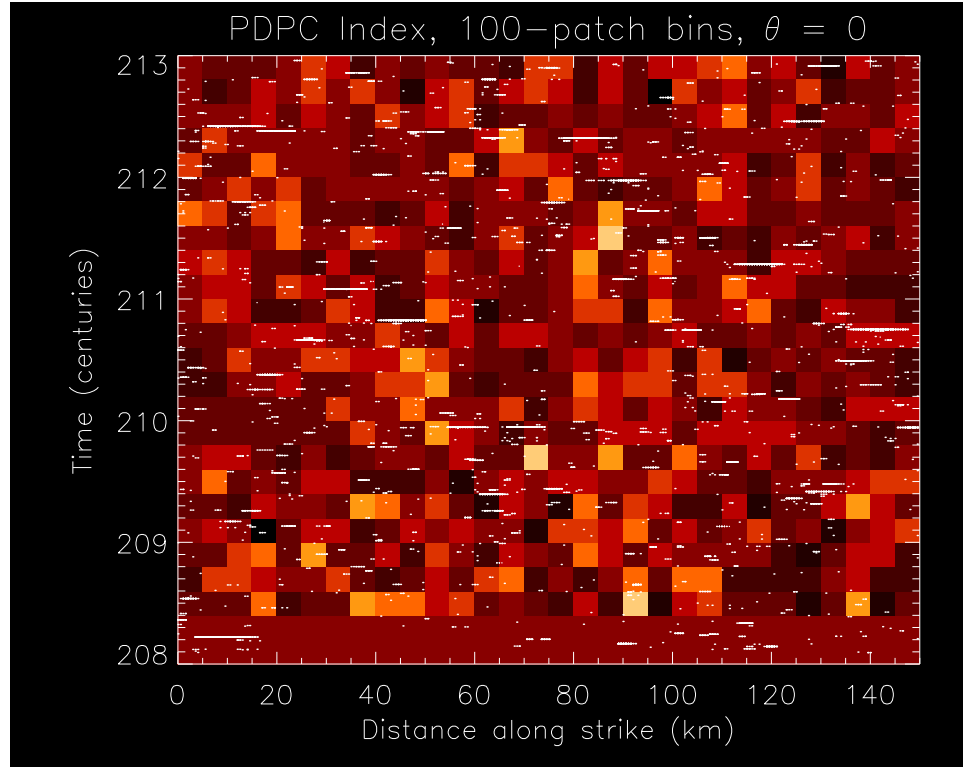


Figure 5.37: The evolution of the PDPC index for synthetic activity on a z-shaped fault with a bend angle of 0 degrees is shown here as a colored intensity field; brighter color indicates a higher relative probability of an event in the future. Ten by ten blocks of fault patches (thirty such “locations” total) were regarded as a single location bin for the purposes of the calculation, and a sliding window 0.2 centuries long was used for the (t_1, t_2) interval. A space-time diagram of activity on the fault is overplotted, showing the time and location of large events. Many of the space-time intervals containing large events, such as those in the vicinity of locations 15, 45, and 85 and respective times 212.4, 210.7, and 212, are now arguably preceded by regions of increased PDPC index, making these calculations much more promising than the unbinned PDPC calculations. However, there are other large events (locations 30 and 140, times 211 and 210.7, for example) that are not preceded by PDPC signal. Lacking a reliable statistical test for the accuracy of PDPC forecasts, the results are at best inconclusive.

patch with an area of 0.25 square kilometers may simply be too large to generate the small-scale activity needed for the PDPC index to detect forthcoming large events.

In addition, the Fault-Patch model remains an in-plane model: the earthquake fault is represented as a single surface. A natural fault is not a geometrically ideal surface, but consists of a zone of broken rock with some thickness to it. There are also innumerable small faults in the vicinity of a main fault, some of which may be the source of fore- and after-shocks, rather than the primary fault itself. In this model, the main fault surface is the only source of seismic activity. If a large region of correlated stress develops, no activity can occur in that region while the stress on it is building up to the failure threshold. The only precursory signal possible is precursory quiescence, and it is well-known that both precursory activation and precursory quiescence can occur before large earthquakes. In nature, this is because while the main fault is locked and unmoving, the many small faults surrounding it can still move. In an in-plane model, the closest equivalent behavior is for nearby regions of the main fault to shift, but that can only happen if they are separated from the region of correlated stress by a steep stress gradient. (If they are not, the rupture will propagate into the correlated region and trigger the large failure, and the nearby failures would then be part of the main shock, rather than nearby background activity.)

Another possibility is that precursory small events in nature are related to the mechanism of stress decay. Laboratory research [85] suggests that as a locked fault approaches the failure threshold, very small slips that relieve some of the stress will occur. One physical explanation for the changes in the background seismicity rate associated with upcoming large events is that they are related to these small slips. While it would be possible to construct a computer model that incorporated that behavior, the Fault-Patch model does not do so; it allows stress to leak away without a modeled physical mechanism. If stress leakage causes seismicity fluctuations detected by the PDPC index, a model which omits the leakage process will fail to produce precursory signals detectable with PDPC analysis.

5.6 Recurrence Plot Analysis

Recurrence plot analysis is useful for its ability to pick out otherwise hidden temporal structure in a dataset. I constructed a recurrence plot for a data set consisting of 100 stress snapshots taken at 500-event intervals, covering 50,000 events total. Analysis of event data showed that on average, there are around 600 events between failures of a given patch. Thus, an interval of 500 events is on the same scale as the seismic cycle for this configuration of the model. Because recurrence plot analysis detects only temporal structure in the data, and because the statistical distribution of events is unchanged for different geometries, I constructed recurrence plots only for a flat (bend angle zero) fault geometry.

The recurrence plot is shown in figure 5.38. Rather than plotting dots where the distance between states is below some threshold, I have mapped distance onto a color scale. Excepting the diagonal, which has a distance of zero, the state distances range from 500 to 840; smaller distances are indicated by darker colors and larger distances by brighter colors. The overall texture of the plot contains many lines of a single color parallel to the diagonal. These lines indicate points in time where two trajectories of the system parallel one another.

Although the existence of diagonal structure in this recurrence plot is clear when compared to a recurrence plot of random data, it is difficult to extract any quantitative measurements from it. In particular, there are many bright diagonal lines, which correspond to trajectories that parallel one another at a constant but relatively large distance. In order to study these lines more closely, I used clustering techniques. Using a version of the clustering algorithm of section 3.4 modified to consider only diagonal neighbors, I found the diagonal segments with similar state distances. A brief survey of various values of the cutoff parameter ϵ showed that the distribution of segment sizes was stable for values between ten and twenty, so I chose to use clusters calculated with $\epsilon = 16$, which is 1% of the range of state distances (excluding the diagonal).

Figure 5.39 shows the diagonal segments found with the modified clustering algorithm.

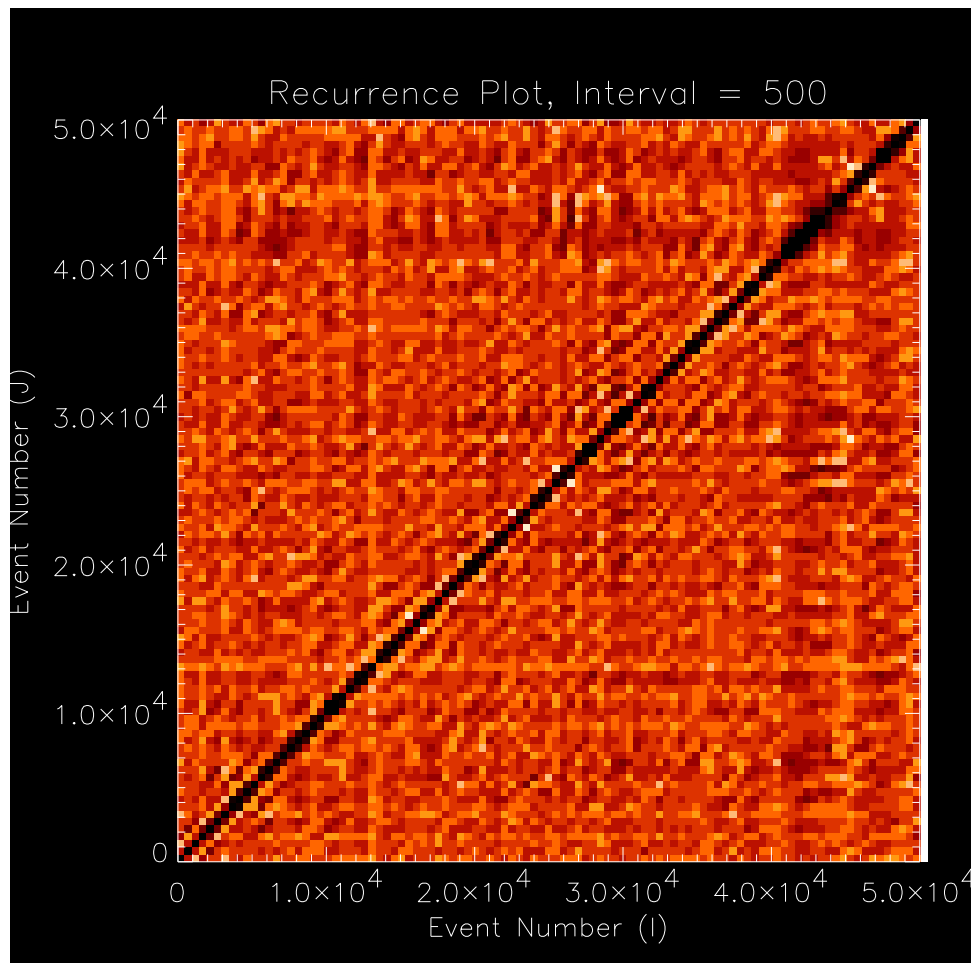


Figure 5.38: A recurrence plot constructed from stress snapshots recorded at intervals of 500 events. Brighter colors indicate greater distance between states. Diagonal structure indicating parallel trajectories is visible, especially near the diagonal itself.

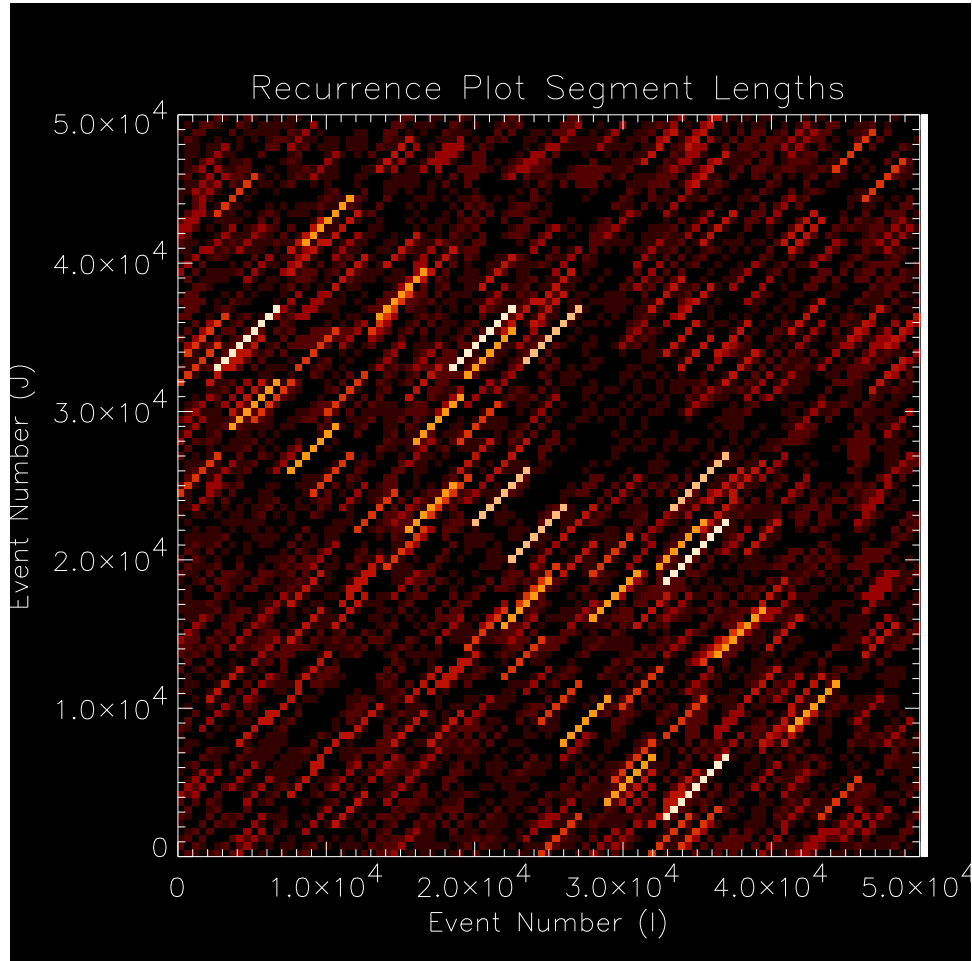


Figure 5.39: The lengths of the diagonal segments in the recurrence plot of figure 5.38, as determined by a modified clustering algorithm. The clustering threshold ϵ is 1% of the range of state distances covered by the recurrence plot. The number of segments of a particular length follows a decaying exponential, with a maximum observed segment length of 9. Segments of size 1 are not plotted.

The number of segments of a given size follows an exponential decay curve. The longest segments have a length of nine, or 4500 events. Using these two facts, we can estimate that less than 1% of all state correlations will persist for longer than 5000 events. This interval is useful in simulation as an estimate of how many steps are required for the system to depart from an initial state configuration.

Chapter 6

Conclusion

6.1 Summary

I created a computer model of earthquakes that represents the surface of the fault as a collection of rectangular sub-faults or “fault patches”. This model is similar to historically well-established faults like the slider-block model of Burridge and Knopoff in most aspects, but implements the interaction between fault elements through three-dimensional tensor stress transfer rather than scalar force transfer, allowing me to simulate earthquake behavior on systems with three-dimensional geometry rather than remaining restricted to a two-dimensional planar geometry. I used simulations of behavior on a planar fault to establish realistic values for the model’s variable parameters such as α , the stress leakage rate, and the SNR connectivity factor. Having done so, I then simulated events on z-shaped faults, both rough and smooth, with a variety of bend angles and loading rates to study the effects of geometry on the behavior of the fault system.

I found that while the geometry of a fault system can have a significant effect on the evolution of the system’s event history, the nature of this effect differs from what one might naively expect. The obvious way in which geometry can influence fault dynamics is through stress transfer; if two fault patches have different orientations, then the influence of one upon the other (that is, the stress increment transferred when one patch slips) will be different than it would be if they had the same orientation. In the absence of normal stress effects on friction,

changes in the shear stress due to orientation do not appear to have a substantial effect on the system dynamics in any but the most extreme case: simulations show that events will propagate unaffected across a bend in a fault until the bend angle begins to approach 90 degrees.

A feature which does act as a barrier to the propagation of events is the presence of a change in the loading rate from one part of the fault to another. In other words, a differential loading rate creates a gradient in the stress field that tends to act as a surface dividing the fault into separate sub-faults. If local stress loading on the fault is the result of a uniform (or very smooth) regional tectonic stress field, the projection of this global stress field onto the fault system will result in sub-faults with different orientations having different loading rates. As a result, the geometric division of a fault system results in the dynamic division of the system, not because of the effects of geometry on shear stress transfer, but because of its effects on the loading rates.

I also found that geometric imperfections do not change the overall behavior of the system. One of the perils of computer simulation is the possibility of inadvertently modeling a metastable subset of the system's dynamics by using a mathematically ideal value. It is possible that the dynamics of this system are different if the fault is represented as a perfectly flat plane, a situation that is easy to achieve in a computer but impossible in reality. This turns out not to be the case; if the fault is "roughened" and the positions of the fault patches allowed to deviate from a geometrically flat plane, the resulting event catalog is not qualitatively different from the ideal case. This result implies that for intra-fault activity, the computationally expensive tensor stress transfer calculations can be replaced with the much simpler cellular automaton or neural-net style linear force transfer rules without loss of realism.

Finally, I found that the Phase Dynamic Probability Change methodology does not detect precursory signals before large events in simulated data. This failure I attribute to two features of the model: first, that the granularity of the model was large, making it impossible for very small events to occur; and second, that the model is restricted to in-plane fault elements, making it impossible for events to occur outside the bounds of the primary fault. These features cause

there to be a much lower level of background activity than is observed in nature, and as a result the PDPC index has little predictive value. The PDPC index is unlikely to be useful for any computer simulation of earthquake activity unless the granularity (the size of the smallest fault element) is very small or/and some way of allowing seismic activity to occur outside the plane of the main fault is found.

6.2 Future Work

The effects of granularity should be studied through simulations of similar faults composed of much larger and much smaller patches. In particular, the question of whether the PDPC methodology is hindered merely by the lower limit on event size, or whether off-plane events are essential to its functioning, should be answered.

The findings on the effects of fault roughness should be verified with comprehensive statistical comparisons of the event distributions for rough faults and smooth faults, and compared to theoretical results.

The simulations should be repeated with normal stress friction included in the strength of the fault patches. It is expected that normal stress effects on friction will have a significant effect on the dynamics of the system, though the degree of that effect is unknown; this research provides a baseline for comparison, and is especially useful as a procedural guide to the exploration of geometric effects. Along with changes to the Coulomb friction, viscoelasticity or some other relaxation mechanism should be included in the simulations. A variety of fault geometries, including more complex systems based on the detailed geometry of natural fault systems should be simulated as well.

Finally, the finding that geometry is insignificant for intra-fault interactions suggests that the effects of geometry could be incorporated into a much simpler model; if a fault system is divided into segments on the basis of stress loading rate or, equivalently, average slip rate, then each segment could be treated as a separate cellular automaton or neural network model. The dynamics of these models would follow very simple (and computationally inexpensive) rules like

those of the classic two-dimensional slider-block model. Stress would be transferred in aggregate over long distances between the segments, using a full three-dimensional tensorial treatment; the interaction coefficients between segments could be calculated in advance and stored to save computation. Each segment could have not only its own loading rate, but also varying frictional and cohesive properties as appropriate for a realistic fault system. Such a model would not only incorporate the effects of geometry into a computationally less expensive simulation, it would also lend itself to easy parallelization, allowing much larger, complex, and realistic fault systems to be simulated in a reasonable time.

Bibliography

- [1] M.S. Abinante and L. Knopoff. Quasidynamic model for earthquake simulations. *Physical Review E*, 52(5, pt.B):5675–8, 1995.
- [2] M. Acharyya and B.K. Chakrabarti. Response to pulsed disturbances in ill-condensed systems and possible prediction of catastrophes. *Diffusion and Defect Data Part B*, 42-43:155–62, 1995.
- [3] M. Acharyya and B.K. Chakrabarti. Study of the response to pulses and possible prediction of catastrophes. *Journal de Physique I*, 5(2):153–8, 1995.
- [4] M. Acharyya and B.K. Chakrabarti. Growth of breakdown susceptibility in random composites and the stick-slip model of earthquakes: Prediction of dielectric breakdown and other catastrophes. *Physical Review E*, 53(1, pt.A):140–7, 1996.
- [5] M. Acharyya and B.K. Chakrabarti. Response of random dielectric composites and earthquake models to pulses: Prediction possibilities. *Physica A*, 224(1-2):254–66, 1996.
- [6] K. Aki. Strong motion prediction using mathematical modeling techniques. *Bulletin of the Seismological Society of America*, 72(6, pt.B):S29–41, 1982.
- [7] K. Aki and P. G. Richards. *Quantitative Seismology: Theory and Methods*. W. H. Freeman, 1980.
- [8] P.G. Akishin, M.V. Altaisky, I. Antoniou, A.D. Budnik, and V.V. Ivanov. Burridge-Knopoff model and self-similarity. *Chaos, Solitons and Fractals*, 11(1-3):207–22, 2000.
- [9] C.J. Allegre, J.L. Le Mouel, H. Duyen Chau, and C. Narteau. Scaling organization of fracture tectonics (SOFT) and earthquake mechanism. *Physics of the Earth and Planetary Interiors*, 92(3-4):215–33, 1995.
- [10] T. F. H. Allen, R. V. O'Neill, and T. W. Hoekstra. Interlevel relations in ecological research and management: Some working principles from hierarchy theory. General Technical Report RM-110, USDA Forest Service, July 1983.
- [11] T. F. H. Allen and Thomas B. Starr. *Hierarchy: Perspectives for Ecological Complexity*. The University of Chicago Press, 1982.
- [12] F. Angulo-Brown and A. Munoz-Diosdado. Further seismic properties of a spring-block earthquake model. *Geophysical Journal International*, 139(2):410–18, 1999.
- [13] Per Bak and Chao Tang. Earthquakes as a self-organized critical phenomenon. *Journal of Geophysical Research*, 94(B11):15635–7, 1989.
- [14] Mark Bebbington. A hierarchical stress release model for synthetic seismicity. *Journal of Geophysical Research*, 102(B6):11677–11687, June 1997.

- [15] Thorsten W. Becker. Deterministic chaos in two state-variable friction sliders and the effect of elastic interactions. In John B. Rundle, Donald L. Turcotte, and William Klein, editors, *GeoComplexity and the Physics of Earthquakes*, number 120 in Geophysical Monograph Series, pages 5–26. AGU Books Board, 2000.
- [16] Y. Ben-Zion and J. R. Rice. Earthquake failure sequences along a cellular fault zone in a three-dimensional elastic solid containing asperity and nonasperity regions. *Journal of Geophysical Research*, 98(B8):14109–14131, August 1993.
- [17] Yehuda Ben-Zion and James R. Rice. Dynamic simulations of slip on a smooth fault in an elastic solid. *Journal of Geophysical Research*, 102(B8):17771–17784, August 1997.
- [18] Pierre Berge, Yves Pomeau, and Christian Vidal. *Order within Chaos*, John Wiley and Sons, 1984.
- [19] Susan L. Bilek and Thorne Lay. Depth dependent rupture properties in circum-Pacific subduction zones. In John B. Rundle, Donald L. Turcotte, and William Klein, editors, *GeoComplexity and the Physics of Earthquakes*, number 120 in Geophysical Monograph series, pages 165–186. AGU Books Board, 2000.
- [20] Jacques Blanc-Talon. Effective computation of 2D coupled map lattices. *Complexity International*, 6, January 1998.
- [21] William J. Bosl. Modeling complex crustal processes. In John B. Rundle, Donald L. Turcotte, and William Klein, editors, *GeoComplexity and the Physics of Earthquakes*, number 120 in Geophysical Monograph Series, pages 245–265. AGU Books Board, 2000.
- [22] William J. Bosl and Amos Nur. Crustal fluids and earthquakes. In John B. Rundle, Donald L. Turcotte, and William Klein, editors, *GeoComplexity and the Physics of Earthquakes*, number 120 in Geophysical Monograph series, pages 267–284. AGU Books Board, 2000.
- [23] D. D. Bowman, G. Ouillon, C. G. Sammis, A. Sornette, and D. Sornette. An observational test of the critical earthquake concept. *Journal of Geophysical Research*, 103(B10):24359–24372, October 1998.
- [24] Daniel J. Brehm and Lawrence W. Braile. Intermediate-term earthquake prediction using the modified time-to-failure method in southern California. *Bulletin of the Seismological Society of America*, 89(1):275–293, February 1999.
- [25] S.R. Brown, C.H. Scholz, and J.B. Rundle. A simplified spring-block model of earthquakes. *Geophysical Research Letters*, 18(2):215–18, 1991.
- [26] J.L. Brun and J.B. Gomez. A four-parameter, two degree-of-freedom block-spring model: Effect of the driver velocity. *Pure and Applied Geophysics*, 143(4):633–53, 1994.
- [27] R. Burridge and L. Knopoff. Body force equivalents for seismic dislocations. *Bulletin of the Seismological Society of America*, 54(6):1875–1888, December 1964.
- [28] R. Burridge and L. Knopoff. Model and theoretical seismicity. *Bulletin of the Seismological Society of America*, 57(3):341–371, June 1967.
- [29] Jr. C. L. Webber. Rhythmogenesis of deterministic breathing patterns. In H. Haken and H. P. Koepchen, editors, *Rhythms in Physiological Systems*, volume 55 of *Springer Series in Synergetics*. Springer-Verlag, 1991.
- [30] M. Campillo, I.R. Ionescu, J.C. Paumier, and Y. Renard. On the dynamic sliding with friction of a rigid block and of an infinite elastic slab. *Physics of the Earth and Planetary Interiors*, 96(1):15–23, 1996.

- [31] J.M. Carlson and J.S. Langer. Mechanical model of an earthquake fault. *Physical Review A*, 40(11):6470–84, 1989.
- [32] J.M. Carlson and J.S. Langer. Properties of earthquakes generated by fault dynamics. *Physical Review Letters*, 62(22):2632–35, 1989.
- [33] J.M. Carlson, J.S. Langer, and B.E. Shaw. Dynamics of earthquake faults. *Reviews of Modern Physics*, 66(2):657–70, 1994.
- [34] J.M. Carlson, J.S. Langer, B.E. Shaw, and C. Tang. Intrinsic properties of a Burridge-Knopoff model of an earthquake fault. *Physical Review A*, 44(2):884–97, 1991.
- [35] J.H.E. Cartwright, E. Hernandez-Garcia, and O. Piro. Burridge-Knopoff models as elastic excitable media. *Physical Review Letters*, 79(3):527–30, 1997.
- [36] M. C. Casdagli. Recurrence plots revisited. *Physica D*, pages 12–44, 1997.
- [37] Jr. Charles L. Webber and Joseph P. Zbilut. Dynamical assessment of physiological systems and states using recurrence plot strategies. *Journal of Applied Physiology*, 76(965-973), 1994.
- [38] Lu Chunsheng, H. Takayasu, A.Yu. Tretyakov, M. Takayasu, and S. Yumoto. Self-organized criticality in a block lattice model of the brittle crust. *Physics Letters A*, 242(6):349–54, 1998.
- [39] S. F. Cox. Faulting processes at high fluid pressure: an example of fault valve behavior from the Wattle Gully Fault, Victoria, Australia. *Journal of Geophysical Research*, 1995.
- [40] A. Crisanti, M.H. Jensen, and A. Vulpiani. Strongly intermittent chaos and scaling in an earthquake model. *Physical Review A*, 46(12):R7363–6, 1992.
- [41] M. de Sousa Vieira. Self-organized criticality in a deterministic mechanical model. *Physical Review A*, 46(10):6288–93, 1992.
- [42] M. de Sousa Vieira. Exponential distributions in a mechanical model for earthquakes. *Physical Review E*, 54(6):5925–8, 1996.
- [43] M. de Sousa Vieira. Chaos and synchronized chaos in an earthquake model. *Physical Review Letters*, 82(1):201–4, 1999.
- [44] M. de Sousa Vieira and H.J. Herrmann. Self-similarity of friction laws. *Physical Review E*, 49(5, pt.B):4534–41, 1994.
- [45] Maria de Sousa Vieira, Giovani L. Vasconcelos, and Sidney R. Nagel. Dynamics of spring-block models: Tuning to criticality. *Physical Review E*, 47(4):R2221–4, 1993.
- [46] James H. Dieterich. Time-dependent friction as a possible mechanism for aftershocks. *Journal of Geophysical Research*, 77(20):3771–3781, July 1972.
- [47] J.H. Dieterich and M.F. Linker. Fault stability under conditions of variable normal stress. *Geophysical Research Letters*, 19(16):1691–4, 1992.
- [48] Terry e. Tullis. Rock friction and its implications for earthquake prediction examined via models of Parkfield earthquakes. *Proceedings of the National Academy of Sciences*, 93:3803–3810, April 1996.
- [49] J.-P. Eckmann, S. Oliffson Kamphorst, and D. Ruelle. Recurrence plots of dynamical systems. *Europhysics Letters*, 4(9):973–977, November 1987.

- [50] Mariana Eneva and Yehuda Ben-Zion. Application of pattern recognition techniques to earthquake catalogs generated by a model of segmented fault systems in three-dimensional elastic solids. *Journal of Geophysical Research*, 102(B11):24513–24528, November 1997.
- [51] J.D. Eshelby. The determination of the elastic field of an ellipsoidal inclusion and related problems. *Proceedings of the Royal Society of London, Series A*, 241:376–393, 1957.
- [52] P. Espanol. Propagative slipping modes in a spring-block model. *Physical Review E*, 50(1):227–35, 1994.
- [53] Philippe Faure and Henri Korn. A new method to estimate the Kolmogorov entropy from recurrence plots: Its application to neuronal signals. *Physica D*, 122:265–279, 1998.
- [54] Hans Jacob S. Feder and Jens Feder. Self-organized criticality in a stick-slip process. *Physical Review Letters*, 66(20):2669–72, 1991.
- [55] C.D. Ferguson, W. Klein, and J.B. Rundle. Spinodals, scaling, and ergodicity in a threshold model with long-range stress transfer. *Physical Review E*, 60(2):1359–73, 1999.
- [56] Daniel S. Fisher, Karin Dahmen, and Sharad Ramanathan. Statistics of earthquakes in simple models of heterogeneous faults. *Physical Review Letters*, 78(25):4885–4888, June 1997.
- [57] Geoffrey C. Fox, Ken Hurst, Andrea Donnellan, and Jay Parker. Introducing a new paradigm for computational earth science: A web-object-based approach to earthquake simulations. In John B. Rundle, Donald L. Turcotte, and William Klein, editors, *GeoComplexity and the Physics of Earthquakes*, number 120 in Geophysical Monograph Series, pages 219–244. AGU Books Board, 2000.
- [58] Y. C. Fung. *Foundations of Solid Mechanics*. Prentice-Hall, 1965.
- [59] A. Garcia and C. Penland. Fluctuating hydrodynamics and principal oscillation pattern analysis. *J. Stat. Phys.*, 64:1121–32, 1991.
- [60] B.J. Gomberg, M.L. Blanpied, and N.M. Beeler. Transient triggering of near and distant earthquakes. *Bulletin of the Seismological Society of America*, 87(2):294–309, 1997.
- [61] P. Grassberger. Efficient large-scale simulations of a uniformly driven system. *Physical Review E*, 49(3):2436–44, 1994.
- [62] S. J. Gross and C. Kisslinger. Stress and the spatial distribution of seismicity in the central Aleutians. *Journal of Geophysical Research*, 99(B8):15291–15303, August 1994.
- [63] Susanna J. Gross. Personal communication.
- [64] Susanna J. Gross. Traveling wave and rough fault earthquake models: Illuminating the relationship between slip deficit and event frequency statistics. In John B. Rundle, Donald L. Turcotte, and William Klein, editors, *GeoComplexity and the Physics of Earthquakes*, number 120 in Geophysical Monograph Series, pages 73–82. AGU Books Board, 2000.
- [65] David Gubbins. *Seismology and Plate Tectonics*. Cambridge University Press, 1992.
- [66] P. Hahner and Y. Drossinos. Dynamics of a creep-slip model of earthquake faults. *Physica A*, 260(3-4):391–417, 1998.
- [67] P. Hahner and Y. Drossinos. Nonlinear dynamics of a continuous spring-block model of earthquake faults. *Journal of Physics A (Mathematical and General)*, 31(10):L185–91, 1998.

- [68] P. Hahner and Y. Drossinos. Scale invariance and intermittency in a creep-slip model of earthquake faults. *Physical Review E*, 59(6):R6231–4, 1999.
- [69] S. Hainzl, G. Zoller, and J. Kurths. Self-organized criticality model for earthquakes: Quiescence, foreshocks and aftershocks. *International Journal of Bifurcation and Chaos in Applied Sciences and Engineering*, 9(12):2249–55, 1999.
- [70] S. Hainzl, G. Zöller, and J. Kurths. Similar power laws for foreshock and aftershock sequences in a spring-block model for earthquakes. *Journal of Geophysical Research*, 104(B4):7243–7254, 1999.
- [71] S. Hainzl, G. Zoller, J. Kurths, and J. Zschau. Seismic quiescence as an indicator for large earthquakes in a system of self-organized criticality. *Geophysical Research Letters*, 27(5):597–600, 2000.
- [72] Ruth A. Harris, Robert W. Simpson, and Paul A. Reasenberg. Influence of static stress changes on earthquake locations in southern California. *Nature*, 375:221–224, May 1995.
- [73] K. Hasselman. PIPs and POPs: The reduction of complex dynamical systems using principal interaction and oscillation patterns. *Geophys. Res.*, 93:11015–21, 1988.
- [74] Brian Hayes. Computing science: The world in a spin. *American Scientist*, 88(5):384–388, September–October 2000.
- [75] F. Heslot, T. Baumberger, B. Perrin, B. Caroli, and C. Caroli. Creep, stick-slip, and dry-friction dynamics: Experiments and a heuristic model. *Physical Review E*, 49(6, pt.A):4973–88, 1994.
- [76] K. M. Hodgkinson, Ross S. Stein, and Geoffrey C. P. King. The 1954 Rainbow Mountain–Fairview Peak–Dixie Valley earthquakes: a triggered normal faulting sequence. *Journal of Geophysical Research*, 101(B11):25459–25471, 1996.
- [77] J. Huang, G. Narkounskiaia, and D.L. Turcotte. A cellular-automata, slider-block model for earthquakes. II. demonstration of self-organized criticality for a 2-D system. *Geophysical Journal International*, 111(2):259–69, 1992.
- [78] Steven C. Jaumé. Changes in earthquake size-frequency distributions underlying accelerating seismic moment/energy release. In John B. Rundle, Donald L. Turcotte, and William Klein, editors, *GeoComplexity and the Physics of Earthquakes*, number 120 in Geophysical Monograph series, pages 199–210. AGU Books Board, 2000.
- [79] Alan Jeffrey. *Handbook of Mathematical Formulas and Integrals*. Academic Press, 1995.
- [80] T. Jonsson and S.F. Marinosson. Correlation functions and power spectra in a model of an earthquake fault. *Physics Letters A*, 207(3-4):165–72, 1995.
- [81] T. Jonsson and S.F. Marinosson. Scaling and correlation functions in a model of a two-dimensional earthquake fault. *Physica Scripta*, 58(3):282–8, 1998.
- [82] Hiroo Kanamori and Don L. Anderson. Theoretical basis of some empirical relations in seismology. *Bulletin of the Seismological Society of America*, 65(5):1073–1097, October 1975.
- [83] Hiroo Kanamori and Emily E. Brodsky. The physics of earthquakes. *Physics Today*, 54(6):34–40, June 2001.
- [84] Hiroo Kanamori and Thomas H. Heaton. Microscopic and macroscopic physics of earthquakes. In John B. Rundle, Donald L. Turcotte, and William Klein, editors, *GeoComplexity and the Physics of Earthquakes*, number 120 in Geophysical Monograph series, pages 147–164. AGU Books Board, 2000.

- [85] Stephen L. Karner and Chris Marone. Effects of loading rate and normal stress on stress drop and stick-slip recurrence interval. In John B. Rundle, Donald L. Turcotte, and William Klein, editors, GeoComplexity and the Physics of Earthquakes, number 120 in Geophysical Monograph series, pages 187–198. AGU Books Board, 2000.
- [86] Geoffrey C. P. King, C. P. King, Ross S. Stein, and Jian Lin. Static stress changes and the triggering of earthquakes. Bulletin of the Seismological Society of America, 84(3):935–953, June 1994.
- [87] W. Klein, M. Anghel, C. D. Ferguson, J. B. Rundle, and J. S. Sá Martins. Statistical analysis of a model for earthquake faults with long-range stress transfer. In John B. Rundle, Donald L. Turcotte, and William Klein, editors, GeoComplexity and the Physics of Earthquakes, number 120 in Geophysical Monograph Series, pages 43–72. AGU Books Board, 2000.
- [88] W. Klein, J.B. Rundle, and C.D. Ferguson. Scaling and nucleation in models of earthquake faults. Physical Review Letters, 78(19):3793–6, 1997.
- [89] L. Knopoff, J.A. Landoni, and M.S. Abinante. Dynamical model of an earthquake fault with localization. Physical Review A, 46(12):7445–9, 1992.
- [90] Matthew Koebbe and Gottfried Mayer-Kress. Use of recurrence plots in the analysis of time-series data. In M. Casdagli and S. Eubank, editors, Nonlinear Modeling and Forecasting, volume XII of SFI Studies in the Sciences of Complexity, pages 361–378. Addison-Wesley, 1992.
- [91] B. V. Kostrov and Shamita Das. Principles of Earthquake Source Mechanics. Cambridge Monographs on Mechanics and Applied Mathematics. Cambridge University Press, 1988.
- [92] Leung Kwantai, J. Mueller, and J.V. Andersen. Generalization of a two-dimensional Burridge-Knopoff model of earthquakes. Journal de Physique I, 7(3):423–9, 1997.
- [93] Thorne Lay and Terry C. Wallace. Modern Global Seismology, volume 58 of International Geophysics. Academic Press, 1995.
- [94] Y.F. Lim and Kan Chen. Dynamics of dry friction: A numerical investigation. Physical Review E, 58(5):5637–42, 1998.
- [95] Ian Main. Apparent breaks in scaling in the earthquake cumulative frequency-magnitude distribution: Fact or artifact? Bulletin of the Seismological Society of America, 90(1):86–97, February 2000.
- [96] L. Mansinha and D. E. Smylie. The displacement fields of inclined faults. Bulletin of the Seismological Society of America, 61(5):1433–1440, October 1971.
- [97] V.M. Maru, P.S. Moharir, and R. Singh. Similitude feasibility of slider-block models. Journal of Geodynamics, 22(1-2):173–88, 1996.
- [98] P. Mora, D. Place, S. Abe, and S. Jaumé. Lattice solid simulation of the physics of fault zones and earthquakes: The model, results, and directions. In John B. Rundle, Donald L. Turcotte, and William Klein, editors, GeoComplexity and the Physics of Earthquakes, number 120 in Geophysical Monograph Series, pages 105–125. AGU Books Board, 2000.
- [99] P. Müller and D. Henderson. Principal component analysis: Basic methods and extensions. In Statistical Methods in Physical Oceanography: Proceedings of the 'Aha Huliko'a Hawaiian Winter Workshop, pages 185–199, 1993.
- [100] C.B. Muratov. Traveling wave solutions in the Burridge-Knopoff model. Physical Review E, 59(4):3847–57, 1999.

- [101] H. Nakanishi. Cellular-automaton model of earthquakes with deterministic dynamics. *Physical Review A*, 41(12):7086–9, 1990.
- [102] H. Nakanishi. Dynamical models of earthquakes. *Physica A*, 229(3-4):530–9, 1996.
- [103] H. Nakanishi. Complex behavior in earthquake dynamics. *International Journal of Modern Physics B*, 12(3):273–84, 1998.
- [104] G. Narkounskiaia and D.L. Turcotte. A cellular-automata, slider-block model for earthquakes. I. demonstration of chaotic behavior for a low-order system. *Geophysical Journal International*, 111(2):250–8, 1992.
- [105] S.P. Nishenko and R. Buland. A generic recurrence interval distribution for earthquake forecasting. *Bulletin of the Seismological Society of America*, 77(4):1382–99, August 1987.
- [106] C. Nostro, Ross S. Stein, M. Cocco, M. E. Belardinelli, and W. Marzocchi. Two-way coupling between Vesuvius eruptions and southern Apennine earthquakes, Italy, by elastic stress transfer. *Journal of Geophysical Research*, 103(B10):24487–24504, 1998.
- [107] David D. Oglesby and Ralph J. Archuleta. A faulting model for the 1992 Petrolia earthquake: Can extreme ground acceleration be a source effect? *Journal of Geophysical Research*, 102(B6):11877–11897, June 1997.
- [108] Yoshimitsu Okada. Internal deformation due to shear and tensile faults in a half-space. *Bulletin of the Seismological Society of America*, 82(2):1018–1040, April 1992.
- [109] Z. Olami and K. Christensen. Temporal correlations, universality, and multifractality in a spring-block model of earthquakes. *Physical Review A*, 46(4):R1720–3, 1992.
- [110] Z. Olami, H.J.S. Feder, and K. Christensen. Self-organized criticality in a continuous, nonconservative cellular automaton modeling earthquakes. *Physical Review Letters*, 68(8):1244–7, 1992.
- [111] M. Otsuka. A simulation of earthquake occurrence. *Physics of the Earth and Planetary Interiors*, 6(4):311–315, December 1972.
- [112] Jon D. Pelletier. Spring-block models of seismicity: Review and analysis of a structurally heterogeneous model coupled to a viscous asthenosphere. In John B. Rundle, Donald L. Turcotte, and William Klein, editors, *GeoComplexity and the Physics of Earthquakes*, number 120 in Geophysical Monograph Series, pages 27–42. AGU Books Board, 2000.
- [113] C. Penland. Random forcing and forecasting using principal oscillation pattern analysis. *Monthly Weather Review*, 117:2165–2185, 1989.
- [114] C. Penland and T. Magorian. Prediction of Nino 3 sea surface temperatures using linear inverse modeling. *J. Climate*, 6:1067–76, 1993.
- [115] C. Penland and P.D. Sardeshmukh. The optimal growth of tropical sea surface temperature anomalies. *J. Climate*, 8:1999–2024, 1995.
- [116] H. Perfettini, Ross S. Stein, Robert W. Simpson, and M. Cocco. Stress transfer by the 1988-1989 $M=5.3$ and 5.4 Lake Elsman foreshocks to the Loma Prieta fault: Unclamping at the site of peak mainshock slip. *Journal of Geophysical Research*, 104(B9):20169–20182, 1999.
- [117] D. Pisarenko and P. Mora. Velocity weakening in a dynamical model of friction. *Pure and Applied Geophysics*, 142(3-4):447–66, 1994.

- [118] R. W. Preisendorfer. Principal Component Analysis in Meteorology and Oceanography. Elsevier Pub. Co., New York, 1988.
- [119] William H. Press, Saul A. Teukolsky, William T. Vetterling, and Brian P. Flannery. Numerical Recipes in C: The Art of Scientific Computing. Cambridge University Press, 1994.
- [120] H. Ramachandran and G. Ananthakrishna. Dynamics of the Burridge-Knopoff model of earthquakes. Diffusion and Defect Data Part B, 42-43:325–33, 1995.
- [121] D. C. Roberts and D. L. Turcotte. Earthquakes: Friction or a plastic instability? In John B. Rundle, Donald L. Turcotte, and William Klein, editors, GeoComplexity and the Physics of Earthquakes, number 120 in Geophysical Monograph series, pages 97–104. AGU Books Board, 2000.
- [122] J.B. Rundle and S.R. Brown. Origin of rate dependence in frictional sliding. Journal of Statistical Physics, 65(1-2):403–12, 1991.
- [123] J.B. Rundle and W. Klein. Scaling and critical phenomena in a cellular automaton slider-block model for earthquakes. Journal of Statistical Physics, 72(1-2):405–12, 1993.
- [124] John Rundle, Eric Preston, Seth McGinnis, and W. Klein. Why earthquakes stop: Growth and arrest in stochastic fields. Physical Review Letters, 80(25):5698–5701, June 1998.
- [125] John B. Rundle. A physical model for earthquakes: 1. fluctuations and interactions. Journal of Geophysical Research, 93(B6):6237–6254, June 1988.
- [126] John B. Rundle. A physical model for earthquakes: 2. application to southern California. Journal of Geophysical Research, 93(B6):6255–6274, June 1988.
- [127] John B. Rundle. A physical model for earthquakes: 3. thermodynamical approach and its relation to nonclassical theories of nucleation. Journal of Geophysical Research, 94(B3):2839–2855, March 1989.
- [128] John B. Rundle and D. D. Jackson. Numerical simulation of earthquake sequences. Bulletin of the Seismological Society of America, 67(5):1363–77, October 1977.
- [129] John B. Rundle and W. Klein. Nonclassical nucleation and growth of cohesive tensile cracks. Physical Review Letters, 63(2):171–174, July 1989.
- [130] John B. Rundle, W. Klein, and Susanna Gross. Dynamics of a traveling density wave model for earthquakes. Physical Review Letters, 76(22):4285–4288, May 1996.
- [131] John B. Rundle, W. Klein, Kristy Tiampo, and Susanna Gross. Dynamics of seismicity patterns in systems of earthquake faults. In John B. Rundle, Donald L. Turcotte, and William Klein, editors, GeoComplexity and the Physics of Earthquakes, number 120 in Geophysical Monograph series, pages 127–146. AGU Books Board, 2000.
- [132] John B. Rundle and William Klein. New ideas about the physics of earthquakes. Reviews of Geophysics, 1995.
- [133] John B. Rundle, William Klein, and Susanna Gross. Rupture characteristics, recurrence, and predictability in a slider-block model for earthquakes. In Rundle, Turcotte, and Klein, editors, Reduction & Predictability of Natural Disasters, volume XXV of SFI Studies in the Sciences of Complexity, pages 167–203. Addison-Wesley, 1996.
- [134] John B. Rundle, William Klein, Susanna Gross, and Donald L. Turcotte. Boltzmann fluctuations in numerical simulations of nonequilibrium lattice threshold systems. Physical Review Letters, 75(8):1658–61, 1995.

- [135] John B. Rundle, Donald L. Turcotte, and William Klein, editors. [GeoComplexity and the Physics of Earthquakes](#). Number 120 in Geophysical Monograph Series. AGU Books Board, 2000.
- [136] P. B. Rundle, J. B. Rundle, K. F. Tiampo, J. S. de sa Martins, S. McGinnis, and W. Klein. Nonlinear network dynamics on earthquake fault systems. Submitted to Phys. Rev. Lett., 2001.
- [137] M.R. Sarkardei and R.L. Jacobs. Dynamical origin of spatial order. [Physical Review E](#), 51(3, pt.A):1929–34, 1995.
- [138] J.C. Savage. Principal component analysis of geodetically measured deformation in Long Valley caldera, eastern California, 1983–1987. [Journal of Geophysical Research](#), 93:13297–13305, 1988.
- [139] Christopher H. Scholz. [The Mechanics of Earthquakes and Faulting](#). Cambridge University Press, 1990.
- [140] D. P. Schwartz and K. J. Coppersmith. Fault behavior and characteristic earthquakes: Examples from the Wasatch and San Andreas fault zones. [Journal of Geophysical Research](#), 89(B7):5681–5698, July 1984.
- [141] C. M. Segedin. Note on a penny-shaped crack under shear. [Proceedings of the Cambridge Philosophical Society](#), 47:396–400, 1950.
- [142] B.E Shaw, J.M. Carlson, and J.S. Langer. Patterns of seismic activity preceding large earthquakes. [Journal of Geophysical Research](#), 1992.
- [143] R.H. Sibson. Loading of faults to failure. [Bulletin of the Seismological Society of America](#), 81(6):2493–7, 1991.
- [144] Freysteinn Sigmundsson, Páll Einarsson, Sigurdur Th. Rögnvaldsson, G. R. Foulger, K. M. Hodgkinson, and Gunnar Thorbergsson. The 1994–1995 seismicity and deformation at the Hengill triple junction, Iceland: Triggering of earthquakes by minor magma injection in a zone of horizontal shear stress. [Journal of Geophysical Research](#), 102(B7):15151–15161, July 1997.
- [145] G. C. Sih and H. Liebowitz. Mathematical theories of brittle fracture. In H. Liebowitz, editor, [Treatise on Fracture](#), volume II, page 67. Academic Press, 1968.
- [146] D. Sornette. Mean-field solution of a block-spring model of earthquakes. [Journal de Physique I](#), 2(11):2089–96, 1992.
- [147] D. Sornette. Sweeping of an instability: an alternative to self-organized criticality to get power laws without parameter tuning. [Journal de Physique I](#), 4(2):209–21, 1994.
- [148] Dietrich Stauffer and Amnon Aharony. [Introduction to Percolation Theory](#). Taylor and Francis, revised 2nd edition, 1994.
- [149] Ross S. Stein, A. A. Barka, and J. H. Dieterich. Progressive failure on the North Anatolian fault since 1939 by earthquake stress triggering. [Geophysical Journal International](#), 128(3):594–604, 1997.
- [150] Ross S. Stein, Geoffrey C. P. King, and Jian Lin. Change in failure stress on the southern San Andreas fault system caused by the 1992 magnitude = 7.4 Landers earthquake. [Science](#), 258:1328–1332, November 1992.
- [151] Ross S. Stein, Geoffrey C. P. King, and Jian Lin. Stress triggering of the 1994 M=6.7 Northridge, California, earthquake by its predecessors. [Science](#), 265(5177):1432–1435, September 1994.

- [152] J. A. Steketee. On Volterra's dislocations in a semi-infinite elastic medium. *Canadian Journal of Physics*, 36:192–205, 1958.
- [153] Jürgen E. Streit and Stephen F. Cox. Fluid pressures at hypocenters of moderate to large earthquakes. *Journal of Geophysical Research*, 106(B2):2235–2243, February 2001.
- [154] Steven H. Strogatz. *Nonlinear Dynamics and Chaos*. Addison-Wesley, Reading, MA, 1994.
- [155] K. F. Tiampo, J. B. Rundle, S. Gross, and S. McGinnis. Parallelization of a large-scale computational earthquake simulation program. Submitted to Concurrency and Computation: Practice and Experience, 2001.
- [156] K. F. Tiampo, J. B. Rundle, and S. J. Gross. Eigenpatterns in southern California seismicity. Submitted to JGR, 2001.
- [157] K. F. Tiampo, J. B. Rundle, S. McGinnis, S. Gross, and W. Klein. The phase dynamics of earthquakes: Implications for forecasting in southern California. Submitted to Phys. Rev. Lett., 2001.
- [158] K. F. Tiampo, J. B. Rundle, S. McGinnis, S. J. Gross, and W. Klein. Observation of systematic variations in non-local seismicity patterns from southern California. In John B. Rundle, Donald L. Turcotte, and William Klein, editors, *GeoComplexity and the Physics of Earthquakes*, number 120 in Geophysical Monograph series, pages 211–218. AGU Books Board, 2000.
- [159] K. F. Tiampo, J. B. Rundle, S. McGinnis, and W. Klein. Pattern dynamics and forecast methods in seismically active regions. To appear in Pure and Applied Geophysics, 2001.
- [160] Kristy F. Tiampo. Personal communication.
- [161] Kristy F. Tiampo. *Pattern Dynamics in Southern California Seismicity*. PhD thesis, University of Colorado, Boulder, 2000.
- [162] S. Toda, Ross S. Stein, Paul A. Reasenberg, J. H. Dieterich, and A. Yoshida. Stress transferred by the 1995 $m_w=6.9$ Kobe, Japan, shock: Effect on aftershocks and future earthquake probabilities. *Journal of Geophysical Research*, 103(B10):24543–24565, 1998.
- [163] Shinji Toda and Ross S. Stein. Did stress triggering cause the large off-fault aftershocks of the 25 March 1998 $m_w=8.1$ Antarctic plate earthquake? *Geophysical Research Letters*, 27(15):2301–2304, August 2000.
- [164] L. L. Trulla, A. Giuliani, J.P. Zbilut, and Jr. C.L. Webber. Recurrence quantification analysis of the logistic equation with transients. *Physics Letters A*, 223:255–260, December 1996.
- [165] D. L. Turcotte, W. I. Newman, and A. Gabrielov. A statistical physics approach to earthquakes. In John B. Rundle, Donald L. Turcotte, and William Klein, editors, *GeoComplexity and the Physics of Earthquakes*, number 120 in Geophysical Monograph series, pages 83–96. AGU Books Board, 2000.
- [166] Donald L. Turcotte. *Fractals and Chaos in Geology and Geophysics*. Cambridge University Press, 1997.
- [167] G.L. Vasconcelos. First-order phase transition in a model for earthquakes. *Physical Review Letters*, 76(25):4865–8, 1996.
- [168] G.L. Vasconcelos, M. de Sousa Vieira, and S.R. Nagel. Phase transitions in a spring-block model of earthquakes. *Physica A*, 191(1-4):69–74, 1992.

- [169] Larry Wall, Tom Christiansen, and Randal L. Schwartz. Programming Perl. O'Reilly & Associates, 1996.
- [170] Jeen-Hwa Wang. Scaling of synthetic seismicity from a one-dimensional dissipative, dynamic lattice model. Physics Letters A, 191(5-6):398–402, 1994.
- [171] Jeen-Hwa Wang. Effect of frictional healing on the scaling of seismicity. Geophysical Research Letters, 24(20):2527–30, 1997.
- [172] Jeen-Hwa Wang. On the frequency distribution of rupture lengths of earthquakes synthesized from a one-dimensional dynamical lattice model. Journal of Physics of the Earth, 45(5):363–81, 1997.
- [173] Jeen-Hwa Wang. Instability of a two-dimensional dynamic spring-slider model of an earthquake fault. Geophysical Journal International, 143(2):389–94, 2000.
- [174] Steven N. Ward. A synthetic seismicity model for southern California: Cycles, probabilities, and hazard. Journal of Geophysical Research, 101(B10):22393–22418, October 1996.
- [175] Eric Weisstein. Eric Weisstein's world of mathematics. <http://mathworld.wolfram.com>, 2000.
- [176] Donald L. Wells and Kevin J. Coppersmith. New empirical relationships among magnitude, rupture length, rupture width, rupture area, and surface displacement. Bulletin of the Seismological Society of America, 84(4):974–1002, August 1994.
- [177] S. G. Wesnousky. Seismicity as a function of cumulative geologic offset: Some observations from southern California. Bulletin of the Seismological Society of America, 80(5):1374–1381, October 1990.
- [178] S. G. Wesnousky, C. H. Scholz, K. Shimazaki, and T. Matsuda. Earthquake frequency distribution and the mechanics of faulting. Journal of Geophysical Research, 88(B11):9331–9340, November 1983.
- [179] Steven G. Wesnousky. Earthquakes, quaternary faults, and seismic hazard in California. Journal of Geophysical Research, 91(B12):12587–12631, November 1986.
- [180] Steven G. Wesnousky. The Gutenberg-Richter or characteristic earthquake distribution, which is it? Bulletin of the Seismological Society of America, 84(6):1940–1959, December 1994.
- [181] K. Wiesenfeld, Chao Tang, and P. Bak. A physicist's sandbox. Journal of Statistical Physics, 54(5-6):1441–58, 1989.
- [182] Stephen Wolfram. Cellular Automata and Complexity. Addison-Wesley, 1994.
- [183] H.-J. Xu, D. Sornette, J.B. Rundle, W. Klein, S. Gross, and D.L. Turcotte. Non-Boltzmann fluctuations in numerical simulations of nonequilibrium lattice threshold systems [and reply]. Physical Review Letters, 78(19):3797–8, 1997.
- [184] Huang-Jian Xu and L. Knopoff. Periodicity and chaos in a one-dimensional dynamical model of earthquakes. Physical Review E, 50(5):3577–81, 1994.
- [185] Teruo Yamashita. Mechanical effect of fluid migration on the complexity of seismicity. Journal of Geophysical Research, 102(B8):17797–17806, August 1997.
- [186] Joseph P. Zbilut and Jr. Charles L. Webber. Embeddings and delays as derived from quantification of recurrence plots. Physics Letters A, 171:199–203, 1992.

- [187] Wu Zhong-Liang. Frequency-size distribution of model seismicity in a statistical mechanical model of earthquakes. Chinese Physics Letters, 16(6):458–60, 1999.

Appendix A

Co-authored Papers

John Rundle, Eric Preston, Seth McGinnis, and W. Klein. *Why Earthquakes Stop: Growth and Arrest in Stochastic Fields*, **Phys. Rev. Letters** v. 80 no. 25, pp. 5698-5701, June 1998

K.F. Tiampo, J.B. Rundle, S. McGinnis, S.J. Gross, and W. Klein. *Observation of Systematic Variations in Non-local Seismicity Patterns from Southern California*, in **GeoComplexity and the Physics of Earthquakes**, AGU Books Board, pp. 211-218, 2000

K.F. Tiampo, J.B. Rundle, S. McGinnis, and W. Klein. *Pattern Dynamics and Forecast Methods in Seismically Active Regions*, to appear in **Pure and Applied Geophysics**, 2001

K.F. Tiampo, J.B. Rundle, S. Gross, and S. McGinnis. *Parallelization of a Large-Scale Computational Earthquake Simulation Program*, submitted to **Concurrency and Computation: Practice and Experience**, 2001

P.B. Rundle, J.B. Rundle, K.F. Tiampo, J.S. de sa Martins, S. McGinnis, and W. Klein. *Nonlinear Network Dynamics on Earthquake Fault Systems*, submitted to **Phys. Rev. Letters**, 2001

Why Earthquakes Stop: Growth and Arrest in Stochastic Fields

John Rundle

Geophysics Program, CIRES & Department of Physics, Colorado Center for Chaos & Complexity, University of Colorado, Boulder, Colorado 80309

Eric Preston

Department of Physics & CIRES, Colorado Center for Chaos & Complexity, University of Colorado, Boulder, Colorado 80309

Seth McGinnis

Geophysics Program and CIRES, Colorado Center for Chaos & Complexity, University of Colorado, Boulder, Colorado 80309

W. Klein

Department of Physics, Boston University, Boston, Massachusetts 02215

(Received 21 November 1997; revised manuscript received 13 March 1998)

Classical theory predicts that earthquakes growing in a homogeneous stress field should not arrest until the fault boundaries are encountered. However, earthquakes on natural faults, where stresses are heterogeneous, are observed over a wide range of sizes. Here we suggest that heterogeneity should be characterized by the Hausdorff dimension H of the walk associated with a stochastic stress difference field. The critical value for arrest, $H = 0.5$, corresponds to a Brownian walk through the stress difference field. [S0031-9007(98)06458-8]

PACS numbers: 91.30.Px

Why do small earthquakes of magnitude $M \sim 3$ not continue growing to the size of a great event of magnitude $M \sim 9$ or larger? According to the classical theory of tensile fracture for elastic solids developed by Griffith [1], as applied to shear fracturing in earthquakes [2–5], an earthquake growing in a homogeneous stress field will not arrest until the boundaries of the fault are encountered. However, a wide range of earthquake sizes are commonly observed on the same fault in Nature [5,6]. The paradox arises because a growing Griffith-type rupture increasingly concentrates stress at the crack edges, making further growth more likely [7]. For a rupture to arrest, there must be a process that balances the increasing stress concentration.

In the earthquake literature, the structures held to be responsible for arrest are “barriers” and “asperities,” which are regions of faults where pinning forces are presumed to be strong [8,9]. As the growing rupture encounters these structures, the Griffith driving force G may decrease below the value needed to sustain growth [10]. Rupture advance slows, and a healing wave arrives at the rupture front, terminating further advance [3]. In many ways, this picture is similar to the growth and arrest of depinning transitions in charge density waves and superconductors [11], and magnetized domains in disordered ferromagnets [12]. Previous work has shown that the problem of fracture nucleation is isomorphic to the classical Gibbs theory of droplet nucleation [13–19], in which the crack surface energy is seen to play the role of a “surface tension.”

Given this picture, the major problem at issue is which statistical distributions of disordered pinning points lead

to rupture (“slip droplet”) arrest, and which allow continued growth. It is also interesting that the conventional Griffith-Gibbs theory contains information about nucleation and initial growth (in homogeneous fields), but no information about self-arrest (in heterogeneous and stochastic fields). We are therefore motivated to construct a theory that enables predictions for growth and arrest of earthquakes in terms of the space (\mathbf{x}) and time (t) varying statistical properties of the stress field $\sigma(\mathbf{x}, t)$ and the disordered (depinning) static frictional stress threshold $\sigma^F(\mathbf{x}, t)$ along the fault. Growth or arrest depends on the statistical properties of the difference field $\Sigma(\mathbf{x}, t) = \sigma^F(\mathbf{x}, t) - \sigma(\mathbf{x}, t)$. Here, regions of large $\Sigma(\mathbf{x}, t)$ could be called barriers, or asperities.

We describe a “stochastic Griffith theory” (SGT) in which the arrest of a quasistatically growing shear crack (earthquake) arises from the spatially averaged, stochastic properties of $\Sigma(\mathbf{x}, t)$. This theory has a positive definite scaling term that involves a Hausdorff dimension H . If $H > 0.5$, the value for Brownian motion, the growing crack must eventually arrest, even in the thermodynamic limit. Alternatively, if $\Sigma(\mathbf{x}, t)$ has a red (blue) spectrum, the crack will arrest (not arrest). The underlying reason for arrest is that the crack can no longer grow as a classical object.

Griffith theory.—The Griffith [1,7] idea of tensile fracture is based upon the construction of an energy change $F = -\Delta E_{el} \Delta \sigma^2 \lambda^2 + 2a_0 \lambda$ due to a circular tensile crack of radius λ . The crack is subject to a tensile stress p , leading to a spatially constant static stress drop $\Delta \sigma = p - \sigma^R$, where σ^R is the residual stress that depends on the dynamic (sliding) friction; a_0 is the

surface energy associated with the creation of a unit of surface on each side of the crack face; and ΔE_{el} is an elastic energy decrease, a numerical function of elastic moduli, sample geometry, and the experimental configuration. $\Delta E_{\text{el}} \propto -\Delta\sigma^2/\pi < 0$, and represents the decrease in elastic (bulk) energy per unit surface area of crack.

Extension of the crack is a competition between the energy input needed to separate the medium at the crack tip (a_0) and the energy released upon growth of the total surface area (ΔE_{el}). In the Griffith model, the crack tip is associated with a stress singularity, which can be removed by introducing a Barenblatt-Dugdale zone of adhesion [7]. The expression for F implies a critical value $\lambda_c = \Delta E_{\text{el}} \Delta \sigma^2 / a_0$ obtained by extremizing F . For a given value of stress drop $\Delta\sigma$, crack lengths $\lambda < \lambda_c$ are stable, whereas cracks with $\lambda > \lambda_c$ are unstable [1,7]. Self-arrest of the crack should depend on spatial variation of $\sigma^F(\mathbf{x}, t)$, which does not appear in the conventional Griffith theory. It is this effect that we address below.

Stochastic Griffith theory (SGT).—For a circular crack of radius λ , define $f_g(r) = \Delta E_{\text{el}} + a_0/\pi r$, the Griffith energy density. F is obtained by integrating $f_g(r)$:

$$\begin{aligned} F &= \int_0^{2\pi} \int_0^\lambda f_g(r) r dr = \int_0^{2\pi} \int_0^\lambda \left(\Delta E_{\text{el}} + \frac{a_0}{\pi r} \right) r dr \\ &= \Delta E_{\text{el}} \Delta \sigma^2 \lambda^2 + 2a_0 \lambda. \end{aligned} \quad (1)$$

Suppose now that a_0 varies with position \mathbf{x} about arbitrary \mathbf{x}_0 , $a_0 \rightarrow a(\mathbf{x}, \mathbf{x}_0)$, and that $a(\mathbf{x}, \mathbf{x}_0)$ is a stochastic variable. For fields $a(\mathbf{x}, \mathbf{x}_0)$ having a normalized probability distribution $P\{a(\mathbf{x}, \mathbf{x}_0)\}$, the statistical average over the field can be calculated

$$\langle a \rangle_r = \int_{-\infty}^{\infty} a(\mathbf{x}, \mathbf{x}_0) dP\{a(\mathbf{x}, \mathbf{x}_0)\}. \quad (2)$$

SGT for the circular crack is obtained from the classical Griffith theory by the replacement $a_0 \rightarrow \langle a \rangle_r$, where $r = |\mathbf{x} - \mathbf{x}_0|$:

$$f_{\text{gs}}(r) = \Delta E_{\text{el}} + \frac{\langle a \rangle_r}{\pi r}. \quad (3)$$

If variations in $\Sigma(\mathbf{x}, t)$ are to lead to arrest of the crack, $a(\mathbf{x}, \mathbf{x}_0)$ must be related to the square of the field $\Sigma(\mathbf{x}, t)$ divided by a modulus, taking account of physical units. The field $a(\mathbf{x}, \mathbf{x}_0)$ must depend on the spatial mean $\Sigma_m(t)$ of $\Sigma(\mathbf{x}, t)$, because if $\Sigma_m(t) = 0$, every site would be at failure. Also, $a(\mathbf{x}, \mathbf{x}_0)$ should depend on stochastic fluctuations about $\Sigma_m(t)$ through an integral of $\Sigma(\mathbf{x}, t)$ that we call W , since the process of crack propagation can be viewed as a process of “integrating” the Σ -noise field. As the crack extends from \mathbf{x}_1 to \mathbf{x}_2 to \dots to \mathbf{x}_n , it must overcome the stress difference $\Sigma(\mathbf{x}_1, t) + \Sigma(\mathbf{x}_2, t) + \dots + \Sigma(\mathbf{x}_n, t)$.

From these considerations, we have

$$\langle a \rangle_r = \frac{1}{2K_L} \langle \Theta^2 \rangle = \frac{1}{2K_L} \left\{ \int_{-\infty}^{\infty} \Theta^2 dP\{W\} \right\}, \quad (4)$$

where the random field Θ depends on $\Sigma_m(t)$ and the r -dependent “walk functional” $W(r, t)$:

$$\begin{aligned} \Theta &= \Sigma_m(t) + W(r, t) \\ &= \Sigma_m(t) + \frac{1}{b} \int_{\mathbf{x}_0}^{\mathbf{x}} \{ \Sigma(\mathbf{x}', t) - \Sigma_m(t) \} d\mathbf{x}'. \end{aligned} \quad (5)$$

The integral is taken over the path of shortest length between \mathbf{x}_0 and \mathbf{x} , and b is a spatial coarse graining length that we take as $b = 1$.

Using the normalized probability distribution $P\{W\}$ for the spatially random field W , we combine (4) and (5) to obtain

$$\langle a \rangle_r = \frac{[\Sigma_m(t)]^2}{2K_L} + \frac{\text{Var}\{W(r, t)\}}{2K_L b^2}. \quad (6)$$

Here K_L is a modulus of elasticity, giving to $\langle a \rangle_r$ the units of an energy density. The first term in (6) represents a contribution to the surface energy due to the spatial mean $\Sigma_m(t)$, and gives rise to a stochastic term representing a growth barrier. The second term represents fluctuations about the mean.

Under general conditions, an integral W of $\Sigma(\mathbf{x}, t)$ about \mathbf{x}_0 will be an r -dependent fractional Brownian motion (fBm) [20–22]. Note that the fBm associated with the two-dimensional noise $\Sigma(\mathbf{x}, t)$, call it $Z(\mathbf{x}, \mathbf{x}_0, t)$, cannot be uniquely reconstructed from $\Sigma(\mathbf{x}, t)$ since the two-dimensional integration paths are not specified. However, we assume that the statistical scaling properties of $Z(\mathbf{x}, \mathbf{x}_0, t)$, e.g., can be uniquely retrieved. This is reasonable since the power spectral exponent of an n -dimensional noise is uniquely related to the exponent of the associated n -dimensional walk.

If $W(r, t)$ is a simple affine fBm walk, the probability density $dP\{W(r, t)\}$ then has properties similar to a Gaussian [21], with a variance

$$\text{Var}\{W(r, t)\} \sim r^{2H}. \quad (7)$$

Thus a simple affine scaling behavior of $\langle a \rangle_r$ arises. The integral in (4) can be related to a more familiar Feynman-Kac path integral [17].

Combining Eqs. (1)–(7), we find a stochastic Griffith energy F_s for the circular shear crack:

$$F_s = -|\Delta E_{\text{el}}|\lambda^2 + 2D\lambda + 2C\lambda^{2H+1}, \quad (8)$$

where

$$D = \frac{\pi}{K_L} [\Sigma_m(t)]^2, \quad C = \frac{\pi}{(2H+1)K_L} \text{Var}\{\Sigma(\mathbf{x}, t)\}. \quad (9)$$

In (8), small $\Sigma_m(t)$ corresponds to a low growth barrier, so that high stress regions can easily break away into larger events. When $\Sigma_m(t)$ is large, the growth barrier is high and breakaway is unlikely. In the third term, a value $H < 0.5$ implies that events with large λ will break away and arrest only at the system boundaries. However, a value $H > 0.5$ can lead to arrest of the growing shear

crack if the prefactor C is large enough. The first and second terms in (8) represent the usual Griffith-type energy “source” and “sink” for crack extension, and the third term represents an additional energy sink that arises from fluctuations in $\Sigma(\mathbf{x}, t)$.

Simulations.—We tested these ideas using simulations of the traveling density wave model for earthquakes [14,16]. In this model, sliding on a fault is driven by tectonic plate motion at a rate V :

$$\begin{aligned} \frac{\partial \phi(\mathbf{x}, t)}{\partial t} = & \left\{ \int T(\mathbf{x} - \mathbf{x}') \phi(\mathbf{x}', t) d^2 \mathbf{x}' \right\} \\ & - 2\gamma\kappa \sin\{\kappa[\phi(\mathbf{x}, t) + Vt + \varepsilon(\mathbf{x}, t)]\} \\ & - h + \eta(\mathbf{x}, t). \end{aligned} \quad (10)$$

The Langevin equation (10) is solved by Newton’s method to a tolerance $\eta = 0.05$ to obtain the slip $s(\mathbf{x}, t)$ at each site from the slip deficit $\phi(\mathbf{x}, t) = s(\mathbf{x}, t) - Vt$. A sudden, large, positive change in $s(\mathbf{x}, t)$ at one or more sites simultaneously represents an earthquake.

The elastic interaction $T(\mathbf{x} - \mathbf{x}')$ between two sites \mathbf{x} and \mathbf{x}' is described by a Green’s function having the form $K_C/|\mathbf{x} - \mathbf{x}'|^3$, $K_C = 1$, truncated beyond $|\mathbf{x} - \mathbf{x}'| = 3$. The system is loaded by springs with constant $K_L = 1$ at a rate $V = 0.01$. The self-interaction is given by $K_L +$ the zeroth moment of $T(\mathbf{x} - \mathbf{x}')$. Annealed abrasion and wear [14,16] of the surface are described by the random parameter $\varepsilon(\mathbf{x}, t)$ on $[0, 2\pi]$, and $h(\mathbf{x}, t)$ has a correlated distribution on $[0, 0.1]$. The amplitude γ and wave number κ of the cohesive force are $\gamma = 10$, $\kappa = 1$. $\sigma^F(\mathbf{x}, t)$ is the local limit of stability of a site, and is estimated by extremizing the right hand side of (10). In these simulations, the spatially averaged residual stress σ^R can be measured. Its value is higher than the “dynamic” (or *point*) frictional residual stress due to stress redistribution and healing during the event.

Results on a 64×64 lattice with open boundary conditions are shown in Fig. 1. The events shown are all substantially smaller than the size of the lattice, and

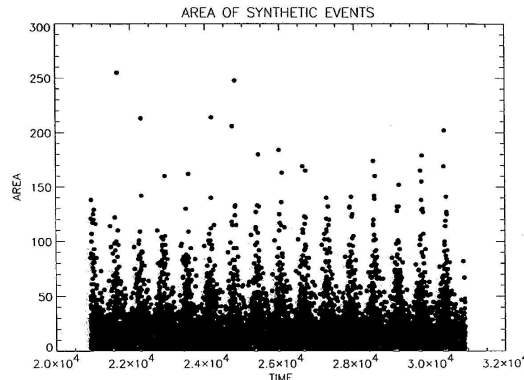


FIG. 1. Area of synthetic earthquakes as a function of time.

thus should be only weakly influenced by finite size effects. About 16 “earthquake cycles” can be seen, with “foreshocks,” a “main shock,” and “aftershocks.” There is clearly a “magnitude gap” between the main shock and smaller events shown in Fig. 1, a behavior that is also seen in real earthquakes [5]. Some earthquake cycles in Fig. 1 do not have a main shock, but instead show “swarmlike” behavior [5]. As described in Ref. [18], earthquakes are caused by the appearance of a low $\Sigma(\mathbf{x}, t)$ region that becomes unstable when foreshocks induce a decrease in the effective rate of stress loading. As shown here, whether the droplets are contained, or break away to form larger main shocks will depend on the statistics of the $\Sigma(\mathbf{x}, t)$ fields.

In Fig. 2 we analyze the statistics of the $\Sigma(\mathbf{x}, t)$ fields generated during the simulations shown in Fig. 1. These events have irregular, but still compact, shapes. We constructed walk functionals for the two-dimensional $\Sigma(\mathbf{x}, t)$ field obtained from simulations, averaging over 50 realizations near time step $t = 20000$ shown in Fig. 1. In Fig. 2 we show the results of these methods applied to (i) the two-dimensional $\Sigma(\mathbf{x}, t)$ field as well as (ii) a two-dimensional field of synthetically generated white noise. Slopes of lines on this plot are $2H - 1$, so that $H = 0.5$ is represented by a horizontal line. In Fig. 3 we construct the entire F_s function by direct integration of simulation data to obtain terms equivalent to the second and third terms in (8), but making no assumptions about Gaussian statistics or crack shape. In these plots, we used $|\Delta E_{el}|$ as a parameter to construct an elastic energy release term in which the area of the failed sites for each event in the simulation multiplies $-|\Delta E_{el}|$. From the top, these curves have the values $|\Delta E_{el}| = 17, 18, 19, 20$. For comparison, measured values of $|\Delta E_{el}|$ for the largest events in the simulation ($>$ size 50) have $|\Delta E_{el}| \sim 18$.

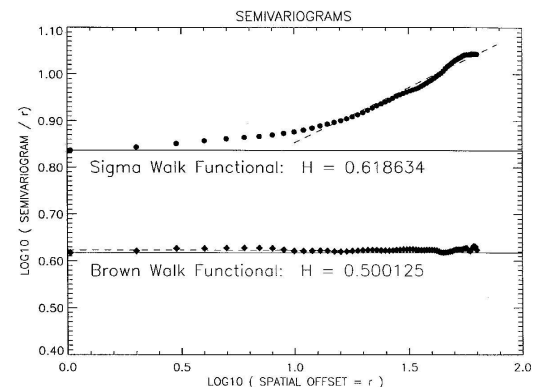


FIG. 2. Lattice average of walk functional (semivariogram), divided by r , for both Σ field from simulations (top) and two-dimensional white noise (bottom). Average of walk functional for white noise gives Brownian fBm.

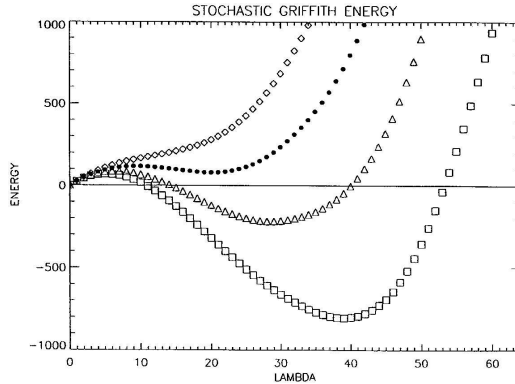


FIG. 3. Complete stochastic Griffith energy parametrized by four values for elastic energy decrease.

Clearly, high stress droplets will not break away if they nucleate and decay on a part of the F_s - λ curve that is increasing with λ . Evidently the magnitude gap between foreshocks/aftershocks and the main shock arises as a result of the statistical “spinodal” for large enough values of the statistical “scaling field” $-|\Delta E_{el}|$.

Research by J. B. R. and E. P. has been supported by NSF Grant No. EAR-9526814 (theory), and by U.S. DOE Grant No. DE-FG03-95ER14499 (simulations), to University of Colorado. Work by S. M. has been supported by NASA Grant No. NGT5-50102 to University of Colorado. Research by W. K. has been supported by U.S. DOE Grant No. DE-FG02-95ER14498 to Boston University. The authors also acknowledge support from the Colorado Center for Chaos & Complexity, and conversations with D. L. Turcotte, S. Gross, J. Goldstein, and V. K. Gupta.

- [1] A. A. Griffith, Philos. Trans. R. Soc. London A **221**, 163 (1921).
- [2] V. C. Li, in *Fracture Mechanics of Rock* (Academic Press, London, 1987), Chap. 9, pp. 351–428.

- [3] T. H. Heaton, Phys. Earth Planet. Inter. **64**, 1–20 (1993).
- [4] Y. Ben-Zion and J. R. Rice, J. Geophys. Res. **98**, 14109 (1993).
- [5] C. H. Scholz, *The Mechanics of Earthquakes and Faulting* (Cambridge University Press, Cambridge, England, 1990).
- [6] J. B. Rundle and W. Klein, Rev. Geophys. Space Phys. Suppl. and Quad. Rept. to the IUGG and AGU **1991–1994**, 283–286 (1995).
- [7] M. F. Kaninen and C. H. Popelar, *Advanced Fracture Mechanics* (Oxford University Press, Oxford, England, 1985).
- [8] T. Lay, H. Kanamori, and L. Ruff, Earthquake Pred. Res. **1**, 3–71 (1982).
- [9] K. Aki, J. Geophys. Res. **84**, 6140 (1979).
- [10] B. V. Kostrov and S. Das, *Principles of Earthquake Source Mechanics* (Cambridge University Press, Cambridge, England, New York, 1988).
- [11] D. S. Fisher, K. Dahmin, S. Ramanathan, and Y. Ben-Zion, Phys. Rev. Lett. **78**, 4885 (1997).
- [12] H. L. Richards, S. W. Sides, M. A. Novotny, and P. A. Rikvold, J. Magn. Magn. Mater. **150**, 37 (1995).
- [13] J. B. Rundle and W. Klein, Phys. Rev. Lett. **63**, 171 (1989).
- [14] J. B. Rundle, W. Klein, and S. Gross, Phys. Rev. Lett. **76**, 4285 (1996).
- [15] W. Klein, J. B. Rundle, and C. D. Ferguson, Phys. Rev. Lett. **78**, 3793 (1997).
- [16] J. B. Rundle, W. Klein, S. Gross, and C. D. Ferguson, Phys. Rev. E **56**, 293 (1997).
- [17] E. Preston, S. McGinnis, J. B. Rundle, and W. Klein (to be published).
- [18] J. Goldstein, H. Gould, W. Klein, and J. B. Rundle (to be published).
- [19] C. Sammis, D. Sornette, and H. Saleur, in *Reduction and Predictability of Natural Disasters*, Proceedings of the Santa Fe Institute, edited by J. B. Rundle, D. L. Turcotte, and W. Klein (Addison-Wesley, Reading, MA, 1996), Chap. XXV, pp. 143–156.
- [20] R. F. Voss, in *The Science of Fractal Images*, edited by H.-O. Peitgen and D. Saupe (Springer-Verlag, Berlin, 1988), Chap. 1, pp. 21–70.
- [21] J. Feder, *Fractals* (Plenum, New York, 1988).
- [22] B. Malamud and D. L. Turcotte, Cornell University report, 1998.

Observation of Systematic Variations in Non-Local Seismicity Patterns from Southern California

K. F. Tiampo, J. B. Rundle, S. McGinnis, W. Klein, and S. J. Gross.

We have discovered systematic space-time variations in the seismicity from southern California using a new technique. Our procedure is based upon the idea that seismic activity corresponds geometrically to the rotation of a pattern state vector in the high-dimensional correlation space spanned by the eigenvectors of a correlation operator. Using our technique it is possible to isolate emergent regions of coherent, correlated seismicity. Analysis of data taken only up to December 31, 1991 reveals that the appearance of the coherent correlated regions is often associated with the future occurrence of major earthquakes in the same areas. These major earthquakes include the 1992 Landers, the 1994 Northridge, and the 1999 Hector Mine events.

KEYWORDS: Earthquakes, Modeling, Threshold Systems, Nonequilibrium Systems, Earthquake Dynamics, Nonlinear Dynamics, Seismic Prediction.,

1. INTRODUCTION

Earthquakes strike without warning, causing great destruction and loss of life. A poignant example is the recent Izmit, Turkey, earthquake of August 17, 1999, which resulted in the deaths of over 17,000 persons. Other recent large events include the $M \sim 7.6$ Taiwan earthquake of September 20, 1999, whose death toll now exceeds 2000 persons, the $M \sim 7.3$ Landers, California, event of June 28, 1992, and the $M \sim 7.1$ Hector Mine, California, earthquake of October 16, 1999. Many similar examples have been documented over the course of time [Richter, 1958; Scholz, 1990].

While a long-sought goal of earthquake research has been the reliable forecasting of these great events, very little progress has been made in developing a successful, consistent methodology [Geller *et al.*, 1997; Kanamori, 1981]. Despite the fact that the largest of these events span distances of more than 500 km, no reliable precursors have ever been detected. It is difficult for most scientists to understand why events of this magnitude are not preceded by at least some causal process, which would presumably imply the existence of premonitory signals. In the past, the search for such signals understandably focused on local regions near the earthquake source. Many of these techniques require intensive and expensive monitoring efforts [Geller *et al.*, 1997]. Various patterns of seismic activity centered on the source region have been proposed, including phenomena such as characteristic earthquakes [Schwartz, *et al.*, 1981; Ellison and Cole, 1997], Mogi donuts [Mogi, 1969; Mogi, 1977], seismic gaps [Haberman, 1981; House *et al.*, 1981], precursory quiescence [Knopoff and Yamashita, 1988; Wyss and Haberman, 1988; Wyss *et al.*, 1996; Kato *et al.*, 1997], precursory activation [Evison, 1977; Shaw *et al.*, 1992; Dodge *et al.*, 1996], Time-to-Failure and Log-Periodic precursory distributions [Bufo *et al.*, 1993; Saleur *et al.*, 1996; Gross and Rundle, 1998], temporal clustering [Frolich, 1987; Dodge *et al.*, 1995; Rundle *et al.*, 1997], and earthquake triggering over large distances [Hill *et al.*, 1993; King *et al.*, 1994; Pollitz and Sacks, 1997]. Since these hypothesized patterns are localized on the eventual source region, the fact that one must know or suspect where the event will occur before they can be applied is a major drawback to their implementation.

Recent observational evidence has suggested that earthquakes can be characterized by strongly correlated dynamics [Bufo and Varnes, 1993; Press and Allen, 1995; Knopoff *et al.*, 1996; Bowman *et al.*, 1998; Brehm and Braile, 1998; Gross and Rundle, 1998; Brehm and Braile, 1999]. Realistic numerical simulations of earthquakes also suggest that space-time pattern structures are non-local in character, another consequence of strong correlations in the

underlying dynamics [Rundle, 1988; Rundle et al., 2000]. Variables in many of these dynamical systems can be characterized by a phase function that involves both an amplitude and a phase angle. The simulations have suggested that seismicity can be described by phase dynamics [Mori and Kuramoto, 1998; Rundle et al. 2000]. Here, the important changes in seismicity are associated primarily with rotations of the vector phase function in a high-dimensional correlation space [Fukunaga, 1970; Holmes et al., 1996]. Changes in the amplitude of the phase function are unimportant, or not relevant. The most familiar examples of these are quantum mechanical systems, but examples also exist in the macroscopic world, including weak turbulence in fluids and reaction-diffusion systems [Mori and Kuramoto, 1998].

These results suggest that space-time patterns of seismic activity directly reflect the existence of space-time correlations in the underlying stress and strain fields. Previous research has indicated that the development of correlations in the stress field is a necessary precondition for the occurrence of large earthquakes [Rundle et al., 2000]. The correlation patterns, which represent emergent space-time structures, evidently form and evolve over time intervals of years preceding the main shock. Longer time intervals and larger correlated areas are associated with larger main shocks. The probability for observing such an anomalous correlation can be computed directly from the simulated seismicity data using the square of the anomalous pattern state vector [Rundle et al., 2000]. These are the methods that we use in the present analysis of data from southern California.

We test the hypothesis that anomalous, non-local space-time patterns and correlations associated with recorded events can be detected in real seismicity data years prior to the main shock. The seismicity data employed in our analysis is taken from existing observations in southern California between the years 1932 and the present. Using only a subset of this data covering the period from January 1, 1980 through December 31, 1991, we compute the probability for finding an anomalous spatial correlation at all sites in southern California over several intervals preceding December 31, 1991. We then superimpose on this map the locations of main shocks larger than 5.0 that occurred between January 1, 1992 and November 1, 1999, that is, the ~ 8 years following the time interval from which we computed the probabilities. We observe a striking correspondence between regions of increased probability and the location of the recent main shocks, tending to support the results first observed in our simulations. In particular, we note that the epicenter of the recent October 16, 1999, $M \sim 7.0$ Hector Mine earthquake in southern California occurred at a location that is identified as one of the high probability locations. From the size of the candidate source regions, the magnitude of the possible events can be estimated as well. A likelihood ratio test of the method on both the real southern California seismicity catalog, and a second catalog in which times of events had been reassigned randomly, indicates that the method does find coherent correlated structures in the data.

2. METHOD

As mentioned above, our method is based primarily on the idea that the time evolution of seismicity can be described by phase dynamics. We therefore define a real-valued seismic phase function, $S(x_i, t_0, t)$, a unit vector whose tail is fixed at the origin, and whose head is constrained to move on the unit sphere in an N -dimensional (N large) correlation space. $S(x_i, t_0, t)$ is a non-local function, and is the mathematical embodiment of the idea that earthquake fault systems are characterized by strongly correlated dynamics. Geometrically, time evolution of $S(x_i, t_0, t)$ corresponds to rotations about the origin in a series of correlated random walk increments through small solid angles on the unit sphere. Formation of an emergent correlated pattern in seismic activity over a time interval Δt is associated with rotation of the \hat{S} -vector in a persistent direction. When these persistent directions are examined, previously undetectable, systematic variations in seismicity become evident, as described in Rundle et al., 2000.

For our analysis, the phase function $S(x_i, t_0, t)$ characterizes the seismic activity in southern California between 32° and 37° latitude, and -115° to -122° longitude. It should also be noted that while our initial choice for total area was relatively arbitrary, we have varied the region size in recent analyses, by as much as a factor of two, and have found it to make little difference in the final results. In addition, the catalog was not declustered, as it is the correlations in the data set,

the best known examples of which are local patterns of seismic activity or quiescence, that are identified by this method. Since it is well known that seismicity in active regions is a noisy function [Kanamori, 1981], we work with temporal averages of seismic activity. The geographic area is partitioned into N square regions approximately 11 km on a side, centered on a point \mathbf{x}_i . Within each box, a time series is defined using the Caltech seismic catalog obtained from the online SCEC database. For southern California, the instrumental data begins in 1932 and extends to the present. The instrumental coverage was sparse in the early years, and is substantially more complete today. In general, the seismicity catalog is considered complete for magnitudes $M \geq 3$.

We define the activity rate $\psi_{obs}(\mathbf{x}_i, t)$ as the number of earthquakes per unit time, of any size, within the box centered at \mathbf{x}_i at time t . The geographic region that $S(\mathbf{x}_i, t_0, t)$ represents is taken large enough so that seismic activity can be considered an incoherent superposition of phase functions. The seismicity function $S(\mathbf{x}_i, t_0, t)$ is then defined as the time average at \mathbf{x}_i of $\psi_{obs}(\mathbf{x}_i, t)$ over the period (t_0, t) ,

$$S(\mathbf{x}_i, t_0, t) = \frac{1}{(t - t_0)} \int_{t_0}^t \psi(\mathbf{x}_i, t) dt.$$

Events included in $\psi_{obs}(\mathbf{x}_i, t)$ or $S(\mathbf{x}_i, t_0, t)$ are restricted to those for which the magnitude $M \geq 3$, so as to ameliorate sensitivity to changes in detection thresholds through time.

Considered as a function of the N locations \mathbf{x}_i , $S(\mathbf{x}_i, t_0, t)$ represents a vector in N-dimensional correlation space with its tail fixed at the origin. The vector space is spanned by the eigenvectors, or eigenpatterns, of an N-dimensional, Karhunen-Loeve correlation matrix $C(\mathbf{x}_i, \mathbf{x}_j)$. The elements of $C(\mathbf{x}_i, \mathbf{x}_j)$ are obtained by cross-correlating a set of N seismic activity time series associated with each box \mathbf{x}_i [Rundle et al., 2000]. As an aside, we note that purely random processes are characterized only by an amplitude in correlation space, not by any preferred direction. This follows from the fact that if the time series defining $C(\mathbf{x}_i, \mathbf{x}_j)$ were uncorrelated, $C(\mathbf{x}_i, \mathbf{x}_j)$ would be the identity matrix.

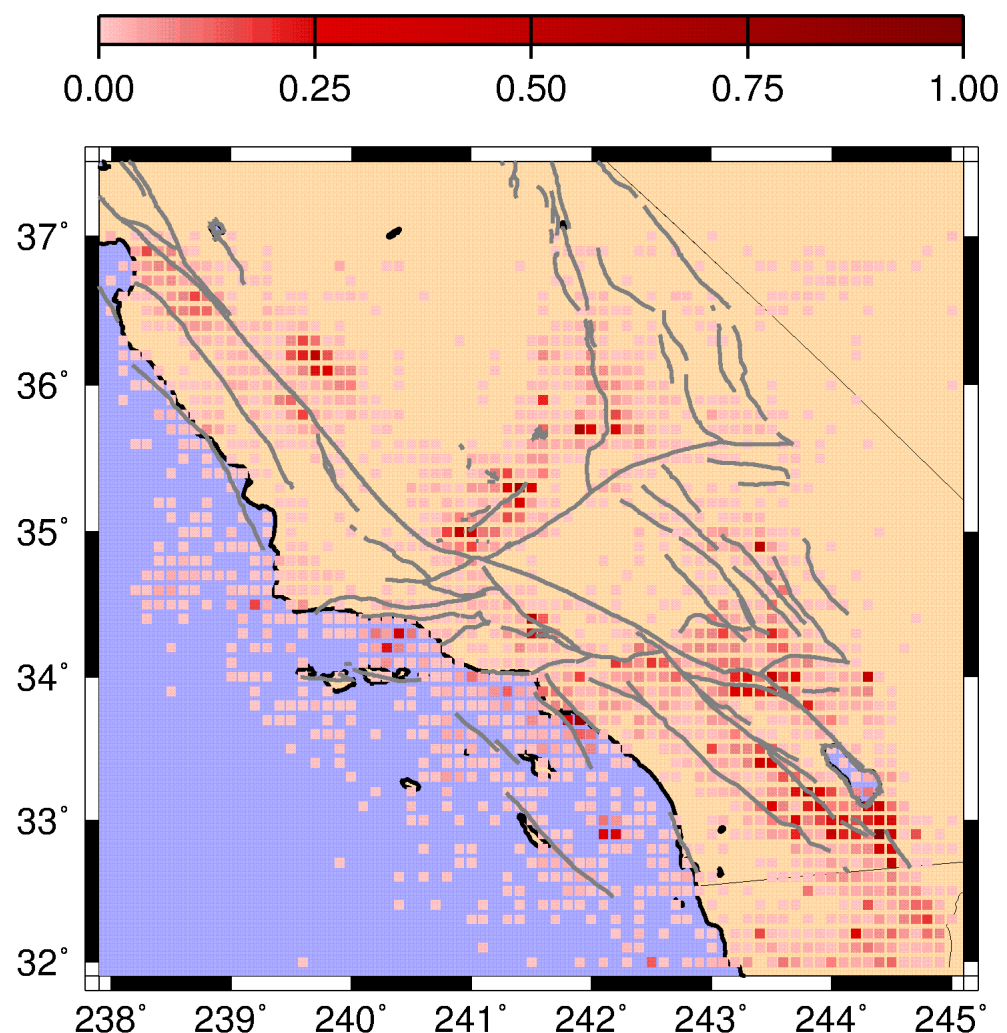
Figure 1 shows one example of $S(1932, 1991)$ superimposed on a map of southern California. It is clear that $S(1932, 1991)$ is an unremarkable function, and appears to show little evidence of any phenomena precursory to the $M \sim 7.3$ Landers, California event that occurred on June 28, 1972.

In the past [Scholz, 1990], investigators have generally focused on attempts to detect systematic variations in the both the amplitude and phase of $S(\mathbf{x}_i, t_0, t)$, or alternatively the amplitude and phase variations in the corresponding rate of seismic activity $R(\mathbf{x}_i, t)$. Following our assumption that seismicity is characterized by phase dynamics, we define $S(\mathbf{x}_i, t_0, t)$ as the unit vector pointing in the direction of $S(\mathbf{x}_i, t_0, t)$ using an L2 norm. As an incoherent superposition of functions must have zero mean, we remove the spatial mean of $S(\mathbf{x}_i, t_0, t)$ and create a unit vector by dividing by the standard deviation. Therefore,

$$\hat{S}(\mathbf{x}_i, t_0, t) = \frac{[S(\mathbf{x}_i, t_0, t) - \bar{S}(\mathbf{x}_i, t_0, t)]}{\sigma},$$

where $\bar{S}(\mathbf{x}_i, t_0, t) = \frac{1}{N} \int_{allx} S(\mathbf{x}_i, t_0, t) dx$, the spatial mean of $S(\mathbf{x}_i, t_0, t)$, and

$$\sigma^2 = \frac{1}{N} \int_{allx} [\hat{S}(\mathbf{x}_i, t_0, t) - \bar{S}(\mathbf{x}_i, t_0, t)]^2 dx,$$



the variance of $S(x_i, t_0, t)$.

Under the phase dynamics assumption, the important changes in seismicity $\Delta S(x_i, t_1, t_2) = S(x_i, t_0, t_2) - S(x_i, t_0, t_1)$ over the time interval (t_1, t_2) correspond to rotations in correlation space about the origin.

Thus the important observable is this difference $\Delta S(x_i, t_1, t_2)$. Recall that $S(x_i, t_0, t)$ is a spatially local function. However, due to the normalization above, which involves information from the entire active region of N boxes, $S(x_i, t_0, t)$ is a spatially non-local function.

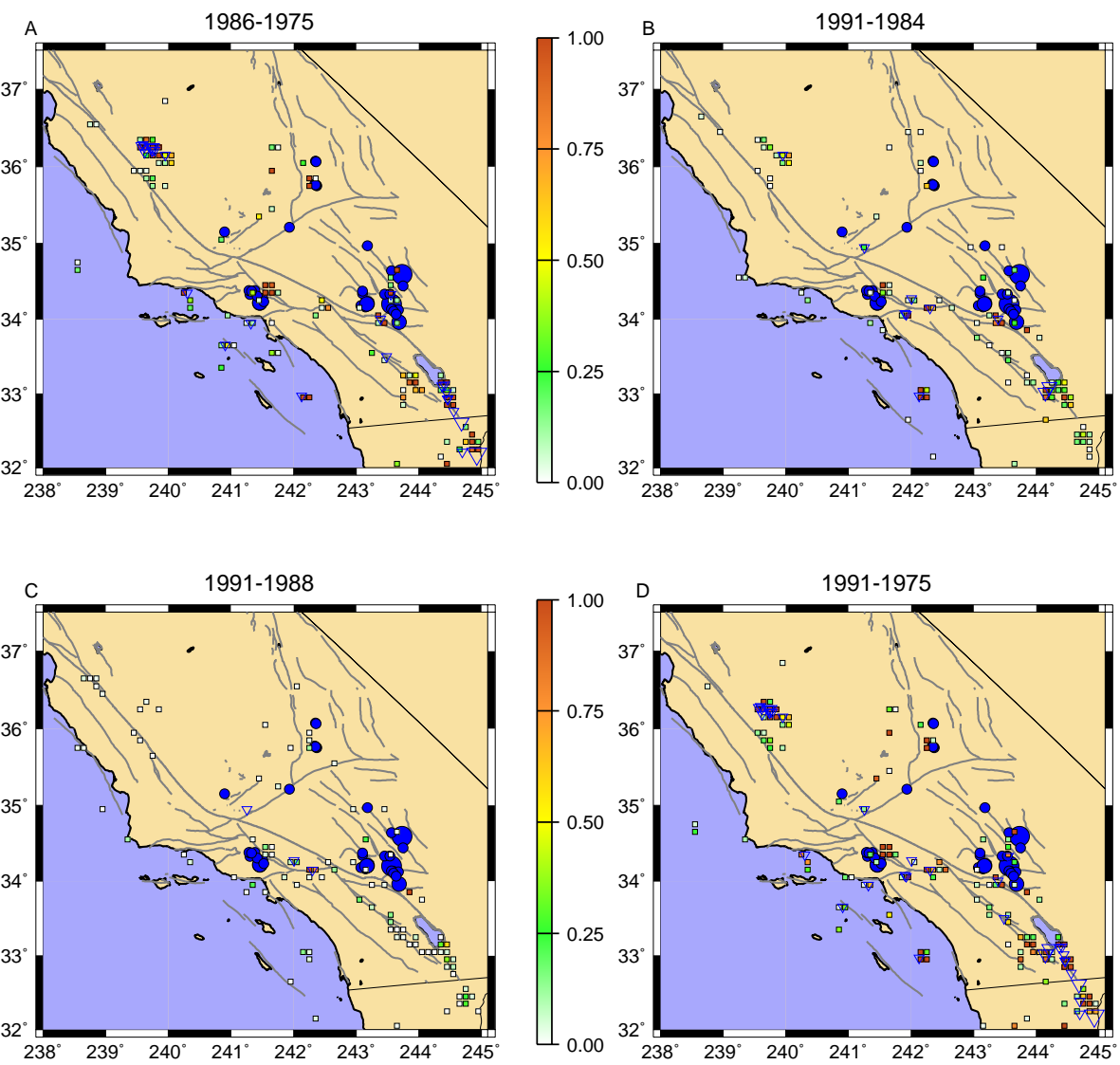
We now compute the increase in probability $\Delta P(x_i, t_1, t_2)$ associated with formation of a spatial correlation at location x_i over the time interval $\Delta t = (t_2 - t_1)$. Because a correlation function can be interpreted as a probability, the eigenvectors of the correlation operator $C(x_i, x_j)$ are effectively the square root of a probability. Any vector such as $S(x_i, t_0, t)$ can be written as a linear expansion of such a complete set of eigenvectors which span the correlation vector space. Thus, the increase in probability $\Delta P(x_i, t_1, t_2)$ is related to the square of $\Delta S(x_i, t_1, t_2)$. In addition, as the principle of conservation of probability implies that the integral over all space of $\Delta P(x_i, t_1, t_2)$ is equal to zero, we find that $\Delta P(x_i, t_1, t_2) = |\Delta S(x_i, t_1, t_2)|^2 - \mu_p$, where μ_p is the spatial mean of $|\Delta S(x_i, t_1, t_2)|^2$.

3. RESULTS AND DISCUSSION

Figure 2 shows plots of all $\Delta P > 0$, using only existing seismicity data acquired prior to January 1, 1992, six months before the June 28, 1992 occurrence of the M ~ 7.3, Landers, CA, earthquake. Recall that the increase in ΔP above the background level as measured by μ_p should be interpreted as a tendency to form a spatially correlated region of seismic activity, and that such regions evidently must be present for larger earthquakes to occur. An increase in ΔP appears to represent an increased chance of an earthquake occurring near that location. The color coding on Figure 3 is scaled to the largest value of ΔP on any of Figures 2 a, b, c or d. The largest 30 percent of points is represented by red, approximately 20 percent by yellow, and approximately 50 percent are between white and green. At the moment, we have not yet found a method to convert these relative numbers into absolute values of probability change, however, we expect that this may be possible with further study. The inverted blue triangles represent events that occurred during the time period covered by the plot, to indicate colored boxes that need not be analyzed further.

Blue circles represent more recent events of magnitude M > 5.0 that occurred after January 1, 1992. It should be emphasized again that no data for these more recent events was used in constructing the colored boxes in Figure 2. In particular, we include circles representing the 1992 Landers sequence and the recent M ~ 7.1 Hector Mine events. These earthquakes are evidently associated with a long-lived arcuate structure of colored boxes cutting across the local fault geometry that began forming prior to 1980. This structure continues down to the southeast of the Landers mainshock, east of the 1992 Joshua Tree earthquake, and the lack of subsequent activity to date may indicate this site as a potential rupture zone in the near future.

Visual examination of Figure 2 indicates that recent large events (blue circles) that occurred after January 1, 1992 are clearly associated with detectable locations of positive ΔP that formed prior to January 1, 1992. However there is clearly some variability, particularly for smaller events, depending on the choice of time interval (t_1, t_2) . Larger events tend to be associated with larger colored regions that form earlier and persist longer after the event. Since earthquake fault dynamics are now believed to be associated with critical phenomena [Rundle and Klein, 1995; Klein et al., 1997; Gell-Mann et al., 2000; Rundle et al., 2000], we hypothesize that there may be a scaling relation between the area A of the correlated region and the time interval t prior to the main shock at which the correlation begins to form such that $t \propto A^\eta$, where η is a critical exponent near 1. Since the linear size of our boxes is approximately 11 km, one should not expect events significantly smaller than M ~ 6, whose characteristic linear source dimension is 10



km, to be well resolved by our procedure. Yet even the smaller circles associated with $M \sim 5 - 6$ events seem to occur in proximity to colored boxes, albeit those that appear only a short time interval before the main shock.

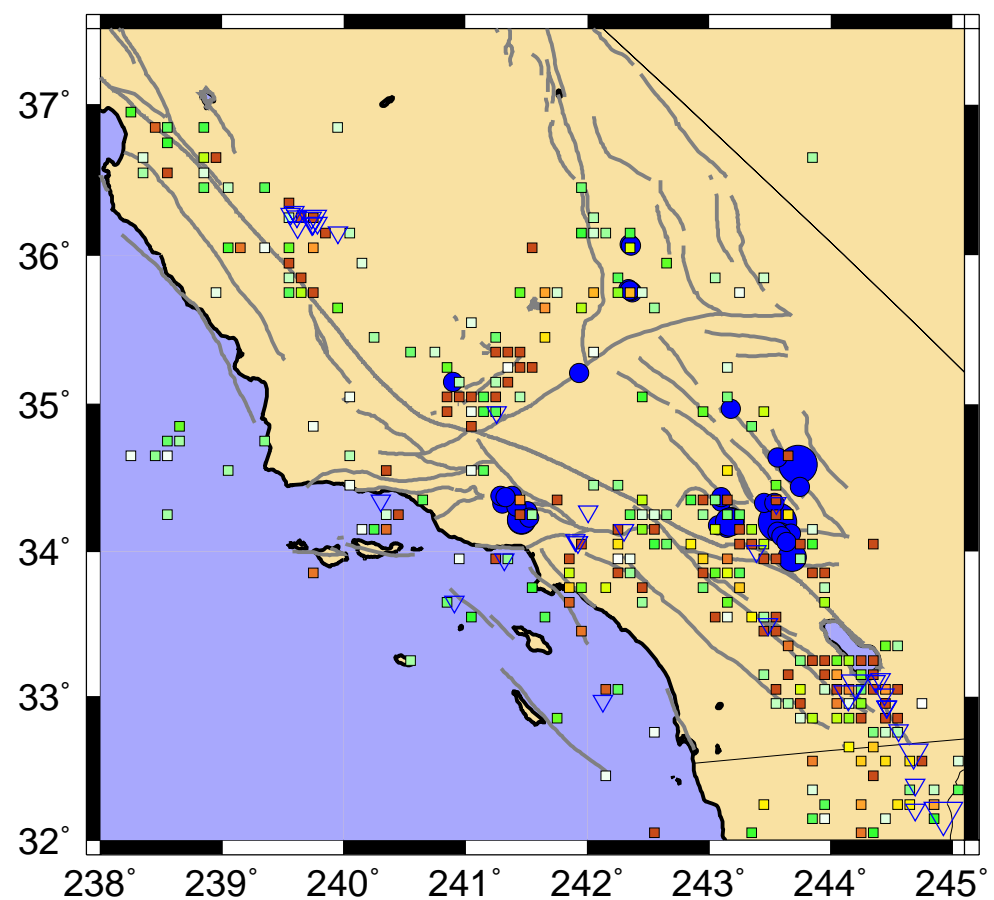
To test the hypothesis that the formation of correlated regions identified by this method are indeed coherent space-time structures that are related to future large events, we carried out a likelihood ratio test [Bevington and Robinson, 1992; Gross and Rundle, 1998] on our model using a comparison to a random seismicity catalog. The random catalog was constructed from the instrumental catalog by using the same number of events at the same locations, but assigning occurrence times drawn from a uniform probability distribution over the years 1932-1991, resulting in a Poisson distribution of interevent times. Randomizing the catalog in this way should destroy whatever coherent space-time structure exists, effectively declustering the catalog. We applied our method to this random catalog and obtained the colored boxes shown in Figure 3, which corresponds to the same time period as Figure 2d, 1991-1975. One can see that there are many more colored boxes in Figure 3 than in 2d, and that the boxes are more broadly distributed in space.

To apply the likelihood ratio test to both Figures 2d and 3, we assumed a probability density function for each box, colored or not, with a Gaussian distribution, whose peak value is $\Delta P(x_i, t_1, t_2) + \mu_p$, since probabilities in a likelihood test must all be positive, and whose width is that of the colored boxes, approximately 11 km. We then calculated the log likelihoods for the blue circles in both Figures 2d and 3, and found values of -14.5439 for Figure 2d and -17.4239 for Figure 3. These values correspond to a likelihood ratio of $e^{2.88} \sim 17.8142$, indicating that the colored boxes obtained from the actual instrumental catalog are more likely to be associated with the locations of the blue circles than the colored boxes obtained from the random catalog. The physical reason for this large ratio is that the likelihood test invokes a penalty for colored boxes that are not sufficiently near to blue circles ("false positives"), and there are many more such boxes in Figure 3 than in Figure 2d. From this test, we conclude that there are coherent space-time correlation structures in the instrumental catalog that our method identifies. This supports the theory that earthquake fault systems contain space-time correlations which are effectively destroyed by declustering the catalog.

In analyzing the meaning of Figure 2 we emphasize that while our method may identify higher risk areas, there is no certainty at this time that every box will be located near the site of a future large earthquake. There are a number of examples in Figure 2 where a box appears during one time period, then disappears over a longer time period without the occurrence of a major earthquake (false negatives). One example of this is the colored boxes which appear near 34.7° latitude, 238.6° longitude, during the period 1975 to 1986, but disappear during the periods 1986 to 1991 and 1988 to 1991. Further attempts at optimization of the method must focus on better spatial location of events and the identification of a minimum number of both false positives and false negatives.

In addition, it appears that, as coherent space-time structures form in the underlying physics which drive the earthquake system, our method attempts to fit the nearest known locations of previous seismicity. One example of this is the four red boxes in the location of the 1971 San Fernando earthquake, as shown in Figure 2d. We hypothesize that these locations are simply the nearest locations available to the method for applying the increased probability associated with the adjacent 1994 Northridge event. In examining the time periods shown, we note that the method described above effectively subtracts out the effects of any San Fernando aftershocks remaining in the catalog in 1975. To test the assumption that the changes in probability are not exclusively associated with the location of aftershock sequences, we plotted the change in $S(x_i, t_0, t)$, $\Delta S(x_i, t_1, t_2)$. The results show that the four squares adjacent to the 1994 Northridge event denote an area of decreased $S(x_i, t_0, t)$, i.e. precursory quiescence, not aftershocks due to the 1971 San Fernando earthquake. Events which go off during this time period, such as the 1983 Coalinga earthquake and the 1979 Imperial Valley event, display seismic activation, while the Landers sequence is a complicated mix of positive and negative $\Delta S(x_i, t_1, t_2)$. These findings support our conclusions from both the numerical simulations and theoretical analysis that this technique does not simply identify areas associated with past events and their aftershock sequences.

1991-1975



4. CONCLUSIONS

In summary, we conclude that we have observed systematic variations in seismicity prior to recent southern California earthquakes. Our method employs data from existing seismic monitoring networks as well as a theoretical understanding obtained from numerical computer simulations to identify coherent space-time structures in seismicity. These space-time patterns in the seismic activity directly reflect the existence of correlated structure in the underlying stress and strain fields, a necessary precondition for the occurrence of large earthquakes. Depending on the nature of future seismic activity in the region, as well as future modifications and extensions of the theory and technique, this procedure may prove useful in analysis of future trends in seismic activity.

Acknowledgements. We would like to thank J. Bernard Minster and Andrea Donnellan for their helpful review and comments during the drafting of this paper. We would also like to acknowledge useful discussions with J. Perez-Mercader and M. Gell-Mann. Work carried out by K.F.T. was supported under NASA Fellowship No. NGT5-30025 to the Cooperative Institute for Research in Environmental Sciences (CIRES) at the University of Colorado, and by a CIRES Fellowship funded under NOAA Grant No. NA67RJ0153. Work by J.B.R. was supported by U.S. Dept of Energy Grant No. DE-FG03-95ER14499 to CIRES and NASA Grant No. NAG5-5168 to CIRES. The work of S.M. was supported by NASA Fellowship No. ESS-97-0110 to CIRES, and the work of W.K. was supported under U.S. Dept of Energy Grant No. DE-FG-2-95ER14498 to the Physics Dept. and Center for Computational Science at Boston University.

REFERENCES

- Bevington, P. R., D. K. Robinson, *Data Reduction and Error Analysis for the Physical Sciences*, McGraw-Hill, N.Y., 1992.
- Bowman, D. D., G. Ouillon, C. G. Sammis, A. Sornette and D. Sornette, *J. Geophys. Res.*, **103**, 24,359, 1998.
- Brehm D. J., and L. W. Braile, *Bull. Seis. Soc. Am.*, **88**, 564, 1998.
- Brehm D. J., and L. W. Braile, *Bull. Seis. Soc. Am.*, **89**, 275, 1999.
- Bufe, C. G., and D. J. Varnes, *J. Geophys. Res.*, **98**, 9871, 1993.
- Dodge, D. A., G. C. Beroza, W. L. Ellsworth, *J. Geophys. Res.*, **100**, 9865, 1995.
- Dodge, D. A., G. C. Beroza, W. L. Ellsworth, *J. Geophys. Res.*, **101**, 22371, 1996.
- Ellsworth, W. I., and A. T. Cole, *Seis. Res. Lett.*, **68**, 298, 1997.
- K. Mogi, *Bull. Earthquake Res. Inst. Tokyo Univ.*, **47**, pp. 395-417, 1969.
- Evison, F. F., *Nature*, **266**, 710, 1977.
- Frohlich, C., *J. Geophys. Res.*, **92**, 13,944, 1987.
- Fukunaga, K., *Introduction to Statistical Pattern Recognition*, Academic Press, N.Y., 1970.
- Geller, R. J., D. D. Jackson, Y. Y. Kagan, F. Mulargia, *Science*, 275, 1616 (1997).
- Gell-Mann, M., J. Perez-Mercader, J. B. Rundle, in *The Physics of Earthquakes*, edited by J. B. Rundle, W. Klein and D. L. Turcotte, AGU, Washington, D.C., 2000.
- Gross, S., and J. Rundle, *Geophys. J. Int.*, **133**, 57, 1998.
- Haberman, R. E., in *Earthquake Prediction: an International Review*, edited by D. W. Simpson, II, and P. G. Richards, pp. 29-42, AGU, Washington, D. C., 1981.
- Hill, D. P., et al., *Science*, **260**, 1617, 1993.
- Holmes, P., J. L. Lumley, G. Berkooz, *Turbulence, Coherent Structures, Dynamical Systems and Symmetry*, Cambridge University Press, U.K., 1996.
- House, L. S., L. R. Sykes, J. N. Davies, K. H. Jacob, in *Earthquake Prediction: an International Review*, edited by D. W. Simpson, II, and P. G. Richards, pp. 81-92, AGU, Washington, D. C., 1981.
- Kanamori, H., in *Earthquake Prediction: an International Review*, edited by D. W. Simpson, II, and P. G. Richards, pp. 1-19, AGU, Washington, D. C., 1981.
- Kato, N., M. Ohtake, T. Hirasawa, *Pure Appl. Geophys.*, **150**, 249, 1997.
- King, G. C. P., R. S. Stein, J. Lin, *Bull. Seis. Soc. Am.*, **84**, 935, 1994.
- Klein, W., J. B. Rundle, C. D. Ferguson, *Phys. Rev. Letters*, **78**, n. 19, 1997.
- Knopoff, L., and T. Yamashita, *Terra Cognita*, **8**, 118, 1988.
- Knopoff, L., T. Levshina, V. I. Keilis-Borok and C. Mattoni, *J. Geophys. Res.*, **101**, 5779, 1996.
- Mogi, K., *Bull. Earthquake Res. Inst. Tokyo Univ.*, **47**, pp. 395-417, 1969.
- Mogi, K., *Proc. Symp. on Earthquake Prediction, Seis. Soc. Japan*, pp. 203-214, 1977.
- Mori H., and Y. Kuramoto, *Dissipative Structures and Chaos*, Springer-Verlag, Berlin, 1998.
- Pollitz, F. F., and I. S. Sacks, *Bull. Seis. Soc. Am.*, **87**, 1, 1997.
- Press F., and C. R. Allen, *J. Geophys. Res.*, **100**, 6421, 1995.

- Richter, C. F., *Elementary Seismology*, Freeman, San Francisco, 1958.
- Rundle, J. B., *J. Geophys. Res.*, **93**, 6255, 1988.
- Rundle, J. B., and W. Klein, *Rev. Geophys. Space Phys., Suppl.*, July 1995.
- Rundle, J. B., S. Gross, W. Klein, C. Ferguson, D. L. Turcotte, *Tectonophysics*, **277**, 147, 1997.
- Rundle, J. B., W. Klein, K. F. Tiampo and S. Gross, *Phys. Rev. E*, in press, March 2000.
- Saleur, H., C. G. Sammis, and D. Sornette, *J. Geophys. Res.*, **101**, 17,661, 1996.
- Scholz, C. H., *The Mechanics of Earthquakes and Faulting*, Cambridge University Press, Cambridge, U.K., 1990.
- Schwartz, D. P., et al., *Earthquake Notes*, **52**, 71, 1981.
- Shaw, B. E., J. M. Carlson, J. S. Langer, *J. Geophys. Res.*, **97**, 479, 1992.
- Wyss, M., and R. E. Haberman, *Pure Appl. Geophys.*, **126**, 319, 1988.
- Wyss, M., K. Shimaziki, T. Urabe, *Geophys. Jour. Int.*, **127**, 735, 1996.

K.F. Tiampo, J.B. Rundle, S. McGinnis and S.J. Gross, Colorado Center for Chaos and Complexity,
Cooperative Institute for Research in Environmental Sciences, University of Colorado, Boulder, CO 80309-
0216.

W. Klein, Dept. of Physics, Boston University, Boston, MA 02215.

Pattern Dynamics and Forecast Methods in Seismically Active Regions

K.F. Tiampo⁽¹⁾, J.B. Rundle⁽²⁾, S. McGinnis⁽¹⁾ and W. Klein⁽³⁾

(1) CIRES, University of Colorado, Boulder, CO USA (e-mail: kristy@fractal.colorado.edu; sethmc@turcotte.colorado.edu; phone: +01-303-492-4779); (2) Dept. of Physics, Colorado Center for Chaos & Complexity, CIRES, University of Colorado, Boulder, CO, 80309, USA, and Distinguished Visiting Scientist, Jet Propulsion Laboratory, Pasadena, CA, 91125, USA (email: rundle@cires.colorado.edu; phone +01-303-492-4779); (3) Dept. of Physics, Boston University, Boston, MA USA and Center for Nonlinear Science, Los Alamos National Laboratory, Los Alamos, NM USA.

Abstract

Large, extended fault systems such as those in California demonstrate complex space-time seismicity patterns, which include repetitive events, precursory activity and quiescence, and aftershock sequences. Although the characteristics of these patterns can be qualitatively described, a systematic quantitative analysis remains elusive. Our research suggests that a new pattern dynamics methodology can be used to define a unique, finite set of seismicity patterns for a given fault system. In addition, while a long-sought goal of earthquake research has been the reliable forecasting of these events, very little progress has been made in developing a successful, consistent methodology. In this report, we document the discovery of systematic space-time variations in seismicity from southern California using a new technique. Here we show examples of this analysis technique on data obtained *prior* to events in seismically active areas that show coherent regions associated with the future occurrence of major earthquakes in the same areas. These results strongly support the hypothesis

**that seismic activity is highly correlated across many space and time scales
within large volumes of the earth's crust.**

Introduction

While the historic earthquake record is not complete, it has long been recognized that earthquake mainshocks occur at quasi-periodic intervals and that, for some parts of the world, average recurrence intervals are well defined (KANAMORI, 1981). In addition, both temporal and spatial clustering is evident in the data, with the result that neither the recurrent nature of the mainshocks, nor the observed phenomena such as foreshocks, aftershocks, seismic gaps, or main-shock triggering, is compatible with a Poisson probability function (JONES and HAUKSSON, 1992; KAGAN and JACKSON, 1992; SAVAGE, 1993; DIETERICH, 1994; GRANT and SIEH, 1994; RUNDLE and KLEIN, 1995; TURCOTTE, 1997; MAIN, 1999B). Much of the recent geophysical research associated with earthquakes themselves has centered on investigating these spatial and temporal patterns in local and regional seismicity data (KANAMORI, 1981). Notable examples include characteristic earthquakes (SWAN *et al.*, 1980; ELLSWORTH and COLE, 1997), repeating earthquakes (BAKUN *et al.*, 1986; MARONE *et al.*, 1995), seismic gaps (HABERMAN, 1981; HOUSE *et al.*, 1981; KAGAN, 1981; KAGAN and JACKSON, 1992; WYSS and WIEMER, 1999), well-defined recurrence intervals (BAKUN and McEVILLY, 1984; LYZENGA *et al.*, 1991; SAVAGE, 1993), Mogi donuts (MOGI, 1969; MOGI 1977), temporal clustering (FROHLICH, 1987; PRESS and ALLEN, 1995; DODGE *et al.*, 1996; ENEVA and BEN-ZION, 1997; JONES and HAUKSSON, 1992; RUNDLE *et al.*, 1997; HUANG *et al.*, 1998), 'slow' earthquakes[LINDE *et al.*, 1996; McGuire, *et al.*, 1996; KERR, 1998], precursory quiescence (YAMASHITA and KNOPOFF, 1989; WYSS *et al.*, 1996; KATO *et al.*, 1997;

WYSS *et al.*, 2000), aftershock sequences (GROSS and KISSLINGER, 1994, NANJO *et al.*, 1998), earthquake triggering over large distances (STEIN *et al.*, 1992; HILL *et al.*, 1993; KING *et al.*, 1994; HILL *et al.*, 1995; DENG and SYKES, 1996; GOMBERG, 1996; STARK and DAVIS, 1996; POLLITZ and SACKS, 1997; STEIN, 1999], scaling relations (RUNDLE, 1989; PACHECO *et al.*, 1992; ROMANOWICZ and RUNDLE, 1993; RUNDLE , 1993; SALEUR *et al.*, 1995; RUNDLE *et al.*, 1999], and time-to-failure analyses (BUFE and VARNES, 1993; BOWMAN *et al.*, 1998; GROSS and RUNDLE, 1998; BREHM and BRAILE, 1999; JAUME and SYKES, 1999; MAIN, 1999a). Although much of this work represents important attempts to describe these characteristic patterns using empirical probability density functions, none of these observations or methodologies systematically identifies all possible seismicity patterns. The quantification of all possible space-time patterns would seem to be a necessary first step in the process of identifying which patterns are precursory to large events, leading to the possible development of new approaches in forecast methodology. Yet, as can be seen in Figure 1, a plot of relative southern California seismicity during the time period 1932-1991, the identification and quantification of these patterns is no easy matter.

Recent large earthquakes include the $M \sim 7.4$ event that struck Izmit, Turkey in August of 1999, the $M \sim 7.6$ Taiwan earthquake that occurred in September of 1999, and the $M \sim 7.1$ Hector Mine, California earthquake of October 1999. Many similar examples have been documented over the course of time (RICHTER, 1958; SCHOLZ, 1990), yet despite the fact that the largest of these events span distances of more than 500 km, no reliable precursors have been detected with any repeatability (KANAMORI, 1981; GELLER, *et al.*, 1997). It is difficult for most scientists to understand why events of this magnitude are not preceded by at least some causal process. While various patterns of seismic activity centered on the source region have been proposed, as

noted above, these efforts to identify the premonitory signals have focused predominantly on local regions near the earthquake source. As a result, these techniques often require intensive and expensive monitoring efforts and have been largely unsuccessful (KANAMORI, 1981). Since these hypothesized patterns are localized on the eventual source region, the fact that one must know or suspect where the event will occur before they can be applied is a major drawback to their implementation.

In this report, we discuss a new pattern dynamics methodology that can be used to define a unique, finite set of seismicity patterns for a given fault system. Similar in nature to the empirical orthogonal functions historically employed in the analysis of atmospheric and oceanographic phenomena (PREISENDORFER, 1988), this method derives the eigenvalues and eigenstates from the diagonalization of a correlation matrix using a Karhunen-Loeve expansion (FUKUNAGA, 1970). This pattern dynamics technique has been successfully applied to the study of numerically modeled seismicity for fault networks similar in character and extent to those found in California (RUNDLE, *et al.*, 2000a). We implement this same methodology in order to analyze historical seismicity in California and derive space-time eigenvalue patterns for the San Andreas fault system. The significant eigenstates for this relatively short period of time can be directly correlated with the known California faults and associated events (TIAMPO *et al.*, 2000).

In this work we present a method for identifying these areas of increased probability of an event. The success of the Karhunen-Loeve decompositions discussed above, coupled with recent observational evidence, suggests that earthquake faults are characterized by strongly correlated space-time dynamics (BUFE *and* VARNES, 1993; PRESS *and* ALLEN, 1995; BOWMAN *et al.*, 1998; TIAMPO *et al.*, 2000). We have extended these results, and observations of their applica-

tion to numerical simulations of earthquake fault systems, to the development of a method for identifying areas of increased probability of an event, $\Delta\mathbf{P}$. Realistic numerical simulations of earthquakes also suggest that space-time pattern structures are non-local in character, a consequence of strong correlations in the underlying dynamics (RUNDLE, 1988; RUNDLE *et al.*, 2000a). The procedure described below is based upon the idea that seismic activity corresponds geometrically to the rotation of a pattern state vector in the high-dimensional correlation space spanned by the eigenvectors of an equal-time correlation operator (RUNDLE *et al.*, 2000b; TIAMPO *et al.*, 2000).

Background and Theory

Earthquake fault systems are now thought to be an example of a complex nonlinear system (BAK *et al.*, 1987; RUNDLE *and* KLEIN, 1995). Interactions among a spatial network of fault segments are mediated by means of a potential that allows stresses to be redistributed to other segments following slip on any particular segment. For faults embedded in a linear elastic host, this potential is a stress Green's function whose exact form can be calculated from the equations of linear elasticity, once the current geometry of the fault system is specified. A persistent driving force, arising from plate tectonic motions, increases stress on the fault segments. Once the stresses reach a threshold characterizing the limit of stability of the fault, a sudden slip event results. The slipping segment can also trigger slip at other locations on the fault surface whose stress levels are near the failure threshold as the event begins. In this manner, earthquakes occur that result from the interactions and nonlinear nature of the stress thresholds.

Karhunen-Loeve methods, a linear decomposition technique in which a dynamical system is decomposed into a complete set of orthonormal subspaces, have been applied to a number of other complex nonlinear systems over the last fifty years, including the ocean-atmosphere interface, turbulence, meteorology, biometrics, statistics, and even geophysics (HOTELLING, 1993; FUKUNAGA, 1970; AUBREY *and* EMERY, 1983; PREISENDORFER, 1988; SAVAGE, 1988; PENLAND, 1989; VAUTARD *and* GHIL, 1989; GARCIA *and* PENLAND, 1991; PENLAND *and* MAGORIAN, 1993; PENLAND *and* SARDESHMUKH, 1995; HOLMES *et al.*, 1996; MOGHADDAM *et al.*, 1998). The notable success of this method in analyzing the ocean-atmosphere interface and such features as the El Nino Southern Oscillation (ENSO), a nonlinear system whose underlying physics is governed by the Navier-Stokes equation, suggested its application to the analysis of the earthquake fault system (NORTH, 1984; PREISENDORFER, 1988; PENLAND *and* MAGORIAN, 1993; PENLAND *and* Sardeshmukh, 1995). Building on these methods for analyzing nonlinear threshold systems, space-time seismicity patterns can be identified in both numerical simulations using realistic earthquake models for southern California (BUFE *and* VARNES, 1993; BOWMAN *et al.*, 1998; GROSS *and* RUNDLE, 1998; BREHM *and* BRAILE, 1999; JAUME *and* SYKES, 1999; RUNDLE *et al.*, 2000a] and actual historic seismicity records (TIAMPO *et al.*, 1999; TIAMPO *et al.*, 2000]. In this paper, we apply this Karhunen-Loeve expansion (KLE) technique (FUKUNAGA, 1970; HOLMES *et al.*, 1996) to the analysis of observed seismicity data from southern California in order to identify basis patterns for all possible space-time seismicity configurations. These basis states represent a complete, orthonormal set of eigenvectors and associated eigenvalues, obtained from the diagonalization of the correlation operators computed for the regional historic seismicity data, and, as such, can be used to reconstitute the data for various subset time periods of the entire data set.

Variables in many dynamical systems can be characterized by a phase function that involves both amplitude and phase angle [MORI AND KURAMOTO, 1998]. Our simulations have suggested that seismicity can be described by pure phase dynamics [MORI AND KURAMOTO, 1998; RUNDLE ET AL., 2000a; RUNDLE ET AL., 2000b], in which the important changes in seismicity are associated primarily with rotations of the vector phase function in a high-dimensional correlation space [FUKANAGA, 1970; HOLMES ET AL., 1998; RUNDLE ET AL., 2000a]. Changes in the amplitude of the phase function are unimportant, or not relevant. Examples of pure phase dynamical systems in the classical world include weak turbulence in fluids and reaction-diffusion systems [MORI AND KURAMOTO, 1998]. Another non-classical example is a quantum system in which the wave function is the phase function. By mapping our problem into the mathematics of quantum mechanics, we are treating the underlying stress-strain dynamics as the hidden variables and the seismicity patterns as the wave functions [RUNDLE AND KLEIN, 1995; RUNDLE ET AL., 2000a; RUNDLE ET AL., 2000b].

Observations and numerical simulations suggest that space-time patterns of seismic activity directly reflect the existence of space-time correlations in the underlying stress and strain fields [RUNDLE ET AL., 2000a; RUNDLE ET AL., 2000b]. A spatially coherent, uniformly high level of stress on a fault is a necessary precondition for the occurrence of a large earthquake. Recently, several groups have found that spatial coherence in the stress field is reflected in a similar coherence in the seismic activity [RUNDLE, 1988; BUFE AND VARNES, 1993; KNOPOFF ET AL., 1996; MAIN, I.G., 1999a; SALEUR ET AL., 1996; BREHM AND BRAILE, 1998; RUNDLE ET AL., 2000a; RUNDLE ET AL., 2000b]. It should therefore be possible to compute the increase in probability of observing such an anomalous correlation, ΔP ,

directly from the observed seismicity data. Using the fact that seismicity is an example of phase dynamics, it follows that ΔP can be calculated from the square of the phase function for the associated pattern state vector [FUKANAGA, 1970; HOLMES ET AL., 1998; RUNDLE ET AL., 2000a]. To emphasize the connection to phase dynamics, we call the function ΔP the Phase Dynamical Probability Change (PDPC).

Finally, we note that the space-time correlations or patterns that lead to a uniformly high stress field on the fault represent emergent space-time structures, which evidently form and evolve over time intervals of years preceding the main shock. Longer time intervals and larger correlated areas should be associated with larger main shocks.

Data

The primary seismicity data set for southern California employed in this analysis is the entire Caltech catalog from 1932 through December of 1999, obtained from the Southern California Earthquake Center (SCEC) database, with all blast events specifically removed from the catalog [<http://www.scec.org>]. Relevant data includes location, in latitude and longitude, and the time the event occurred. Seismic events between -115° and -123° longitude and 32° and 37° latitude were selected, and all quality events were acquired. Separate analyses were performed for the entire data set, consisting of all events of magnitude greater than or equal to 0.0, and on another data set in which only those events of magnitude greater than or equal to 3.0 were included in the binning process described below. The time periods evaluated were from 1932 to 1991, and 1932 through August of 1999. In both cases, the seismicity was binned into squares of 0.1° latitude and 0.1° longitude to a side, and a time series constructed for each location square,

boxes of approximately 11 km to a side. Each time step is given an initial value of 1.0 if one or more events occur in that time period, or a value of 0.0 otherwise. Subsequently, the mean for each time series is removed from the data.

For the time period 1932 through August of 1999, the seismicity was analyzed using the entire data set, including the entire areal extent and events of all quality. The time interval for this decomposition was increased to one day, so that the total number of time steps is approximately 24,333. In addition, all locations from the entire database, and all quality events, were included, even those where no event occurred for the more than 67 years. The number of location time series affected by the seismicity, p , therefore is 3621. For the time period 1932 to 1991, the time interval for the analysis was again one day, so that the total number of time steps is approximately 21,535. Again, all locations, and all quality events, were included, even those where no event occurred for the entire 59 years. The total number of location time series remains constant at 3621.

Method

Karhunen-Loeve Decomposition

Pattern evolution and prediction in nonlinear systems is complicated by nonlinear mode coupling and noise, but understanding such patterns, which are the surface expression of the underlying dynamics, is critical to understanding and perhaps characterizing the physics which control the system. Karhunen-Loeve expansion (KLE) methods can be used to define a unique,

complete pattern basis set for a given dynamical system (FUKUNAGA, 1970; NORTH, 1984; PENLAND, 1989; HOLMES *et al.*, 1996]. For driven threshold systems, an adaptation of these KLE methods can be employed to characterize both the space-time patterns of threshold transitions, i.e. "firings", as well as the underlying, usually unobservable Markov variables that define the dynamics (FUKUNAGA, 1970; HOLMES *et al.*, 1996; RUNDLE *et al.*, 2000). In either case, the patterns are defined by the eigenstates and eigenvalues of one of an appropriately constructed family of correlation operators.

Earthquake fault systems are examples of driven nonlinear threshold systems, comprised of interacting spatial networks of statistically identical, nonlinear units that are subjected to a persistent driving force (SCHOLZ, 1990; RUNDLE *and* Klein, 1995; FISHER *et al.*, 1997; RUNDLE *et al.*, 1997; FERGUSON *et al.*, 1999). Numerous examples of such systems exist, including neural networks (HERTZ *et al.*, 1990; HERZ *and* HOPFIELD, 1995), sandpiles (BAK *et al.*, 1987), and superconductors (FISHER *et al.*, 1997), of which earthquakes are but another example. Such systems are composed of cells which fire, or fail, when the driving force causes the force or potential, $\sigma(x,t)$, on a cell at location x and time t , to reach a predefined threshold value σ^F . The behavior of these systems is determined by parameters such as threshold values, residual stresses, quenched disorder and noise (BAK *et al.*, 1987; RUNDLE *and* Klein, 1995; FISHER *et al.*, 1997). Complex spatial and temporal firing patterns result that are difficult to analyze deterministically (OUCHI, 1993; NIJHOUT, 1997). In the case of an earthquake fault system, the driving force is tectonic plate motion, and the internal potential is the stress on each fault cell or patch. The firing, or failure of each patch results in an increase in the internal state variable $s(x,t)$ and a decrease in the cell potential to some residual value σ^R . The interactions between the cells, or fault patches, may be excitatory, bringing another closer to failure, or inhibitory, in which the

failure of one cell can move neighboring cells further from failure. The spatial and temporal firing patterns, $\psi(\mathbf{x},t)$, of these driven threshold systems are complex and often difficult to understand and interpret from a deterministic perspective, as these patterns are emergent processes that develop from the obscure underlying structures, parameters, and dynamics of a multidimensional nonlinear system (OUCHI, 1993; NIJHOUT, 1997).

Analysis of a number of these driven threshold systems often is complicated by the fact that the underlying dynamics and the state variables which control the physics of the system, $s(\mathbf{x},t)$, are unknown and difficult to observe. The earthquake fault system is no exception. While it is not only probable, but essential, that space-time patterns and correlations exist in the variables and interactions which control earthquake dynamics, $s(\mathbf{x},t)$ and $\sigma(\mathbf{x},t)$, from which the observable surface patterns and correlations, $\psi(\mathbf{x},t)$ arise, those true dynamical patterns are difficult or impossible to observe within the earth (SCHOLZ, 1990; TURCOTTE, 1997). The schematic shown in Figure 2 illustrates the physical problem. As the state variable $s(\mathbf{x},t)$ at a particular location \mathbf{x} evolves in time under the deterministic dynamics \mathbf{D}_t to a value $s(\mathbf{x},t+\Delta t)$, the force or potential $\sigma(\mathbf{x},t)$, also evolves to $\sigma(\mathbf{x},t+\Delta t)$. While the values of $s(\mathbf{x},t)$ and $\sigma(\mathbf{x},t)$, along with the specifics of \mathbf{D}_t , are hidden from view below the dashed line of Figure 2, the firing patterns of $\psi(\mathbf{x},t)$ are observable. In the earth, there is no means at present to measure the stress and strain at every point in an earthquake fault system, or the constitutive parameters, which characterize the heterogeneous medium and its dynamics. However, the seismicity, which is the surface expression of its firing activity, can be located in both space and time with considerable accuracy (BA-KUN *and McEVILLY*, 1984; SIEH *et al.*, 1989; HILL *et al.*, 1990). For example, the firing ac-

tivity, $\psi(\mathbf{x},t)$, can be represented as a set of time series at all positions \mathbf{x} , where $\psi(\mathbf{x},t) = 1$ if an event occurs in the time interval between t and $t + \Delta t$, and $\psi(\mathbf{x},t) = 0$ otherwise.

Observations and numerical simulations suggest that space-time patterns of seismic activity directly reflect the existence of space-time correlations in the underlying stress and strain fields (PRESS and ALLEN, 1995). A spatially coherent, uniformly high level of stress on a fault is a necessary precondition for the occurrence of a large earthquake. Recently, several groups have found that spatial coherence in the stress field is reflected in a similar coherence in the seismic activity (BUFE and VARNES, 1993; BOWMAN *et al.*, 1998; RUNDLE *et al.*, 2000a).

RUNDLE *et al.* [2000] extended the standard KLE methods to include the construction of pattern states that can be used to forecast events in time, in much the same manner as EOF analysis is used to predict El Niño events in meteorology (PREISENDORFER, 1988; PENLAND, 1989; GARCIA *and* PENLAND, 1991). This procedure involves constructing a correlation operator, $C(x_i, x_j)$, for the sites that contains the spatial relationship of slip events over time. $C(x_i, x_j)$ is decomposed into the orthonormal spatial eigenmodes for the nonlinear threshold system, e_j , and their associated time series, $a_j(t)$.

The Karhunen-Loeve expansion is obtained from the p time series that record the deformation history at particular locations in space. Each time series, $y(x_s, t_i) = y_i^s$, $s = 1, \dots, p$, consists of n time steps, $i = 1, \dots, n$. The goal is to construct a time series for each of a large number of locations that records, for a given short period of time, whether an earthquake occurred at that location (value = 1) or did not occur (value = 0). If, for example, the time interval was decimated

into units of days, the result would be a time series of 365 time steps for every year of data, with either a zero or a one at each time step. These time series are incorporated into a matrix, \mathbf{T} , consisting of time series of the same measurement for p different locations, i.e.

$$\mathbf{T} = [\bar{y}_1, \bar{y}_2, \dots, \bar{y}_p] = \begin{bmatrix} y_1^1 & y_1^2 & \dots & y_1^p \\ y_2^1 & y_2^2 & \dots & y_2^p \\ \vdots & \vdots & \ddots & \vdots \\ y_n^1 & y_n^2 & \dots & y_n^p \end{bmatrix}.$$

\mathbf{T} is therefore an $n \times p$, matrix of real values (FUKUNAGA, 1970). The covariance matrix, $S(x_i, x_j)$, for these events is formed by multiplying \mathbf{T} by \mathbf{T}^T , where S is a $p \times p$ real, symmetric matrix. The covariance matrix, $S(x_i, x_j)$, is converted to a correlation operator, $C(x_i, x_j)$, by dividing each element of $S(x_i, x_j)$, by the variance of each time series, $y(x_i, t)$ and $y(x_j, t)$, as follows.

$$\sigma_p = \sqrt{\frac{1}{n} \sum_{k=1}^n (y_k^p)^2},$$

and

$$C = \begin{bmatrix} \frac{s_{11}}{\sigma_1 \sigma_1} & \frac{s_{12}}{\sigma_1 \sigma_2} & \dots & \frac{s_{1p}}{\sigma_1 \sigma_p} \\ \frac{s_{21}}{\sigma_2 \sigma_1} & \frac{s_{22}}{\sigma_2 \sigma_2} & \dots & \frac{s_{2p}}{\sigma_2 \sigma_p} \\ \vdots & \vdots & \circ & \vdots \\ \frac{s_{p1}}{\sigma_p \sigma_1} & \frac{s_{p2}}{\sigma_p \sigma_2} & \dots & \frac{s_{pp}}{\sigma_p \sigma_p} \end{bmatrix}.$$

This equal-time correlation operator, $C(x_i, x_j)$, is decomposed into its eigenvalues and eigenvectors in two parts. The first employs the trireduction technique to reduce the matrix C to a symmetric tridiagonal matrix, using a Householder reduction. The second part employs a ql algorithm to find the eigenvalues, λ_j^2 , and eigenvectors, e_j , of the tridiagonal matrix (PRESS, *et al.*, 1992].

These eigenstates thus represent the orthonormal basis vectors arranged in order of decreasing correlation, and reflect the relative importance of the various modes over the time interval of interest. Dividing each corresponding eigenvalue, λ_j^2 , by the sum of the eigenvalues, yields that percent of the correlation accounted for by that particular mode. The associated orthonormal time series can be reconstructed by projecting the initial data set onto these basis vectors (PREISENDORFER, 1988; HOLMES *et al.*, 1996]. The time dependent expansion coefficients, $a_j(t)$, which represent temporal eigenvectors, are reconstructed by multiplying the original data matrix by the eigenvectors, i.e.

$$a_j(t_i) = e_j^T \cdot T = \sum_{s=1}^p e_j y_i^s,$$

where $j, s = 1, \dots, p$ and $i = 1, \dots, n$. This eigenstate decomposition technique produces the orthonormal spatial eigenmodes for this nonlinear threshold system, e_j , and the associated principal component time series, $a_j(t)$. These principal component time series represent the signal associated with each particular eigenmode over time. For purposes of clarity, the spatial eigenvectors are designated "KLE modes" and the associated time series "Principal Component (PC)" vectors.

Phase Dynamical Probability Change

Our method is based on the idea that the time evolution of seismicity can be described by pure phase dynamics (MORI and KURAMOTO, 1998; RUNDLE *et al.*, 2000a; RUNDLE *et al.*, 2000b). We therefore construct a real-valued seismic phase function $\hat{S}(x_i, t_0, t)$. For our analysis, the phase function $\hat{S}(x_i, t_0, t)$ characterizes the seismic activity in southern California between 32° and 37° latitude, and -115° to -123° longitude. It should be noted that this southern California catalog *has not been declustered*, because the space-time clustering carries the information about the space-time correlations that we seek to identify. Since seismicity in active regions is a noisy function (KANAMORI, 1981), we work with temporal averages of seismic activity. The geographic area is partitioned into $N = 3621$ square regions approximately 11 km on a side, centered on a point x_i . Within each box, a time series is defined using the Caltech seismic catalog obtained from the online SCEC database. For southern California, the instrumental data begins in 1932 and extends to the present.

We define the activity rate $\psi_{obs}(x_i, t)$ as the number of earthquakes per unit time, of any size, within the box centered at x_i at time t . The geographic region that $\hat{\mathbf{S}}(x_i, t_0, t)$ represents is taken large enough so that seismic activity can be considered an incoherent superposition of phase functions. To construct the phase function $\hat{\mathbf{S}}(x_i, t_0, t)$, we define the time-averaged seismicity function $\mathbf{S}(x_i, t_0, t)$ over the interval $(t - t_0)$:

$$\mathbf{S}(x_i, t_0, t) = \frac{1}{(t - t_0)} \int_{t_0}^t \psi_{obs}(x_i, t) dt$$

Since there are N numbers $\mathbf{S}(x_i, t_0, t)$, and if we assume t_0 to be a fixed time, we can then consider $\mathbf{S}(x_i, t_0, t)$ to be the i^{th} component of a general, time-dependent vector evolving in an N -dimensional space. In previous work, we showed that this N -dimensional *correlation space* is spanned by the eigenvectors of an $N \times N$ correlation matrix (RUNDLE *et al.*, 2000a; RUNDLE *et al.*, 2000b).

Denoting spatial averages over the N boxes by $\langle \rangle$, the phase function $\hat{\mathbf{S}}(x_i, t_0, t)$ is then defined to be the mean-zero, unit-norm function obtained from $\mathbf{S}(x_i, t_0, t)$:

$$\hat{\mathbf{S}}(x_i, t_0, t) = \frac{\mathbf{S}(x_i, t_0, t) - \langle \mathbf{S}(x_i, t_0, t) \rangle}{\|\mathbf{S}(x_i, t_0, t)\|},$$

where $\|\mathbf{S}(x_i, t_0, t)\|$ is the norm over all spatial boxes. Note that

$$\|\mathbf{S}(x_i, t_0, t)\| = \{\langle (\mathbf{S}(x_i, t_0, t) - \langle \mathbf{S}(x_i, t_0, t) \rangle)^2 \rangle\}^{1/2}.$$

Based upon the assumption of pure phase dynamics (RUNDLE *et al.*, 2000a; RUNDLE *et al.*, 2000b), the important changes in seismicity will be given by

$\Delta\hat{\mathbf{S}}(x_i, t_1, t_2) = \hat{\mathbf{S}}(x_i, t_0, t_2) - \hat{\mathbf{S}}(x_i, t_0, t_1)$, which is a pure rotation of the N-dimensional unit vector $\hat{\mathbf{S}}(x_i, t_0, t)$ in time.

In order to both remove the last free parameter in the system, the choice of base year, as well as to reduce the random noise component, we sum over all base years, t_0 , from 1932 through t_2 , such that

$$\Delta\hat{\mathbf{S}}(x_i, t_1, t_2) = \frac{\int_{1932}^{t_2} [\Delta\hat{\mathbf{S}}(x_i, t, t_2) - \Delta\hat{\mathbf{S}}(x_i, t, t_1)] dt}{\int_{1932}^{t_2} dt}$$

In phase dynamical systems, probabilities are related to the square of the associated vector phase function (MORI and KURAMOTO, 1998; RUNDLE *et al.*, 2000b). Thus we find

$$\Delta\mathbf{P}(x_i, t_1, t_2) = \{\Delta\hat{\mathbf{S}}(x_i, t_1, t_2)\}^2 - \mu_P$$

In other words, μ_P is the spatial mean of $\{\Delta\hat{\mathbf{S}}(x_i, t_1, t_2)\}^2$, and $\Delta\mathbf{P}(x_i, t_1, t_2)$ is the square of the value of $\Delta\hat{\mathbf{S}}(x_i, t_1, t_2)$ at each x_i minus that spatial mean. Note that the integral of $\Delta\mathbf{P}(x_i, t_1, t_2)$ over all N sites vanishes for all time intervals $[t_1, t_2]$, as it should, to conserve probability. Finally, note again that there are *no remaining free parameters in this method*. For any given catalog, up to the present, it is possible to compute the relative change in probability of an event over any given time period.

Results

The decomposition of nonlinear systems into their orthonormal eigenfunctions has been used successfully in the atmospheric sciences for many years (PREISENDORFER, 1988; PENLAND and MAGORIAN, 1993). The Karhunen-Loeve approach, the theoretical basis for EOF techniques, represents these space-time patterns as a set of eigenvectors, or normal modes, of an equal-time correlation function, their associated time series, and N total eigenfrequencies, where N is the total number of locations. The eigenvectors provide information about the spatial correlations of the patterns; the time series characterize each eigenvectors temporal pattern; the eigenfrequencies provides information about how often they occur in the data. In a number of applications, a complex, linear correlation operator is constructed in order to extrapolate future system

behavior such as the El Nino southern oscillation (PENLAND and MAGORIAN, 1993). Here we apply this decomposition method to historical seismicity data in southern California in order to identify basis patterns for all possible space-time seismicity configurations. These basis states are a complete, orthonormal set of eigenvectors and associated eigenvalues that are obtained from the diagonalization of the correlation operators computed for this regional historic seismicity data.

Time Period 1932 through August, 1999.

In our first analysis example, the time period starting in 1932 and continuing through the end August of 1999 was analyzed using the entire data set, including the entire areal extent and events of all quality. Figure 3a is a plot of the first 25 normalized eigenvalues, while Figure 3b is the first 1000 normalized eigenvalues, plotted on a log-log scale. Figure 4 shows the first two modes for southern California, for this data set. The absolute maximum value in each plot is normalized to one, where squares are positive and diamonds are negative, i.e. squares and diamonds are anticorrelated. The correct interpretation is that while a square location is “on”, a diamond location is “off”, and vice versa. The first mode is effectively a background hazard map, where small events are correlated with each other throughout southern California, while the second mode is the Landers event. The accompanying PC time series are shown in Figures 4a and 4c. The influence of spatial and temporal variations due to the density and completeness of network coverage is visible in the PC time series. For example, note the distinctive wave associated with the Landers sequence and its large numbers of aftershocks, punctuated by the occurrence of the Northridge event.

Figure 4d shows the second KLE mode. Here the region surrounding the 1992 Landers event is “on” (squares) whereas the rest of the southern San Andreas fault system is “off” (dia-

monds). The Coalinga earthquake is visible in this mode, and an apparent correlation between Landers and a set of events in eastern Nevada is revealed. As can be seen in Figures 5 and 6, a number of the KLE eigenpatterns are lower order harmonics of the second mode. Interestingly, Figure 6b, KLE7, illustrates the correlations between the North Palm Springs event and other major southern California earthquake, but with minimal correlation with the Landers sequence.

Typically, the higher order KLE modes display signal on shorter spatial and temporal scales than the initial, lower modes. This is illustrated in Figure 6. Figure 6c, KLE8, is a smaller scale harmonic of Figure 6a, KLE6, while KLE9, Figure 6d, shows the Landers sequence, essentially isolated, with the Joshua Tree earthquake anticorrelated with the Landers event to the north and Big Bear to the northwest.

Time Period: 1932 through December, 1991.

One of the interesting questions which arises in studying the results above is how exactly the dominance of the Landers sequence, and its associated instrumentation, affects the eigenpatterns. This encouraged the removal of that event from the data set by cutting off the time series before its occurrence, at the end of 1991. For this time period, 1932 to 1991, the time series interval was again one day, so that the total number of time steps is approximately 21,535. Again, all locations from the entire database, and all quality events, were included in the decomposition, so that the number of location time series is 3621. Figure 7a shows the first 25 normalized eigenvalues, while Figure 7b is the first 1000 normalized eigenvalues, plotted on a log-log scale. The eigenvalue plot is now smoother, without the large drop after the first mode that was a function of the large wave in the first PC time series generated by the Landers aftershocks (see Figure 4b).

KLE modes one and two are shown in Figure 8, where KLE1 is the mode associated with background seismicity. As expected, there is no large signal for Landers visible in Figure 8b. In addition, many of what were the lower modes in the previous analysis have moved up in the eigenvalue ranking, replacing the large number of Landers harmonics. KLE2 (Figure 8d) is the 1983 Coalinga earthquake, anticorrelated with the 1986 Oceanside and North Palm Spring events. The 1971 San Fernando event is a single diamond, correlated with the Coalinga earthquake.

Figure 9 again demonstrates both the addition of lower order harmonics and increasingly smaller spatial and temporal scales with increasing mode number. The fourth KLE mode shown in Figure 9a is the 1987 Superstition Hills and Elsinore ranch events correlated with the Whittier Narrows earthquake and anticorrelated with the North Palm Springs and Oceanside events. Figure 9b, KLE mode five, also shows the North Palm Springs and Oceanside events correlated with each other. In KLE7, Point Mugu appears correlated with the 1971 San Fernando event. The Tejon Ranch earthquake of 1988, in addition to the 1979 Homestead Valley earthquake, south of Landers, is also correlated with these events, while Imperial Valley is anticorrelated with these events. KLE8 again shows the 1979 Homestead Valley event, now anticorrelated with Point Mugu. Note the arcuate structure, which cuts across the faults at the location of the 1992 Landers earthquake. This is a feature of the local seismicity that has only been recognized in recent years with the occurrence of the 1992 Landers sequence and the 1999 Hector Mine earthquake, but which was clearly visible in this decomposition as early as 1991 (Figure 9d). It should be noted again that *no seismicity data after December, 1992, is included in this analysis*.

Analysis of this same data set, 1932 through 1991, but with a magnitude cut of 3.0 applied to the data, yields the KLE modes shown in Figures 10 and 11. The application of a magnitude cut has allowed events from earlier in the data set to have a greater prominence. Interestingly, while the background mode has dropped out, the first mode is not Coalinga, the second mode in the entire data set (see Figure 8b above), but the 1971 San Fernando event. The 1983 Coalinga earthquake is now the third KLE mode, behind the 1969 Avila Beach earthquake (see Figure 10). The correlation between the 1979 Imperial Valley and 1987 Superstition Hills sequence is the fourth mode. The 1952 Kern County event has appeared as the seventh mode (Figure 11a), while the eighth mode is also new to the decomposition - the 1968 Borrego Mountain earthquake (Figure 11b). Figure 11 also shows KLE modes ten and eleven, now harmonics of the earlier modes, on smaller spatial and temporal scales. One interesting feature of KLE mode 11 is the anticorrelation between the 1983 Coalinga event and the historic location of the Parkfield earthquake to the west, which has not taken place in recent years as expected. This mode supports speculation that the Coalinga event delayed its occurrence.

Precursory Modes

The presence of both large and small scale correlations in the data, evident in the KLE decompositions shown above, prompted a study of the change in these modes for each year, in an attempt to identify modes which consistently appear over some identifiable time period prior to an event. While a complex rate correlation operator, $K(x_i, x_j)$, can be used to compute the probability of future events on a fault patch model producing events over time periods of thousands of years (RUNDLE *et al.*, 2000a), its application to historic seismicity data is limited. Neither the long time periods nor the large number of moderate to large events produced by numerical simu-

lations are available in the actual data, nor is the same accuracy in time and space possible. Consequently, the following method was developed.

If the seismicity in a given year, S is known, and the eigenmodes, or eigenvectors e_i , are calculated using all seismicity data ($i = 1, \dots, N$, $N = 3621$ sites), then the eigenvectors are a complete, orthonormal set of basis functions, and any seismicity over that space can be decomposed into those eigenvectors.

$$S = \sum_{i=1}^N \alpha_i e_{ji},$$

where α_i are the eigenvalues for that particular year. The eigenvalues, α_i , are then computed from

$$\alpha_i = \sum_{i=1}^N e_{ji} S_i.$$

Computing the α_i for any given year, given the KLE decompositions above, is a relatively simple process. The data set used was that described above, for the time period 1932 through 1991, with a magnitude cutoff of 3.0. The resulting $(\alpha_i)^2$, i.e. the power spectrum of the eigenmodes, for each year prior to the 1992 Landers sequence, are plotted in Figure 12. Note again, that no data after December of 1991 is included in this analysis. Events that occur in the data set, for example, the 1979 Imperial Valley event or the 1983 Coalinga earthquake, have signal in the

corresponding eigenmodes, and would be expected to produce signal prior to those events. In addition, several of the higher order eigenmodes, on smaller spatial and temporal scales, appear to change in a large way over the several years prior to 1992. Interestingly, a number of the modes that increase are those that include signal for the 1992 Landers earthquake sequence. For example, in Figure 13 is shown KLE modes 46, 49, 58, and 62, which, while noisy, contain significant correlations for the Joshua Tree, Landers and Big Bear events.

Figure 14 shows the $(\alpha_i)^2$, plotted for the seismicity over each year, summed sequentially from 1987 through 1991. Systematic changes now appear in the $(\alpha_i)^2$. These show the growth in the smaller scale Landers modes over time, as the fault system becomes increasingly correlated prior to the 1992 event. Again, it is important to remember that no data after December 31, 1991, is included in the analysis of either these eigenmodes or the associated $(\alpha_i)^2$.

Note that a multidimensional vector can be formed from the seismic activity by assuming that each of the locations on the grid of southern California is one of the dimensions, and that as the amount of seismicity at each location changes in time, the vector undergoes a rotation about some mean. If the seismicity patterns, as described by the correlations in the $(\alpha_i)^2$, are undergoing a systematic change due to the growth of precursory modes, such as seen in Figures 12 and 14, then the vector is no longer experiencing a random walk about some mean. It undergoes a persistent rotation away from that mean that is quantifiable and can be converted into a probability of current and future events.

Probability of an Earthquake

Our simulations have suggested that the correlations in the seismicity represented by the KLE modes above can be described by phase dynamics. Phase dynamics is a method used in various branches of physics to describe the behavior of important parameters of the physical system (FUKUNAGA, 1970; MORI and KURAMOTO, 1998). Variables in many dynamical systems can be characterized by using this phase dynamical technique, represented as a phase function that involves both amplitude and phase angle. Changes in the amplitude of the phase function are unimportant, or not relevant. Examples of pure phase dynamical systems in the classical world include weak turbulence in fluids and reaction-diffusion systems. Another non-classical example is a quantum system in which the wave function is the phase function.

In the case of earthquake fault systems, the important changes in seismicity are associated primarily with rotations of the vector phase function in a high-dimensional correlation space. Using the assumption that seismicity is an example of pure phase dynamics, it follows that ΔP can be calculated from the square of the phase function for the associated pattern state vector (RUNDLE *et al.*, 2000a). It should therefore be possible to compute the increase in probability of observing an anomalous correlation, ΔP , directly from the observed seismicity data and its rotation. To emphasize the connection to phase dynamics, we call the function ΔP the Phase Dynamical Probability Change (PDPC) (TIAMPO *et al.*, 2000).

The technique described here is not a model, rather it is a new method for processing seismicity data to reveal underlying space-time structure. The purpose of the remainder of this paper is to exhaustively test the method, without regard to its formulation, and to apply it to the forecast of future earthquakes.

The seismicity data employed in our analysis is the same as that used above. Using only the subset of this data at locations \mathbf{x} in southern California and covering the period from January 1, 1932 through December 31, 1991, we compute the PDPC function $\Delta\mathbf{P} = \Delta\mathbf{P}(x_i, 1932, 1991)$ for detecting anomalous spatial correlations at sites in southern California *prior* to January 1, 1992. Note that we use only events having magnitude $M \geq 3$, to ensure completeness of the catalog. The hypothesis to be tested is that these anomalous correlated regions are associated with large main shocks that occurred *after* January 1, 1992. Figure 15a showed the relative seismic activity for this period, $\mathbf{S}(x_i, 1932, 1991)$, superimposed on a map of southern California. The intensity scale is logarithmic, where the scale value indicates the exponent, to the base ten, of the grayscale intensity value. It is clear that $\mathbf{S}(x_i, 1932, 1991)$ is an unremarkable function. For example, there is little evidence of any phenomena precursory to the $M \sim 7.3$ Landers, California event that occurred on June 28, 1992.

Figure 15b shows the PDPC anomalies in southern California for the time period 1978 to 1991. Note that no data after December of 1991 was used in this analysis. The triangles denote events of $M > 5$ which go off during this time period, while the open circles are events which occur after 1991. Note the frequent occurrence of large earthquakes at the locations of increased relative probability.

Figure 15b shows plots of all $\Delta\mathbf{P} > 0$, using only existing seismicity data acquired *prior* to January 1, 1992, six months before the occurrence of the Landers earthquake sequence. The increase in $\Delta\mathbf{P}$ above the background level, as measured by μ_P , the spatial mean of $\Delta\mathbf{P}$, should be interpreted as the formulation of a spatially coherent region of either anomalous activation or quiescence, associated with an increased chance of a major earthquake. The scale is again loga-

rithmic, scaled to the largest value of ΔP on any of Figure 15b. ΔP indicates only a relative, not an absolute change in probability. The inverted triangles represent events that occurred during the time period covered by the plot, indicating locations associated with large events that are present in the data used to construct ΔP . At a minimum, the method should identify areas of increased ΔP associated with the triangles, and it is clearly successful. Of most interest are regions of increased ΔP with no triangles near them. According to our hypothesis, these locations may represent sites for future large earthquakes.

We then superimpose on this map the locations of main shocks larger than 5.0 that occurred between January 1, 1992 and November 1, 1999, that is, the ~ 8 years *following* the time interval from which we computed the probabilities. Black circles denote these locations. One can observe an obvious correspondence between regions of increased probability and the location of the subsequent main shocks, tending to support the results first observed in our simulations. Included are circles representing the 1992 Landers sequence, the 1994 Northridge earthquake, and the recent Hector Mine event. These earthquakes are evidently associated with a long-lived arcuate structure cutting across the local fault system.

Figure 15b shows that the recent large earthquakes occurring *after* January 1, 1992 are associated with areas of $\Delta P > 0$ that formed *prior* to January 1, 1992. In particular, a bright area has developed close to the epicenter of the Joshua Tree event, latitude 33.95° , longitude 243.7° , which occurred in April of 1992. The anomalous area north of that location corresponds to the Landers earthquake sequence of June 1992. The epicenter of the recent October 16, 1999, M \sim 7.0 Hector Mine also occurred on the northernmost end of that anomaly.

There is clearly variability, particularly for smaller events, depending on the choice of time interval. Larger events tend to be associated with larger anomalous regions that form earlier and persist longer after the main shock. Since earthquake fault dynamics are now believed to be associated with critical phenomena (RUNDLE and KLEIN, 1995; GELLER *et al.*, 1997; KLEIN, *et al.*, 1997) we hypothesize that there may be a scaling relation between the area A of the correlated region and the time interval τ prior to the main shock at which the anomalous correlation begins to form, such that $\tau \propto A^\eta$, where η is a critical exponent near 1. Since the linear size of our location grid boxes is approximately 11 km, one should not expect events significantly smaller than $M \sim 6$, whose characteristic linear source dimension is 10 km, to be well resolved by our procedure. Yet even the smaller circles associated with $M \sim 5 - 6$ events often seem to occur in proximity to these anomalous areas. One such example is the China Lake event that occurred at approximately latitude 36.75° , longitude 242.25° . Here we also should note that a number of the anomalies correspond to events with magnitude less than 5, but that display persistent moderately seismicity, such as the Durrwood Meadows swarm, highlighted with a black square, at 35.5° latitude, 241.75° longitude. This set of events, which included an earthquake of magnitude 4.9, occurred from late 1983 through mid-1984.

These results suggest that the anomalies are correlated with total seismic moment release. The large, intense anomaly associated with the Coalinga event in 1983, for example, was followed by numerous aftershocks of magnitude 5.0 or greater. While there are earthquakes of $M > 5$ which occur without the formation of an area of increased probability (“false negatives”), this may be the result of a lower total seismic moment release. In the future, we will investigate whether this technique can be extended to estimate the potential magnitude and time of occur-

rence of forecast events from both the sizes of the candidate source regions and the temporal persistence and duration.

Likelihood Tests

To test the hypothesis that the formation of correlated regions of anomalous activity can be identified by our method, and are related to future large events, we carried out thousands of likelihood ratio tests (BEVINGTON and ROBINSON, 1992; GROSS and RUNDLE, 1998) on the method using values of ΔP obtained from random seismicity catalogs that were used as null hypotheses. In the likelihood ratio test, a probability density function (PDF) is required. For our PDF we used a Gaussian distribution whose width is that of our original location grid, approximately 11 km, and whose peak value is given by $\Delta P + \mu_P$, because in a likelihood ratio test the value of probability at all sites must be positive. The log likelihood is then calculated for the circles, which identify the locations of future events, as shown in Figure 15b, and provides a measure of how well the colored regions predict the actual events as quantified by the locations of the circles.

Each random catalog was constructed from the instrumental catalog by using the same total number of events, but assigning occurrence times from a uniform probability distribution over the years 1932-1991, and distributing them uniformly over the original locations. This procedure produces a Poisson distribution of events in space with an exponential distribution of interevent times. Randomizing the catalog in this way destroys whatever coherent space-time structure may exist in the data, *thus effectively declustering the catalog*. While random “Poisson clustering” may remain, there will be no “Omori clustering” left in these catalogs.

Likelihood ratio tests were then performed on thousands of such random catalogs, comparing calculations of ΔP from the actual catalog with calculations of ΔP from each random catalog. Success of the prediction is scored by how well the circles are forecasted by the colored areas. The better the prediction, the larger the likelihood value. Figure 16 shows the distribution of likelihood values for five hundred of the random catalogs, for the same time period as shown in Figure 15b. Superimposed on this plot as a dashed line is the likelihood ratio value for Figure 15b, computed from the actual catalog. One can see that the value of likelihood computed from the actual catalog is always substantially better than likelihoods computed from the random catalogs.

For purposes of illustration, we compute ΔP for one random catalog whose likelihood value is close to the mean of the distribution in Figure 16, as shown in Figure 15c. One can see that there are many more anomalous areas in Figure 15c than in Figure 15b, these regions are far more broadly distributed in space, and contain many more dark areas. The specific likelihood value for Figure 15b equals -311.665 , whereas that for Figure 15c equals -363.344 . These values correspond to a likelihood ratio $e^{51.68} \approx 10^{22.44}$, indicating that the locations of increased probability obtained from the actual instrumental catalog are far more likely to be associated with the locations of the circles than those obtained from the random catalog. The physical reason for this large ratio is that the likelihood test invokes a penalty for predictions that are not sufficiently near to the circles ("false positives"), and there are many more such locations in Figure 15c than in Figure 15b.

In addition, we computed the likelihood ratio using Figure 15a, as the null hypothesis that may be taken to correspond to a map of relative hazard based upon recent instrumental seismic

intensity. The likelihood value for this map is -322.557 , equating to a likelihood ratio of $e^{11.22} \approx 10^{4.87}$. When compared to the computations for Figure 15b, this suggests that our method is far more successful at forecasting the locations of future major earthquakes than the current practice of relying on hazard maps to predict broad areas of increased seismic potential. From these statistical tests, we conclude that there are coherent, anomalous space-time correlation structures in the instrumental catalog that our method identifies, and that these correlations are effectively destroyed by the common practice of declustering seismicity catalogs.

Discussion

We emphasize that while our method may identify higher risk areas, there is no certainty at this time that every location of increased $\Delta\mathbf{P}$ will be located near the site of a future large earthquake. There are a number of examples in Figure 15b where a colored area appears without the occurrence of a major earthquake between 1992 and 1999 ("false negative"). One example appears near 34° latitude, 244.25° longitude. Further attempts at optimization of the method must focus on better spatial location of events and minimizing the numbers of both false positives and false negatives.

As discussed below, we have seen that regions with $\Delta\mathbf{P} > 0$ may correspond either to anomalous seismic activity or anomalous quiescence. In some locations, a region that had been the site of a recent major earthquake may evidently indicate values of $\Delta\mathbf{P} > 0$ that are linked with a future large event that will occur at a neighboring, but somewhat disjoint, location. The positive value of $\Delta\mathbf{P}$ may appear only at the location of the past event, rather than at the neighboring location of the future event. In these cases, we have found that the neighboring aftershock zone

of the past event is participating in the anomalous activity or quiescence that defines the future event. In addition, it is possible that anomalous activation or quiescence may appear in events having magnitudes less than the uniform cutoff we use, $M = 3$. While we have performed this analysis with other magnitude cuts and have found the results to be relatively insensitive between values of 2.5 and 4.0, this may not apply to other tectonic settings, based on the quality of the data available. The appropriateness of various magnitude cutoffs should therefore be tested in future work.

An example of these effects is the anomalous area at the location of the 1971 San Fernando earthquake, shown in Figure 15b, that is evidently associated with the coming 1994 Northridge event. This area is present *not* because it represents aftershock activity from the 1971 San Fernando event (anomalous seismic activity), rather it represents an area of relative anomalous quiescence. To further illustrate the point that the San Fernando region is anomalously quiescent prior to Northridge, we plot the change in the phase function $\Delta\hat{S}(x_i, 1978, 1991)$, as defined in the method section above, over the years 1978-1991. In Figure 17, a positive value of $\Delta\hat{S}$ represents anomalous seismic activity, and a negative value of $\Delta\hat{S}$ represents anomalous quiescence. The intense anomaly near Northridge-San Fernando seen in the plot of $\Delta\mathbf{P}$ in Figure 15b is seen to be negative in Figure 17, indicating that the positive value of $\Delta\mathbf{P}$ arises from anomalous quiescence in the San Fernando aftershock zone. In addition, it will be seen below that the construction of $\Delta\mathbf{P}(x_i, 1978, 1991)$ actually subtracts away the effect of any changes in seismicity prior to 1978, so San Fernando aftershock activity between 1971-1978 does not contribute to the calculation. Figure 17 also shows that the 1983 Coalinga earthquake displays seismic activation, as would be expected since it occurred during this time period, while the Landers sequence is a mix of anomalous quiescence and activation. These results support the conclusion that the PDPC

function does not simply identify areas associated with past events and their aftershock sequences, rather it quantifies the underlying stress coherence and correlations associated with the regional seismicity.

Finally, we calculate the PDPC for all of California over three additional time periods. Figure 18a shows the increased probability for the time period 1968 through 1978. Again, the intensity scale is as shown in Figure 15, and the inverted triangles represent those events that occur during the time period, while the open circles are those earthquakes that occur in over the next ten years. Despite the sparser networks in place in California at that time, which affects the spatial completeness of the catalog, the 1979 Imperial Valley earthquake, $M = 6.4$, occurs near a bright set of anomalies, which includes anomalies for the 1987 Superstition Hills and Elmore Ranch events. Also clearly visible is the upcoming 1983 Coalinga event at 36.25° latitude, 239.75° longitude, a previously unanticipated hidden thrust event.

Figure 18b shows the PDPC for the time period 1978 through 1988. Clearly visible is another relatively unexpected event at the time, the 1989 Loma Prieta earthquake. The epicenter of the main shock occurs within 10 kms of the nearest anomaly, which extends down through the aftershock zone. Again, the Durrwood Meadows swarm, at 35.5° latitude, 241.75° longitude, including one earthquake of magnitude 4.9, is plotted as a square box.

Finally, Figure 19 shows a forecast for roughly the next ten years, using a white to yellow to red logarithmic intensity scale. The PDPC analysis is performed for the time period 1989 through 1999. The persistent anomaly located at the northeast end of the White Wolf Fault, 35.25° latitude, 241.5° longitude, corresponds to an area of recurrent seismicity throughout the

1980s and 1990s, which may represent the birth of a newly forming structure, a blind strike-slip fault connecting the Kern County and Walker Pass, California, earthquakes (BAWDEN *et al.*, 1999). Or, the orange zones at 33° latitude, 244° longitude, may identify a silent earthquake that occurred in the mid-1990s at that location (Paul Vincent, personal communication). Note that the northwestern most anomaly, at 38.75° latitude, 237.2° longitude, identifies the location of a series of events, $M = 4$, followed by a number of smaller events, which occurred in January of 2000.

Figure 19 identifies some areas that may be destined for activity in the next 5-10 years. For example, the yellow area just to the north of the 1988 Loma Prieta event, along the southern Hayward fault, is one potential area of concern. However, in agreement with deformation work by Burgmann *et al.*, 2000, the northern section of the Hayward fault shows a lesser potential for an independent event. In southern California, the area just to the north of the 1992 Landers sequence, as well as the site of the 1983 Coalinga earthquake, display a large PDPC anomaly. Finally, several areas of relative probability increase are visible along the southern San Andreas and San Jacinto faults. We must point out that, for reasons already detailed, absolute probabilities cannot be attached to these anomalies at this time. In addition, these anomalies represent areas of varying seismic activity - it is possible that some or all of these locations may represent areas of either recurring moderate events of magnitude less than 5.0, or locations of silent earthquakes occurring between 1989 and 1999. Finally, the occurrence of one or more of these events could modify the underlying dynamics of the system, requiring the revision of subsequent forecasts into the future.

Conclusions

This pattern dynamics approach that we have applied to historical seismicity data in southern California reveals a wealth of interesting spatial patterns. In particular, it provides a new methodology for classifying all of the possible seismicity patterns that can exist in terms of mutually orthogonal eigenstates. In fact, a number of the descriptive patterns cited earlier can be readily identified among the eigenstates depicted in Figures 4 through 12. For example, Figure 4d can be interpreted either as seismic activation within the Landers epicentral region, or else as quiescence near Landers coincident with seismic activity surrounding the region, i.e. a ``Mogi donut".

Our results argue strongly for the development of realistic numerical simulations of fault systems such as those in southern California (RUNDLE, 1988; TIAMPO *et al.*, 1999; RUNDLE *et al.*, 2000a). Because the historic data set is incomplete worldwide, construction of such numerical simulations is necessary to more accurately define the most significant eigenpatterns, which can be applied to understanding the nature of the observed seismicity. For example, while a magnitude cutoff of 3.0 may be appropriate for southern California, it may not be applicable for other tectonic settings. Simulations can help to better define the sensitivity of the analysis to parameters such as this.

Moreover, computer simulations will be of critical importance for relating the observable pattern basis set for the seismicity data to the pattern basis set for stress, strains, and displacements through time. While seismicity is readily observable by standard methods, stress and strain within the earth are not. However, stress and strain are the primary dynamical variables, and are also the Markov variables in which the underlying nonlinear dynamics are almost certainly for-

mulated. It will be most important to relate a readily observable, seismicity pattern basis set to the actual, unobservable dynamical pattern basis set, so that mode-shaping techniques can be applied to the underlying dynamics (FUKUNAGA, 1970; HOLMES *et al.*, 1996). In this manner it may be possible to characterize the spatially coarse-grained features of local and regional stress levels, coefficients of friction, failure and residual stress levels, and fault interactions. Finally, RUNDLE *et al.* (2000a), demonstrated using simulations that such methods can in principle forecast future events with accuracies considerably better than a standard Poisson process. With the development of a quantitative, readily reproducible technique for characterizing all possible seismicity patterns, these methods may allow us to test the hypothesis that large damaging earthquakes on a given subset of faults are preceded by one of a small set of characteristic precursory seismicity patterns. If this hypothesis is true, then it may well be possible to develop a quantitative method to forecast large, infrequent events using the patterns of seismic activation and quiescence associated with smaller, more frequent events on local and regional fault systems.

Finally, our results suggest that systematic variations in seismicity prior to recent southern California earthquakes can be observed. Our method employs data from existing seismic monitoring networks as well as a theoretical understanding obtained from numerical computer simulations to identify anomalous activity or quiescence in seismicity. These space-time patterns in the seismic activity directly reflect the existence of correlated structure in the underlying stress and strain fields, a necessary precondition for the occurrence of large earthquakes. While at this time we offer this forecast for scientific evaluation only, depending on the nature of future seismicity in the region, as well as ongoing modifications and extensions of the theory and technique, this procedure may prove a useful tool for forecasting seismic activity.

Acknowledgements

This work has been supported by CIRES and NASA student fellowships to KFT and SM; by US DOE grant DE-FG03-95ER14499 to JBR. Research by WK was supported by US DOE/OBES grant DE-FG02-95ER14498 and W-7405-ENG-6 at LANL. WK would like to acknowledge the hospitality and support of CNLS at LANL.

References

- Aubrey, D.G. and Emery, K.O., 1983. Eigenanalysis of recent United States sea levels, Continental Shelf Research, **2**, 21-33.
- Bak, P. and Tang, C., 1989. Earthquakes as a self-organized critical phenomena. J. Geophys. Res., **94**, 15,635-15637.
- Bawden, G.W., Michael, A.J., Kellogg, L.H. Birth of a fault: Connecting the Kern County and Walker Pass, California, earthquakes, Geology, **27**, 601-601 (1999).
- Bakun, W.H., King, G.C.P., and Cockerham, R.S., 1986. Seismic slip, aseismic slip, and the mechanics of repeating earthquakes on the Calaveras fault, California. Earthquake Source Mechanics, AGU Monograph, AGU, Washington, D.C., 195-208.
- Bakun, W.H., and McEvilly, T.V., 1984. Recurrence models and Parkfield, California, earthquakes. J. Geophys. Res., **89**, 3051-3058.
- Bowman, D.D., Ouillon, G., Sammis, C.G., Sornette, A., and Sornette, D., 1998. An observational test of the critical earthquake concept. J. Geophys. Res., **103**, 24,359-24,372.
- Brehm, D.J. and Braile, L.W., 1999. Intermediate-term earthquake prediction using the modified time-to-failure method in southern California. BSSA, **89**, 275-293.

- Bufe, C.G. and Varnes, D.J., 1993. Predictive modeling of the seismic cycle of the greater San Francisco bay region. *J. Geophys. Res.*, **98**, 9871-9883.
- Burgmann, R., et al. (2000) Earthquake potential along the northern Hayward fault, California, *Science*, **289**, 1178-1182.
- Deng, J.S. and Sykes, L.R., 1996. Triggering of 1812 Santa Barbara earthquake by a great San Andreas shock: Implications for future hazards in southern California. *Geophys. Res. Lett.*, **23**, 1155-1158.
- Dieterich, J.H., 1994. A constitutive law for rate of earthquake production and an application to earthquake clustering. *J. Geophys. Res.*, **1994**, 2601-2618.
- Dodge, D.A., Beroza, G.C., and Ellsworth, W.L., 1996. Detailed observations of California foreshock sequences: Implications for the earthquake initiation process. *J. Geophys. Res.*, **101**, 22,371-22,392.
- Ellsworth, W.I., and Cole, A.T., 1997. *Seis. Res. Lett.*, **68**, 298.
- Ellsworth, W.I., Cole, A.T., & Dietz, L (1998). Repeating earthquakes and the long-term evolution of seismicity on the San Andreas fault near Bear Valley, California. *Seis. Res. Lett.*, **69**.
- Eneva, M. and Ben-Zion, Y., 1997. Techniques and parameters to analyze seismicity patterns associated with large earthquakes. *J. Geophys. Res.*, **102**, 17,785-17,795.
- Evison, F. F. Fluctuations of seismicity before major earthquakes. *Nature*, **266** (1977).
- Ferguson, C., Klein, W., and Rundle, J.B., 1999. Spinodals, scaling and ergodicity in a model of an earthquake fault with long-range stress transfer. *Phys. Rev. E.*, **60**, 1359-1373.
- Fisher, D.S., Dahmen, K., Ramanathan, S., and Ben-Zion, Y., 1997. Statistics of earthquakes in simple models of heterogeneous faults. *Phys. Rev. Lett.*, **78**, 4885-4888.
- Frohlich, C., 1987. Aftershocks and temporal clustering of deep earthquakes. *J. Geophys. Res.*, **92**, 13,944.

- Fukunaga, K., 1970. Introduction to Statistical Pattern Recognition, Academic Press, N.Y.
- Garcia, A. and Penland, C., 1991. Fluctuating hydrodynamics and principal oscillation pattern analysis. *J. Stat. Phys.*, **64**, 1121-1132.
- Geller, R.J., Jackson, D.D., Kagan, Y.Y., & Mulargia, F (1997). Enhanced: earthquakes cannot be predicted. *Science*, **275**.
- Gomberg, J., 1996. Stress/strain changes and triggered seismicity following the M_W 7.3 Landers, California, earthquake. *J. Geophys. Res.*, **101**, 751-764.
- Grant, L. and Sieh, K., 1994. Paleoseismic evidence of clustered earthquakes on the San Andreas fault in the Carrizo Plain. *J. Geophys. Res.*, **99**, 6819-6842.
- Gray, C.M., 1997. Synchronous oscillations in neuronal systems: Mechanisms and functions. *Pattern Formation in the Physical and Biological Sciences*, Lecture Notes V, SFI, Addison-Wesley, Reading, MA, 93-134.
- Gross, S.J. and Kisslinger, C., 1994. Tests of models of aftershock rate decay. *BSSA*, **84**, 1571-1579.
- Gross, S. and Rundle, J.B., 1998. A systematic test of time-to-failure analysis. *Geophys. J. Int.*, **133**, 57-64.
- Haberman, R.E., 1981. Precursory seismicity patterns: stalking the mature seismic gap. *Earthquake Prediction: An International Review*, AGU Monograph, AGU, Washington, D. C. 29-42.
- Hertz, J., Korgh, A., and Palmer, R.G., 1990. *Introduction to the Theory of Neural Computation*, Lecture Notes I, SFI, Addison-Wesley, Reading, MA.
- Herz, A.V., and Hopfield, J.J., 1995. Earthquake cycles and neural reverberations: Collective oscillations in systems with pulse-coupled threshold elements. *Phys. Rev. Lett.*, **75**, 1222-1225.

- Hill, D., Eaton, J.P., and Jones, L.M., 1990. Seismicity, 1980-86. The San Andreas Fault System, California, USGS Prof. Paper 1515, U.S. GPO, Washington, D.C., 115-152.
- Hill, D.P., Johnston, M.J.S., Langbein, J.O., and Bilham, R., 1995. Response of Long Valley caldera to the $M_w = 7.3$ Landers, California, earthquake. J. Geophys. Res., **100**, 12,985-13,005.
- Hill, D.P. et al. (1993). Seismicity remotely triggered by the magnitude 7.3 Landers, California, earthquake. Science, **260**.
- Hill, D.P., Reasenberg, P.A., Michael, A., Arabaz, W.J., Beroza, G., Brumbaugh, D., Brune, J.N., Castro, R., Davis, S., Depolo, D., Ellsworth, W.L., Gomberg, J., Harmsen, S., House, L., Jackson, S.M., Johnston, M.J.S., Jones, L., Keller, R., Malone, S., Munguia, L., Nava, S., Pechmann, J.C., Sanford, A., Simpson, R.W., Smith, R.B., Stark, M., Stickney, M., Vidal, A., Walter, S., Wong, V., and Zollweg, J., 1993. Seismicity remotely triggered by the Magnitude 7.3 Landers, California, earthquake. Science, **260**, 1617-1623.
- Holmes, P., Lumley, J.L., and Berkooz, G., 1996. Turbulence, Coherent Structures, Dynamical Systems and Symmetry, Cambridge University Press, Cambridge, U.K.
- Hotelling, H., 1933. Analysis of a complex of statistical variables into principal components. Jour. Educ. Psych., **24**, 417-520.
- House, L.S., Sykes, L.R., Davies, J.N., and Jacob, K.H., 1981. Identification of a possible seismic gap near Unalaska Island, eastern Aleutians, Alaska. Earthquake Prediction: An International Review, AGU Monograph, AGU, Washington, D. C. 81-92.
- Huang, Y., Saleur, H., Sammis, C., and Sornette, D., 1998. Precursors, aftershocks, criticality and self-organized criticality, Europhys. Lett., **41**, 43-49.
- Jaume, S.C. and Sykes, L.R., 1999. Evolving towards a critical point: a review of accelerating seismic moment/energy release prior to large and great earthquakes. Pure Appl. Geoph., **155**, 279-306.

- Jones, L.M. and Hauksson, E., 1997. The seismic cycle in southern California: Precursor or response? *Geophys. Res. Lett.*, **24**, no. 4, 469-472.
- Kagan, Y.Y. and Jackson, D.D., 1992. Seismic gap hypothesis, ten years after. *J. Geophys. Res.*, **96**, 21,419-21,431.
- Kanamori, H., 1981. The nature of seismicity patterns before large earthquakes. *Earthquake Prediction: An International Review*, AGU Monograph, AGU, Washington, D. C., 1-19.
- Kato, N., Otake, M., and Hirasawa, T., 1997. *Pure Appl. Geoph.*, **150**, 249.
- Kerr, R.A., 1998. A slow start for earthquakes. *Science*, **279**, 985.
- King, G.C.P., Stein, R.S., and Lin, J., 1994. Static stress changes and the triggering of earthquakes. *BSSA*, **84**, 935-953.
- Klein, W., Rundle, J.B., and Ferguson, C (1997). Scaling and nucleation in models of earthquake faults. *Phys. Rev. Ltrs.*, **78**, 3793-3796.
- Linde A.T., Gladwin, M.T., Johnston, M.J.S., Gwyther, R.L., and Bilham, R.G., 1996. A slow earthquake sequence on the San Andreas fault. *Nature*, **383**, 65-68.
- Lyzenga, G.A., Raefsky, A., and Mulligan, S.G., 1991. Models of recurrent strike-slip earthquake cycles and the state of crustal stress. *J. Geophys. Res.*, **96** 21,623-21,640.
- Main, I.G. Applicability of time-to-failure analysis to accelerated strain release before earthquakes and volcanic eruptions. *Geophys. J. Int.* **139**, 1999a.
- Main, I.G. Is the reliable prediction of individual earthquakes a realistic scientific goal? Nature website debate, http://helix.nature.com/debates/earthquake/equake_frameset.html 1999b.
- Marone, C., Vidale, J.E., and Ellsworth, W.L., 1995. Fault healing inferred from time-dependent variations in source properties of repeating earthquakes. *Geophys. Res. Lett.*, **22**, 3095-3098.
- McGuire, J.J., Imhle, P.F., and Jordan, T.H., 1996. Time-domain observations of a slow precursor to the 1994 Romanche transform earthquake. *Science*, **274**, 82-85.

- Moghaddam, B., Wahid, W., and Pentland, A., 1998. Beyond eigenfaces: probabilistic matching for face recognition. Third IEEE Intl. Conf. on Automatic Face & Gesture Recognition, 1-6.
- Mogi, K., 1969. Some features of recent seismic activity in and near Japan, (2) Activity before and after great earthquakes. Bull. Earthquake Res. Inst., Tokyo Univ., **47**, 395-417.
- Mogi, K., 1977. Seismic activity and earthquake predictions. Proc. Symp. on Earthquake Prediction, Seis. Soc. Japan, 203-214.
- Mogi, K. (1979). Two kind of seismic gaps. *Pageoph*, **117**.
- Mori H., & Kuramoto, Y (1998). Dissipative Structures and Chaos, Springer-Verlag, Berlin.
- Nanjo, K., Nagahama, H., and Satomura, M., 1998. Rates of aftershock decay and the fractal structure of active fault systems. Tectonophysics, **287**, 173-186.
- Nijhout, H.F., 1997. Pattern formation in biological systems. Pattern Formation in the Physical and Biological Sciences, Lecture Notes V, SFI, Addison Wesley, Reading, MA, 269-298.
- North, G.R., 1984. Empirical orthogonal functions and normal modes. Jour. Atm. Sc., **41**, no. 5, 879-887.
- Ouchi, T., 1993. Population dynamics of earthquakes and mathematical modeling. Pure Appl. Geophys., **140**, 15-28.
- Pacheco, J.F., Scholz, C.H., and Sykes, L.R., 1992. Changes in frequency-size relationship from small to large earthquakes. Nature, **355**, 71-73.
- Penland, C., 1989. Random forcing and forecasting using principal oscillation pattern analysis. Monthly Weather Review, **117**, 2165-2185.
- Penland, C. and Magorian, T., 1993. Prediction of Nino 3 sea surface temperatures using linear inverse modeling. J. Climate, **6**, 1067-1076.
- Penland, C. and Sardeshmukh, P.D., 1995. The optimal growth of tropical sea surface temperature anomalies. J. Climate, **8**, 1999-2024.

- Pollitz, F.F., and Sacks, I.S., 1997. The 1995 Kobe, Japan, earthquake: A long-delayed aftershock of the offshore 1944 Tonankai and 1946 Nankaido earthquakes. BSSA, **87**, 1-10.
- Preisendorfer, R.W., 1988. Principle Component Analysis in Meteorology and Oceanography, Elsevier, Amsterdam.
- Press, F. and Allen, C., 1995. Patterns of seismic release in the southern California region. J. Geophys. Res., **100**, 6421-6430.
- Press, W.H., Flannery, B.P., Teukolsky, S.A., and Vetterling, W.T., 1992. Numerical Recipes in C, 2nd Edition, Cambridge University Press, Cambridge, U.K.
- Richter, C.F. (1958). Elementary Seismology, Freeman, San Francisco.
- Romanowicz, B. and Rundle, J.B., 1993. On scaling relations for large earthquakes. BSSA, **83**, 1294-1297.
- Rundle, J.B., 1988. A physical model for earthquakes: 2. Applications to southern California. J. Geophys. Res., **93**, 6255-6274.
- Rundle, J.B., 1989. Derivation of the complete Gutenberg-Richter magnitude-frequency relation using the principle of scale invariance. J. Geophys. Res., **94**, 12,337-12,342.
- Rundle, J.B., 1993. Magnitude-frequency relation for earthquakes using a statistical mechanical approach. J. Geophys. Res., **98**, 21,943-21,950.
- Rundle, J.B., Gross, S., Klein, W., Ferguson, C., and Turcotte, D.L., 1997. The statistical mechanics of earthquakes. Tectonophysics, **277**, 147-164.
- Rundle, J.B., and Klein, W., 1995. New ideas about the physics of earthquakes. Rev. Geophys. Space Phys. Suppl. (July) **283**, 283-286.
- Rundle, J.B., Klein, W., and Gross, S., 1999. Physical basis for statistical patterns in complex earthquake populations: Models, predictions and tests, Pure Appl. Geoph., **155**, 575-607.

- Rundle, JB, Klein, W., Tiampo, K., and Gross, S., 2000a. Linear pattern dynamics in nonlinear threshold systems, Phys. Rev. E., **61**, 2418-2432.
- Rundle, J.B., Klein, W., Gross, S., & Tiampo, K.F. (2000b). Dynamics of seismicity patterns in systems of earthquake faults, *Geocomplexity and the Physics of Earthquakes*, AGU Monograph, Washington, D.C., 127-146.
- Saleur, H., Sammis, C.G., and Sornette, D., 1995. Discrete scale invariance, complex fractal dimensions, and log-periodic fluctuations in seismicity. J. Geophys. Res., **17**, 661-17,677.
- Savage, J.C., 1988. Principal component analysis of geodetically measured deformation in Long Valley caldera, eastern California, 1983-1987, J. Geophys. Res., **93**, 13,297-13,305.
- Savage, J.C., 1993. The Parkfield prediction fallacy. BSSA, **83**, 1-6.
- Scholz, C.H., 1990. The Mechanics of Earthquakes and Faulting, Cambridge University Press, Cambridge, U.K.
- Schwartz, D.P. (1984). Fault behavior and characteristic earthquakes – examples from the Wasatch and San Andreas fault zones. J. Geophys. Res., **89**.
- Sieh, K., Stuiver, M. and Brillinger, D., 1989. A more precise chronology of earthquakes produced by the San Andreas fault in southern California. J. Geophys. Res., **94**, 603-623.
- Stark, M.A. and Davis, S.D., 1996. Remotely triggered microearthquakes at The Geysers geothermal field, California. Geophys. Res. Lett., **23**, n. 9, 945-948.
- Stein, R.S., 1999. The role of stress transfer in earthquake occurrence. Nature, **402**, 605-609.
- Stein, R.S., King, G.C.P., and Lin, J., 1992. Change in failure stress on the southern San Andreas fault system caused by the 1992 Magnitude = 7.4 Landers earthquake. Science, **258**, 1328-1331.

- Swan, F.H., Schwartz, D.P., and Cluff, L.S., 1980. Recurrence of moderate to large magnitude earthquakes produced by surface faulting on the Wasatch fault zone, Utah. BSSA, **70**, 1431-1462.
- Tiampo, K.F., Rundle, J.B., Klein, W., and Gross, S.J., 1999. Systematic evolution of nonlocal space-time earthquake patterns in southern California. Eos Trans. AGU, **80**, 1013.
- Tiampo, K.F., Rundle, J.B., Klein, W., McGinnis, S., and Gross, S.J. Observation of systematic variations in non-local seismicity patterns from southern California. *Geocomplexity and the Physics of Earthquakes*, AGU Monograph, Washington, D.C. (2000).
- Turcotte, D.L., 1997. Fractals and chaos in geology and geophysics, 2nd edition, Cambridge University Press, Cambridge, U.K.
- Vautard, R. and Ghil, M., 1989. Singular spectrum analysis in nonlinear dynamics, with applications to paleodynamic time series. Physica D, **35**, 395-424.
- Wyss, M. & Haberman, R. E. (1988). Precursory quiescence before the August 1982 Stone Canyon, San Andreas fault, earthquakes. Pure Appl. Geophys., **126**.
- Wyss, M., Schorlemmer D., and Wiemer, S., 2000. Mapping asperities by minima of local recurrence time: San Jacinto-Elsinore fault zones. J. Geophys. Res., **105**, 7829-7844.
- Wyss, M., Shimazaki, K., and Urabe, T., 1996. Quantitative mapping of a precursory seismic quiescence to the Izu-Oshima 1990 (M6.5) earthquake, Japan. Geophys. Jour. Int., **127**, 735-743.
- Wyss, M. and Wiemer, S., 1999. How can one test the seismic gap hypothesis? The case of repeated ruptures in the Aleutians. Pure Appl. Geoph., **155**, 259-278.
- Yamashita, T. and Knopoff, L., 1989. A model of foreshock occurrence. Geophys. Jour., **96**, 389-399.

Captions

Figure 1: Seismicity for southern California, 1932-1991, normalized to the maximum number of events for the period.

Figure 2: Schematic diagram of threshold systems

Figure 3: a) The first 25 normalized eigenvalues, for the time period 1932-1999. b) The first 1000 normalized eigenvalues, plotted on a log-log scale.

Figure 4: First two KLE modes for southern California seismicity, 1932-1999. Diamonds are negative, square boxes are positive. a) PC time series for first KLE mode; b) first KLE mode, normalized to maximum; c) PC time series for second KLE mode; and d) second KLE mode, also normalized to the maximum.

Figure 5: KLE modes three and four for southern California seismicity, 1932-1999. a) PC time series for third KLE mode; b) third KLE mode, normalized to maximum; c) PC time series for fourth KLE mode; and d) fourth KLE mode, also normalized to the maximum.

Figure 6: KLE modes six through nine for southern California seismicity, 1932-1999, each normalized to its maximum. a) Sixth KLE mode; b) seventh KLE mode; c) eighth KLE mode; and d) ninth KLE mode.

Figure 7: a) The first 25 normalized eigenvalues, for the time period 1932-1991. b) The first 1000 normalized eigenvalues, plotted on a log-log scale.

Figure 8: First two KLE modes for southern California seismicity, 1932-1991. a) PC time series for first KLE mode; b) first KLE mode, normalized to maximum; c) PC time series for second KLE mode; and d) second KLE mode, also normalized to the maximum.

Figure 9: a) Fourth KLE mode; b) fifth KLE mode; c) seventh KLE mode; and d) eighth KLE mode for southern California seismicity, 1932-1991, each normalized to its maximum.

Figure 10: a) First KLE mode; b) second KLE mode; c) third KLE mode; and d) fourth KLE mode for southern California seismicity, magnitudes ≥ 3.0 , 1932-1991, each normalized to its maximum.

Figure 11: a) Seventh KLE mode; b) eighth KLE mode; c) tenth KLE mode; and d) eleventh KLE mode for southern California seismicity, magnitudes ≥ 3.0 , 1932-1991, each normalized to its maximum.

Figure 12: Eigenvalue power, $(\alpha_i)^2$, for the individual years 1987-1991, decomposed using eigenmodes derived using southern California seismicity, magnitudes ≥ 3.0 , 1932 through 1991.

Figure 13: a) KLE mode 46; b) KLE mode 49; c) KLE mode 58; and d) KLE mode 62 for southern California seismicity, magnitudes ≥ 3.0 , 1932-1991. The color scale is linear, blue to white to red, where blue is negative.

Figure 14: Eigenvalue power, $(\alpha_i)^2$, for the individual years summed from 1987 through 1991, decomposed using eigenmodes derived using southern California seismicity, magnitudes ≥ 3.0 , 1932-1991.

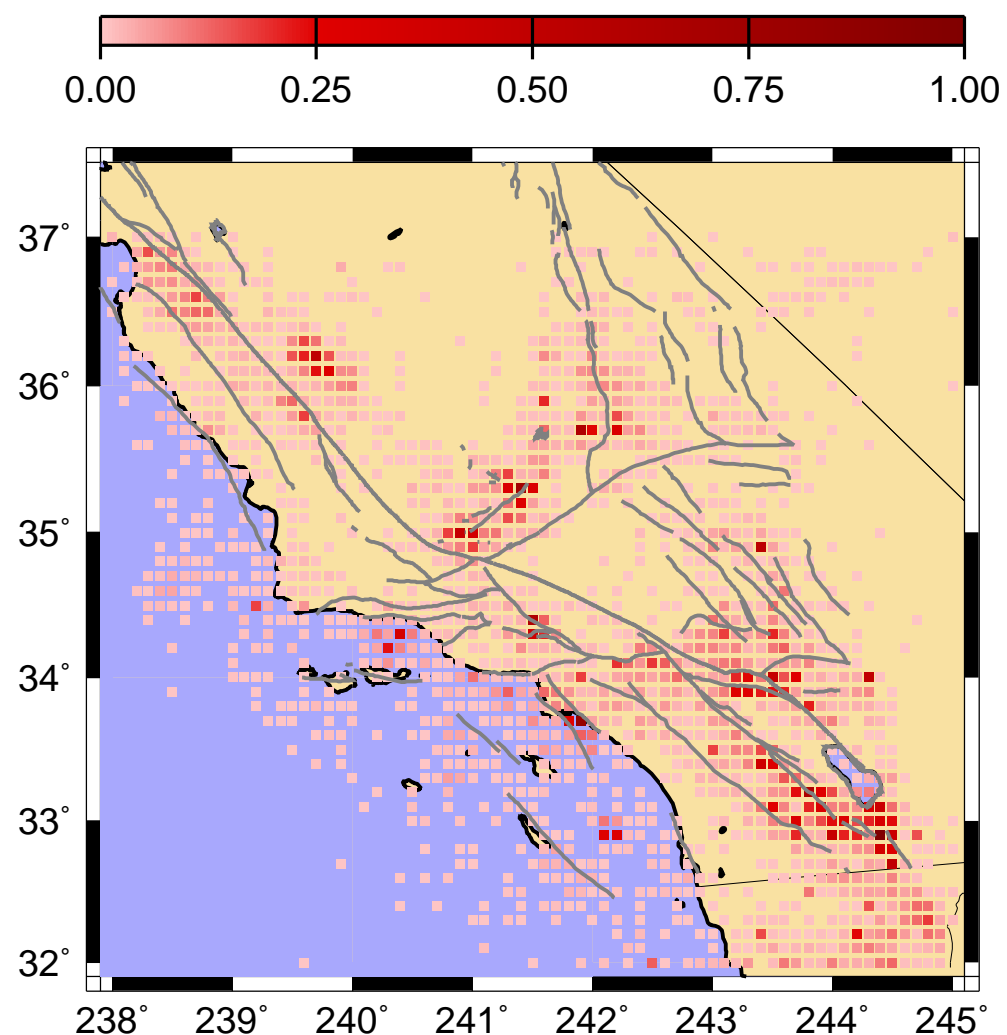
Figure 15: a) Seismicity function, $S(1932,1991)$, $M \geq 3.0$, on a logarithmic scale, normalized to the maximum number of events, for southern California; b) maps of ΔP for the time interval 1991-1978 for actual data; and c) randomized catalog. In constructing these maps, no data is used from time periods after December 31, 1991. The coding is logarithmic, where the scale value indicates the exponent, to the base ten, of the gray intensity value. Inverted triangles represent events that occurred during the indicated time periods, with three sizes corresponding to magnitudes M of: $5 < M < 6$, $6 \leq M < 7$, $7 \leq M$. Open circles represent events that occur after January 1, 1992. Three increasing circle sizes again correspond to the same magnitude ranges as for the inverted triangles.

Figure 16: Histogram of likelihood values for one hundred random catalogs of southern California seismicity. In addition, the likelihood value for the actual catalog, as shown in Figure 15b, is superimposed on this plot as a dashed line, and the likelihood value for the relative southern California seismicity as shown in Figure 15a is plotted as the dash-dotted line.

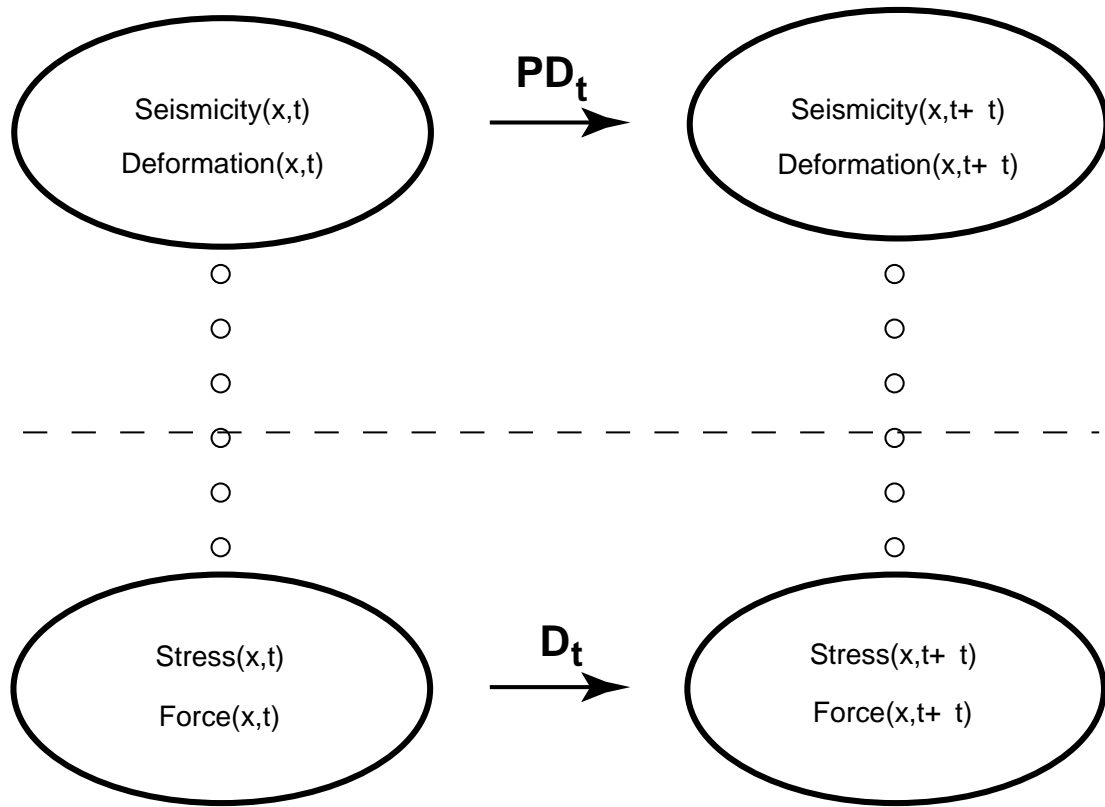
Figure 17: Contour plot of $\hat{S}(x_i, t_1, t_2)$, normalized to the maximum absolute value, for the time period 1991 - 1978.

Figure 18: Maps of $\Delta\mathbf{P}$ for a) for the time period 1978-1968, and for b) the time period 1988-1978. In constructing these maps, no data is used for time periods after the final year. The color scale is the same as in Figure 15. Inverted triangles represent events that occurred during the indicated time periods, as before. Open circles represent events that occur during the ten years after the referenced time period. Three increasing sizes again correspond to the same magnitude ranges as Figure 15.

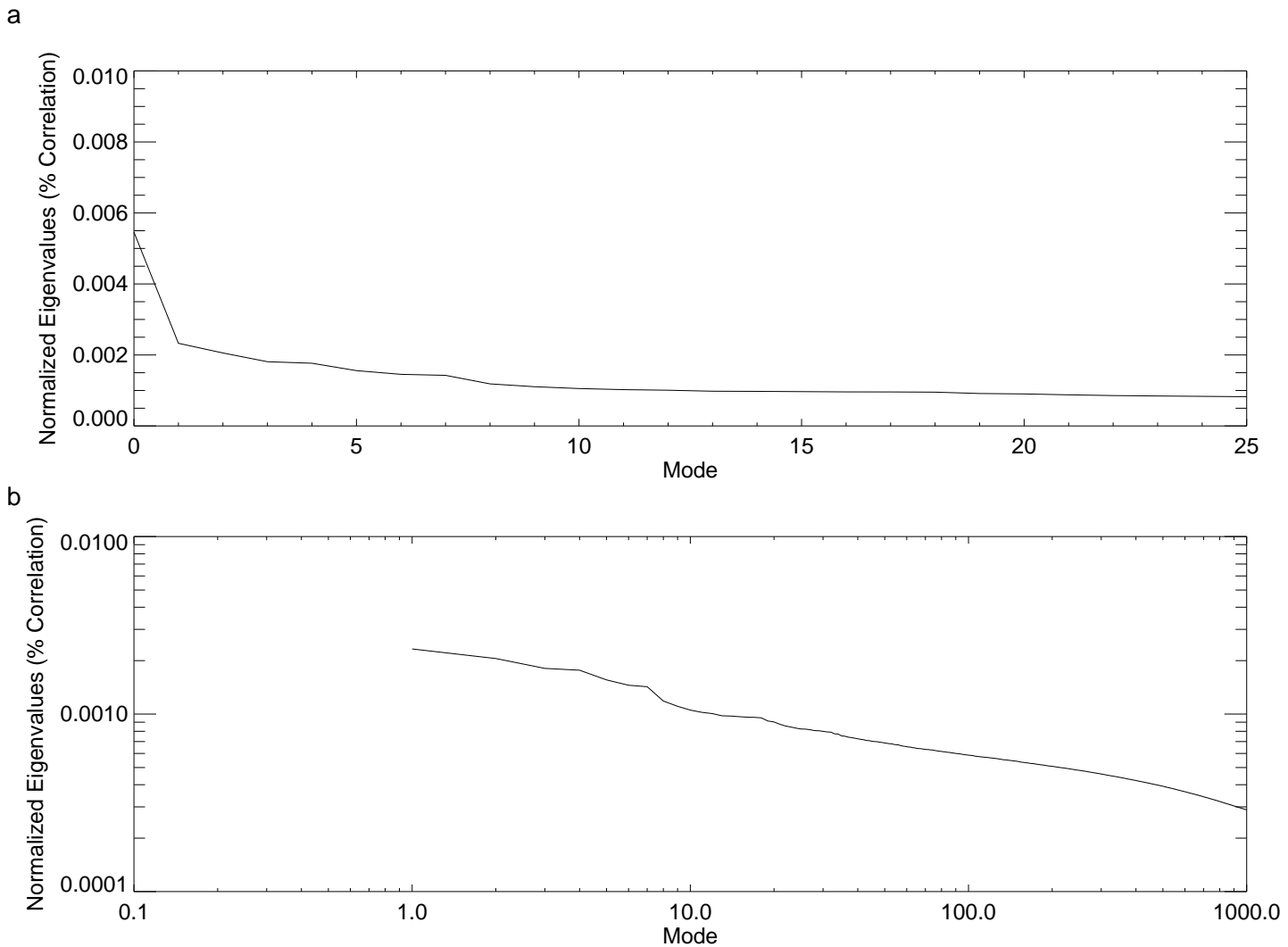
Figure 19: Map of $\Delta\mathbf{P}$ for the time period 1999-1989. In constructing this map, no data is used for the year 2000. The color scale is still logarithmic, as in Figure 15. Inverted triangles represent events that occurred during the indicated time periods, as before. Open circles represent events that occur during the ten years after the referenced time period. Three increasing sizes again correspond to the same magnitude ranges as Figure 15.

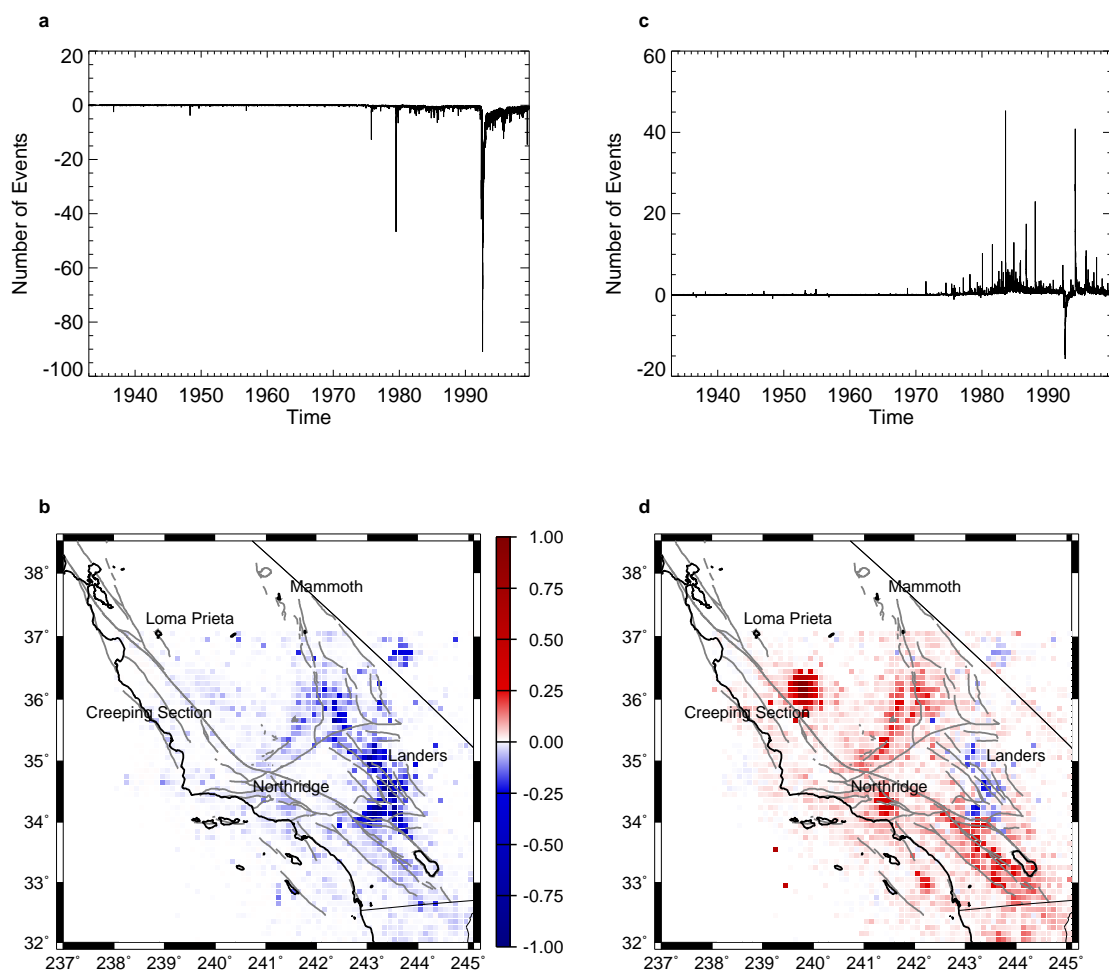


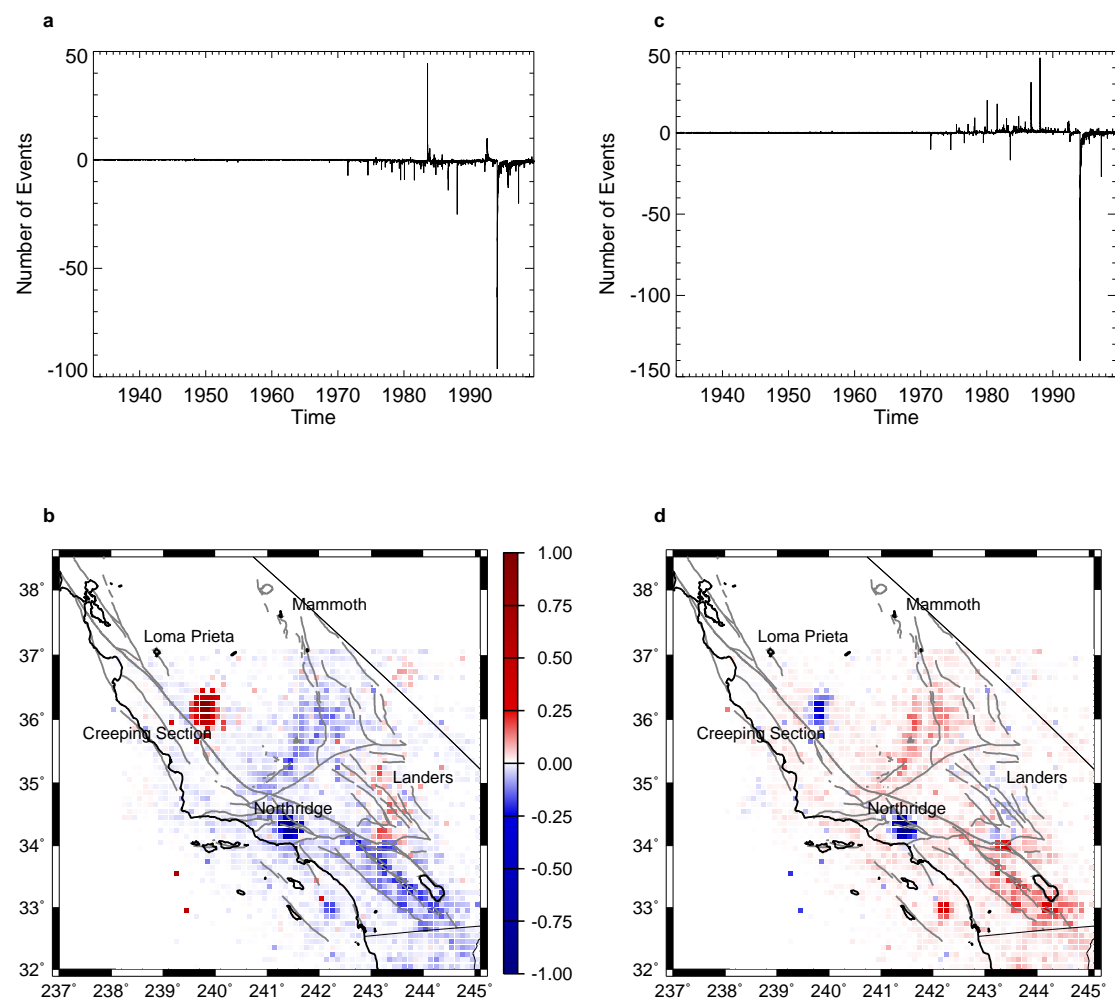
Observable Pattern Dynamics

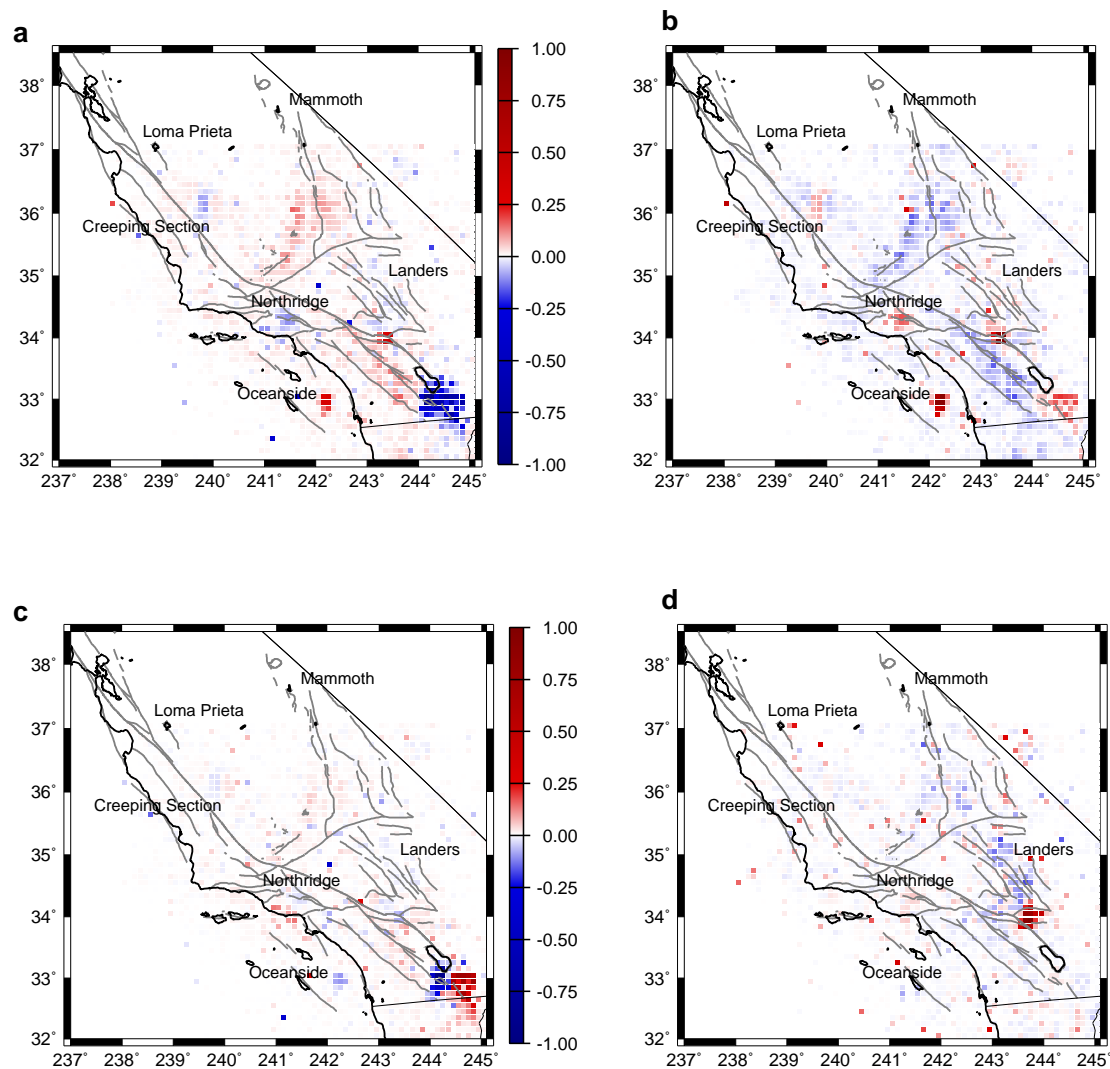


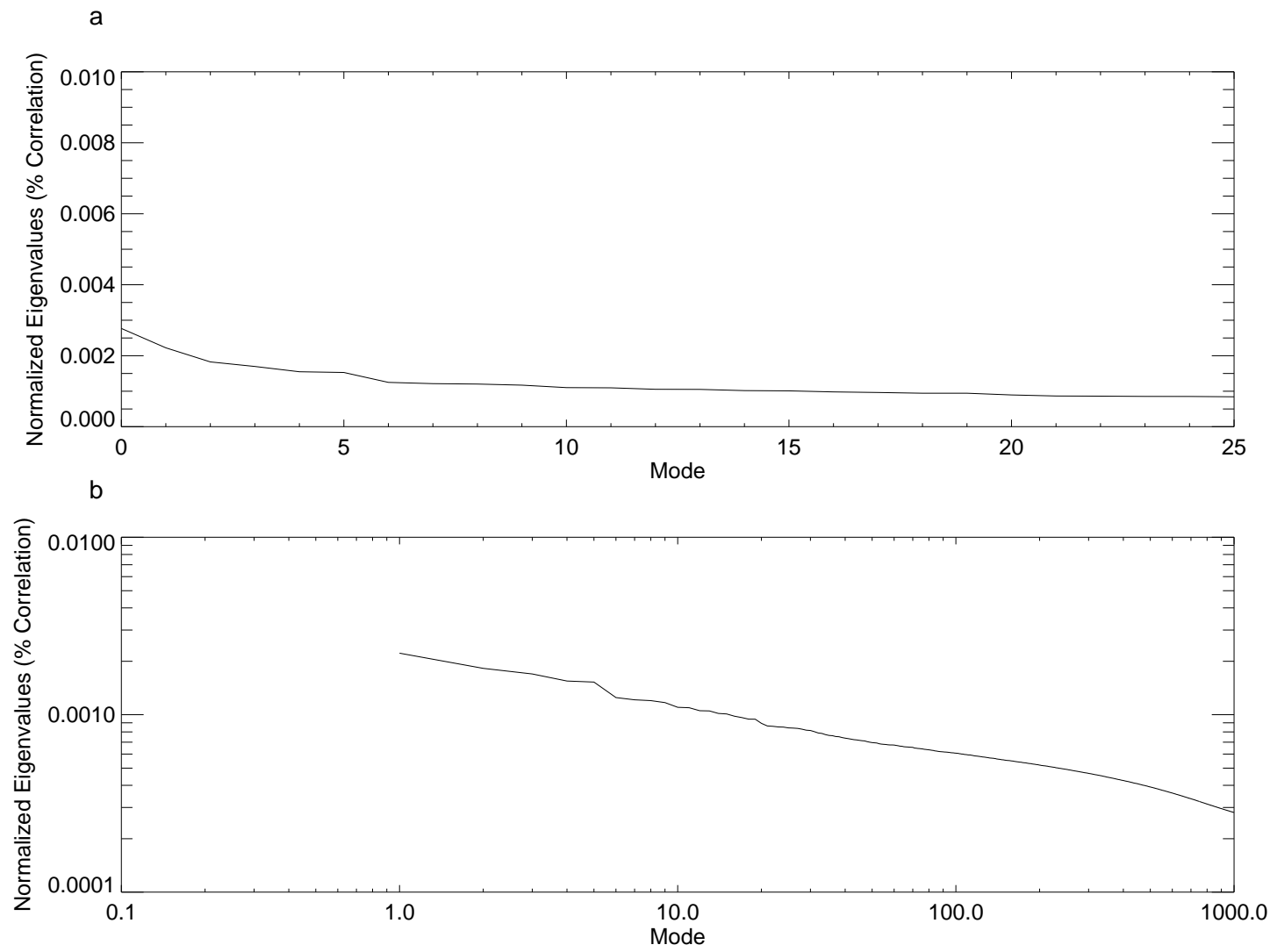
Unobservable Deterministic Dynamics

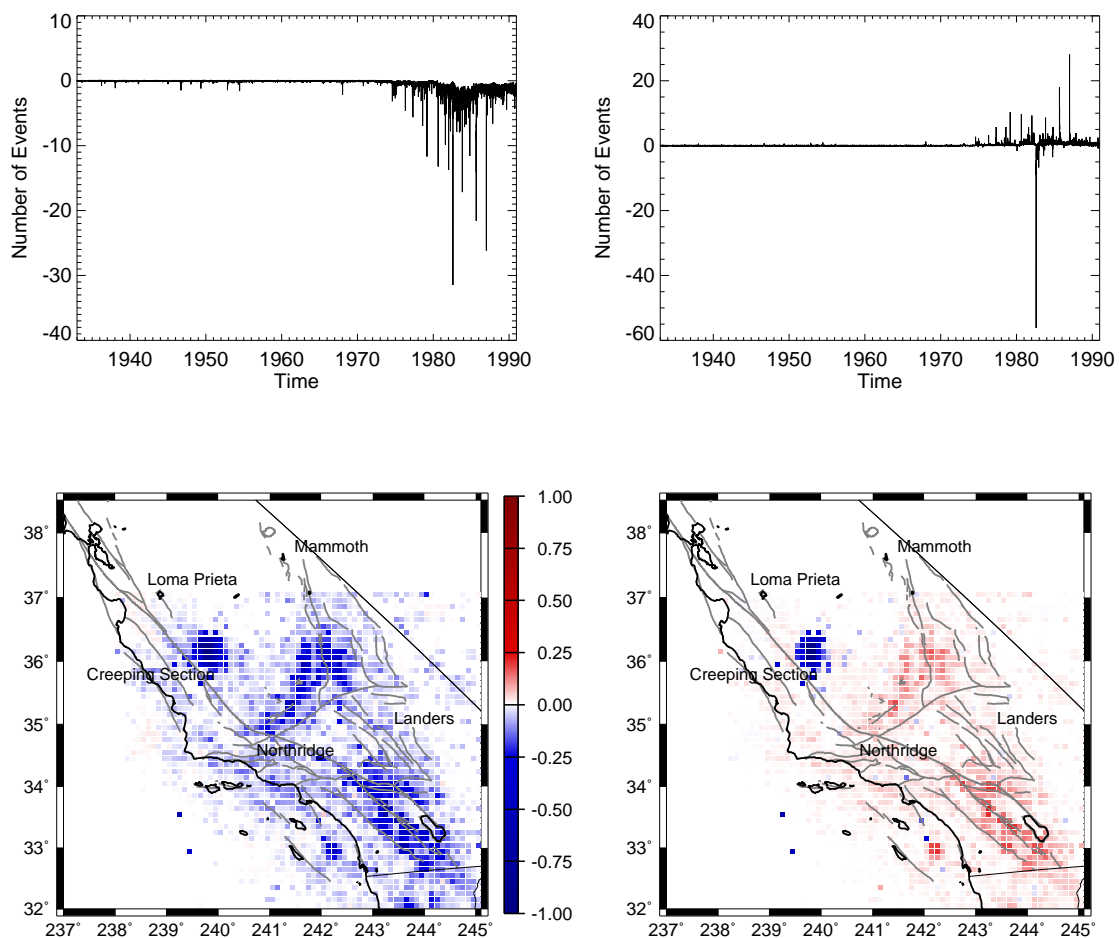


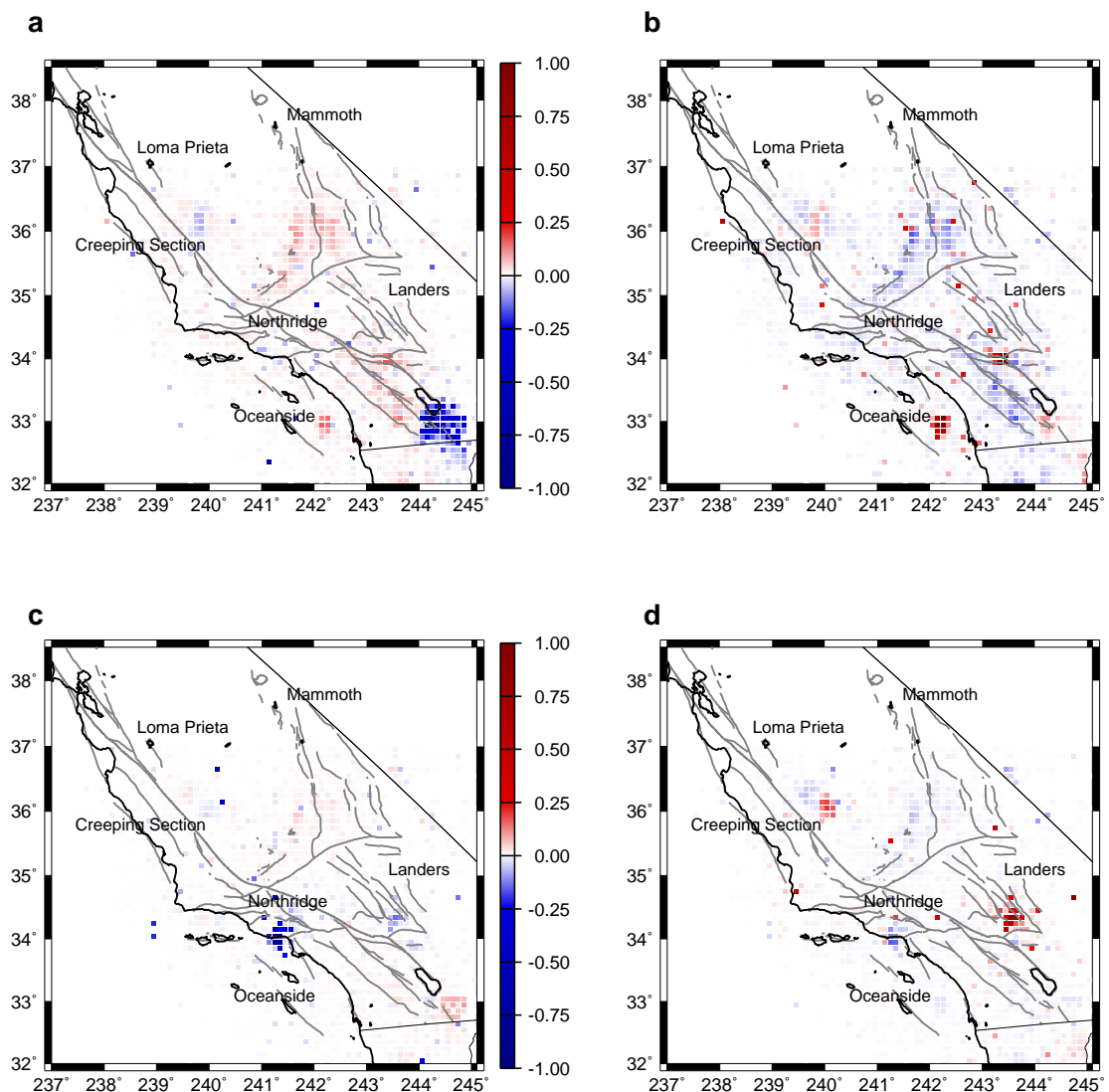


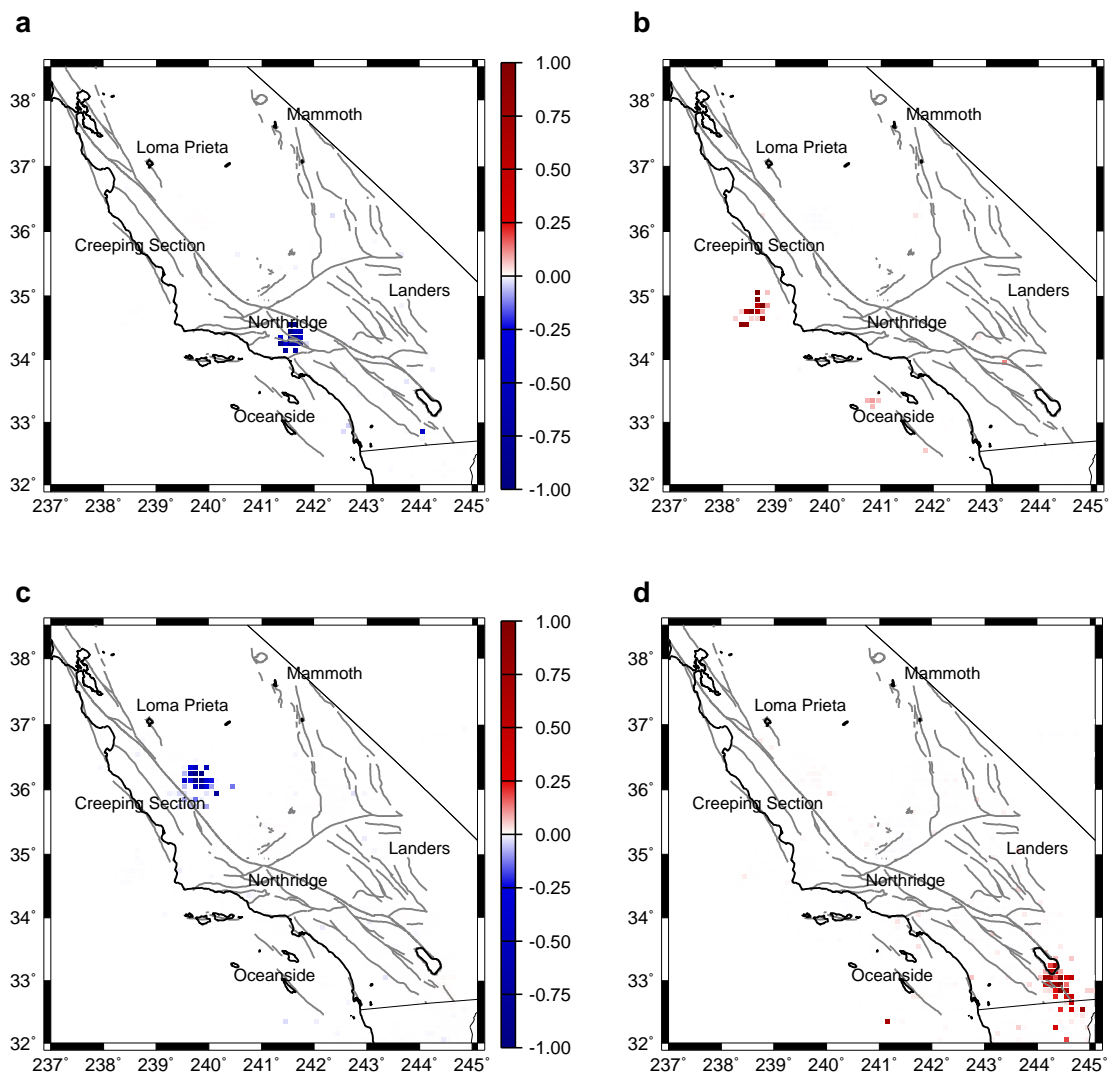


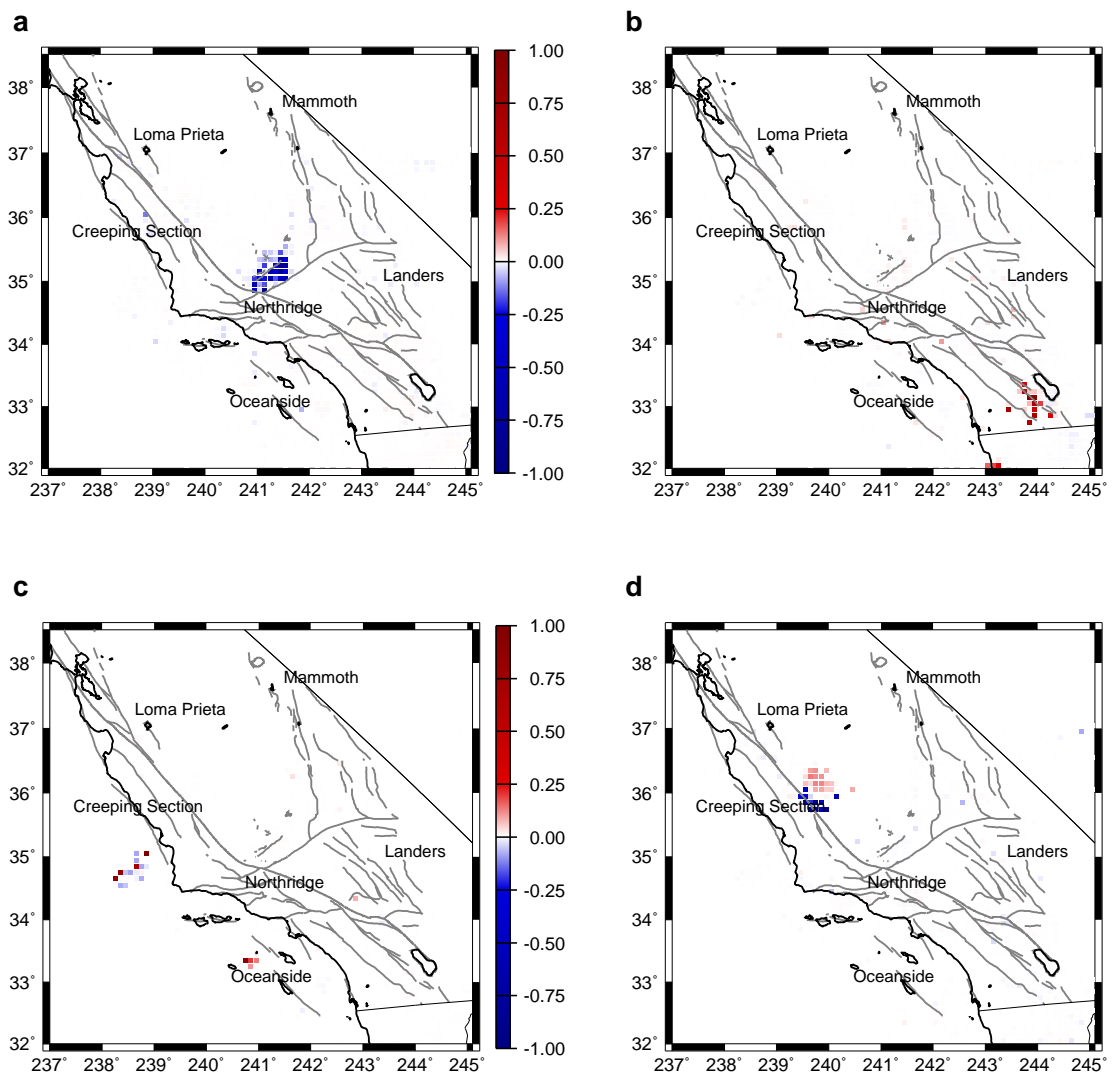


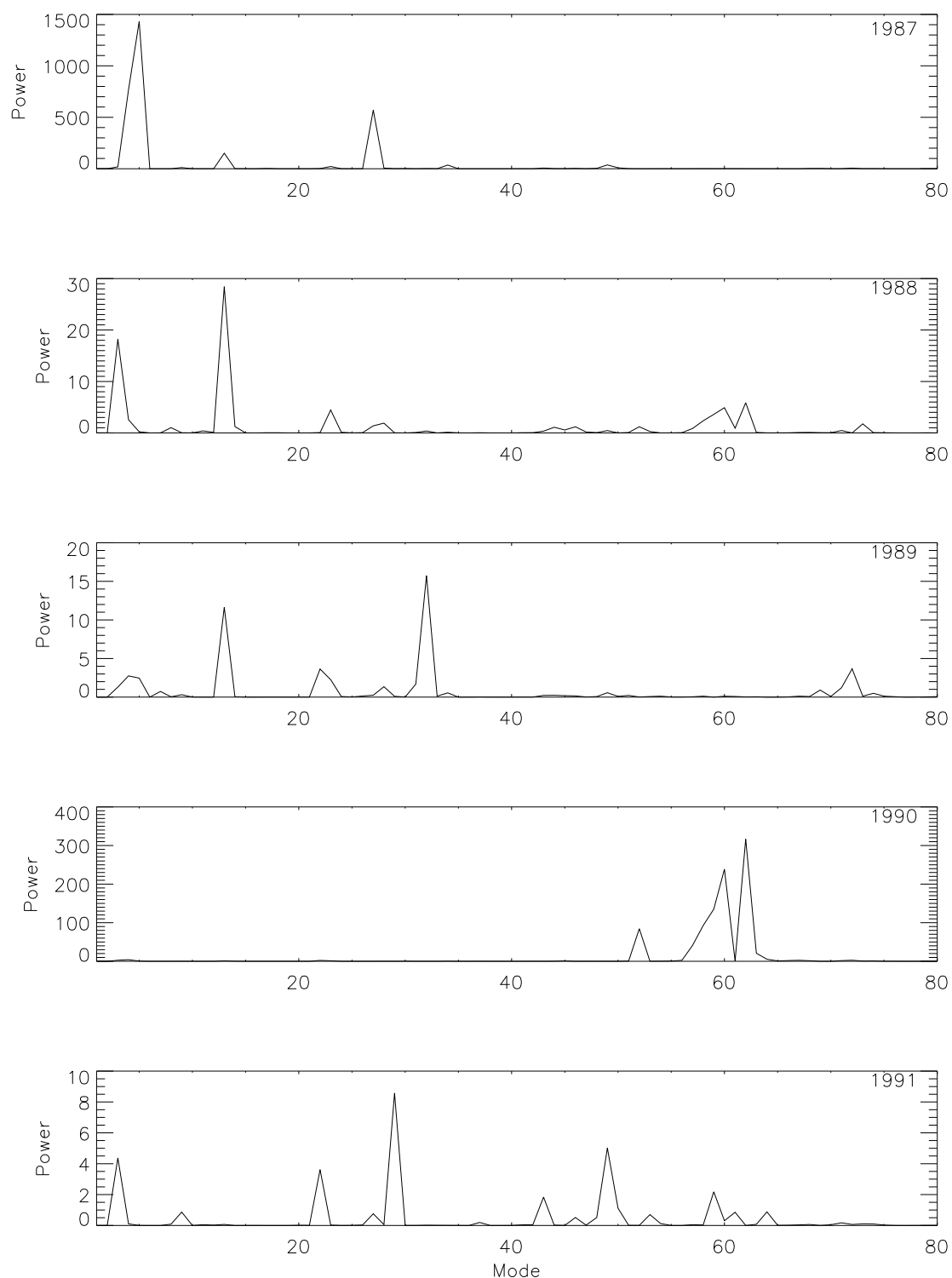


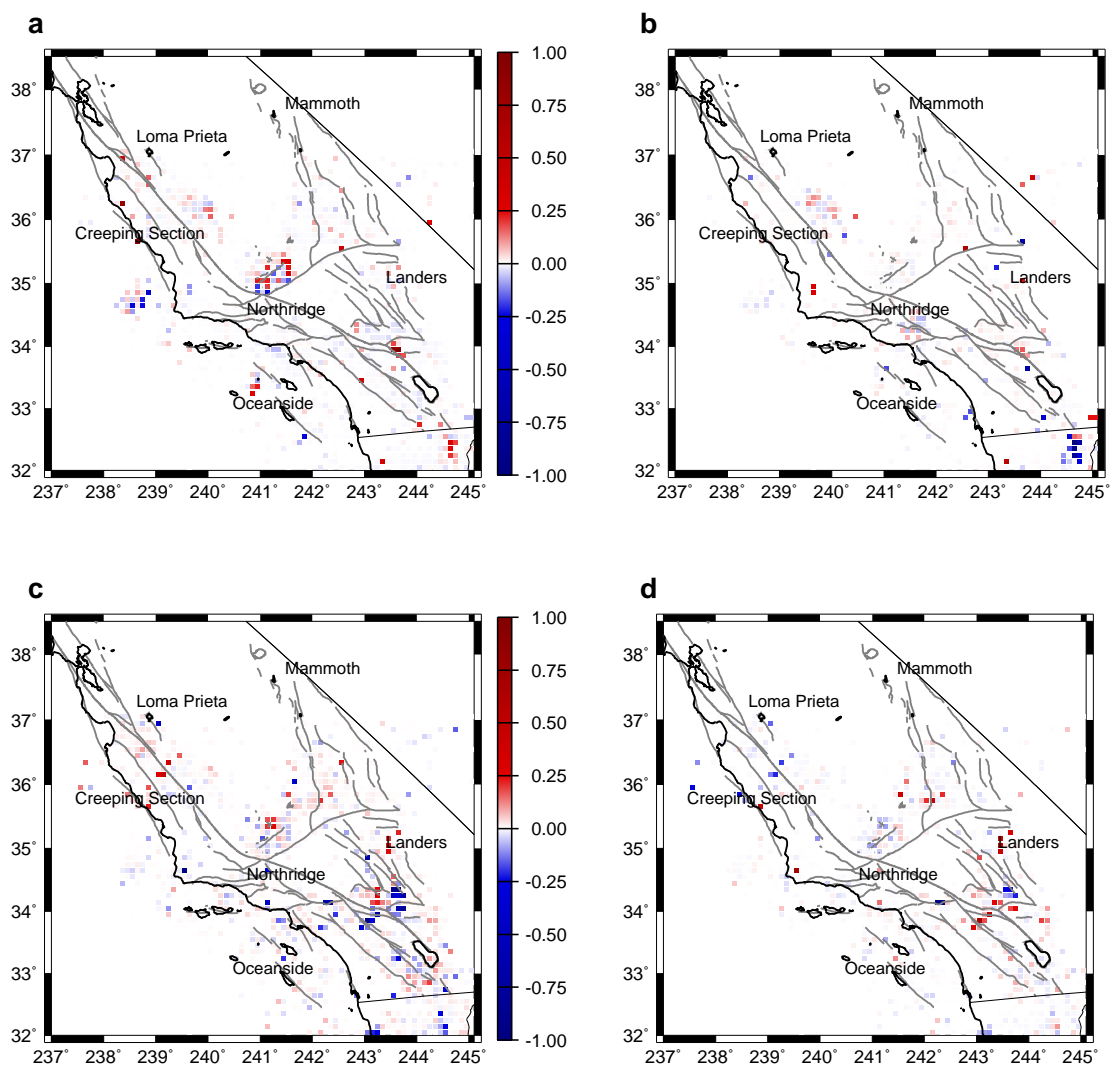


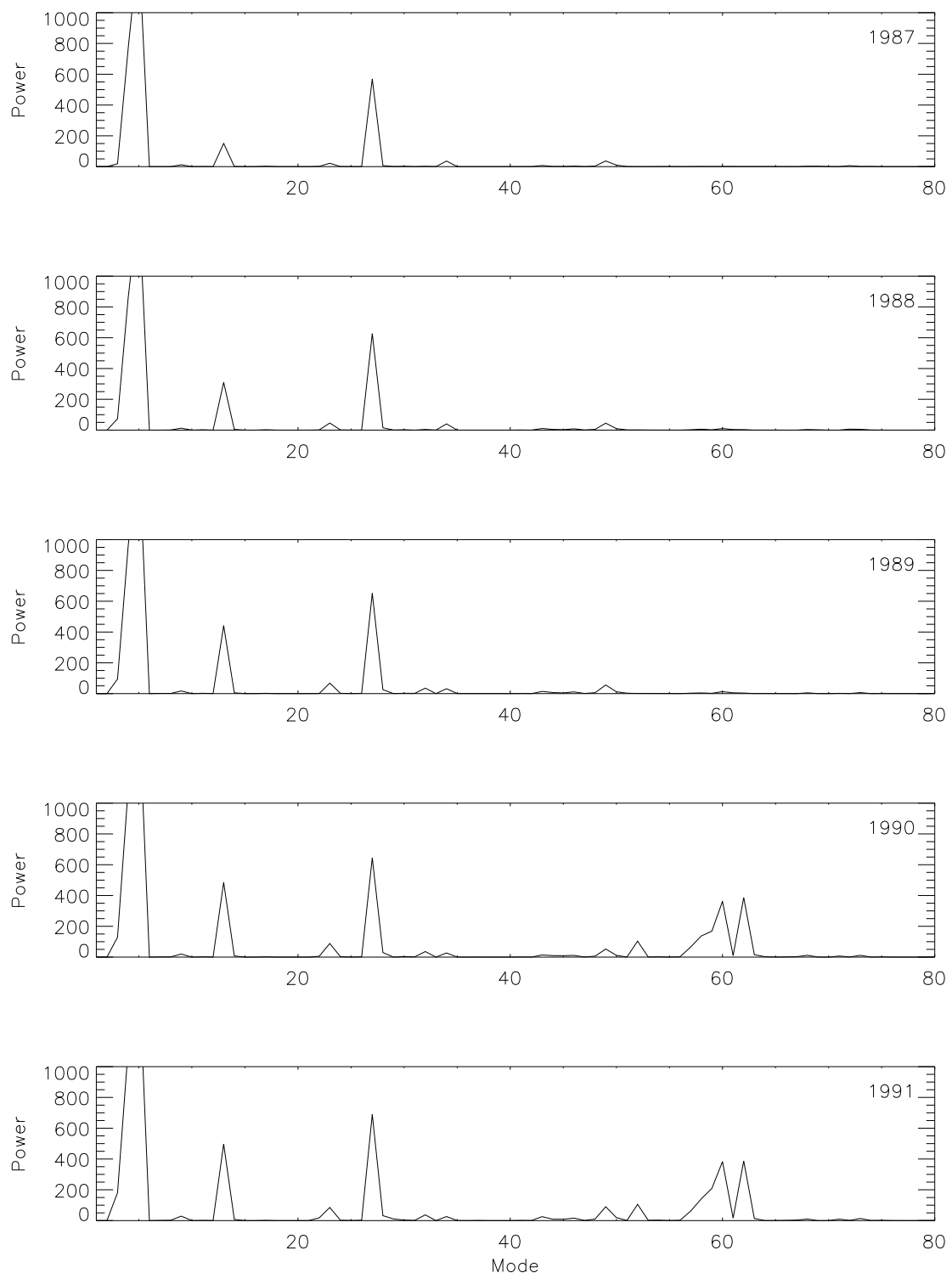


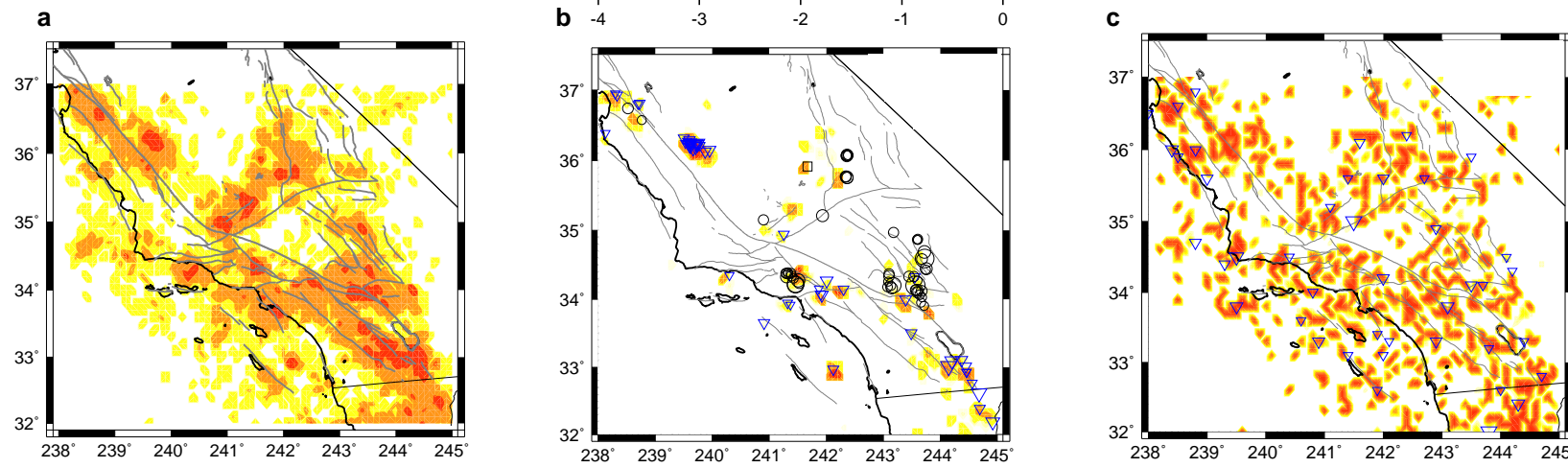


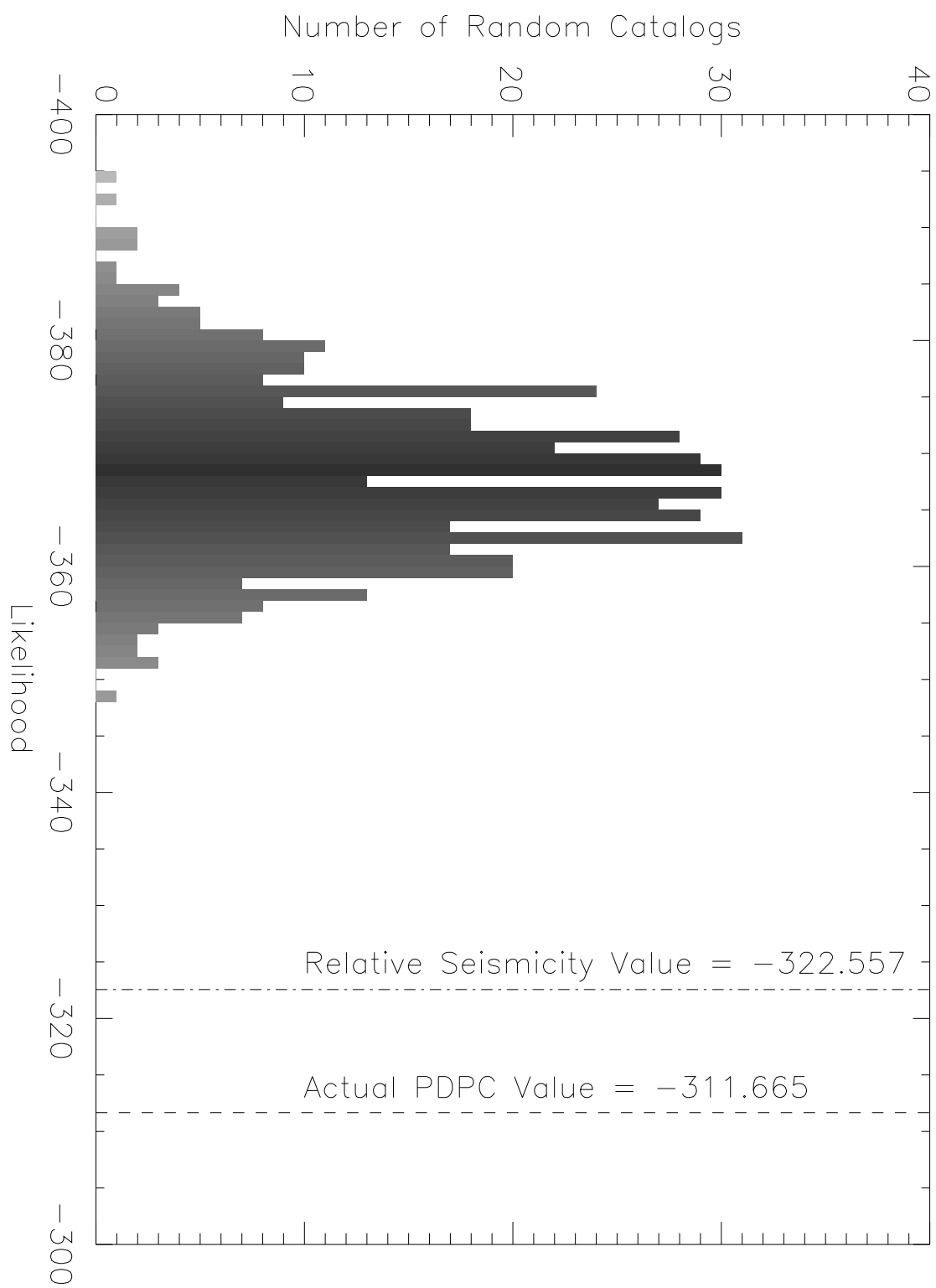


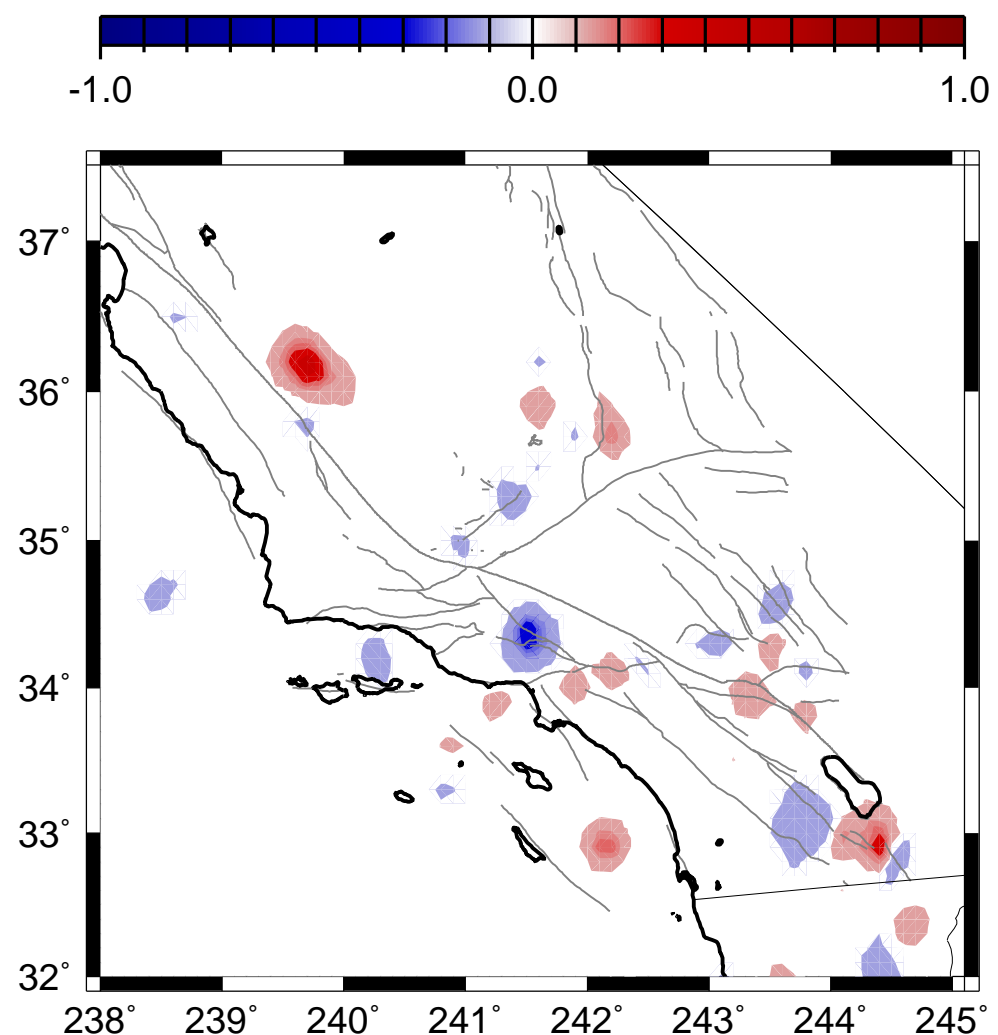


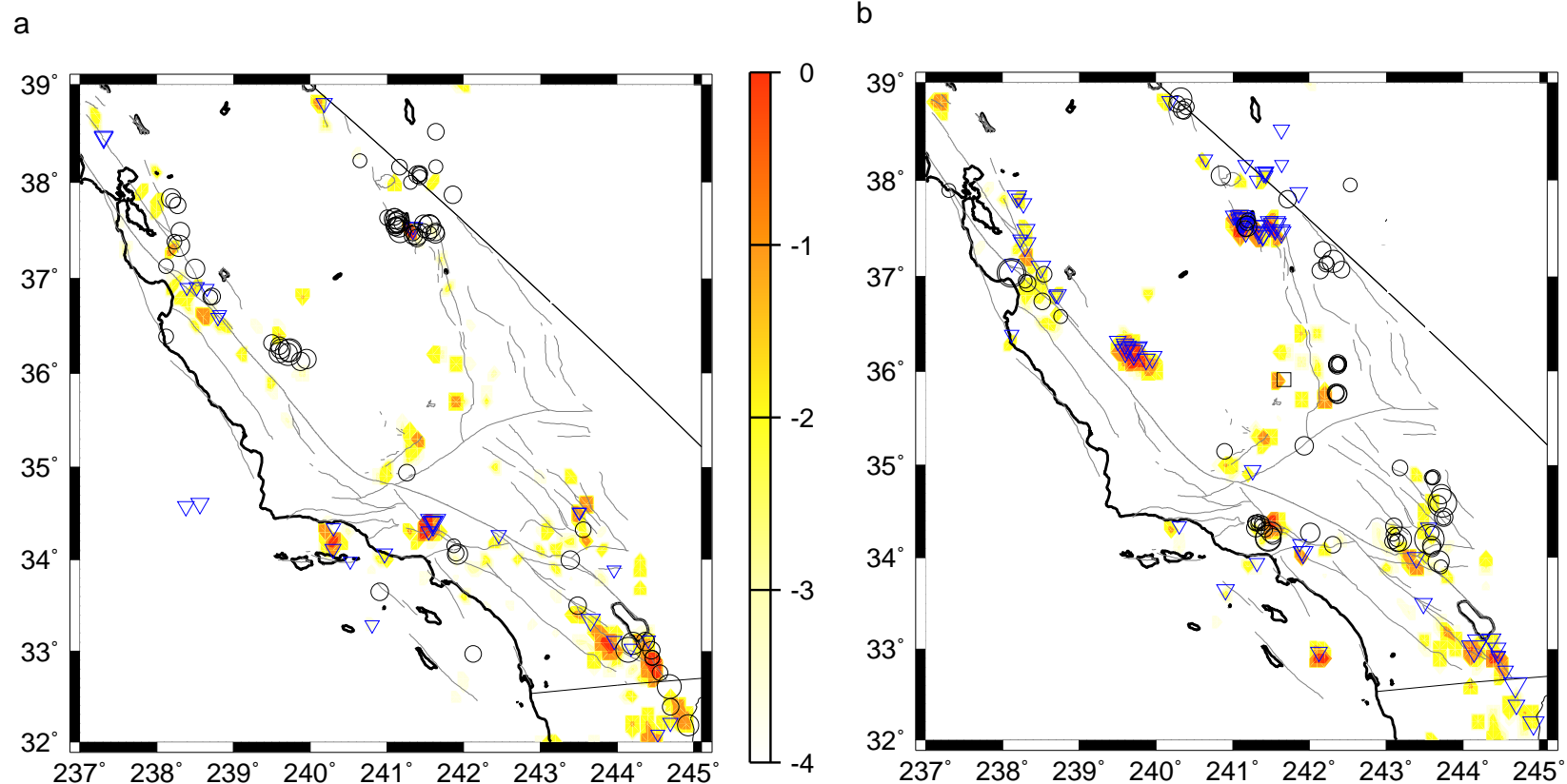


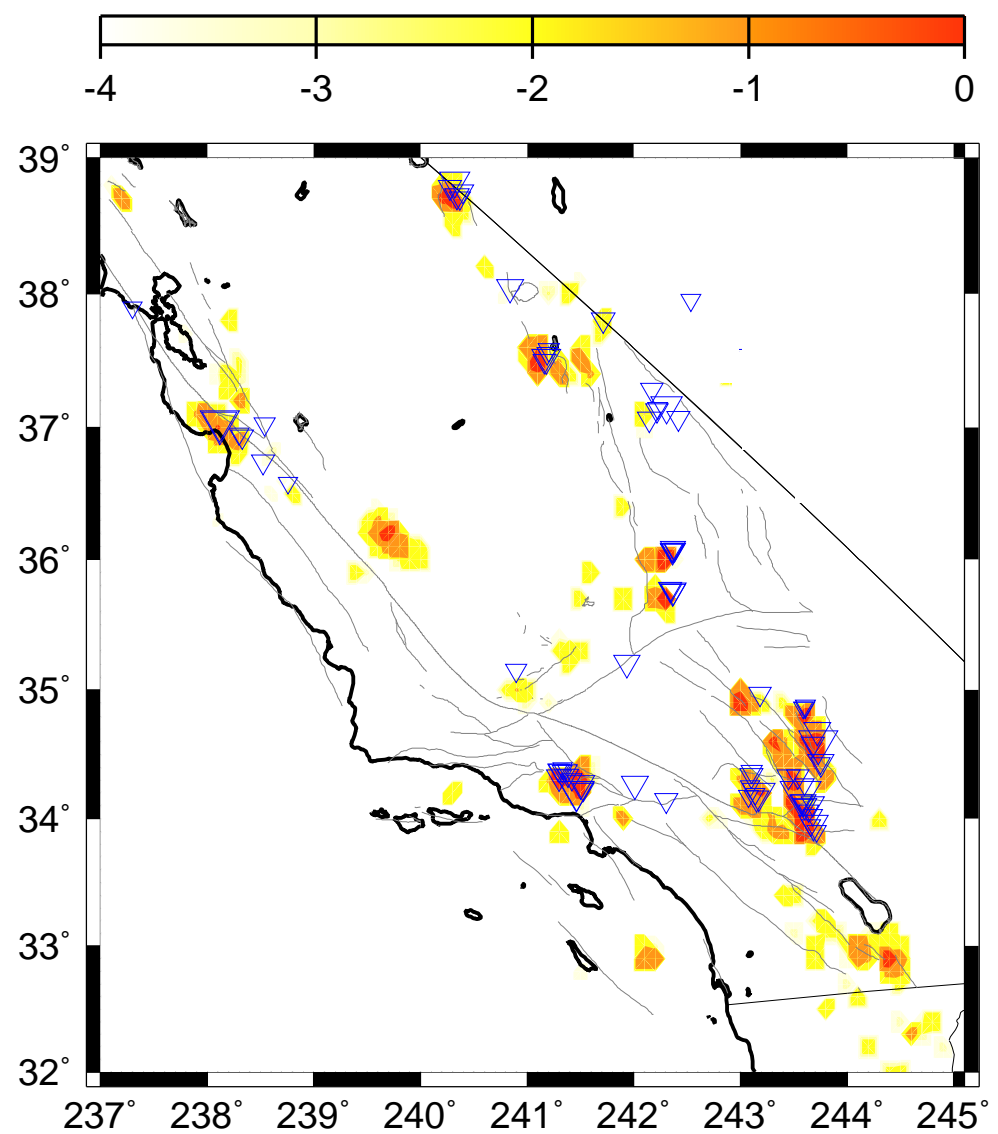












Parallelization of a Large-Scale Computational Earthquake Simulation Program

K.F. Tiampo⁽¹⁾, J.B. Rundle⁽²⁾, S. Gross⁽¹⁾ and S. McGinnis⁽¹⁾

(CIRES, University of Colorado, Boulder, CO USA (e-mail: kristy@fractal.colorado.edu; sethmc@turcotte.colorado.edu); phone: +01-303-492-4779); (2) Dept. of Physics, Colorado Center for Chaos & Complexity, CIRES, University of Colorado, Boulder, CO, 80309, USA, and Distinguished Visiting Scientist, Jet Propulsion Laboratory, Pasadena, CA, 91125, USA (email: rundle@cires.colorado.edu; phone +01-303-492-4779).

Abstract

Here we detail both the methods and preliminary results of first efforts to parallelize two General Earthquake Model (GEM)-related codes: 1) a relatively simple data mining procedure based on a Genetic Algorithm; and 2) the *Virtual California* simulation of GEM . These preliminary results, using a simple, heterogeneous processor system, existing freeware, and with an extremely low cost of both manpower and hardware dollars, motivate us to more ambitious work with considerably larger-scale computer earthquake simulations of southern California. The GEM computational problem, which is essentially a Monte Carlo simulation, is well suited to optimization on parallel computers, and we outline how we are proceeding in implementing this new software architecture.

1.0 Introduction

With the increasing availability of computer and network hardware, accompanied by decreasing cost and ever better processor speed, the construction of parallel computational systems from off-the-shelf components, in lieu of purchasing CPU time on expensive supercomputers, has become ever more practical and attractive. In this paper we describe a preliminary attempt to adapt existing C code for parallel computing on a simple, heterogeneous processor system, the benefits of such a casual implementation, and future plans to parallelize a large-scale computer earthquake simulation of southern

California, the *Virtual California* simulation of the General Earthquake Model (GEM) project.

2.0 Parallelization Methods

2.1 Hardware

The term Beowulf class systems has come to describe, in general, multi-computer architecture that supports parallel computing [1]. While not true in every case, it frequently consists of a server node, and multiple client nodes connected via Ethernet or other network components. These networks can range from a small set of machines connected through Ethernet cable and a switch, as in our present case, or a large number (on the order of hundreds) of linux processors connected via fast switches, as in our future plans [1].

Our current hardware consists of a heterogeneous mix of eight stand-alone PCs, with CPU speeds ranging from 266 MHz to 800 MHz, connected by an Asante FriendlyNet FS3208, supplying 10 BaseT internally. These machines all run some version of the linux operating system, depending upon their age.

Future plans are to implement our parallelized codes on either a large-scale Beowulf cluster, or the Maui MHPCC symmetric multi-processor (SMP) supercomputer. The Beowulf cluster, CoSMIC, is currently under construction by the Physics department at the University of Colorado, and will consist of 352 dual processor 800 MHz Pentium IIIs, each with 512 Mbytes of RAM and an ≈ 10 Gbyte disk,

configured as an integrated set of subclusters each consisting of 32 dual processors. Eight subclusters will be networked using fast Ethernet, each on their own fast Ethernet switch, effectively isolating them from most network traffic. There also will be three subclusters networked using Myrinet, resulting in a 96-node cluster optimized for multi-node applications. The 10 Gbyte disks will provide both short-term storage, as well as swap space, and will contain any local operating system and software. Long term storage will be provided by 3.6 Tbytes of disk space, consisting of 9 RAID devices installed in three file servers, and backed up to a DLT7000 tape drive. This system is designed to provide both large-scale, load balanced serial or parallel computations in conjunction with low cost localized scientific visualization.

2.2 Software

Parallelization can be described as either implicit or explicit. Implicit methods are those where the parallelism is determined by the compiler, examples of which include FORTRAN 90, High Performance FORTRAN (HPF), Bulk Synchronous Parallel (BSP), and others. Explicit methods are those where the parallelism is determined by the user. In this case, the user modifies the computer source code specifically for a parallel computer, adding messages using Parallel Virtual Machine (PVM) or Message Passing Interface (MPI), or POSIX threads [1]. For our initial attempts, we opted for explicit parallelization only.

2.2.1 PVM

PVM is a portable, freeware message-passing library, obtainable via http://www.epm.ornl.gov/pvm/pvm_home.html, which supports single-processor and

SMP machines as well as clusters of linked machines. Its primary advantage is that it works across a variety of different types of processors, networks, and configurations. This ability to interface over heterogeneous clusters is offset by the significant overhead associated with the message handling [2,3].

2.2.2 MPI

MPI is the new official standard for message passing, available at <http://www.mcs.anl.gov:80/mpi>. While MPI includes a number of features that go beyond the basic message passing model of PVM, such as remote memory access (RMA) and parallel file I/O, these make it necessary to learn an almost entirely new language in order to implement these features. In addition, MPI assumes that the system is either a massively parallel processor (MPP), or a cluster of nearly identical machines [2,4].

3.0 Trial Parallelization

After having studied the options above, we determined to run a trial attempt at parallelism using our existing system, as described above, and by modifying a C program which has been employed for data mining and geophysical inversions for a number of years. The program is a genetic algorithm (GA) inversion code. Genetic algorithms are notoriously parallelizable, and conversion of the code to a parallel implementation provided an opportunity to test the difficulty level of the conversion as well as to benchmark the potential time savings associated with such a heterogeneous network.

Many geophysical optimization problems are nonlinear and result in objective functions with a rough fitness landscape and several local minima. Consequently, local optimization techniques, e.g., linearized matrix inversion, steepest descent, conjugate gradients, etc. can converge prematurely to a local minimum. Genetic algorithms have proven themselves an attractive global search tool suitable for the irregular, multimodal fitness functions typically observed in nonlinear optimization problems in the physical sciences.

In general, geophysical inverse problems involve employing large quantities of measured data, in conjunction with an efficient computational algorithm that explores the model space to find the global minimum associated with the optimal model parameters. In a GA, the parameters to be inverted for are coded as genes, and a large population of potential solutions for these genes is searched for the optimal solution. After starting with an initial range of models, the fitness of each solution is measured by a quantitative, objective function. The fittest members of each population then are combined using probabilistic transition rules to form a new offspring population. This procedure is repeated through a large number of generations until the best solution is obtained, based on the fitness measure [5]. It has been demonstrated that those members of the population with a fitness greater than the average fitness of the population itself will increase in number exponentially, effectively accelerating the convergence of the inversion process [6,7,8]. Our program, shown schematically in Figure 1, employs a random number generator to produce an initial set of 100 potential values for each of the model parameters, which are then coded as genes. One gene for each model parameter is

assigned to a particular member of that initial population, creating 100 potential solutions to the inversion problem. These members are ranked, from best to worst, according to an external fitness function. The members with the lowest chi-square value are the fittest and are selected to contribute to the next generation. After completion of both crossover and mutation, the population is reevaluated as above, and the process is repeated over subsequent generations, exploiting information in past generations to search the parameter space with improved performance.

As shown schematically in Figure 1, the GA must evaluate 100 members of the population, using the fitness function, for each generation. In the original program, this operation is performed in serial, but if performed in parallel, there is a significant potential for faster performance.

3.1 GA Inversion Code

Parallelizing the GA code requires modifications to the main program in the evaluation module, and in the fitness function itself (see Figure 1). We opted to use PVM for the message passing, due to the heterogeneity of our networked system [9]. The programming modifications and debugging took approximately one day, performed by someone familiar with the GA. The PVM additions are relatively simple, constituting less than 100 lines of code. The following is a pseudocode version of the parallelization procedure, showing first the original serial version, followed by the revised parallel implementation.

3.1.1 Serial

3.1.1.1 Inversion program

```

main():

initialize_random_genes()

WHILE best_fitness() < target

    select_top_ten(genes)

    breed_new_population(genes)

    FOREACH gene

        evaluate_fitness(gene)

    END FOREACH

END WHILE

```

3.1.1.2 Fitness Function

```

evaluate_fitness():

locs[] = read_observation_locations()

real_deform[] = read_observed_data()

source_parameters = F(gene)

model_deform[] = calculate_displacements(locs[], source_parameters)

FOREACH loc

    chisq += ( model_deform[loc] - real_deform[loc] )**2

END FOREACH

return fitness = exp( - chisq )

```

3.1.2 Parallel (Master/Slave)

3.1.2.1 Master Inversion Program

```

main():

initialize_random_genes()

WHILE best_fitness() < target

    select_top_ten(genes)

    breed_new_population(genes)

    DO
        IF receive_ready_message()
            pack_gene_into_message()
            send_message_to_slave_process()
            ++outstanding
        END IF
        IF outstanding && receive_finished_message()
            receive_fitness_message()
            unpack_fitness_from_message()
            --outstanding
        END IF
    UNTIL outstanding == 0 && num_evaluated == num_genes

    END DO

END WHILE

```

3.1.2.2 Slave fitness program

```

main():

locs[] = read_observation_locations()

real_deform[] = read_observed_data()

```

```

LOOP FOREVER

    send_ready_message()

    receive_gene_message()

    unpack_source_parameters_from_message()

    model_deform[] = calculate_displacements(locs[], source_parameters)

    FOREACH loc

        chisq += ( model_deform[loc] - real_deform[loc] )**2

    END FOREACH

    fitness = exp( - chisq )

    pack_fitness_into_message()

    send_result_message()

END LOOP

```

3.2 Results

Table 1 shows the results for various configurations of a two-processor system. Koch is an 800 MHz machine, while Richter has a 266 MHz processor. We benchmarked both the fitness function for a spherical point source, as well as a fitness function for an ellipsoidal point source, which takes a substantially longer processor time to run. We ran each GA inversion on each machine singly, and then on both machines using PVM. One variation on the two-processor configuration is that we compared the results using one machine as the master, with the other as a slave, and then reversed them. The average CPU time, in seconds, is shown for a thousand generations.

The results in Table 1 show a significant increase in runtime savings for two processors over one, with the greatest increase coming if Koch, the faster machine, is used as the master. A greater percentage in timesavings is accomplished for the elliptical source, the fitness function which takes a much greater time to run. These results for what is a relatively casual attempt at parallelization, with an investment of only a few hours time, and using a heterogeneous mixture of machines inside a relatively slow switch which can be purchased today for less than \$100, leads us to optimistically view our future attempts to parallelize the GEM computer simulation for California.

4.0 Computational Structure of the Earthquake Simulation Problem

The GEM computational model for the numerical simulation of earthquakes involves a layered series of codes whose structure we now describe. Although at present, the simulation and data mining analysis codes are written in a series of C and Fortran 77, the problem is essentially a Monte Carlo simulation and is therefore well suited to optimization on a parallel computers such as the Maui MHPCC SMP machine, or on a Beowulf Linux cluster.

4.1 Model Physics

We first begin with a description of the physics that we simulate. General methods for carrying out the network simulations have been discussed in refs. [10,11,12]. Briefly, one defines a fault geometry in an elastic medium, computes the stress Greens functions (i.e., stress transfer coefficients), assigns frictional properties to each fault, then drives the system via the slip deficit (defined below). The elastic interactions produce

mean field dynamics in the simulations [10]. We focus here on the major horizontally slipping strike-slip (horizontal motion) faults in southern California that produce the most frequent and largest magnitude events. We used the tabulation of strike slip faults and fault properties as published in ref [13]. All major faults in southern California, together with the major historic earthquakes, are shown in Figure 2. Figure 3 shows our model fault network. Each fault was assigned a uniform depth of 20 km, the maximum depth of earthquakes in California, and was subdivided into segments having a horizontal scale size of approximately 10 km each.

Several friction laws are described in the literature, including Coulomb failure [14], slip-dependent or velocity-dependent friction [14], and rate-and-state [15]. Here we use a parameterization of recent laboratory friction experiments [16,17], in which the stiffness of the loading machine is low enough to allow for unstable stick-slip when a failure threshold $\sigma^F(V)$ is reached, where $\sigma^F(V)$ is a weak (logarithmic) function of the load point velocity V . Sudden slip then occurs in which the stress decreases to the level of a residual stress $\sigma^R(V)$, again a weak function of V . Stable precursory slip, characterized by a leakage parameter α , is observed to occur whose velocity increases with stress level, reaching a magnitude of a few percent of the driving load point velocity just prior to failure at $\sigma = \sigma^F(V)$. For the simplest model that describes this frictional physics displayed in the experiments, we find that

$$\alpha = \frac{2 s_{ss}}{V T^2}, \quad (1)$$

where V is the plate velocity as before, T is the average interval between sudden unstable slip events, and s_{ss} is the total stable slip that occurs during T . The fraction of stable to total slip that occurs in a laboratory experiment or on a fault is in principle observable, and has in fact been tabulated for a variety of faults in California [13]. The observable quantity $\sigma^F(V) - \sigma^R(V)$ determines the magnitude of the unstable slip. Thus the important parameters of the model that describes laboratory friction can be readily set by either laboratory or field observations.

4.2 Computational Structure

The *Virtual California* simulation of the GEM project is a Monte Carlo, Cellular Automaton version of a Langevin-type dynamics. The actual geometric structure of the fault system in California can be implemented as a coarse-grained mesh of fault segments embedded in a layered elastic half space. The various pieces of the fault segments interact by means of elastic interactions. Parameters for the friction law must be specified on each of the fault segments, together with the long-term rate of slip, $V(\mathbf{x}_i)$, on the segment centered at \mathbf{x}_i .

The implementation of the model is carried out in three layers of codes, beginning with two data files. The first data file, **Fault_Data.d**, contains the basic geometry of the N fault segments, specifically the coordinates of each of the four corners of the fault segments. This data file also contains the long-term rate of slip $V(\mathbf{x}_i)$ for each of the segments. A second data file, **Fault_Friction.d**, contains the average recurrence time

intervals T_i between unstable slip events on the i^{th} segment, as well as values of α for each segment.

These two data files are used, together with standard methods [11] from elasticity theory to compute the stress Greens functions (stress transfer coefficients) by a code **SG_Compute.c**. Since the form of the elastic stress transfer coefficients is known analytically, the computations performed by **SG_Compute.c** are simply function evaluations. The output from this code is contained within a data file **SG_Coefficients.d**, and is a set of N^2 stress transfer coefficients (including the self-stress term) for all of the fault segments. These stress transfer coefficients, together with the fault slip rate data in **Fault_Data.d** and friction data in **Fault_Friction.d**, then are used as the basic inputs to the earthquake simulation code **EQ_Simulator.c**. The latter is essentially a Monte Carlo algorithm that encodes the CA Langevin dynamics, assuming a random component during each unstable fault slip event. The equations for the solved on the i^{th} fault segment are:

$$\frac{ds_i}{dt} = \frac{\Delta\sigma_i}{K_i} \left\{ \alpha_i + (1 + \eta_i) \delta(t - t_F) \right\} - \varepsilon_i F(Vt - s_i) - \phi_i^* \quad (2)$$

$$\sigma_i = \sum_j T_{ij} \left(V_j t - s_j \right) \quad (3)$$

where $\Delta\sigma_i = \sigma_i - \sigma_i^R$, T_{ij} is the matrix of stress transfer coefficients, $K_i = \sum_j T_{ij}$, and

$F()$ is an odd (nonlinear function) of s with amplitude ε_i and parameter ϕ_i^* [11]. The parameter t_F is any time t at which $\sigma_i(t) \geq \sigma_i^F$, δ is the Dirac delta function, and η is random noise (overshoot or undershoot). The nonlinear function $F()$ is present because all of the eigenvalues of the linear part of (2) are negative, and therefore the physics has an instability similar to a Peierls instability [18]. Physically, the functions $F()$ and parameters ϕ_i^* correspond to a potential well on a high-dimensional rough energy landscape upon which the system evolves. The set of N parameters $\{\phi_i^*\}$ represent a fixed point about which the system fluctuates. This physical picture has been established through the use of simulations that demonstrate that the mean field dynamics of the model, a result of the long-range elastic interactions, induces local ergodicity [19,20]. The exact form of $F()$ is unimportant, since for small fluctuations about $\{\phi_i^*\}$ are controlled by the first nonlinear term in $F()$, which is always cubic.

The output from **EQ_Simulator.c** is a record of the slip events and stress history of the dynamics for a fixed time period, and we can call it **EQ_History_01.d**. The 01 denotes the fact that **EQ_History_01.d** can be input back into **EQ_Simulator.c** as an initial condition to produce a second earthquake history file **EQ_History_02.d** which continues the dynamical evolution of the fault system to later times. Once the output data files **EQ_History_xx.d** have been computed, their data can be displayed in various ways, for example by a general visualization code **EQ_Visualize.pro** written in IDL or other script.

In addition to slip histories, deformation that would be expected on the surface of the half space can be computed, deformation that could in principle be observed via GPS or satellite radar interferometry. To enable this calculation, kinematic Green's functions must be computed via a code **KG_Compute.c** that produces an output file **KG_Coefficients.d**. This data file is then used in a code **EQ_Deformation.c** to compute the surface deformation file **Surface_Deformation.d**, which is then used as input to the general visualization code **EQ_Visualize.pro**.

The flow diagram for this set of computation, simulation, and visualization codes is shown in Figure 4. Examples of the visualized output from these codes can be found in ref. [21].

4.3 Parallelization Procedures

We begin by schematically illustrating the structure of the two codes, 1) **SG_Compute.c** and 2) **EQ_Simulator.c**, as they exist for serial computation, in Appendix B. We then show (again schematically) how these codes are adapted to parallel computation. For the parallel implementation, we will assume that the multiprocessor is an SMP system. The codes **KG_Compute.c** and **EQ_Deformation.c** are similarly structured and modified. Here N is the number of fault segments.

5.0 Conclusions

The promising results of a trial attempt at parallelization of a GA program encourage us to more ambitious work with the large-scale computer earthquake

simulation of southern California, the *Virtual California* simulation of the General Earthquake Model (GEM) project. These preliminary results, using a simple, heterogeneous processor system, existing freeware, and at an extremely low cost of both manpower and hardware dollars, lead us to believe that conversion of the GEM computational problem, which is essentially a Monte Carlo simulation, is well suited to optimization on a parallel computers such as the Maui MHPCC SMP machine, or on a Beowulf Linux cluster.

Appendix A — Genetic Algorithm Program Code

A.1 Serial

A.1.1 Main Program — Inversion.c (Evaluation function)

```
/*********************************************
/* Evaluation function: This takes a user defined function. */
/* Each time this is changed, the code has to be recompiled. */
/* The current function is a data calculation and chisquare fit. */
/********************************************

void evaluate(void)
{
int mem;
int k;
double x[NVARS+1];

for (mem = 0; mem < POPSIZE; mem++)
{
    for (k = 0; k < NVARS; k++)
        x[k+1] = population[mem].gene[k];

    population[mem].fitness = fit(x[1], x[2], x[3], x[4]);
}

}
```

A.1.2 Fitness Function — Fit.c

```
***** Inversion definitions and variables *****
```

```

#define MAXGENS 5000           /* max. number of generations */
#define NSPH 1    /* no. of spheres */
#define NNORM 0 /* no. of normal faults */
#define NUMELL 0 /* no. of ellipses */
#define NUMLIN 100   /* no. of potential lines */
#define NGPS 1000   /* no. of potential gps points */
#define NUP 4000    /* no. of potential uplift points */
#define NFIXUP 40   /* no. of potential fixed pts for leveling */
#define NUPEACH 100 /* no. of potential uplift pts for each fixed
levelling pt */
#define NLASER
#define NDATA 8100   /* no. of potential data points */
#define S 0.23873241 /* (3/4)/pi */
#define SS 0.026525824 /* (1/12)/pi */
#define PI 3.1415926535

int numlin, numspfh, numell, num_normal, nup, nup1, nup2, nup3, nup4,
nup5, nup6, nup7, ndata, ngps, nfixup, nupeach, nlaser; /* see
definitions in function below */
int generation;           /* current generation no. */
int upeach[7];

double datav[NDATA], data[NDATA], error[NDATA];
double xwline[NUMLIN], xeline[NUMLIN];
double ywline[NUMLIN], yeline[NUMLIN];
double xgps[NGPS], ygps[NGPS], zgps[NGPS];
double xup[NUP], yup[NUP];
double xlaser[NLASER],ylaser[NLASER];
double xfixup[NFIXUP], yfixup[NFIXUP];
double xfix, yfix, uxcalr, uycalr;

FILE * in_file;
FILE *out;

double uxsph(double, double, double, double); /* subroutines for
spherical point source displacements */
double uysph(double, double, double, double); /* called by fit
function */
double uzsph(double, double, double);

/*********************************************
/* This is the fitness function subroutine for the genetic algorithm
for inverting geodetic data for two volcanic sources - one spherical,
one elliptical, and a normal fault.

```

Definitions:

gene(NMOD)	-- Model vector
data(NDATA)	-- Data vector
vardat(NDATA)	-- Data variances
xeline(NUMLIN)	-- x coord. of east end of trilateration line
yeline(NUMLIN)	-- y coord. of east end of trilateration line
xwline(NUMLIN)	-- x coord. of west end of trilateration line
ywline(NUMLIN)	-- y coord. of west end of trilateration line
uex, uey	-- x and y displacements @ east end of line
uwx, uzy	-- x and y displacements @ west end of line

```

xe, ye, xw, yw      -- Distance from endpoints to sphere(s)
length               -- Length of trilateration line
unitx, unity          -- Unit vectors along line, east to west
xsph, ysph            -- Sphere x and y coordinates
sphdep               -- Sphere depth
volexp                -- Sphere point volume expansion
xfix, yfix             -- Benchmark location x and y coordinates
uxf, uyf, uzf           -- x, y, z displacement of benchmark due to
sphere
    xgps, ygps, zgps -- GPS point locations
    x(NGPS or NUP)   -- Distance in x direction from
sphere
    y(NGPS or NUP)   -- Distance in y direction from
sphere
    uxcal(NGPS)     -- x displacement of GPS point due to sphere
    uycal(NGPS)     -- y displacement of GPS point due to sphere
    uzcal(NGPS)     -- z displacement of GPS point due to sphere
    uzup(NUP)        -- z displacement of uplift point due to
sphere
    n                  -- Number of data points = NUMLIN + NUP +
3*NGPS
    dataav(n)         -- Calculated change in data points;
                        for lines, equals line expansion;
                        for points, equals difference between motion
                        at GPS or uplift point and benchmark.
    chisqr             -- Value of reduced chi square. */
    
```

```

double fit(double A, double B, double C, double D)
{
int n, m, i, j, k, nmod, upsum;
double phiback, squares;

    double uex, uey, uwx, uwy, uexx, ueyy,                      uwxx, uwyy, xe, xw, ye,
yw, uxf, uyf, uzf;
    double length, powx,          powy, unitx, unity;
    double chisq, chisqr;
    double x, y, r, s;
    double diff;
    double xr, yr, xer, yer, xwr, ywr, uxfr,                      uyfr;
    double uxcal[ngps], uycal[ngps], uzcal[ngps];
    double tuygps[ngps], tuygps[ngps], tuzgps[ngps];
    double uexp, ueyp, uwxp, uwyp, xep, yep, xwp, ywp, theta1;
    double uzup[nup], tuzup[      nup];
    double uzlaser[nlaser];
    double xsph[NSPH], ysph[NSPH], sphdep[NSPH], volexp[NSPH];

FILE * output_file;
FILE * test_file;

***** Initialize data vector indices *****/
n = 0;
numspf = NSPH;
numell = NUMELL;
num_normal = NNORM;
    
```

```

in_file = fopen("fit1.in", "r");

/* Unpack the model vector, get point source locations */

fscanf(in_file, "%i %i %i %i %i %i %i %i %i %i", &numlin, &ngps,
&nfixup, &nup1, &nup2, &nup3, &nup4, &nup5, &nup6, &nup7, &nlasers);
fclose(in_file);

nup = nup1 + nup2 + nup3 + nup4 + nup5 + nup6 + nup7;

xsph[0] = A;
ysph[0] = B;
sphdep[0] = C;
volexp[0] = D;

/* Trilateration lines */

/* Compute the line vectors */

for (i=0; i < numlin; i++){

    powx = pow((xeline[i] - xwline[i]),2);
    powy = pow((yeline[i] - ywline[i]),2);
    length = sqrt(powx + powy);
    unitx = (xeline[i] - xwline[i])/length;
    unity = (yeline[i] - ywline[i])/length;

    /* Initialize displacements */

    uex = uey = uwx = uwy = 0.;
    uexx = ueyy = uwxx = uwyy = 0.;
    xer= yer = xwr = ywr = 0.0;

    /* Calculate isotropic point expansions */

    for (j=0; j < numsph; j++){

        xe = xeline[i] - xsph[j];
        ye = yeline[i] - ysph[j];
        xw = xwline[i] - xsph[j];
        yw = ywline[i] - ysph[j];

        uex = uxsphe( sphdep[j],xe,ye,volexp[j]) + uex;
        uey = uysphe( sphdep[j],xe,ye,volexp[j]) + uey;
        uwx = uxsphe( sphdep[j],xw,yw,volexp[j]) + uwx;
        uwy = uysphe( sphdep[j],xw,yw,volexp[j]) + uwy;

    }

    /* Calculate line expansion, data point */

    /* Count each line data point */

    n++;
    datav[n] = ((uex - uwx) * unitx) + ((uey - uwy) * unity);
    /*fprintf(test_file,"%lf\n",datav[n]);*/
}

```

```

/* GPS point displacements */
/* First calculate expansion @ benchmark */

uxf = uyf = uzf = 0.;
x = y = 0.0;
xr = yr = 0.0;

for (i = 0; i <      numsph; i++){

    x = xfix - xsph[i];
    y = yfix - ysp[hi];

    uxf = uxsph( sphdep[i],x,y,volexp[i]) + uxf;
    uyf = uysph( sphdep[i],x,y,volexp[i]) + uyf;
    uzf = uzsph( sphdep[i],x,y,volexp[i]) + uzf;
}

/* Initialize and calculate the GPS displacement */

for (i = 0; i <      ngps; i++){

    uxcal[i] = 0.;
    uycal[i] = 0.;
    uzcal[i] = 0.;
    xr = yr = 0.0;

/* Isotropic point expansion */

    for (j = 0; j <      numsph; j++){

        x = xgps[i] - xsph[j];
        y = ygps[i] - ysp[hi];
        uxcal[i] = uxsph( sphdep[j], x, y, volexp[j]) + uxcal[i];
        uycal[i] = uysph( sphdep[j], x, y, volexp[j]) + uycal[i];
        uzcal[i] = uzsph( sphdep[j], x, y, volexp[j]) + uzcal[i];
    }

/* Add data point to point count, n */

/* Calculate difference between motion of benchmark and GPS */

    n++;
    datav[n] = uxcal[i] - uxf;
    n++;
    datav[n] = uycal[i] - uyf;
    n++;
    datav[n] = uzcal[i] - uzf;
}

/* End of GPS loop */

/* Leveling lines */

/* Initialize z-displacement */

upsum=0;

for (k=0; k < 7; k++){

```

```

/* First calculate expansion @ leveling loop benchmark */

uxf = uyf = uzf = 0.;
x = y = 0.0;
xr = yr = 0.0;

for (i = 0; i <      numspf; i++){

    x = xfixup[k] - xsph[i];
    y = yfixup[k] - ysph[i];
    uxf = usph( sphdep[i],x,y,volexp[i]) + uxf;
    uyf = uysph( sphdep[i],x,y,volexp[i]) + uyf;
    uzf = uzsph( sphdep[i],x,y,volexp[i]) + uzf;
}

/* Now calculate displacements on leveling loops      */

for (i = upsum; i < (upsum +           upeach[k]); i++){

    uzup[i] = 0.;
    xr = yr = 0.0;

/* Calculate isotropic point expansions */

    for (j = 0; j <      numspf; j++){

        x = xup[i] - xsph[j];
        y = yup[i] - ysph[j];
        uzup[i] = uzsph(     sphdep[j],x,y,volexp[j]) + uzup[i];
    }

/* Calculate difference between motion and benchmark, increment n */

    n++;
    datav[n] = uzup[i] - uzf;
}

upsum= upsum + upeach[k];

}

/* End of uplift loop */
/* Uplift points (laser altimeter) */

for (i=0; i < nlaser; i++){

x = y = 0.0;
xr = yr = 0.0;
uzlaser[i] = 0.;

/* Calculate isotropic point expansions */

    for (j = 0; j <      numspf; j++){

        x = xlaser[i] - xsph[j];
        y =ylaser[i] - ysph[j];
}

```

```

        uzlaser[i] = uzsph(      sphdep[j],x,y,volexp[j]) + uzlaser[i];
    }
    n++;
    datav[n] =     uzlaser[i];
}

/* End of laser calculations */

/* Calculate chi square; number of data points equals n */

ndata = n;

/* Check that ndata = numlin + nup + 3*ngps + nlaser */

m = numlin + nup + 3*ngps + nlaser;
numlin + nup +
if (n != m)
{
fprintf(output_file, "Caution: ndata does not equal
3*ngps + nlaser! n=%d", n);
fprintf(output_file, "%i %i \n", n, upsum);
}

diff = 0.0;
chisq = 0.0;
squares = 0.0;
chisqr = 0.0;

for (i = 1; i <= ndata; i++){
    diff = (data[i] - datav[i])/error[i];
    chisq = chisq + pow(diff,2.0);
}

squares = exp(-chisq);

return squares;
}

/*****************************************/
/* Functions */

/* Expansions - compute displacements due to dilating sphere */

/* X-displacements due to a dilating sphere */

double uxsph(double h, double x, double y, double volexp)
{
    double r, ux, r3;
    r = sqrt((h*h) + (y*y) + (x*x));
    r3 = pow(r,3.);
    ux = ((S*x)*volexp)/(r3);

    return ux;
}

/* Y-displacements due to a dilating sphere */

```

```

double uysph(double h, double x, double y, double volexp)
{
    double r, uy, r3;
    r = sqrt((h*h) + (y*y) + (x*x));
    r3 = pow(r,3.);
    uy = ((S*y)*volexp)/(r3);

    return uy;
}

/* Z-displacements due to a dilating sphere */

double uzsph(double h, double x, double y, double volexp)
{
    double r, uz, r3;
    r = sqrt((h*h) + (y*y) + (x*x));
    r3 = pow(r,3.);
    uz = ((S*h)*volexp)/(r3);

    return uz;
}

```

A.2 Parallel — Master/Slave

A.2.1 Master Program — Inversion.c (Evaluation Function)

```

/*****************************************/
/* Evaluation function: This takes a user defined function. */
/* Each time this is changed, the code has to be recompiled. */
/* The current function is a data calculation and chisquare fit. */
/*****************************************/

void eval_pvm(void)
{
    int i, j, k, l;
    int next, outstanding;
    int tid, msgtag, bytes;
    int bufid, status, done;

    double xx[NVARS];
    double fit;

    outstanding=0;
    next = 0;
    done = 0;

    /* So we know - a message tag of 6, from the slave(s), means they
       are ready for data. A message tag of 3, is sent from here, to send
       the packed genome data. A message tag of 8 means that there is a
       slave ready to send data, and a message tag of 7 is the data to be
       received from the slave. */

```

```

while (!done)
{
    /* Check to see if there is a slave ready */

    if ((bufid= pvm_nrecv(-1, 6)) != 0)
    {
        if(bufid == 0)
        {

            /* Get the id of the ready slave */

            pvm_bufinfo(bufid, &bytes, &msgtag, &tid);

            /* Create the data set, and send to that slave */

            for (k = 0; k < NVARS; k++)
            {
                xx[k] = population[next].gene[k];
            }

            pvm_initsend(PvmDataDefault);
            pvm_pkdouble(xx, NVARS, 1);
            pvm_pkdouble(datatest,NTEST*NTEST,1);
            pvm_send(tid,3);

            /* Increment outstanding to keep track of how
               many slaves are out there computing away */

            outstanding++;
        }
        else
        {
            printf("Error from pvm_nrecv, to fit: %i\n", bufid);
        }
        next++;
    }

    /* If there are computations out to the slaves, check to see if
       one is ready to send data back. */

    if (outstanding == 0 && (bufid= pvm_nrecv(-1, 8)) != 0)
    {
        if (bufid == 0)
        {
            /* Get data from willing slave. Place in
               temporary file so as not to overwrite best fitness
               ( stored in population[POPSIZE].fitness.*)

            pvm_bufinfo(bufid, &bytes, &msgtag, &tid);
            pvm_recv( tid, 7);
            pvm_upkdouble(&fit, 1, 1);
            temp_fit[next] = fit;
        }
        else
        {
            printf("Error from pvm_nrecv, from fit: %i\n",bufid);
        }
    }
}

```

```

        }

/* Decrease number of outstanding computations at slaves.
 */

        outstanding--;
    }

/* Check to see if done. */

if (next == POPSIZE && outstanding == 0) done = 1;
}

/* Copy over temporary fitnesses to correct array for GA
manipulations. Dump extras created by faster processors. */

for (i=0; i < POPSIZE; i++){
    population[i].fitness = temp_fit[i];
}

}

```

A.2.2 Slave Fitness Function — Fitsphere.c

```

#include "pvm3.h"
#include <stdio.h>
#include <stdlib.h>
#include <math.h>

***** Inversion definitions and variables *****

#define NSPH 1 /* no. of spheres */
#define NNORM 0 /* no. of normal faults */
#define NUMELL 0 /* no. of ellipses */
#define NVARS 4*NSPH + 7*NUMELL + 1*NNORM /* Number of inversion
variables */
#define NUMLIN 100 /* no. of potential lines */
#define NGPS 200 /* no. of potential gps points */
#define NFIXUP 40 /* no. of potential fixed pts for leveling */
#define NUPEACH 100 /* no. of potential uplift pts for each fixed
levelling pt */
#define NLASER 0
#define NUP 200
#define NDATA 200 /* no. of potential data points */
#define S 0.23873241 /* (3/4)/pi */
#define SS 0.026525824 /* (1/12)/pi */

int numlin, numspfh, numell, num_normal, nup, nup1, nup2, nup3, nup4,
nup5, nup6, nup7, ndata, ngps, nfixup, nupeach, nlaser; /* see
definitions in function below */
int generation; /* current generation no. */
int upeach[7];

int n, m, i, j, k, nmod, upsum;
int mytid, master;

```

```

int done, status, bufid, bytes, msgtag, tid;

double xx[NVARS];
double squares;

double uex, uey, uwx, uwv, uexx, ueyy, uwxx, uwyy, xe, xw, ye, yw, uxf,
uf, uzf;
double length, powx, powy, unitx, unity;
double chisq, chisqr;
double x, y, r, s;
double diff;
double xr, yr, xer, yer, xwr, ywr, uxfr, uyfr;
double xsph[NSPH], ysph[NSPH], sphdep[NSPH], volexp[NSPH];

double datav[NDATA], data[NDATA], error[NDATA];
double xwline[NUMLIN], xeline[NUMLIN];
double ywline[NUMLIN], yeline[NUMLIN];
double xgps[NGPS], ygps[NGPS], zgps[NGPS];
double xup[NUP], yup[NUP];
double xlabel[NLASER], ylabel[NLASER];
double xfixup[NFIXUP], yfixup[NFIXUP];
double xfix, yfix, uxcalr, uycalr;
double xnfe[NNORM], ynfe[NNORM], xnfw[NNORM], ynfw[NNORM];
double dip[NNORM], ntop[NNORM], nbottom[NNORM];
double xmid[NNORM], ymid[NNORM], semi_lngth[NNORM], thetaf[NNORM];
double uxcal[NGPS], uycal[NGPS], uzcal[NGPS];
double tuxgps[NGPS], tuygps[NGPS], tuzgps[NGPS];
double uexp, ueyp, uwxp, uwyp, xep, yep, xwp, ywp, thetal;
double uzup[NUP], tuzup[NUP];
double uzlaser[NLASER];

FILE * in_file;
FILE *out;
FILE * output_file;

double uxsph(double, double, double); /* subroutines for
spherical point source displacements */
double uysph(double, double, double); /* called by fit
function */
double uzsph(double, double, double);
void read_field_data(void);

/*********************************************
/* This is the fitness function subroutine for the genetic algorithm
for inverting geodetic data for a spherical source.

```

Definitions:

gene(NMOD)	-- Model vector
data(NDATA)	-- Data vector
vardat(NDATA)	-- Data variances
xeline(NUMLIN)	-- x coord. of east end of trilateration line
yeline(NUMLIN)	-- y coord. of east end of trilateration li
xwline(NUMLIN)	-- x coord. of west end of trilateration line
ywline(NUMLIN)	-- y coord. of west end of trilateration line

```

uex, uey      --  x and y displacements @ east end of line
uwx, uzy      --  x and y displacements @ west end of line
xe, ye, xw, yw --  Distance from endpoints to sphere(s)
length        --  Length of trilateration line
unitx, unity   --  Unit vectors along line, east to west
xsph, yspf    --  Sphere x and y coordinates
sphdep        --  Sphere depth
volexp        --  Sphere point volume expansion
xfix, yfix    --  Benchmark location x and y coordinates
uxf, uyf, uzf --  x, y, x displacement of benchmark due to
sphere
xgps, ygps, zgps --  GPS point locations
x(NGPS or NUP) --  Distance in x direction from
sphere
y(NGPS or NUP) --  Distance in y direction from
sphere
uxcal(NGPS)   --  x displacement of GPS point due to sphere
uycal(NGPS)   --  y displacement of GPS point due to sphere
uzzcal(NGPS)  --  z displacement of GPS point due to sphere
uzup(NUP)     --  z displacement of uplift point due to
sphere
n             --  Number of data points = NUMLIN + NUP +
3*NGPS
datav(n)      --  Calculated change in data points;
                  for lines, equals line expansion;
                  for points, equals difference between motion
                  at GPS or uplift point and benchmark.
chisqr        --  Value of reduced chi square. */

main()
{
done = 0;
while(!done){

/* Unpack the model vector, get point source locations */

mytid = pvm_mytid();
master = pvm_parent();

pvm_initsend(PvmDataDefault);
pvm_send(master, 6);

pvm_recv(master, 3);
pvm_upkdouble(    xx, NVARS, 1);

pvm_upkdouble(    datatest, NTEST*NTEST, 1);

xsph[0] = xx[0];
ysph[0] = xx[1];
sphdep[0] = xx[2];
volexp[0] = xx[3];

/*********/
/* Initialize and read in data */
/*********/

```

```

read_field_data();
n = 0;
numspf = NSPH;

nup = nup1 + nup2 + nup3 + nup4 + nup5 + nup6 + nup7;

/* Trilateration lines */
/* Compute the line vectors */

for (i=0; i < numlin; i++){

    powx = pow((xeline[i] - xwline[i]),2);
    powy = pow((yeline[i] - ywline[i]),2);
    length = sqrt(powx + powy);
    unitx = (xeline[i] - xwline[i])/length;
    unity = (yeline[i] - ywline[i])/length;

    /* Initialize displacements */

    uex = uey = uwx = uwy = 0.;
    uexx = ueyy = uwxx = uwyy = 0.;
    xer= yer = xwr = ywr = 0.0;

    /* Calculate isotropic point expansions */

    for (j=0; j < numspf; j++){

        xe = xeline[i] - xsph[j];
        ye = yeline[i] - ysph[j];
        xw = xwline[i] - xsph[j];
        yw = ywline[i] - ysph[j];

        uex = uxsph( sphdep[j],xe,ye,volexp[j]) + uex;
        uey = uysph( sphdep[j],xe,ye,volexp[j]) + uey;
        uwx = uxsph( sphdep[j],xw,yw,volexp[j]) + uwx;
        uwy = uysph( sphdep[j],xw,yw,volexp[j]) + uwy;

    }

    /* Calculate line expansion, data point */
    /* Count each line data point */

    n++;
    datav[n] = ((uex - uwx) * unitx) + ((uey - uwy) * unity);
}

/* GPS point displacements */
/* First calculate expansion @ benchmark */

uxf = uyf = uzf = 0.;
x = y = 0.0;
xr = yr = 0.0;

for (i = 0; i < numspf; i++){

    x = xfix - xsph[i];
}

```

```

y = yfix - ysph[i];

uxf = uxsph( sphdep[i],x,y,volexp[i]) + uxf;
uyf = uysph( sphdep[i],x,y,volexp[i]) + uyf;
uzf = uzsph( sphdep[i],x,y,volexp[i]) + uzf;
}

/* Initialize and calculate the GPS displacement */

for (i = 0; i < ngps; i++){

    uxcal[i] = 0.;
    uycal[i] = 0.;
    uzcal[i] = 0.;
    xr = yr = 0.0;

    /* Isotropic point expansion */

    for (j = 0; j < numspfh; j++){

        x = xgps[i] - xsph[j];
        y = ygps[i] - ysph[j];
        uxcal[i] = uxsph( sphdep[j], x, y, volexp[j]) + uxcal[i];
        uycal[i] = uysph( sphdep[j], x, y, volexp[j]) + uycal[i];
        uzcal[i] = uzsph( sphdep[j], x, y, volexp[j]) + uzcal[i];
    }
    /* Add data point to point count, n */
    /* Calculate difference between motion of benchmark and GPS */

    n++;
    datav[n] = uxcal[i] - uxf;
    n++;
    datav[n] = uycal[i] - uyf;
    n++;
    datav[n] = uzcal[i] - uzf;
/*fprintf(test_file,"%lf\n",datav[n]);*/
}

/* End of GPS loop */

/* Leveling lines */

/* Initialize z-displacement */

upsum=0;

for (k=0; k < 7; k++){

    /* First calculate expansion @ leveling loop benchmark */

    uxf = uyf = uzf = 0.;
    x = y = 0.0;
    xr = yr = 0.0;

    for (i = 0; i < numspfh; i++){

        x = xfixup[k] - xsph[i];

```

```

y = yfixup[k] - yspf[i];
uxf = uxsph( sphdep[i],x,y,volexp[i]) + uxf;
uyf = uysph( sphdep[i],x,y,volexp[i]) + uyf;
uzf = uzsph( sphdep[i],x,y,volexp[i]) + uzf;
}

/* Now calculate displacements on leveling loops      */

for (i = upsum; i < (upsum +           upeach[k]); i++){

    uzup[i] = 0.;
    xr = yr = 0.0;

/* Calculate isotropic point expansions */

    for (j = 0; j <      numspf; j++){
        x = xup[i] - xsph[j];
        y = yup[i] - yspf[j];
        uzup[i] = uzsph(      sphdep[j],x,y,volexp[j]) + uzup[i];
    }

/* Calculate difference between point motion and benchmark, increment
n */

    n++;
    datav[n] =      uzup[i] - uzf;
}

upsum= upsum + upeach[k];
}

/* End of uplift loop */

/* Uplift points (laser altimeter) */

for (i=0; i < nlaser; i++){

    x = y = 0.0;
    xr = yr = 0.0;
    uzlaser[i] = 0.;

/* Calculate isotropic point expansions */

    for (j = 0; j <      numspf; j++){
        x = xlaser[i] - xsph[j];
        y = ylaser[i] - yspf[j];
        uzlaser[i] = uzsph(      sphdep[j],x,y,volexp[j]) + uzlaser[i];
    }

    n++;
    datav[n] =      uzlaser[i];
}

/* End of laser calculations */

```

```

/* Calculate chi square; number of data points equals n */

ndata = n;

/* Check that ndata = numlin + nup + 3*ngps + nlaser */

m = numlin + nup + 3*ngps + nlaser;

if (n != m)
{
    fprintf(output_file, "Caution: ndata does not equal
3*ngps + nlaser! n=%d", n);                                numlin + nup +
    fprintf(output_file, "%d %d \n", n, upsum);
}

diff = 0.0;
chisq = 0.0;
squares = 0.0;
chisqr = 0.0;

for (i = 1; i <= ndata; i++){
    diff = (data[i] - datav[i])/error[i];
    chisq = chisq + pow(diff,2.0);
}

squares = exp(-chisq);

pvm_initsend(PvmDataDefault);
pvm_send(master, 8);

pvm_initsend(PvmDataDefault);
pvm_pkdouble(&squares, 1, 1);
pvm_send(master, 7);

}

pvm_exit();
}

/*****************************************/
/* Functions */
/*****************************************/

/* Expansions - compute displacements due to dilating sphere */

/* X-displacements due to a dilating sphere */

double uxsph(double h, double x, double y, double volexp)
{
    double r, ux, r3;
    r = sqrt(h*h + (y*y) + (x*x));
    r3 = pow(r,3.);
}

```

```

    ux = ((S*x)*volexp)/(r3);

    return ux;
}

/* Y-displacements due to a dilating sphere */

double uysph(double h, double x, double y, double volexp)
{
    double r, uy, r3;
    r = sqrt((h*h) + (y*y) + (x*x));
    r3 = pow(r,3.);
    uy = ((S*y)*volexp)/(r3);

    return uy;
}

/* Z-displacements due to a dilating sphere */

double uzsph(double h, double x, double y, double volexp)
{
    double r, uz, r3;
    r = sqrt((h*h) + (y*y) + (x*x));
    r3 = pow(r,3.);
    uz = ((S*h)*volexp)/(r3);

    return uz;
}

/*****************/
/* A procedure for reading in field data.          */
/* The field data should be stored in "fit1.in"      */
/*****************/

void read_field_data()
{
int i, k;
double semix_normal[NNORM], semiy_normal[NNORM];

FILE * in_motion;
FILE * in_error;

in_file = fopen("/pvm_temp/fit/fit1.in", "r");
in_motion = fopen("/pvm_temp/fit/motion.in", "r");
in_error = fopen("/pvm_temp/fit/error.in", "r");

num_normal=NNORM;

fscanf(in_file, "%i %i %i %i %i %i %i %i %i %i", &numlin, &ngps,
&nfixup, &nup1, &nup2, &nup3, &nup4, &nup5, &nup6, &nup7, &nlaser);

nup = nup1 + nup2 + nup3 + nup4 + nup5 + nup6 + nup7;

ndata = numlin + 3*      ngps + nup + nlaser;

upeach[0]=nup1;
}

```

```

upeach[1]=nup2;
upeach[2]=nup3;
upeach[3]=nup4;
upeach[4]=nup5;
upeach[5]=nup6;
upeach[6]=nup7;

/* Get trilateration line locations */

for (i=0; i < numlin; i++){
    fscanf(in_file, "%lf %lf %lf %lf", &xeline[i], &yeline[i],
&xloline[i], &yloline[i]);
    fprintf(out, "%lf %lf %lf %lf \n", xeline[i], yeline[i],
xloline[i], yloline[i]);
}
/* GPS point displacements */
/* First get location of benchmark, initialize displacements */

fscanf(in_file, "%lf %lf", &xfix, &yfix);

/* Then get GPS locations */

for (i=0; i < ngps; i++)
{
    fscanf(in_file, "%lf %lf %lf", &xgps[i], &ygps[i], &zgps[i]);
}
/* Finally, get uplift point locations */
/* First, get fixed point locations */

for (k=0; k < 7; k++)
{
    fscanf(in_file, "%lf %lf", &xfixup[k], &yfixup[k]);
}

for (i=0; i < nup; i++)
{
    fscanf(in_file, "%lf %lf", &xup[i], &yup[i]);
}

/* Oh, yeah, get laser locations */

for (i=0; i < nlaser; i++)
{
    fscanf(in_file, "%lf %lf", &xlaser[i], &ylaser[i]);
}

fclose(in_file);

for (i = 1; i <= ndata; i++){

    fscanf(in_motion, "%lf ", &data[i]);
}

fclose(in_motion);

for (i = 1; i <= ndata; i++){

```

```

        fscanf(in_error, "%lf ", &error[i]);
    }
fclose(in_error);
}

```

Appendix B — Virtual California Program Code

B.1 Serial

B.1.1 Main, SG_Compute.c:

```

Procedure Main SG_Compute ;

/*Computes the stress transferred from fault i to fault      j when fault i slips by a unit
amount. */
Procedure Stress_Greens_Function(N,N);

Main
{
FILE *in_file;
FILE *out_file;

/* Read in data on fault geometry */

in_file = fopen("Fault_Data.d", "r");
fscanf(in_file, Fault_Geometries );
fclose(in_file);

/* Open output file */

out_file=fopen( SG_Coefficients.d, w );

/*
* Begin stress Green s function computation loop */
    For (i=0; i<N; i++);
    {
        For (j=0; j<N; j++);
        {
/* Compute each stress transfer coefficient */
            Procedure Stress_Greens_Function(i,j);

/* Print result to output file */

```

```

        printf,2,Stress_Greens_Functions ;
    }
}

/* Close output file and exit */

fclose(out_file);
end ;
}

```

B.1.2 Main, EQ_Simulator.c:

```

Procedure Main EQ_Simulator ;

/*Computes the state of stress on segment i at time t. */
Procedure Stress_State_Compute(N,s,Number_time_steps);

Main
{
    double s(N);           /* Current slip state vector */

    FILE *in_file;
    FILE *out_file;

    /* Read in data on fault data, friction data, and stress
    transfer coefficients */

    in_file = fopen(Fault_Data.d, r );
    fscanf(in_file, Slip_Rates );
    fclose(in_file);

    in_file = fopen(Friction_Data.d, r );
    fscanf(in_file, Friction_Parameters );
    fclose(in_file);

    in_file = fopen(SG_Coefficients.d, r );
    fscanf(in_file, Stress_Greens_Functions );
    fclose(in_file);

    /* Open output file */
    out_file = fopen(EQ_History_01.d, w );

```

```

/* Time Loop */
    For (time_index=0; time_index<Number_time_steps;
time_index++);
{
    time = time + time_index * time_step;

/* Compute new value of stress on segment i */
    Procedure Stress_State_Compute(i,time);

/* Check to see which segments have  $\sigma_i(t) \geq \sigma_i^F$  */
    while (any  $\sigma_i(t) \geq \sigma_i^F$  )
{
    for (i=0; i<N; i++)
{
/*
Update slip s(i) */
    s(i)= s(i) +  $\Delta\sigma_i / K_i$  + random number;
}

/* Check to ensure all  $\sigma_i(t) < \sigma_i^F$  */
    if ( $\sigma_i(t) < \sigma_i^F$  )
endwhile;
elseif ( $\sigma_i(t) \geq \sigma_i^F$  ) repeat;
}

/* Record time and state of slip in EQ_History.d */
printf, 4, time, s(N);

/* End of time loop */
}

/* Close output file and exit */

fclose(out_file);
end;
}

```

B.2 Parallel Code (Master/Slave)

B.2.1 Master - SG_Compute.c

```

/*Computes the stress transferred from fault i to fault j when fault i slips by a unit
amount. */

```

```

Main
{
    int i, j, k, l;
    int next, outstanding;
    int tid, msgtag, bytes;
    int bufid, status, done;

    FILE *in_file;
    FILE *out_file;

    /* Read in data on fault geometry */

    in_file = fopen("Fault_Data.d", "r");
    fscanf(in_file, Fault_Geometries );
    fclose(in_file);

    /* Open output file */

    out_file=fopen( SG_Coefficients.d, w );

    /* Begin stress Green s function computation loop */

    next = 0;
    done = 0;

    while (!done)
    {
        /* Check to see if there is a slave ready */

        if ((bufid=pvm_nrecv(-1, 6)) != 0)
        {
            if(bufid  0)
            {

                /* Get the id of the ready slave */

                pvm_bufinfo(bufid, &bytes, &msgtag, &tid);

                /* Send data to the slave to compute each stress transfer coefficient*/

                pvm_initsend(PvmDataDefault);
                pvm_pkdouble(SG_Coefficients, N, 1);
                pvm_send(tid,3);
}

```

```

/* Increment outstanding to keep track of how
many slaves are out there computing away */

outstanding++;
}

else
{
    printf("Error from pvm_nrecv, to fit: %i\n", bufid);
}

next++;
}

/* If there are computations out to the slaves, check to see if
one is ready to send data back. */

if (outstanding > 0 && (bufid=pvm_nrecv(-1, 8)) != 0)
{
    if (bufid == 0)
    {
        /* Get data from willing slave. Place in
temporary file so as not to overwrite best fitness
(stored in population[POPSIZE].fitness.*)

pvm_bufinfo(bufid, &bytes, &msgtag, &tid);
pvm_recv(tid, 7);
pvm_upkdouble(&Stress_Greens_Functions, N, 1);

/* Print result to output file */

fprintf(out_file, Stress_Greens_Functions );

    }
else
{
    printf("Error from pvm_nrecv, from fit: %i\n",bufid);
}
}

/* Decrease number of outstanding computations at slaves. */

outstanding--;
}

/* Check to see if done. */

if (next == NUMSEGMENTS && outstanding == 0) done = 1;
}

```

```
/* Close output file and exit */

    fclose(out_file);
    end;
}
```

B.2.2 Master, EQ_Simulator.c

```
/*Computes the state of stress on segment i at time t. */
```

```
Main
```

```
{
```

```
int next, outstanding;
int tid, msgtag, bytes;
int bufid, status, done;
```

```
double s(N);           /* Current slip state vector */
```

```
FILE *in_file;
FILE *out_file;
```

```
/* Read in data on fault data, friction data, and stress
transfer coefficients */
```

```
in_file = fopen(Fault_Data.d, r );
fscanf(in_file, Slip_Rates );
fclose(in_file);
```

```
in_file = fopen(Friction_Data.d, r );
fscanf(in_file, Friction_Parameters );
fclose(in_file);
```

```
in_file = fopen(SG_Coefficients.d, r );
fscanf(in_file, Stress_Greens_Functions );
fclose(in_file);
```

```
/* Open output file */
out_file = fopen(EQ_History_01.d, w );
```

```
/* Time Loop */
```

```
For (time_index=0; time_index<Number_time_steps;
time_index++);
{
    time = time + time_index * time_step;
```

```

/* Compute new value of stress on segment i */

while (!done)
{
    /* Check to see if there is a slave ready */

    if ((bufid=pvm_nrecv(-1, 6)) != 0)
    {
        if(bufid  0)
        {

            /* Get the id of the ready slave */

            pvm_bufinfo(bufid, &bytes, &msgtag, &tid);

            /* Send data to the slave to compute each stress transfer coefficient*/

            pvm_initsend(PvmDataDefault);
            pvm_pkdouble(Slip_Rates, N, 1);
            pvm_pkdouble(Friction_Parameters, N, 1);
            pvm_pkdouble(SG_Coefficients, N, 1);
            pvm_send(tid,3);

            /* Increment outstanding to keep track of how
               many slaves are out there computing away */

            outstanding++;
        }
        else
        {
            printf("Error from pvm_nrecv, to fit: %i\n", bufid);
        }
        next++;
    }

    /* If there are computations out to the slaves, check to see if
       one is ready to send data back. */

    if (outstanding  0 && (bufid=pvm_nrecv(-1, 8)) != 0)
    {
        if (bufid  0)
        {
            /* Get data from willing slave. Place in
               temporary file so as not to overwrite best fitness

```

```

(stored in population[POPSIZE].fitness.*)

pvm_bufinfo(bufid, &bytes, &msgtag, &tid);
pvm_recv(tid, 7);
pvm_upkdouble(&S, N, 1);

/* Print result to output file */

fprintf(out_file, S(N));

}

else
{
    printf("Error from pvm_nrecv, from fit: %i\n",bufid);
}

/* Decrease number of outstanding computations at slaves. */

outstanding--;
}

/* Check to see if done. */

if(next = NUMSEGMENTS && outstanding == 0) done = 1;
}

/* Check to see which segments have  $\sigma_i(t) \geq \sigma_i^F$  */
while (any  $\sigma_i(t) \geq \sigma_i^F$ )
{
    for (i=0; i<N; i++)
    {

/* Update slip  $s(i)$  */
         $s(i) = s(i) + \Delta\sigma_i / K_i + \text{random number};$ 
    }
}

/* Check to ensure all  $\sigma_i(t) < \sigma_i^F$  */
if ( $\sigma_i(t) < \sigma_i^F$ )
endwhile;
elseif ( $\sigma_i(t) \geq \sigma_i^F$ ) repeat;
}

/* Record time and state of slip in EQ_History.d */
printf(4, time, s(N);

/* End of time loop */

```

```
    }  
  
/* Close output file and exit */  
fclose(out_file);  
end;  
  
}
```

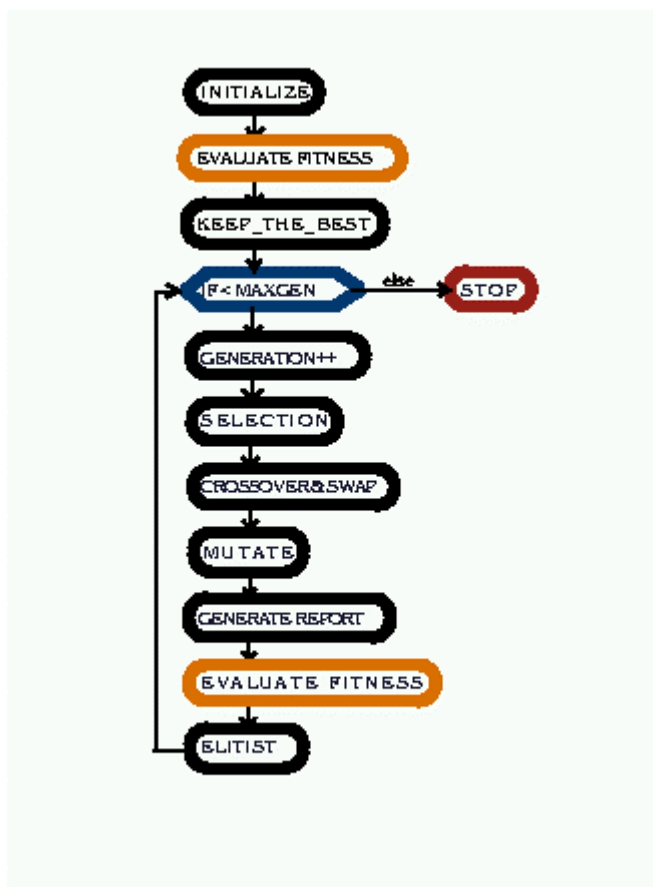


Figure 1: Flow chart, genetic algorithm inversion program.

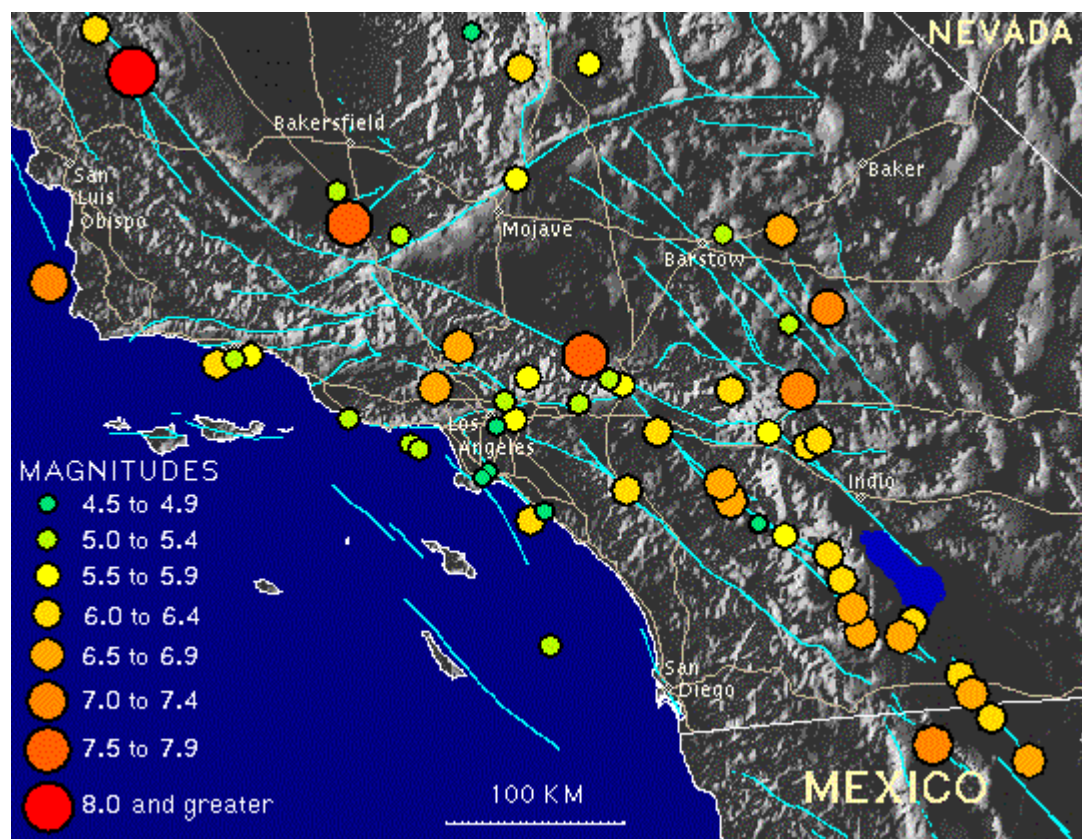


Figure 2: Historic seismicity, southern California (Southern California Earthquake Center, <http://www.scec.org/clickmap.html>).

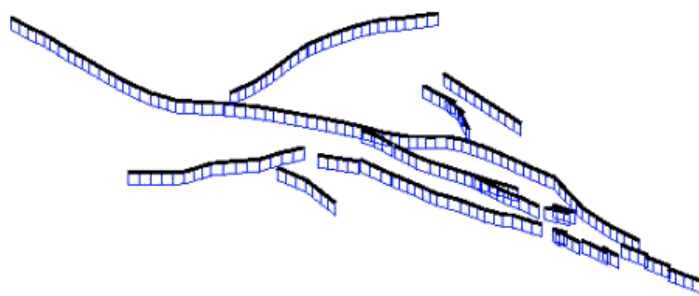


Figure 3: Map of the 215 fault segments used in the implementation of the Virtual California simulation. Only the strike slip faults are represented in this simplified model.

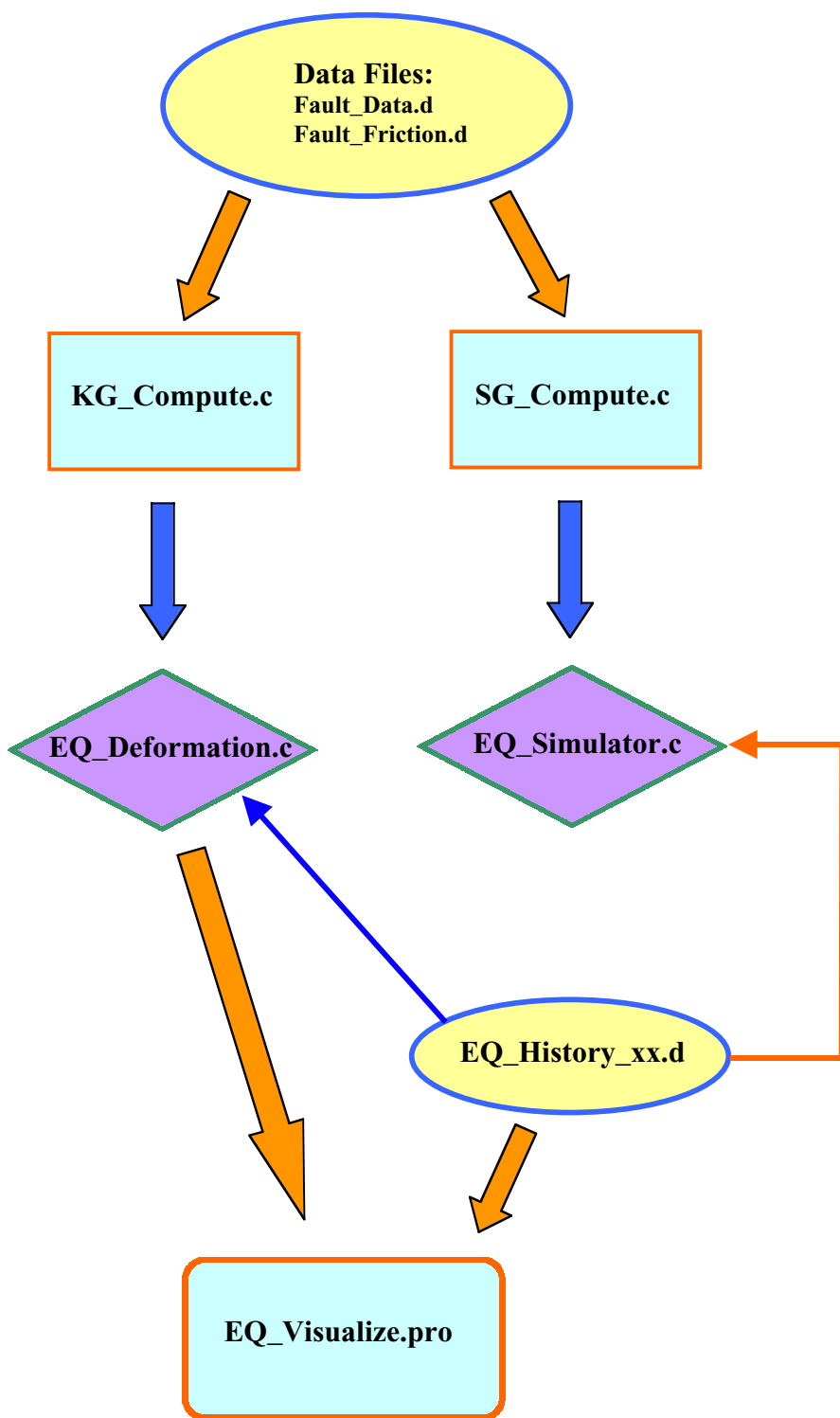


Figure 4: Flow diagram for parallelization of *Virtual California* earthquake simulation program.

FUNCTION	RICHTER	RICHTER TO KOCH	KOCH	KOCH TO RICHTER
SPHERE	3940	1025	545	420
ELLIPSE	6300	1220	830	625

TABLE 1: Time, in seconds, to process 1000 generations with the processors listed. "Richter to Koch" means that the master process was resident on Richter and there were two slave processes, one on Richter and one on Koch.

References

- [1] J. Radajewski and D. Eadline, *Linux Beowulf How-To*, www.ibiblio.org/mdw/HOWTO/Beowulf-HOWTO.html (1998).
- [2] H. Dietz, *Parallel Processing How-To*, www.ibiblio.org/mdw/HOWTO/Parallel-Processing-HOWTO.html (1998).
- [3] PVM website, www.epm.ornl.gov/pvm/pvm_home.html.
- [4] MPI website, www.unix.mcs.anl.gov/mpi/.
- [5] Z. Michalewicz, Z., *Genetic Algorithms + Data Structures = Evolution Programs*. Springer-Verlag, New York, NY (1992).
- [6] J.H. Holland, *Adaptation in Natural and Artificial Systems*. MIT Press, Cambridge, MA (1975).
- [7] D.E. Goldberg, *Genetic Algorithms in Search, Optimization, and Machine Learning*. Addison Wesley, Reading, MA (1989).
- [8] M. Mitchell, *Proc. First Int. Conf. Artificial Life*. Paris, France, 245 (1992).
- [9] A. Geist, A. Beguelin, J. Dongarra, W. Jiang, R. Manchek, and V. Sunderam, *PVM: Parallel Virtual Machine — A Users Guide and Tutorial for Networked Parallel Computing*. MIT Press, Cambridge, MA (1994).
- [10] J.B. Rundle, W. Klein, K.F. Tiampo and S.J. Gross, *Phys. Rev. E*, **61**, 2418 (2000).
- [11] J.B. Rundle, *J. Geophys. Res.*, **93**, 6255 (1988).
- [12] S.N. Ward, *Bull. Seism. Soc. Am.*, **90**, 370 (2000).
- [13] J. Deng and L.R. Sykes, *J. Geophys. Res.*, **102**, 9859 (1997).
- [14] B.N.J. Persson, *Sliding Friction, Physical Principles and Applications* (Springer-Verlag, Berlin, 1998).
- [15] J. Dieterich, *J. Geophys. Res.*, **84**, 2161 (1979).
- [16] T.E. Tullis, *Proc. Nat. Acad. Sci.*, **93**, 3803 (1996).
- [17] S. L. Karner and C. Marone, in *GeoComplexity and the Physics of Earthquakes*, ed. JB Rundle, DL Turcotte and W. Klein (Amer. Geophys. Un., Washington DC, 2000)
- [18] See for example, R. Peierls, *Phys. Rev.*, **54**, 918 (1934).
- [19] Rundle, J.B., W. Klein, S. Gross, and D.L. Turcotte, *Phys. Rev. Lett.*, **75**, 1658-1661 (1995).
- [20] W. Klein, JB Rundle and CD Ferguson, *Phys. Rev. Lett.*, **78**, 3793 (1997).
- [21] J.B. Rundle, P.B. Rundle, W. Klein, J. de sa Martins, K. F. Tiampo, A. Donnellan, and L. H. Kellogg, *PAGEOPH*, submitted.

Nonlinear Network Dynamics on Earthquake Fault Systems

by

Paul B. Rundle¹, John B. Rundle², Kristy F. Tiampo³,
Jorge de sa Martins³,Seth McGinnis³, and W. Klein⁴

¹Fairview High School, Boulder CO 80309
(Now at: Department of Physics
301 E 12th St., Harvey Mudd College,
Claremont, CA 91711)

²Colorado Center for Chaos & Complexity
CIRES, and Department of Physics, CB 216
University of Colorado, Boulder, CO 80309
and

Distinguished Visiting Scientist, Jet Propulsion Laboratory
Pasadena, CA 91125

³Colorado Center for Chaos & Complexity
and CIRES, CB 216
University of Colorado, Boulder, CO 80309

⁴Department of Physics, Boston University
Boston, MA 02215
and
Center for Nonlinear Science
Los Alamos National Laboratory, Los Alamos, NM 87545

Abstract

Earthquake faults occur in networks that have dynamical modes not displayed by single isolated faults. Using simulations of the network of strike-slip faults in southern California, we find that the physics depends critically on both the interactions among the faults, which are determined by the geometry of the fault network, as well as on the stress dissipation properties of the nonlinear frictional physics, similar to the dynamics of integrate-and-fire neural networks.

Earthquake forecasting and prediction is complicated by the fact that earthquake faults in nature occur in strongly interacting fault networks. To date however, recent work has focussed primarily on models for single isolated faults. Yet it is likely that emergent modes may appear in complex fault networks that are not properties of single faults [1,2]. Such "network modes" [3-9] in nature include enhanced seismic triggering, retardation, temporary quasi-periodic behavior such as observed at Parkfield, California, "Mogi donuts", precursory quiescence or activation, and clustering. Qualitatively similar phenomena are seen in integrate-and-fire neural networks, where complex dynamical patterns arise through the interactions of simple voltage-threshold neural cells [1,2,10]. Here we examine the dynamics of the geometrically complex network of horizontally-slipping strike-slip faults existing in southern California to develop clues for understanding the failure modes characterizing interacting fault networks.

To summarize our results: We found that strongly correlated, geometrically complex mean field fault networks have dynamics very different from single isolated faults. We also find that the stress-dissipation properties of the fault friction law plays an important role in the on-off switching of dynamical activity on the network, as well as in the nature and configuration of the failure modes. The dynamics can be illuminated by the construction of Coulomb Failure Functions, illustrating the influence of one fault on another.

General methods for carrying out the network simulations have been discussed in refs. [8,11,12]. Briefly, one defines a fault geometry in an elastic medium, computes the stress Greens functions (i.e., stress transfer coefficients), assigns frictional properties to each fault, then drives the system via the slip deficit (defined below). The elastic interactions produce mean field dynamics in the simulations [8]. We focus here on the major horizontally-slipping strike-slip (horizontal motion) faults in southern California that produce the most frequent and largest magnitude events. We used the tabulation of strike slip faults and fault properties as published in ref [13]. All major faults in southern California, together with the major historic earthquakes, are shown in figure 1. Figure 2 shows our model fault network. Each fault was assigned a uniform depth of 20 km, the maximum depth of earthquakes in California, and was subdivided into segments having a horizontal scale size of approximately 10 km each.

Several friction laws are described in the literature, including Coulomb failure [14], slip-dependent or velocity-dependent friction [4,14], and rate-and-state [15]. Here we use a parametrization of recent laboratory friction experiments [16], in which the stiffness of the loading machine is low enough to allow for unstable stick-slip when a

failure threshold $\sigma^F(V)$ is reached, where $\sigma^F(V)$ is a weak (logarithmic) function of the load point velocity V . Sudden slip then occurs in which the stress decreases to the level of a residual stress $\sigma^R(V)$, again a weak function of V . Stable precursory slip is observed to occur whose velocity increases with stress level, reaching a magnitude of a few percent of the driving load point velocity just prior to failure at $\sigma = \sigma^F(V)$.

The simplest form of the friction equations describing these experiments can be obtained from space-time coarse-graining procedures applied to simple planar fault models [17]. For a single block sliding on a frictional surface, the mean field form of these equations reduces to:

$$\frac{ds}{dt} = \frac{\Delta\sigma}{K} \left\{ \alpha + \delta(t - t_F) \right\} \quad (\text{Friction Stress}) \quad (1)$$

$$\sigma = K(Vt - s) \quad (\text{Elastic Load Stress}) \quad (2)$$

where $s(x,t)$ is slip at position x and time t , $\sigma(x,t)$ is shear stress, K is a elastic stiffness (change in stress per unit slip), and stress drop $\Delta\sigma = \sigma - \sigma^R(V)$. For laboratory experiments, K is the {machine + sample} stiffness, and for simulations, represents the stiffness of a coarse-grained element of the fault of scale size L . α represents the ratio of the effective stiffness modulus KL to a surface viscosity η , $\alpha = KL / \eta$. $\delta()$ is the Dirac delta, and t_F is any time at which $\sigma(x,t_F) = \sigma^F(V)$. The quantity $(s - Vt)$ is the slip deficit referred to above. Here we examine models with $\alpha = \text{constant}$. Both σ^F and σ^R can be parametrized as functions of the normal stress χ by means of coefficients of static μ_S and ("effective") kinetic μ_K coefficients of friction, $\sigma^F = \mu_S \chi$, $\sigma^R = \mu_K \chi$. The latter relation implicitly assumes that dynamical overshoot or undershoot during sliding is approximately constant [14].

An interesting result with important implications can be obtained by considering two sliding blocks, coupled to one another by a spring with constant K_C , and each coupled to a loader plate by a spring with constant K_L . Consider a set of reduced equations, which for block 1 are:

$$\frac{ds_1}{dt} = \frac{\Delta\sigma_1}{(K_L + K_C)} \alpha \quad (3)$$

$$\sigma_1 = K_L(Vt - s_1) + K_C(s_2 - s_1) \quad (4)$$

An analogous set of equations holds for block 2. If the difference in stress at time $t=0$ is given by $\delta\sigma(0) = \sigma_2(0) - \sigma_1(0)$, then at a time t later:

$$\delta\sigma(t) = \delta\sigma(0) e^{-\beta t}, \text{ where } \beta = \alpha \left(\frac{K_L + 2K_C}{K_L + K_C} \right) \quad (5)$$

For $\alpha > 0$, differences in stress decay exponentially in time, a process of *stress smoothing*. If either $\alpha < 0$ or that $K_C < 0$, conditions that can occur in more general elastic or frictional systems [17, 18, 19], variations in stress grow exponentially in time, a process of *stress roughening*. For general three-dimensional fault network models, both stress smoothing and stress roughening should occur [18], as well as smoothing-to-roughening transitions.

Earthquake data obtained from the historical record as well as geological field studies represent the primary physical signatures of how the earthquake cycle is affected by the frictional properties that exist on the faults. The timing, magnitude and complexity of these historical events are a direct reflection of the values of the frictional parameters: α , σ^F , σ^R . Since the dynamics (1)-(2) depends on the characteristic length scale L for each segment, all of these frictional parameters should be regarded as scale-dependent functions of L : $\alpha = \alpha(\Delta\sigma, L)$, $\sigma^F = \sigma^F(L, V)$, $\sigma^R = \sigma^R(L, V)$. For simulations in which one or more distinct scales L are chosen for each fault segment (length and width, for example), one must choose α , σ^F , σ^R in such a way that the historical record of activity on the fault network is matched as closely as possible. This is the *data assimilation* problem for which we have developed a simple, but physically motivated method.

For historical earthquakes, there can be considerable uncertainty about where the event was located [4]. Modern studies [4, 19, 20] of earthquakes indicate that slip or seismic moment M_o ([4]: also defined in (4) below) is often distributed regionally over a number of faults and sub-faults. Therefore our technique assigns a weighted average of the scalar seismic moments for given historic or pre-historic events during an observational period to *all* of the faults in the system. To be physically plausible, the weighting scheme should assign most of the moment M_o to faults near the location of maximum ground shaking and decay rapidly with distance. Since the seismic moment is the torque associated with one of the moment tensor stress-traction double couples, it is most reasonable to use the (inverse cube power of distance r) law that describes the decay of stress with distance [21]. Comparisons with data indicate that this method yields average recurrence intervals similar to those found in nature.

Step 1: Assignment of Moment Rates. All historical events in southern California since 1812 are used (ref [13]). For each of the 215 fault segments in the model, the contribution of moment release rate from the j^{th} historical earthquake $dM_o(t_j)/dt$ to the rate on the i^{th} fault segment, dm_i/dt , is :

$$\frac{dm_i}{dt} = \Gamma \left[\frac{\sum_j \frac{dM_o(t_j)}{dt} r_{ij}^{-3}}{\sum_j r_{ij}^{-3}} \right] \quad (6)$$

where $r_{ij} = |x_i - x_j|$ is the distance between the event at location x_j and time t_j , and the fault segment at x_i . The factor Γ accounts for the limited period of historical data available compared to the length of the earthquake cycle, and is determined by matching the total regional moment rate, $\sum_i dm_i/dt$, to the observed current regional moment rate. We find $\Gamma \approx .44$. Application of (6) when $x_i \approx x_j$ is understood to be in the limiting sense. Equation (6) arises if one regards r_{ij}^{-3} as a probability density function, and assumes that each earthquake is a point source. We correct for the largest events, which are long compared to the depth, by representing the large event as a summation of smaller events distributed along the fault.

Step 2: Determination of Friction Coefficients. The seismic moment is:

$$M_o(t_j) = \mu \langle s(t_j) \rangle A \quad (7)$$

where μ is shear modulus, $\langle s(t_j) \rangle$ is average slip at time t_j , and A is fault area. For a compact fault, the average slip in terms of stress drop $\Delta\sigma$ is [22]:

$$\langle s \rangle = \frac{f \Delta\sigma \sqrt{A}}{\mu} \quad (8)$$

where f is a dimensionless fault segment shape factor having a value typically near 1. Standard assumptions of $f \sim 1$, $\Delta\sigma \sim 5 \times 10^6$ Pa, $\mu \sim 3 \times 10^{10}$ Pa yield reasonable slip values. The average slip is converted to a difference between static and kinetic friction, $(\mu_s - \mu_k)_i$ for the i^{th} fault segment via the relation:

$$(\mu_s - \mu_k)_i \approx \frac{m_i}{f A^{3/2} \chi_i} \quad (9)$$

obtained by combining (7), (8), and $\Delta\sigma \approx \sigma^F - \sigma^K$. To compute $(\mu_s - \mu_k)_i$, a typical value of χ_i for each segment is computed from the average gravitationally-induced compressive stress. Since the stochastic nature of the dynamics depends only on the differences $(\mu_s - \mu_k)_i$ [8,11], we set $\mu_k = .001$ (all i).

Step 3. Aseismic Slip Factor: Earthquake faults are characterized by varying amounts of aseismic creep (slow slip generating no elastic waves) that arises from the "stress leakage" factor α . Analogously in a neural network, α represents the current leakage through the cell membrane. The most famous example of aseismic creep is the

region of the San Andreas fault in central California, in which no seismic slip has ever been observed. The average fraction of slip on each fault that is aseismic is equal to $\alpha_i/2$, and has also been tabulated for southern California faults in ref [13].

Figures 3 and 4 are illustrations of the space-time behavior of the Coulomb Failure Function $CFF(\mathbf{x}_i, t) = \{\sigma(\mathbf{x}_i, t) - \mu_S(\mathbf{x}_i)\} \chi(\mathbf{x}_i, t)\}$ for all of the 215 fault segments, placed end-to-end along the horizontal axis, in the southern California network model (see figure 2). A horizontal line represents an earthquake, which occurs on a segment when $CFF(\mathbf{x}_i, t) = 0$. In figure 3, values for α_i have been assigned using the data in ref [13], whereas in figure 4, all $\alpha_i = 0$.

From figures 3 and 4, it can be seen that changing the values of α_i has a profound effect on the network dynamics. For larger α_i (Figure 3) and excitatory interactions, the stress field is increasingly smoothed and the earthquakes tend to be larger ("decreasing complexity"). For smaller α_i or even inhibiting interactions, the stress field tends to roughen (Figure 4) and the corresponding events are smaller ("increasing complexity"). With smaller α_i (Figure 4), the various fault segments tend to behave more independently than for larger α_i (Figure 3). One can speak of a "roughness length" for the stress field similar in many respects to a correlation length [23, 24]. We predict that physical manifestations of friction laws on faults are revealed by the space-time patterns in the network dynamics. Dynamical switching of activity due to fault interactions should also be observed. An example is shown in figure 3, in which the south-central region of the San Andreas (left arrow) tends to switch off activity on the eastern Garlock fault (right arrow). Dynamical switching of activity may have already been revealed through observations of real fault networks [3,9]. We are not at present aware of any existing observations in nature relating to stress smoothing or stress roughening transitions. Similar smoothing and roughening processes for the cellular potential should be present in neural networks due to the current leakage through the cell membrane.

Acknowledgments. Research by PBR was supported by the Southern California Earthquake Center (Contribution 540) under NSF grant EAR-8920136. Research by JBR was funded by USDOE/OBES grant DE-FG03-95ER14499 (theory), and by NASA grant NAG5-5168 (simulations). Research by WK was supported by USDOE/OBES grant DE-FG02-95ER14498. KFT and SM were funded by NGT5-30025 (NASA), and JdsM was supported as a Visiting Fellow by CIRES/NOAA, University of Colorado at Boulder. We would also like to acknowledge generous support by the Maui High Performance Computing Center, project number UNIVY-0314-U00.

References

- [1] Y. Bar-Yam, *Dynamics of Complex Systems* (Addison-Wesley, Reading, MA, 1997).
- [2] H.F. Nijhout, L. Nadel, D.L. Stein, *Pattern Formation in the Physical and Biological Sciences* (Addison-Wesley, Reading, MA, 1997).
- [3] R. A. Harris, *J. Geophys. Res.*, **103**, 24347 (1998).
- [4] C.H. Scholz, *The Mechanics of Earthquakes and Faulting* (Cambridge University Press, Cambridge, UK, 1990).
- [5] D.D. Bowman, G. Ouillon, C.G. Sammis, A. Sornette and D. Sornette, *J. Geophys. Res.*, **103**, 24359 (1998).
- [6] J.B. Rundle, W. Klein, D. L. Turcotte and B. Malamud, *Pure. Appl. Geophys.* (in press)
- [7] S.J. Gross and C. Kisslinger, *Bull. Seism. Soc. Am.*, **84**, 1571 (1994).
- [8] J.B. Rundle, W. Klein, K.F. Tiampo and S.J. Gross, *Phys. Rev. E*, **61**, 2418 (2000).
- [9] R.S. Stein, *Nature*, 402, 605 (1999).
- [10] J..J. Hopfield, *Physics Today*, **47**, 40 (1994).
- [11] J.B. Rundle, *J. Geophys. Res.*, **93**, 6255 (1988).
- [12] S.N. Ward, *Bull. Seism. Soc. Am.*, **90**, 370 (2000).
- [13] J. Deng and L.R. Sykes, *J. Geophys. Res.*, **102**, 9859 (1997).
- [14] B.N.J. Persson, *Sliding Friction, Physical Principles and Applications* (Springer-Verlag, Berlin, 1998).
- [15] J. Dieterich, *J. Geophys. Res.*, **84**, 2161 (1979).
- [16] S. L. Karner and C. Marone, in *GeoComplexity and the Physics of Earthquakes*, ed. JB Rundle, DL Turcotte and W. Klein (Amer. Geophys. Un., Washington DC, 2000)
- [17] W. Klein, JB Rundle and CD Ferguson, *Phys. Rev. Lett.*, **78**, 3793 (1997).
- [18] JB Rundle, W.Klein, M. Anghel, J. de sa Martins, to be published.
- [19] LB Grant and K. Sieh, *J. Geophys. Res.*, **99**, 6819 (1994).
- [20] D. Massonet and K.L. Feigl, *Rev. Geophys.*, **36**, 441 (1998).
- [21] JD Eshelby, *Proc. Roy. Soc. Lon. Ser.A*, **241**, 376 (1957).
- [22] H. Kanamori and DL Anderson, *Bull. Seism. Soc. Am.*, **65**, 1073 (1975).
- [23] JB Rundle, E. Preston, S. McGinnis and W. Klein, *Phys. Rev. Lett.*, **80**, 5698 (1998).
- [24] To be published.

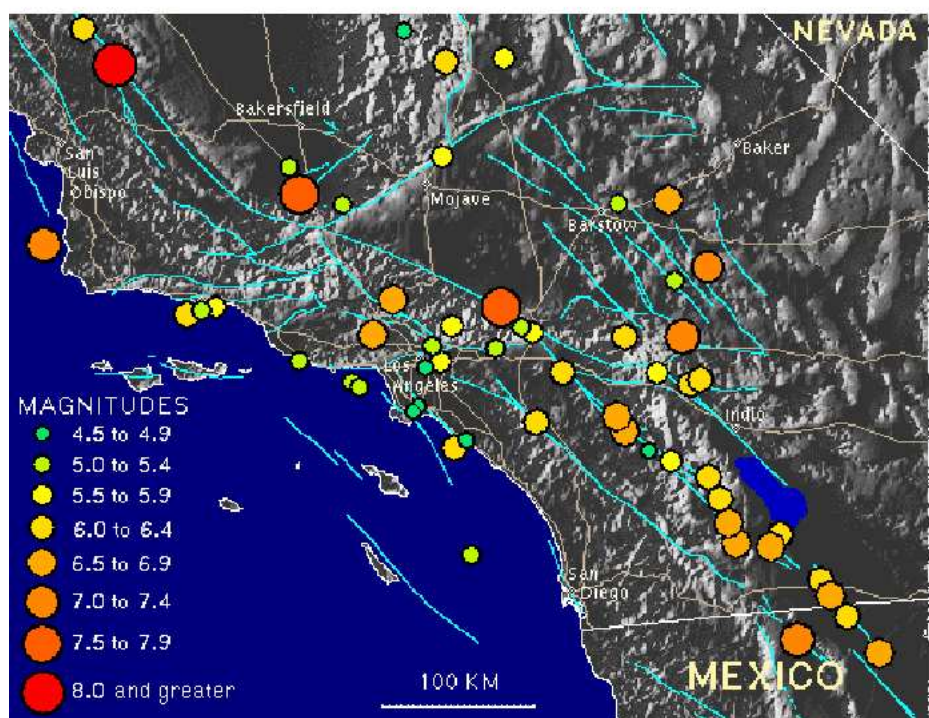
Figure Captions.

Figure 1. Map of the major faults (blue lines) in southern California, together with largest historic earthquakes (colored circles) occurring since 1812 (from <http://www.scec.org/clickmap.html/>)

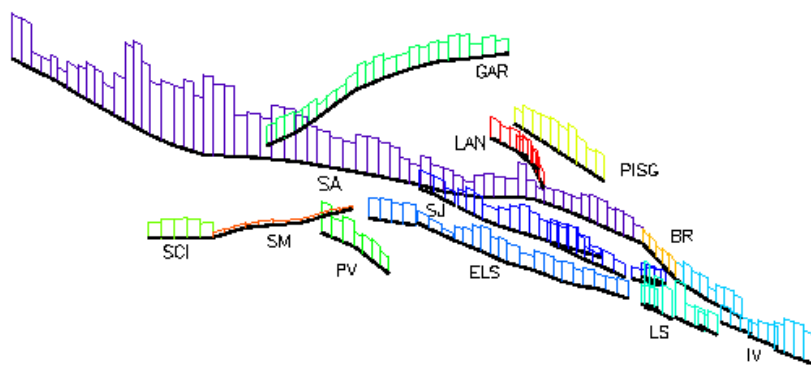
Figure 2. Major strike-slip faults in southern California used in the model. Relative scaled values of friction difference ($\mu_s - \mu_k$) are shown superposed above each fault. (Fault Key: SA, San Andreas; SJ, San Jacinto; ELS, Elsinore; IV, Imperial Valley; LS, Laguna Salada; GAR, Garlock; PV, Palos Verdes; SC, Santa Cruz Island; PISG, Pisgah; BR, Brawley; SM, Santa Monica; LAN, Landers)

Figure 3. Plot of Coulomb Failure Functions plotted as a function of time vs spatial location for 2000 simulation years for a set of values $\{\alpha_i\}$ obtained by approximately matching the ratio of aseismic creep to seismic slip on various fault segments from tabulated data in ref [13]. We actually plot $\text{Log}\{1 - \text{CFF}(x,t)\}$ so that subtle differences can be seen. Low CFF(x,t)'s are represented by cool colors, high CFF(x,t)'s near 0 are represented by hot colors.

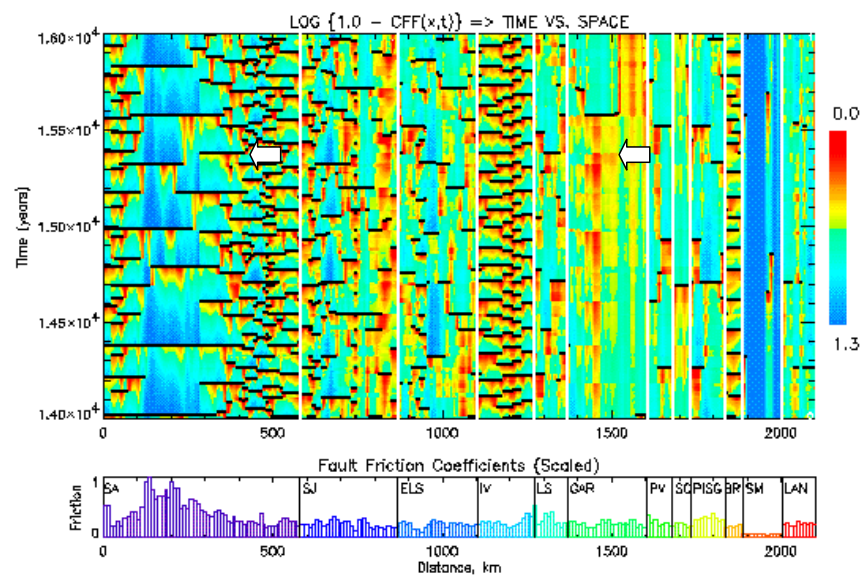
Figure 4. Same as figure 3 but with all $\alpha_i = 0$.



10



Color-Coded Fault-Friction Map



12

